THE UNIVERSITY *of* EDINBURGH

Disentangling composite forcings on river channel steepness in heterogeneous landscapes

Boris Gailleton

Submitted for the degree of Doctor of Philosophy

The University of Edinburgh

2020

Abstract

Early geomorphological studies quickly realised the close relationship between the geometrical characteristics of river networks with the geological, tectonic and climatic context of the regions the river crosses - the most striking example perhaps being the upstream migration of steepened reaches (or "knickpoints"), which rejuvenate landscapes following a base level change via faulting or eustatic variations. Amongst all the morphologies related to the river network, channel gradient has been a particularly important one: following the observation that declivity enhances erosion, any forcing affecting the channel slope potentially also affects erosion and creates a signal that can be interpolated through space and time to reconstruct climatic or tectonic events modulated by local lithology. Parallel to these qualitative observations, geomorphological studies developed tools and metrics to quantify the large-scale shape of river long profiles. Rivers systematically steepen towards the headwaters, which makes the direct use of river slope difficult, so several authors successfully developed a semi-empirical relationship describing the systematic increase of channel gradient with a power-law relationship. This relationship links the steepening component (k_s) to the rate at which slope increases as drainage area decreases (θ); later followed by a normalised river length coordinate χ. Later work on this topic demonstrated a positive relationship between these metrics and the underlying tectonic or lithologic forcings, allowing the systematic comparison of different field sites across the world and large-scale testing of the early qualitative observations. The rise in availability of global scale Digital Elevation Models and external proxies to quantify exhumation/erosion rates (e.g. thermochrononometers, CRN), has made such large scale studies increasingly fast and accessible, making the geomorphometrics described above widely used as spatial and temporal interpolations of tectonics and climatic variations. However, (i) the metrics are affected by different forcings, meaning that a single morphology can be generated by a range of different factors and hence potentially misinterpreted, and (ii) θ varies spatially and will determine

the normalisation parameter to calculate k_s and χ. This thesis focuses on developing and applying tools to investigate the different expression of these metrics in heterogeneous landscapes. First, I describe an algorithm to extract and quantify knickpoint morphologies. The aim of this algorithm is to allow the objective comparison of knickpoints in different contexts. They are quantified using k_s and sudden changes in elevation in order to detect the location and the magnitude of the knickpoints. I explore the performance and limitations of the algorithm in different settings, and describe how to constrain and interpret this novel work. Secondly, I explore the spatial variability of θ in order to achieve multiple goals. (i) I develop and thoroughly test a method to finely explore the variations of θ while also assessing how a specific θ value fits a watershed in case a non-optimal value has to be fixed. (ii) From the observed range of θ variation, I analytically and numerically explore how a non-optimal θ can affect k_s and χ, respectively. I identify cases where this caveat can lead to the generation/exaggeration of spurious signals or to the diminution/inversion of existing ones. Thirdly, I apply such algorithms, alongside with field measurements and observations, in a heterogeneous landscape: the eastern Carpathians. The eastern Carpathians are highly heterogeneous with (i) sharp lithologic contrasts, (ii) high spatial and temporal contrasts in vertical motion, and (iii) spatially variable θ. I demonstrate with systematic comparison of steepness across θ with lithologic and tectonic forcings that in that case lithology is the dominant forcing expressed in k_s, although tectonic forcing can be retrieved. I discuss and successfully integrate my conclusions into local tectonic models and show larger scale implications for interpreting these metrics.

Lay summary

The Earth's surface, referred to as surface topography, sits at the interface between the atmosphere and the rock substrate. Its shape is ultimately a result of the competition between the factors controlling the two. Climate affects the the topography by determining the amount of water available in an area, as well as the rate of soil creation via precipitation intensity, temperature, wind or other processes. The rock substrate is emplaced by deep processes such as faulting or folding which change the surface. Theses are ultimately controlled by large-scale plate tectonics pulling, pushing and deforming continents on geological timescales. They also juxtapose different kind of rocks, which affect the surface topography by inducing differential resistance to erosion: granite, for example, does not respond to erosion the same way clay does. Interconnection between surface and deep processes means that one can get some information about long term tectonics by studying the surface of the earth. This is particularly important as the latter is easily accessible information compared to buried rocks affected by processes acting on million year timescales. This accessibility has been revolutionised in the past decade by the relentless development of satellites and numerical methods. The first provides spatially continuous access to the topography of the whole earth while the second provides the means to process such datasets. Unravelling tectonic information, such as the timing and extent of active faulting, is important to manage seismic hazard, whereas understanding how tectonics shape the topography is important in terms of flood dynamics and associated hazards.

Among all the morphologies and geographic features composing a landscape, the river network is the most efficient in term of conducting erosion, and research has focused on relating its shape to tectonics. The base principle is straightforward: steeper rivers have more erosive power, and tectonic motions tend to steepen the landscape. Tectonic motion therefore "fires" migrating steepened reaches upstream of the displacement and can theoretically be reconstructed even

if the tectonic event happened millions of years ago. However, rivers do not yield such information easily as the river slope is closely related to the size of the river, and hence to its location within a watershed. In addition, as tectonics is not the only forcing affecting river gradient, it can be challenging to be certain that a steepening is due to tectonic events. This thesis challenges existing methods extracting channel steepness by (i) developing methods to quantify and compare channel steepness at large scales, and (ii) to use these methods to unravel tectonics from fluvial morphology in a heterogeneous landscape, the Eastern Carpathians, where different rock types are closely associated with active faulting.

After detailing the literature background and the numerical method utilised in the work, I firstly describe a novel algorithm extracting the location and magnitude of the boundaries between steepened reaches. These boundaries are very important to precisely identify the reaches affected by past events, and the new techniques focus on providing an objective and well-constrained method. Secondly, I explore the spatial variability of a normalisation parameter used to compare river morphology across different locations. Controls on this parameter are only partially understood, and I focus my work on objectively constraining it as a first step. I then extract it in thousands of watersheds across the globe and detail its range of values. I finally assess the impact of using a wrong normalisation and the subsequent distortion of normalised metrics. Thirdly, I demonstrate that in the Eastern Carpathians, tectonic signals are overprinted by lithology in the river morphology. However, I also demonstrate that systematic and careful assessment of the river gradient, combined with lithologic analysis, allows the isolation of the tectonic signal from the more prominent lithologic one. Finally I discuss the global implications of this thesis for geomorphological research and future work.

Version Française:

La surface de l'écorce terrestre se trouve à l'interface entre l'atmosphère et le substrat rocheux. Les processus affectant ces deux entités se contrebalancent pour créer la forme de cette surface. Les processus climatiques modulent l'efficacité de l'érosion de surface, via l'intensité des précipitations ou des taux de production de sol. Le substrat rocheux est mis en place par les processus

tectoniques profonds. Ces derniers sont contrôlés par la tectonique des plaques a large échelle, qui pousse, tire et déforme l'écorce. Ces mêmes processus juxtaposent différent types de roches ensemble, participant passivement aux formes de la surface topographique et régulant l'érosion, un granite ne s'érodant pas de la même manière qu'une argile par exemple. Cette inter-convertibilité est très importante, puisqu'elle permet d'étudier des changements de régimes tectoniques à partir de la forme des paysages. C'est particulièrement intéressant puisque ces mouvements tectoniques se déroulent sur des millions d'années alors que la forme des paysages est accessible à échelle mondiale. Cette accessibilité a été accrue ces dernières décennies par un constant progrès dans les équipements satellitaires et informatiques. Les premiers permettent d'accéder numériquement à la forme des paysages sur l'entièreté du globe alors que les seconds donnent les moyens de traiter ces informations. Extraire des informations sur l'activité tectonique, telle que la localisation et l'intensité des failles de surface, est cruciale pour estimer les risques sismiques. Comprendre les différents facteurs contrôlant la topographie de la surface terrestre est également important: cela module les flux d'eau et de sédiments et donc le risque d'inondations.

Parmi toutes les différentes entités composant un paysage, le réseau de rivières est le moteur érosif le plus efficace. Le principe de base est assez simple: une rivière plus pente est plus à même d'éroder son substrat puisqu'elle procure des écoulements plus rapides. Puisque les mouvements tectoniques vont changer la topographie terrestre, ils vont aussi déclencher la formation de tronçons de rivières plus pentées qui à leurs tours migrent vers l'amont par érosion régressive. Ces morphologies peuvent être "inversées" et permettent de retrouver l'origine et l'intensité du mouvement tectonique. Cependant, les rivières ne révèlent pas cette information facilement: la pente d'une rivière est aussi affectée par l'importance des rivières au point de mesure et de la quantité d'eau disponible. Des méthodes de normalisations doivent être utilisées pour exploiter les résultats, affectant la donnée de base. De plus, il n'est parfois pas évident de déterminer si la tectonique est la cause principale régissant la forme des rivières, quand différentes roches se juxtaposent par exemple. Cette thèse étend les connaissances liées à la

compréhension des différents facteurs affectant la forme des rivières de plusieurs manières. Premièrement cette thèse décrit de nouvelles méthodes pour décrire objectivement et quantitativement ces morphologies et deuxièmement, elle démontre l'importance de considérer diffèrents facteurs conjointement pour expliquer les formes fluviales dans un terrain très hétérogène: les Carpates de L'Est, ou le type de roche vari spatialement avec l'activité des failles.

Après une revue des travaux existant et des méthodes numériques utilisés dans cet ouvrage, je décris le développement d'un algorithme extrayant les limites géographiques des tronçons de rivières avec différentes pentes. Cet algorithme est optimisé pour dépeindre objectivement leurs localisations et l'intensité du changement de pente. Ensuite, j'étudie et explore les variations du paramètre optimal de normalisation des pentes. Il est important de comprendre comment cette normalisation varie, puisqu'elle est utilisée pour uniformiser les interprétations tectoniques à différentes échelles. Je démontre l'ordre de magnitude à laquelle il varie à échelle mondiale puis quantifie les distorsions liées à une mauvaise normalisation. Enfin, je montre que dans les Carpates de l'Est, les différences de types de roches sont le facteur principal contrôlant les morphologies fluviales. Je démontre cependant qu'une caractérisation systématique des pentes normalisées et corrélées aux différentes unités lithologiques permet d'extraire le signal tectonique malgré son caractère secondaire. Enfin, j'intègre les résultats de cette thèse dans un contexte global et suggère les futurs axes de recherches.

Declaration

I declare that this thesis has been composed solely by myself, and that it contains only my work except where otherwise specified, or where the work is explicitly indicated below to have formed part of a jointly-authored publication. This work has not been submitted for any other degree or professional qualification.

Boris Gailleton

April 2020

Acknowledgements

This PhD would not have been possible without the Brodbingnagian support of far too many people to all be mentioned here, but I will give it a go. I would like to point to any reader of my PhD thesis that I wrote these acknowledgments last minute after months of intense writing and lockdown, I barely expect these to be intelligible and they are also obviously not hierarchical. First I would like to thank my supervisors for their outstanding supports and for being a never-ending source of inspiration. I am very grateful to Hugh Sinclair for all the very motivating and fruitful research meetings we conducted during these years. Hugh reminded me the importance of keeping processes in mind even when focusing on methods as well as being incredibly supportive and approachable. Finally he demonstrated me that my sense of organisation and planning should not harm my academic career. I hope to keep on working with him in the future. I would also like to thank Simon Mudd. First for introducing me to C++, python and the crucial importance of reproducibility and open-source science, I am not actually sure I should thank him regarding the obsession I developed for these subjects but I am very happy with it. I would also thank Simon for the impressive imitations of nearly all existing accents he made through all our meetings and for many scientific advices, which truly shaped what will hopefully become my research career. I know I will keep on working on many subject with him! I would finally like to thank Mikael Attal, for sharing relentless enthusiasm and funny anecdotes withal, as well as for his inspirational scientific rigour. I also thank Liviu Matenco for the very important advising role and the outstanding presentation of the Romanian Carpathians on field. I know I will keep on working with all of you in the future.

J'aimerais aussi bien entendu remercier ma fiancée Delphine, pour son soutien inconditionnel (passé et futur) et pour avoir supporté mon charabia à propos de chi, de souris et d'ours et d'avoir enduré avec moi la distance. Je n'aurais jamais eu la motivation ou la volonté de faire une thèse sans elle. Tant que je parle

français, je tiens aussi à remercier mes parents, JJ et Cécile, pour m'avoir inculpé l'esprit scientifique et la curiosité de la nature depuis mon enfance ; ainsi que ma sœur Karen, mon frère Bastien, Lulu, Jacques, mes cousins, tantes, oncles, nièce, ... pour toutes les conversations de familles sur WhatsApp (et dans la vrai vie aussi hein !) qui m'ont grandement aidé pendant la réalisation de ces recherches. Pour en finir avec le français, je suis très reconnaissant envers le soutien apporté par mes amis de l'université et d'avant, en particulier Dumbledore's b*****s et the WRONG CONV and Sans Cassou et al.,2029 dont le flot incessant de messages a été source sure de divertissements et d'évasion pendant ces années.

I would also like to thank all the colleagues/friends (the difference is hard to make there) who worked with me during this PhD. Emma Graf for the exceptional support, the hours of proofreading, teaching me how to knit because why not, for the hours of fun during covfefe and during all the dinners (although I know Will was the one cooking, thanks Will, and for being my personal barber as well!). Laura Quick for the crucial support she brought during these years and all the "I have a stupid question" which were not stupid and very agreeable to answer. I would also really like to thanks Fiona Clubb for all the coffee break At the start of my PhD and her patience teaching me LSDTopoTools, Lauren for the nice bullying and English grammar/vocabulary help, Monika for being the last EU survivors of Lower Lewis (Nedo tikatise), Louis for the many words I can now use to get kicked out of any moderated chat, the Lower Lewis crew Charlie, Polly, Rosie, Delf, Josh, Paul, Damon, Luca, Lizzie, Alexis; the Saint Kilda friends Aythya, Andy, Marina, Thomas, Guillaume (see section about field assistants), Goris, Dave, Rowan, and probably many people I forgot to mention here. I would really like to thank non-Drummond people with who I had a lot of pleasure working with: Becky, Jorien, Chrystiann, Stuart, Martin, Daniel. I really thanks as well all the SUBITOP persons who with I really enjoy having trainings and fruitful debates. Niels and Micha deserves a particular thank for handling the organisation of the network. Finally I would address a special thanks to my flatmates Michael, Josh, Emiel, Rene, Lou, Sally and unnamed mouse for all the Mario Kart and very enjoyable weekends/evening which kept me going

through most of my PhD, and the recent lockdown. I really hope to see/work with all of you again soon.

I would like to address special thanks to my field assistants for enduring my organisation of Romanian trip: Guillaume "his name is not Will" Goodwin even though he manage to break an impressive amount of field equipment and blame me for it (fake news); Antoine Auzemery even though I claimed many more nests, hotels and stokes than him but I forgive him for failing to overpass me; and finally Laura for the "sieve and feed straight dogs" field trip. I would also thank Elaine McDougall for processing my sample in the lab, keeping me updated with all the stages and finally for some very motivating chats. Finally I would like to thanks many academics I met conferences and trainings and inspiring/motivating me in my research: Luca Malatesta, Jean Braun, Benoit Bovy, Sean Willett, Jeroen Van Hunen, Duna Roda-Boluda, Louise Slatter, ...

I really want to hand in now, but I feel that I have not said enough about each of you! Let's have a special tribute to Johnathan "Johnny" Clegg for his music but also his very inspiring philosophy. The 30,000 hours of listening time in the sole 2017 year should be enough to testify I really enjoy his music and could not have written without it. Right, I am deeply sorry for anyone I forgot. Time to hand in. I might add some after the corrections.

List of Figures

Contents

List of Tables

Chapter 1

Introduction

1.1 Overview

The surface topography of the Earth is dictated by the relentless competition between deep and surface processes. The deep processes, ultimately driven by long recognised plate motions (Wegener and Skerl, 1925), generate surface motions *via* various processes such as faulting or folding. These motions redistribute mass over the Earth's surface with the creation of mountain ranges and sedimentary basins (*e.g.* Dickinson, 1974). Surface processes gradually try to re-equilibrate the system through erosion and sediment transport (Allen, 2017). This constant struggle for balance has been a keystone for landscape evolution studies highlighting that information about deep processes could be unravelled from topography (*e.g.* Hurst et al., 2013; Kirby and Whipple, 2012; Mudd, 2017). Surface processes even have the ability to affect the long-term deep processes: as advection fluxes accrete material to the mountain wedge during subduction and collision, the overall steepness of relief increases and reach critical stages at which it cannot be sustained and has to widen (*e.g.* Dahlen, 1990). The overall relief of the mountain is then controlled by the ability of the mountain range to reach this critical state before expanding. Surface processes modulate this ability *via* lowering the slope through erosion and actively affecting the rates of mountain building (*e.g.* Avouac and Burov, 1996a; Willett, 1999). The system then tends toward a steady states where surface processes balance the motions, until external or inter-

nal forcings change the system (Willett and Brandon, 2002b). In the surroundings of these reliefs, isostasy and lithospheric flexure balance the mass excess of the topographic growth with the creation of basins and subsequent accommodation space (Beaumont, 1981; Naylor and Sinclair, 2008). These basins will receive the mass excess from the mountain and the surface process control the basin geometry by their ability to evacuate the erosion products of the mountain, which itself will affect the overall relief of the region (Tucker and Beek, 2013). Isostasy also produces relief via responding to the removal of dense materials from an area by surface processes, initiating in rare cases deeper processes (Braun et al., 2014).

River networks in mountain ranges are the main engines of erosion in unglaciated landscapes (Ahnert, 1970), and early geomorphologists quickly recognised the potential of linking river landforms with geological processes. This is mainly linked to the recognition that "declivity" enhances erosion, as stated by Gilbert (1877). As tectonically induced vertical motions can steepen the landscape, changes in river steepness potentially relate to present or past tectonic activity, and in contrast with the sparse distribution of geological outcrops, topography offers a spatially continuous dataset over the Earth's surface. This empirical observation leads to the establishment of tectonic geomorphology as a discipline and the recognition of key geomorphological features as markers for external forcings, including tectonics. For example Davis (1889) recognised the importance of waves of rejuvenation following a base level change due to tectonic or climatic forcings, the waves being expressed as migrating steepening which separates an "older", smoother, upstream landscape to an "newer", sharpened downstream one. Knopf (1924) identified the fluvial boundary between the two landscapes as key indicator for unraveling the timing of the perturbation, and named the morphology knickpoint, from the German word "inflexion point", due to its convex up morphology contrasting with the usual concave up shape river long profiles. This is just an example of key relations between fluvial morphology and external forcing making the basis of modern geomorphology, already recognised at the time (Lapparent and Lapparent, 1896).

Relating fluvial geomorphology to deep processes beyond qualitative concepts

is not an easy task. With the exception of extreme events (e.g. Baynes et al., 2015; Howard and Kerby, 1983), most of river incision happens at non-observable timescale, this is also true for surface expression of deep processes. Estimation of exhumation rates and erosion rates became respectively possible with the development of thermochronology (e.g. Gleadow et al., 1983) and exposure dating (e.g. Lal, 1991). Exhumation at geological timescales became possible to link with millenial-scale erosion rates and subsequently river geometry, with the recognition that contrasts in river gradient could be directly correlated with rock uplift (Burbank et al., 1996; Harkins et al., 2007). Parallel to the direct measurement of rates, numerical experiments of river evolution through time developed semi-empirical laws to simulate erosion rates through long timescales and characterise the theoretical response of river morphology to tectonic forcings (e.g. Howard and Kerby, 1983; Lague, 2014; Tucker and Slingerland, 1996). The increase in available global satellite data providing continuous information about earth surface topography (e.g. Farr et al., 2007) allowed the systematic comparison of fluvial morphology with theoretical behaviours and measured rates (Wobus et al., 2006c). However, quantifying river morphology to make these comparisons possible is complicated by the fact that river channels get steeper toward the headwaters. Comparing gradients is quickly obscured by that fact (Wobus et al., 2006c). To circumvent that issue, a number of studies (e.g. Flint, 1974; Morisawa, 1962) focused on representing the river network with comprehensive metrics allowing consistent comparison of river shape across the scales, the aim being to provide independent geometrical description of the profile before relating it to processes. They suggested that reaches of river long profiles reveal a systematic power-law relationship between river gradient and its discharge, or its proxy drainage area. Two parameters quantify the reach morphology: k_s, or steepness index, which account for the overall steepness of the reach no matter its value of drainage area; and θ, or concavity index, which represents the rate at which slope decreases as drainage area increases. More recently, Perron and Royden (2013) developed a third related metric χ which allows for the direct integration of concavity and drainage area in a transformed coordinate and the

representation of transformed long profiles with river of different size normalised to a common referential. These metrics have been widely correlated with external proxies for external forcings and successfully unravelled tectonics from topography (e.g. Kirby and Whipple, 2012; Perron and Royden, 2013; Wobus et al., 2006a), correlating with erosion rates at global scales (e.g. Harel et al., 2016).

If tectonics is an important forcing controlling channel morphology, it is not the only one. Lapparent and Lapparent (1896) already recognised the effect of "passive tectonic" on river morphology with inactive faults and folds still shaping the landscape by juxtaposing different rock strength or fracture zones. This is relatively instinctive, as harder fresh rocks are harder to erode than fractured soft rocks and require steeper rivers. A number of studies highlight the importance of lithologic forcing on channel steepness, with a recent focus on the subject (e.g. Bernard et al., 2019; Bishop, 2007; Campforts et al., 2019; Duvall, 2004; Gabet, 2019). Similar observations can be made on climate, which regulates the amount of water available and hence the discharge, affecting channel steepness at lesser extent (e.g. Crosby and Whipple, 2006; Perron, 2017). Equal combinations of k_s, θ and χ can translate into multiple combinations of forcings, leading to ambiguous interpretations of their genesis. It is not straightforward to make sure the signals observed are not spuriously related to the wrong forcings (e.g. Gabet, 2019). In addition, a methodological limitation within the method itself adds some uncertainty. In order to interpret χ and k_s across different locations, they need to be calculated with a fixed θ value (Wobus et al., 2006c). This last metric is strongly suspected to vary spatially (e.g. Mudd et al., 2018; Tucker and Whipple, 2002) and k_s and χ will inevitably be calculated with non-adapted θ when studying multiple watersheds. It is not straightforward to anticipate the magnitude of the subsequent distortion linked to non-adapted θ and it raises the question whether the values falling under such conditions are expressing actual geomorphic processes or mathematical artefacts.

This thesis builds on existing knowledge and studies about unravelling forcings from k_s, θ and χ to challenge their application in heterogeneous landscapes, where multiple forcings and factors jointly affect these metrics. First, it reviews

the theoretical background about channel steepness and its application: how it has become an important metric and how it relates to either differences in rock strength, differential rock uplift or base level change for example. Then, I explain in detail the methods used to systematically quantify these metrics and I detail the numerical framework I used to develop my tools. In term of methodological development, I first describe the development of an algorithm determining the objective location and magnitude of the main break in slope in landscape. I then explore the spatial variability of θ and the extent of the distortion resulting from not constraining its value on χ and k_s. Finally, I challenge the use of the geomorphometrics to unravel tectonics information in the Eastern Carpathians, where lithologic and tectonic forcings vary at short wavelength. Global implications of this thesis' results and future work about the understanding of channel steepness are finally stated.

1.2 Theoretical background

1.2.1 Early geomorphology

The keystones on which fluvial tectonic geomorphology relies on have been established before the 20^{th} century. This thesis does not intend to provide a full review of the history of geomorphology, but rather to give a rapid overview of key qualitative principles which lead to modern studies. The dynamic nature of topography, *i.e.* the constant and gradual adaptation of the surface of the Earth to external forcings has long been recognised. For example Buffon (1767), reported that over the lifespan of a man, the church of a neighbouring village became apparent after the height of the hill separating the places lowered of few metres. They deducted that the river at the bottom of the hill steepened the hill slope via eroding its base and gradually decaying its overall height. Gilbert (1877) stated "We have already seen that erosion is favoured by declivity. Where the declivity is great the agents of erosion are powerful; where it is small they are weak; where there is no declivity they are powerless", recognising the importance of channel gradient and its link to erosion. Such work led authors such as Davis (1889)

or Knopf (1924) to conclude that landscapes could be rejuvenated by tectonics event through the process of changing relative base level. Hence, older rounded landscapes could be made sharp and high again under the effect of a rejuvenation wave following the fall of a base level relative to an area. This fall could correspond to a climatic event and the variation of sea level, or tectonic event with the activity of a fault. In his review about physical geography, Lapparent and Lapparent (1896) expand on this observation, suggesting that steepened reaches applying the rejuvenation waves were modulated by local conditions. They separate the effect of "active tectonics" and "passive tectonics". The term active tectonics is here slightly different than the present-days definition which describe ongoing vertical motions. Here, active is related to any vertical movement that is or has been generated by tectonics. It describes any fault-related change of base level. Passive tectonics refer to any element put in place on the landscape and affecting the morphology. It includes folding, fracturing or juxtaposing of different rock types. They argue that these factors are equally important when considering the interpretation of fluvial land forms. They even suggest that differential lithology could by itself generate migrating reaches, taking as example the Niagara falls (Ontario, Canada) which are retreating through a single rock layer (Gilbert, 1877). The importance of channel gradient alongside with the role of tectonics and local geological context echo the present study of geomorphology which takes advantage of computation and digital elevation model to quantify and globalise these early qualitative principles.

Early quantification of river profiles and the development of mathematical expressions

Parallel to early observations linking river network morphology to landscape evolution and geological characteristics, authors from agricultural and hydrological fields began to take an interest in quantifying large-scale river geometry and relating this to surface processes. Quantity, quality and chemical composition of water received by a farmland are important factors in soil cultivation, sustaining industries and providing water supplies to the population. The first careful at-

tempts to quantify bulk watershed dynamics aimed to understand the controlling factors on water and sediment fluxes in order to better manage water supplies for irrigation, power production or transport of material and goods. As one example amongst many, Forbes (1902) measured and linked the drainage area, precipitation, discharge and river length of major rivers in Arizona (USA), in order to approximate how nutrients and pollutants would spread within the irrigation network. Glenn (1911) systematically related "stream erosion" and "surface erosion" (respectively within and in between the rivers) to local geological conditions in order to enhance the comprehension of erosion in the Appalachian region. They established local relationships between drainage area and river and hillslope gradient to quantify, and possibly predict, local erosion in a semi-qualitative manner (*i.e.* without systematic or global representation of the data). Later, studies like Duley and Miller (1923) conducted experiments on agricultural soils and quantified erosion function of runoff, precipitations, area and topographic gradient in an experimental agricultural soil.

These selected examples depict a growing trend in the scientific literature of the early 20th century: calculating river characteristics (*e.g.* river gradient or discharge) and relating them to surface process efficiency for particular locations. However, these studies were case specific and did not attempt to place observations in a global context. In order to compare specific systems to each others, one needs to take a level of abstraction from specific cases and develop generic metrics to ensure comparability. Another factor that complicates making the analyses of channel gradient more general at the time: Houk (1918) highlighted the technical difficulties encountered when gathering data, particularly river slope, and the inaccuracies mainly linked to the small magnitudes of river gradients.

1.2.2 Quantifying the shape of rivers

The difficulties related to gathering data and the need to compare the results across field sites highlight the necessity of developing methods allowing comparison of entire river networks or long-profiles. This is required in order to understand the different forcings affecting fluvial geomorphology. The most logical

way to achieve that goal is to mathematically express the shape of river profiles. Thus, the river is described with objective parameters, variations in which can be interpreted as meaningful forcings or process changes. This section presents a variety of studies which have undertaken this exercise with different approaches. It focuses on the reasoning that led to a comprehensive and meaningful expression of channel morphology.

Early mathematical expressions of river long profiles

One of the first studies, if not the first as suggested by Shulits (1936), indirectly attempted to mathematically express large-scale river long profiles developed from from the field of hydrology and the study of the sediment transport within rivers. In their seminal paper, Sternberg (1875) suggested a semi-empirical equation describing the fining rate of pebbles in rivers:

$$P(x) = P_0 e^{-ax} \tag{1.1}$$

where P is the weight of the pebble at distance x from its source, P_0 the original weight of the pebble at the source and a a coefficient of abrasion depending on the physical properties of the pebble (*e.g.* lithology, shape). This law has become a reference in modelling grain size evolution in rivers (*e.g.* Attal and Lavé, 2006). Assuming that the river width increases downstream and that particle movement increases proportionally with flow velocity, Sternberg (1875) determined a semi-empirical law describing the slope of the river profile function of distance and grainsize. Shulits (1936) expresses a simplified version of the equation as:

$$S(x) = S_0 e^{-ax} \tag{1.2}$$

where S_0 is the original slope at $x = 0$. With $S = \frac{dz}{dx}$ and z being the elevation of the river bed, Shulits (1936) integrates the equation to express $z(x)$:

$$z(x) = -\frac{S_0}{a} e^{-ax} + C \tag{1.3}$$

where $C = z_0 - \frac{S_0}{a}$) if we define z_0 the elevation at $x = 0$. This leads to the

general equation:

$$(z_0 - z) = (\frac{S_0}{a})(1 - e^{-ax}) \tag{1.4}$$

which describes the elevation of a river as a function of distance. Equation 1.4 can be used to approximate river profiles or reaches, and Shulits (1936) applied the same formula to foresee the effect of cutting off a meander on the downstream slope. Later, Shulits (1941) (and references therein) tested and reviewed worldwide existing river long profiles in the literature with this equation. They concluded that it successfully approximates their shape and was suitable to apply to river engineering projects. Long river profiles estimated after this equation is illustrated on Figure 1.1.

Parallel to this approach, a geology-orientated geomorphological study by Jones (1924) expressed a different mathematical equation for river long profiles. With their study of the Upper Towy drainage network (Wales, UK), they aimed to use the shape of the drainage system to determine the causes of dissection by rivers of a plateau in Wales. Jones (1924) demonstrated that the shape of the river long profiles, very tedious to calculate from contour maps or field data, could be approximated by smoothing a curve through regularly spaced points. This way, they were able to estimate with reasonable accuracy the average slope and the elevation at different points of the profile – they recommended every $\frac{1}{5}^{th}$ miles for this particular study. They further suggested fitting a logarithmic curve through the points with the equation:

$$z(x) = c - k\log[x + a] + b(x + a) \tag{1.5}$$

with a, b, c and k constants. Jones (1924) argued that $b = 0$ if the outlet of the river is the sea. With equation 1.5, the study "*strikingly shows*" the changes in gradient on the river profile. After a sharp decrease within the two first miles of the headwaters, gradient would diminish slowly toward the mouth of the river. Jones (1924) also used the overall shape of that profile to depict a difference between the river profile and its vicinity with the surrounding plateau, suggesting

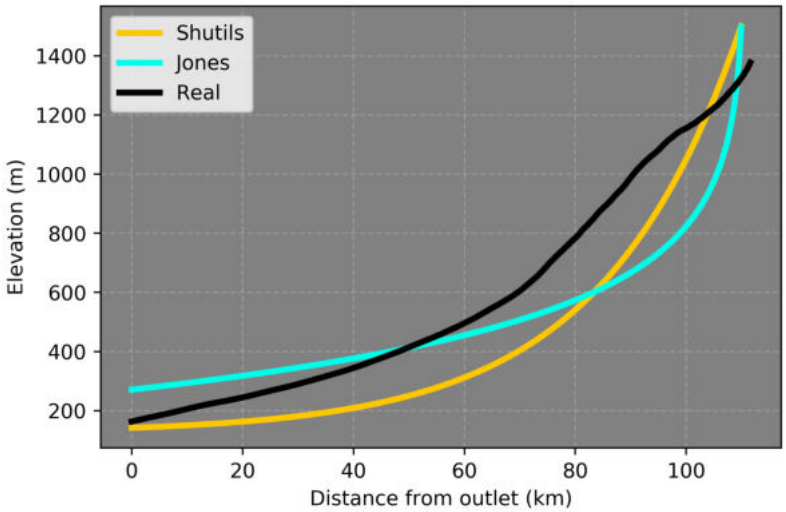

Figure 1.1: River long profiles estimated with the equations 1.4 and 1.5 compared to a long profile extracted from a real landscape (Putna river, outlet close to Focşani, Romania). The real profile has been chosen to represent a complex river profile to illustrate the difficulty of these laws to approximate "imperfect" rivers. For Shutils, I used $z_0 = 1500$, $S_0 = 0.055$ and $a = 4e^{-5}$; for Jones, I used $a = 600$, $b = 0$, $c = 3000$ and k=235. The constants are arbitrarily chosen and different combination of values could give reasonable profiles.

both morphologies being linked to separated events. Long river profiles estimated after this equation is illustrated on Figure 1.1.

These two early studies were the first attempts and examples to express river long profiles; later works developed many different laws to approximate river profiles with different exponential, power and logarithmic fitting methods (Ohmori, 1991) . Ohmori (1991) reviewed the different laws and applied them on a number of rivers in Japan. They concluded that these laws could be used, amongst other applications, to determine the migration of depositional reaches. However they also pointed out a limitation: models approximating river profiles as a whole continuous equation are not wholly compatible with the graded nature of rivers. In addition, these different approximations rely on a high number of different constants, which are difficult to relate to processes and forcings, as illsutrated on Figure 1.1.

The concept of graded rivers was developed by Mackin (1948), based on earlier work from Gilbert (1877) and Davis (1889). It described the concept of a graded

river as a stream, or part of a stream, with stream power just sufficient enough to transport all the supplied material from upstream, taking account of sediment load, discharge, underlying erosion, local slope. Mackin (1948)'s definition implies that river profiles can be separated into multiple reaches, with their own gradient, discharge, local erodibility, and other characteristics. Some of the reaches can be ungraded: they may either erode into the bedrock or aggrade by depositing sediments. Hence, describing a river profile with only equations used to describe a graded river is limiting. This either requires a high number of terms, constants or powers in order to approximate the river shape and any meaningful interpretation of these is tricky; or the simplistic approach only matches relatively homogeneous rivers with "ideal" long profiles. Additionally, the geometry of the whole river network will affect the river profiles themselves, and two "similar" rivers in terms of characteristics can show different profiles linked to different tributary junctions. I direct the interested reader towards Horton (1945), who explored the varying geometry of river networks as a function of the stream position in the network (*i.e.* the stream order).

Drainage area as tool for generalising river morphology

Integrating information about the channel network, e.g., the structure of its tributaries, in representing its long profile can be made using the drainage area along the profile. In his seminal paper, Hack (1957) investigated relationships between a number of metrics derived from seven areas of Virginia and Maryland (United States of America). These metrics included aspects of the shape of the river itself and of the upstream network – *e.g.,* river width, channel gradient, length, or drainage area – but also intrinsic characteristics of the river, namely the discharge and the composition of the bed load. Systematic cross-correlations on scatter plots led Hack to the formulation of a now widely used relationship approximating the shape of the downstream evolution of drainage area with a power-law:

$$L = 1.4A^{0.6} \tag{1.6}$$

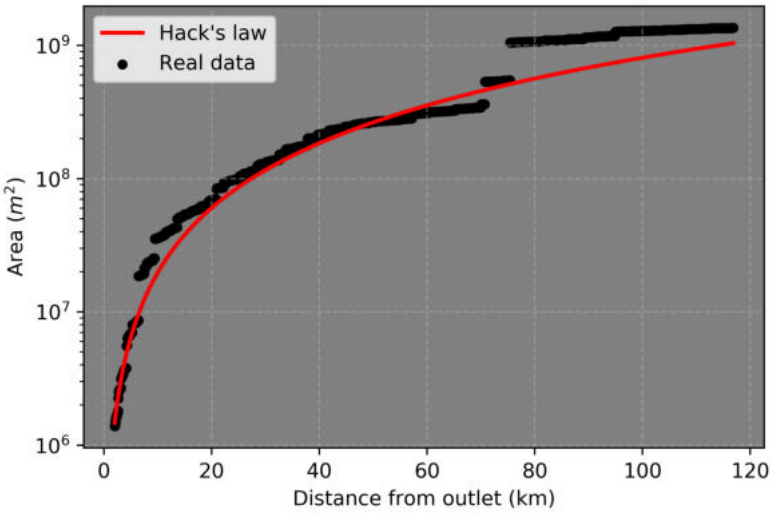

Figure 1.2: Drainage area data from a long profile extracted from a real landscape (Putna river, outlet close to Focşani, Romania), versus drainage area pattern estimated with Hack's law, using $h = 0.65$. Note how the approximation is accurate compared to the overall shape of the drainage area, but fails to account for jumps in drainage area.

where A is the drainage area and L the length of the river calculated from a chosen outlet and the river source. This has later been generalised into the widely used "Hack's law" (*e.g.* Maritan et al., 1996; Rigon et al., 1996; Willemin, 2000) and can be rewritten:

$$L \propto A^h \tag{1.7}$$

where h becomes a coefficient commonly between 0.5 and 0.6. Figure 1.2 illustrates Hack's law against real data.

Hack (1957) also determined case-specific power-law relationships relating grain size, bed load and channel geometry, suggesting that intrinsic forcings also play a role in shaping the river profiles. The same author later linked river length with its long profile geometry in Hack (1973), where he developed a method to extract the river gradient taking account of steepening along the river length with the following expression, as expressed in the original manuscript:

$$SL = \frac{\Delta H L}{\Delta L} \tag{1.8}$$

where SL is referred to as the stream-gradient index, H is the elevation at a point of the river profile and L the stream length. Hack (1973) suggests that this metric is useful to compare the steepness of streams of different length across large regions, and can be used to detect variations in geologic, climatic and intrinsic forcings of the river network. This approach has been used in later studies to unravel forcings on the river network (*e.g.* Chen et al., 2003; Font et al., 2010; Troiani and Della Seta, 2008).

However, comparing the length of a single river to its drainage area or slope is subject to several limitations. Rivers get steeper when reaching headwaters, *i.e.* as drainage area decreases. Although equation 1.7 suggests drainage area can be approximated as a function of river length, this only stands for one single river, as the geometry of drainage basins varies from one basin to another. The difficulty in generalising the expression of $A(x)$ is worsened by the ubiquitous occurrence of tributary junctions which result in jumps in A.

Toward a comprehensive expression of channel geometry

A comprehensive mathematical expression of river long profile geometry should therefore meet the following criteria: (i) It should be independent of the planform geometry of the river network; (ii) It should be able to be segmented for river reaches so reaches can be compared regardless of their position within the river network. The instinctive approach to tackle both of these points is to link the metrics to the river discharge, as this will ultimately control the stream power.

Shaler (1899) observed that channel gradient seemed to decrease as discharge increased. Leopold and Maddock (1953) stated a power-law relationship between mean river velocity (v) and discharge (Q) could be described as:

$$v = k_v Q^{m_v} \tag{1.9}$$

where k_v and m_v are constant for a given river reach, although Leopold and Maddock (1953) did not expand on the range of values for the constants. Later, Wolman (1955) linked the channel slope to mean velocity using the Chezy for-

mula:

$$v = C_{wol}\sqrt{RS} \tag{1.10}$$

where C_{wol} is a coefficient of resistance, R is the hydraulic radius – *i.e.* the area of the wetted cross section divided by the wetted perimeter (R is in dimensions of length) and S the channel gradient. Subsequent simplifications led to:

$$S = t_w Q^{z_w} \tag{1.11}$$

where t_w and z_w are constants. Wolman (1955) observed that slope systematically decreases as discharge increases, and related this pattern to sediment load. One of the limitations of this law is that it requires the computation of discharge. This typically requires expensive stream gauging instrumentation, to which which early geomorphological studies did not have access. This problem is tackled in another section of Hack (1957)'s seminal study, which proposed a number of relationships that would lay the groundwork for many future studies of fluvial geomorphology. First, Hack (1957) plotted the relatively instinctive observation (*e.g.* Lapparent and Lapparent, 1896) that drainage area could be successfully used as a proxy for discharge (Figure 1.3).

Secondly, Hack (1957) visualised channel gradient and drainage area in log scale. All of the rivers investigated in their study suggested a power-law relationship between slope and drainage area. Drainage area and slope, respectively, decrease and increase at a certain rate when reaching headwaters following a non-linear power-law. This is illustrated in Figure 1.4.

Hack (1957) did not attempt to generalise this relationship. Instead, he correlated the slope, $S(x)$, and the drainage area, $A(x)$, to the grain size of the bed load:

$$S(x) = 18(\frac{M}{A(x)})^{0.6} \tag{1.12}$$

with $M(x)$ being the median particle size in millimetres. However, the observation that A could be an effective proxy for Q led Morisawa (1962) to explore

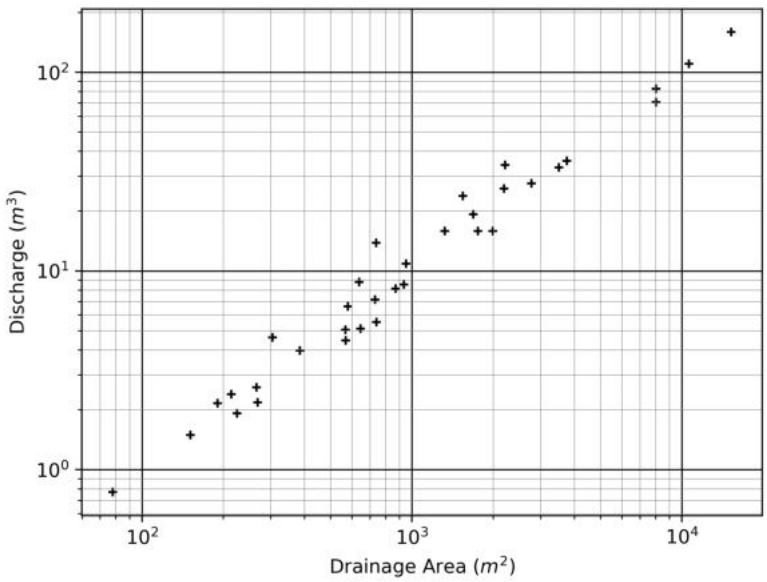

Figure 1.3: Linear relationship between drainage area and discharge observed from field measurements. Adapted from Hack (1957).

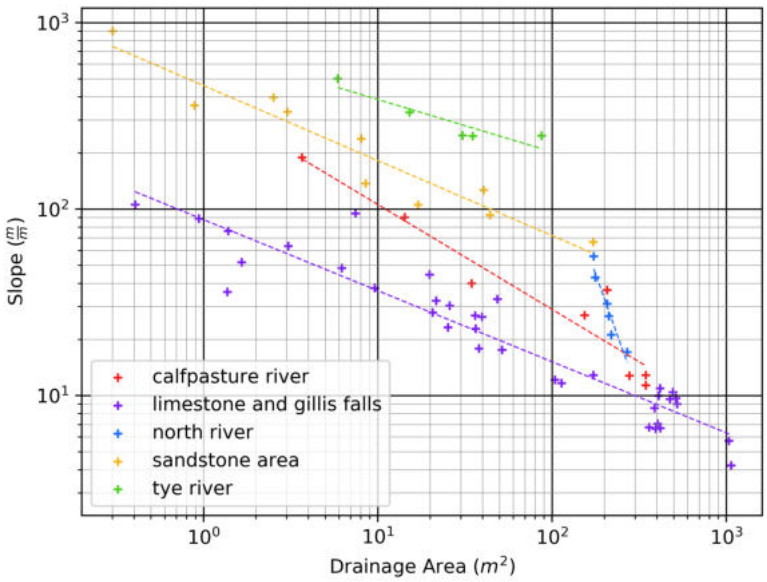

Figure 1.4: Relationship between river slope and drainage area in log space. Adapted from Hack (1957).

this relationship in the Appalachian Plateau. They suggested that a number of observed relationships followed a power law under the general form:

$$Y = aX^b \tag{1.13}$$

where X and Y are two morphometrics, and a and b constants valid for a river, or a reach. Morisawa (1962) explicitly mentioned that this law could be applied with $S(x)$ and $A(x)$ and that constant values could be extracted. They did not directly write the relationship, however equation 1.13 with $Y = S$ and $X = A$ assuming that $A \propto Q$ as suggested in Figure 1.3, this relationship reverts to equation 1.11. Flint (1974) later expressed that law directly, although with more constants:

$$S = t_f a_f^{x_f} A^{x_f z_f} \tag{1.14}$$

where t_f is the stream slope for a certain discharge, a_f and x_f are constants linked to the relationship between discharge and drainage area, and z_f a negative exponent equal to the rate of change of gradient with discharge. Tarboton et al. (1992), based on observations from Leopold and Miller (1962), Leopold and Maddock (1953), and Wolman (1955), simplified the equation in:

$$S = C_t A^{-\theta} \tag{1.15}$$

where C_t is a constant encompassing a number of characteristics including channel steepness and θ an exponent, which the authors suggest to be linked to ratios of tributary slopes and area across the network. Later works (Wobus et al., 2006c, and references therein) reformulated equation 1.15 into the widely used form:

$$S = k_s A^{-\theta} \tag{1.16}$$

where k_s is the steepness index, *i.e.* the steepness of the river reach normalised for a given rate of changes in drainage area, and θ is the concavity index which represents the rate at which the channel gradient decreases as drainage area

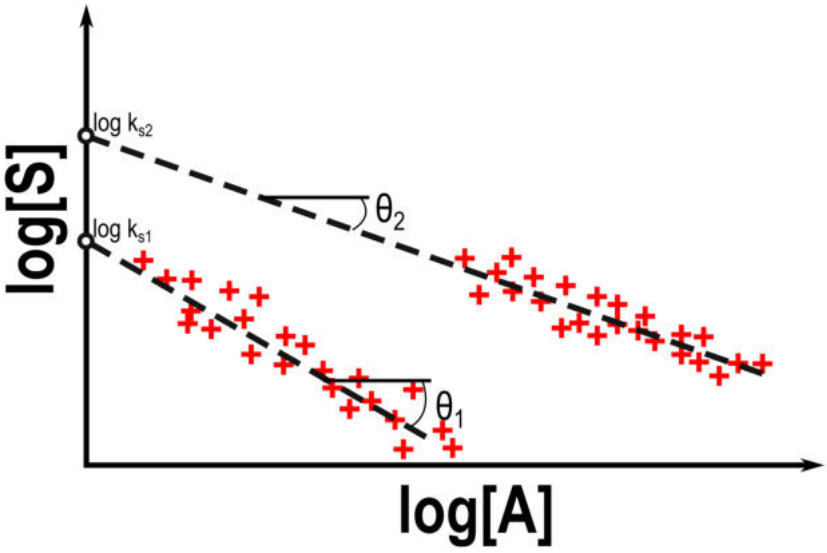

Figure 1.5: Linear relationship between drainage area and discharge observed from field measurements. Adapted from Hack (1957).

increases. k_s and θ provide two metrics allowing comparison of river reaches in different contexts achieving the needs described at the start of this section. Figure 1.6 illustrates the expression of k_s and θ on a slope area plot.

It is important to note that k_s, in order to be comparable across different areas, needs to be calculated with a fixed value of θ. θ can be considered as the "normalisation" parameter of the slope, to the rate at which it increases as drainage area decreases. If θ varies spatially and k_s is calculated with different values of θ, the values of k_s can range over several orders of magnitude just as an artifact of choosing a different value of θ (see equation 1.16. To circumvent this issue, a method has been suggested by Sklar and Dietrich (1998): k_s and θ can be calculated for a reference slope S_{ref} at a chosen reference drainage area A_{ref}:

$$S_{ref} = k_s A_{ref}^{-\theta} \tag{1.17}$$

and systematic variations of θ and k_s can be interpreted for streams of similar size. This method has been used in a few studies (*e.g.* Kirby et al., 2003; Sklar and Dietrich, 1998), but restricts the comparison to a fixed drainage area which restricts the possibility of applications, especially across basins of different size. The most common method suggested by Wobus et al. (2006c) consists in fixing

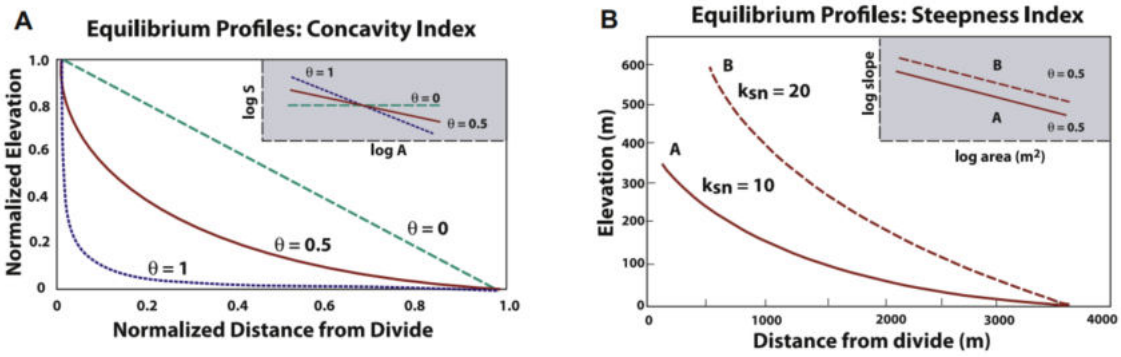

Figure 1.6: Expression of θ (A) and k_{sn} (B) on synthetic river profiles. Adapted from Kirby and Whipple (2012).

a reference value for θ in order to calculate k_s using the same reference value of θ, θ_{ref}:

$$S = k_{sn} A^{-\theta_{ref}} \tag{1.18}$$

where k_{sn} stands for normalised channel steepness. Although widely used (Kirby and Whipple, 2012, and references therein), this method suffers from the limitation that it does not account for spatial variations in θ and may calculate k_{sn} with a non-optimal normalisation parameter. The implications of varying θ_{ref} on the interpretation of landscapes is explored in Chapter 4.

These metrics have been widely applied to interpret variations in channel geometry in terms of forcings and processes (*e.g.* Kirby and Whipple, 2012; Wobus et al., 2006c). The aim of this section is to explore ways in which to quantify the geometry of the channel network and compare values across field sites. The applications and links to forcings and processes are explored in a later part of this chapter.

Recent development of the integral approach

Recent studies (*e.g.* Mudd et al., 2018, 2014; Perron and Royden, 2013; Wobus et al., 2006c) suggest a number of limitations to using the S–A relationship directly. The geometric limitations are mostly linked to two aspects. First, any dataset used to calculate channel gradient is subject to inevitable topographic

noise linked to data acquisition (*e.g.* Schwanghart and Scherler, 2017) which implies the use of data processing techniques to use the data. This inherently leads to data losses and approximations. This point is more thoroughly explored in Chapters 3 and 4. Secondly, using the S–A to visualise the data can make the interpretation more difficult when dealing with more than one river. Visualising river long profiles allows simple comparisons between data points and their location in the landscape, but S–A data does not yield this information easily, as many points will show similar area, and both slope and drainage area are not "instinctive" metrics to read from a DEM.

To circumvent these limitations, Royden et al. (2000) and later Perron and Royden (2013) introduced a transformed coordinate which directly normalises the distance from outlet to a concavity index, allowing one to account for changes in concavity to be directly integrated into a transformed long profile. First, equation 1.16 can be rewritten:

$$\frac{dz}{dx} = k_s A^{-\theta} \tag{1.19}$$

where z is the elevation of the river bed and x the distance from outlet. Following the formulation adopted by Whipple et al. (2017b), one can integrate equation 1.19, resulting in

$$z(x) = z(x_b) + \left(\frac{k_s}{{A_0}^{\theta}}\right) \int_{x_b}^{x} \left(\frac{A_0}{A(x)}\right)^{\theta} dx, \tag{1.20}$$

where A_0 is a reference drainage area, introduced to nondimensionalize the area term within the integral in equation (4.3). One can then define a longitudinal coordinate, χ:

$$\chi = \int_{x_b}^{x} \left(\frac{A_0}{A(x)}\right)^{\theta} dx. \tag{1.21}$$

The coordinate χ has dimensions of length, and is defined such that at any point in the channel:

$$z(x) = z(x_b) + \left(\frac{k_s}{{A_0}^{\theta}} \right) \chi. \tag{1.22}$$

Using χ allows finer representation of k_s while integrating θ directly within river profiles. The main drawback is that θ needs to be fixed to a reference value, the consequences of this caveat are explored in Chapter 4.

The field of geomorphology has been revolutionised by the ever-increasing availability of Digital Elevation Models (this particular point is developed in the next chapter). It has allowed geomorphologists to thoroughly explore χ and k_s at global scales. An number of studies have adopted this approach, with even world-scale studies comparing global values of k_s (e.g. Hilley et al., 2019) and χ (e.g. Giachetta and Willett, 2018c). The limitations and relevance of extracting these metrics at very large-scale with a constant concavity index is explored in Chapter 4.

1.2.3 Channel steepness as proxy for erosion

Developing robust landscape metrics to describe and compare river networks would be meaningless if they could not be correlated with processes and forcings shaping river profiles. Recent developments in quantifying exhumation across geological ages (*via* high to low-temperature thermochronometers), exposure and denudation rates at millenial scales (cosmogenic nuclides) have revolutionised the correlations between morphometry and processes (Bishop, 2007). I demonstrate in this section how channel steepness can be linked to erosion or incision rates at different scales, as prerequisite to link channel morphology to other forcings.

Expression of basin-averaged denudation rates in channel steepness

As stated in Section 1.2.1, it has been observed that "declivity enhances erosion" (e.g. Gilbert, 1877). Although k_s allows the systematic extraction of steepness across multiple river reaches of different size, the observation is particularly difficult to quantify as river incision rates or basin averaged erosion rates happen at timescales not observable by humans, with rare exception linked to extreme

events (*e.g.* Howard and Kerby, 1983), and cannot be directly measured from DEMs. However during the last two decades, progresses in cosmogenic nuclides (or CRN analysis) analysis lead to the development of methods to analyse basin-averaged denudation rates over timescales (*i.e.* 10^3 to 10^6 years) (*e.g.* Biermann and Steig, 1996).

The principle is based on cosmic rays altering the atomic composition of matter, generating unstable elements which decay through time. Measurements of the concentration of unstable nuclides cross-correlated with their half-life (*i.e.* the speed at which their concentration is divided by two) can unravel crucial information about the timing of a system, the most well-known application being the dating of archaeological objects using ^{14}C (*e.g.* Libby et al., 1949).

Applied to geomorphology, this method has been widely used to dates surface exposure of geomorphic materials (*e.g.* Hein et al., 2011) but can also be applied to relate to long-term erosion rates. Biermann and Steig (1996) suggests that ^{10}Be and ^{27}Al can be measured from the sediments of a river and represents average erosion rates of the upstream area. As they near the surface, rocks start to accumulate cosmic nuclides which when eroded to sediments are host to crucial information about the timing of exhumation. Rivers naturally mix sediment from all parts of the watershed, therefore can reveal the ranges of exposure time across the watershed and basin-averaged erosion rates can be determine, for the drained area above the sampling point (Figure 1.7).

Quantifying basin-averaged erosion rates makes it possible to compare channel geometry with erosion rates (Brown et al., 1995). Safran et al. (2005) first conducted this exercise by estimating erosion rates for 48 basins in the Bolivian Andes and comparing these rates with $k_s n$. They found a positive correlation between the two metrics (Figure 1.8).

Large numbers of studies have reported basin averaged cosmogenic nuclide concentrations over the past three decades, generating a database of denudation rates for a wide range of basins (Codilean et al., 2018, and references therein). The relatively high density of worldwide data allows a possible generalisation of Safran et al. (2005)'s observations at global scale. This is exactly the exercise conducted

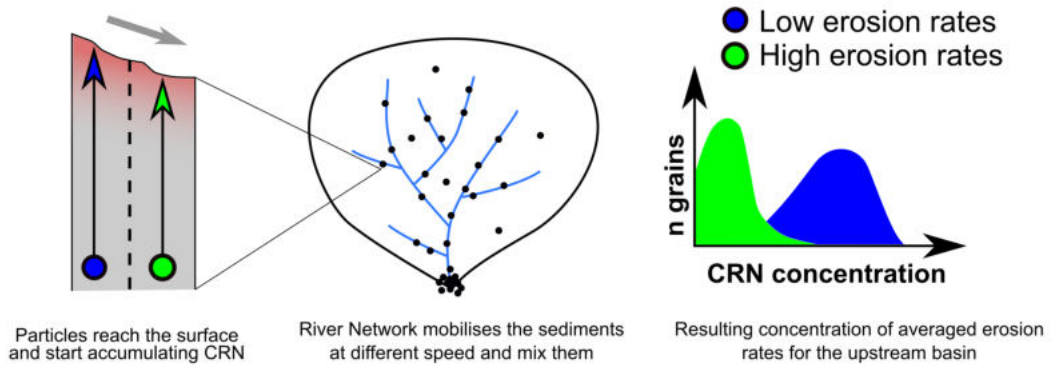

Figure 1.7: Simplistic illustration of the concept behind quantifying basin-average denudation rates using detrial cosmogenic nuclides. The colors represent two erosion rates. Fast eroding landscapes bring material faster to the surface and have less time to accumulate Cosmo-Radio Nuclides (CRN). When sampled at the outlet of a watershed, higher concentration of CRN can therefore be interpreted as slower erosion rates, as depicted on the right panel.

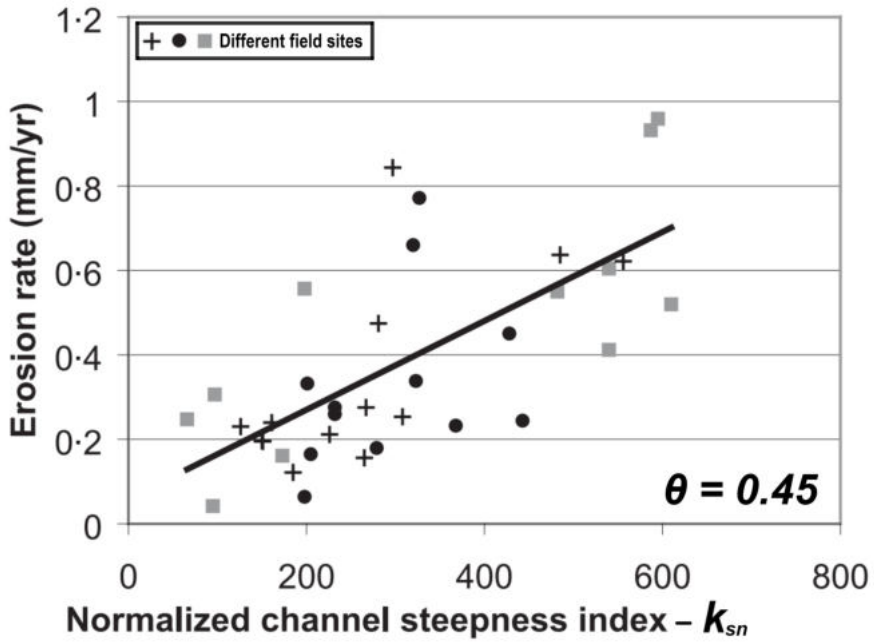

Figure 1.8: Normalised channel steepness index (k_{sn}) versus erosion rates derived from cosmogenic nuclides analysis. The different symbols are representing different field sites from the Andes, modified from Safran et al. (2005) for full details.

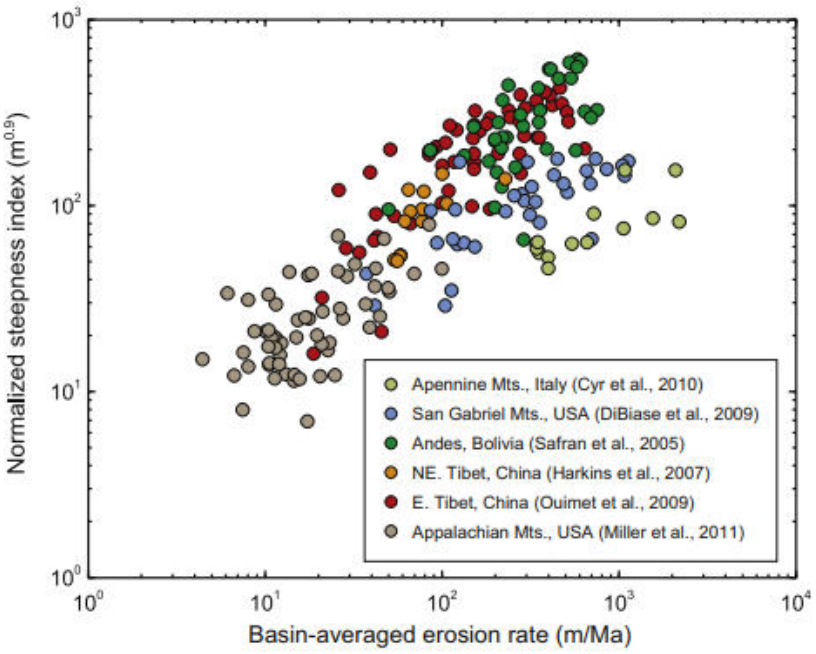

Figure 1.9: Normalised channel steepness index (k_{sn}) versus erosion rates derived from cosmogenic nuclides analysis at global scale, calculated from $\theta = 0.45$. From Kirby and Whipple (2012).

by Kirby and Whipple (2012) and Harel et al. (2016). Both of these studies explore the relationship between quantified erosion rates and channel morphology, relating them to several metrics, amongst them normalised channel steepness, their results are illustrated in Figures 1.9 and 1.10.

These studies show a broad positive correlation between k_s and denudation rates at basin scales. In addition, these studies also highlight that other factors are important in controlling both denudation rates and channel steepness, and therefore knowledge about the geological and geographical context of the river system is required to interpret such values. Harel et al. (2016) determined subsets of the global dataset where the dominant forcing is suggested to be respectively climate, tectonic activity and lithologic contrasts.

Calculation of CRN-derived denudation rates is also subjected to potential biases. The denudation rates are calculated from quartz particles or quartz-rich sediments (*e.g.* Biermann and Steig, 1996; Brown et al., 1995; Lal, 1991) which by definition only take account of the sections of the watershed bearing quartz-rich rocks and is subjected to biases when rocks show differential quartz content.

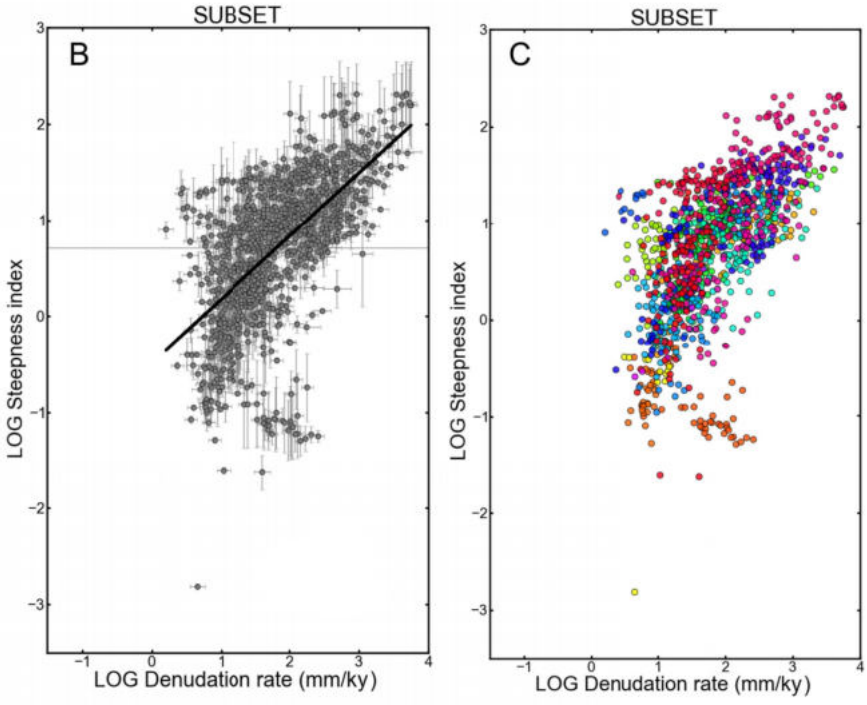

Figure 1.10: Normalised channel steepness index (k_{sn}) versus erosion rates derived from cosmogenic nuclides analysis at global scale, each color correspond to a site with the same θ. Modified from Harel et al. (2016).

Variety amongst sediment production and transport to and in the rivers can also introduce biases in the measurements: stochastic events such as landslides can, in particular, alter the process or generate ambiguous signatures (*e.g.* Dingle et al., 2018; Niemi et al., 2005; Yanites et al., 2009). Finally some factors can affect production rates (*i.e.* how much nuclides are generated) and therefore the spatial validity of the measurement, topographic shielding being the most prominent example (*e.g.* Brown et al., 1995).

Theoretical expression of erosion through channel steepness

This thesis does not attempt to provide an exhaustive review of the different laws modelling erosion and landscape evolution at long timescale (e.g. Davy and Lague, 2009; Lague, 2014; Whipple, 2004). However, as expressed in the previous sections and by many literature reviews (*e.g.* Kirby and Whipple, 2012), power laws can provide relevant approximations of some geomorphic processes and shapes. They have been successfully used to demonstrate key aspects of

understanding the numerous forcings and processes expressed through channel morphology (*e.g.* Attal et al., 2011; Braun et al., 2014; Davy and Lague, 2009; Mudd, 2017; Whipple, 2004) and can be used to a certain extent to demonstrate the geometric expression of some forcings and processes on river channel. Davy and Lague (2009) suggested a general formulation of the mass-balance equation governing the relationship between river and topography through time:

$$\frac{\delta z}{\delta t} = \frac{-\dot{e} + \dot{d}}{1 - \Phi} + T_U \tag{1.23}$$

where z is the elevation of the river bed, t is the time, $\dot{e}$ and $\dot{d}$ are respectively the erosion and deposition fluxes expressed in total volume of sediment eroded or deposited per unit of area and time, T_U is the relative uplift to a reference (*e.g.* representing fault displacements or sea level variations) and Φ is the sediment mass porosity which to converting of sediments into topography and accounting for volume change. Most of the Landscape Evolution Models follow such equation, eventually coupled with hillslope processes (*e.g.* Mudd, 2017). Studies test different ranges of forcings to observe the morphological expressions generated. The differences between models lie in the exact expressions of the fluxes and their numerical implementations both altering the results (Armitage, 2019).

Erosion fluxes are determined by the ability of the river to incise into bedrock or mobilise sediments of the bed load (*e.g.* Lague, 2014; Wickert and Schildgen, 2019). It can, however, be estimated using the widely used stream power-law, first suggested by Howard and Kerby (1983) work on a newly created badland landscape following the stripping of vegetation on a field in Virginia (United States of America). (Howard and Kerby, 1983) had the rare opportunity to observe the erosion on a very soft landscape over time, allowing him to formulate the equation fluxes function of river discharge and topographic slope. For consistency, we express here the generalised version of (Davy and Lague, 2009):

$$\dot{e} = KQ^m S^n - \dot{e}_c \tag{1.24}$$

where K is the erodibility, *i.e.* the erosion efficiency depending on the local

conditions (*e.g.* lithology, fracture density, climatic conditions), m and n are dimensionless exponents, and $\dot{e}_c$ a threshold limiting factor, representing for example the minimum amount of stream power necessary to enable erosion. The m, n and K constants are not straightforward to constrain (*e.g.* Croissant and Braun, 2014) and wide ranges of values have been suggested from independent constrains (Harel et al., 2016), as illustrated in figure 1.11.

Despite the difficulties in constraining parameters in the stream power law, some general geomorphic observations can guide its application. If we consider a simplistic landscape with negligible deposition and threshold processes, one can relate the channel steepness to erosion (see Mudd et al. (2014) for an example of derivation):

$$z(x) = z(x_b) + (\frac{E}{K A_0^m})^{-n} \chi \tag{1.25}$$

where A_0, x_b and χ are directly from equation 1.22 and 1.21. When calculated with $A_0 = 1$, k_s is the direct gradient of $z(\chi)$:

$$k_s = \frac{E}{K}^{-n} \tag{1.26}$$

This equation predicts a positive relationship between erosion rates and k_s, which is modulated by the exponent n. Direct correlations between channel steepness and erosion across a whole landscape, *i.e.* considering that steeper sections erode more, only holds if the erodibility coefficient K is constant. Of course, landscapes and river long profiles are controlled by more complex processes than solely simple river incision (*e.g.* Turowski, 2020), but threshold processes as well as deposition processes will only modulate that relationship in (at least partially) eroding landscapes (e.g. Gasparini and Brandon, 2011; Guerit et al., 2019; Wickert and Schildgen, 2019; Yuan et al., 2019). It implies that interpreting landscapes requires knowledge about the local conditions, in term of erodibility biases and depositions constrains. Once these factors acknowledged, k_s can be linked to erosion. This aspect is explored in chapter 5 more thoroughly using topographic analysis and field knowledge.

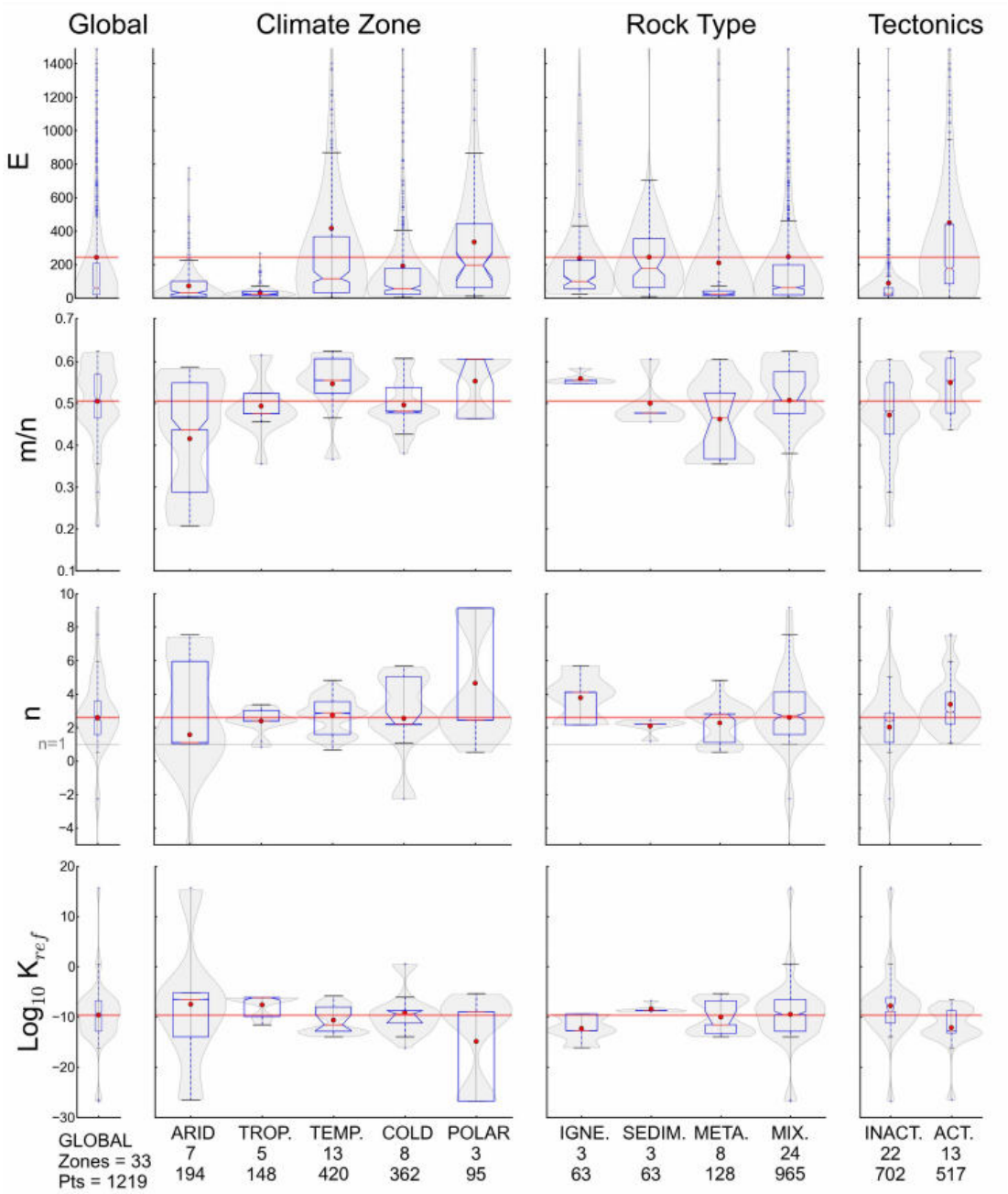

Figure 1.11: Ranges of values for the Stream Power-Law constants, derived from a combination of topographic analysis and CRN erosion rates for a selection of watershed by Harel et al. (2016). The watersheds have been separated by subsets whereby different forcings are dominant. E = Erosion rate; TROP.= Tropical; TEMP. = Temperate; IGNE. = Igneous; SEDIM. = Sedimentary; META. = Metamorphic; MIX. = Mixed; INACT. = Inactive and ACT. = Active.

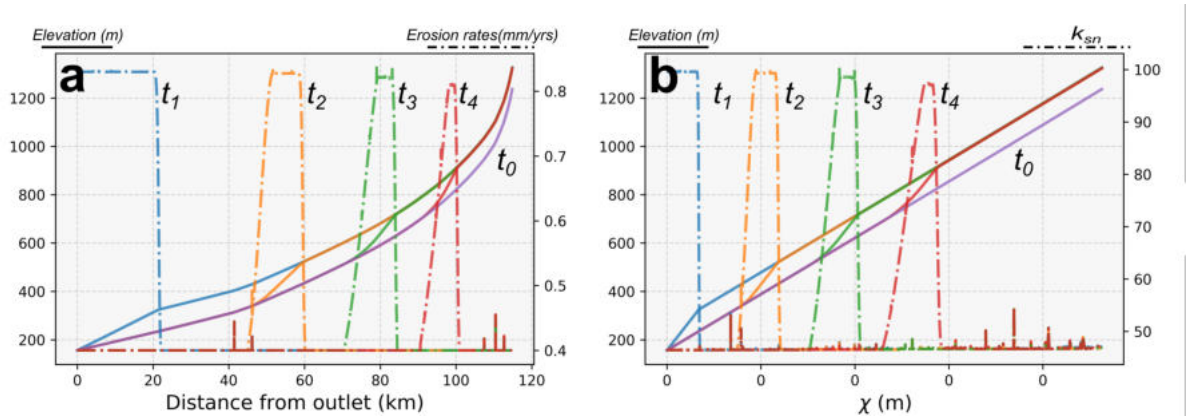

Figure 1.12: Erosional response to base level fall simulated with equation 1.24, with $\dot{e}_c = 0$, $n = 1.11$, $m = 0.5$, $K = 10^{-5}$ and $T_U = 0.001 m.yrs^{-1}$. a) illustrates the increase of erosion along the river long profile and b) represents the same river in χ - Elevation space, with k_{sn}. Note how k_{sn} and erosion are perfectly correlated. For the sake of illustrating the concept, equation is solved with a simple, explicit forward modelling scheme, with flow distance and drainage area extracted from the river described in Figure 1.1.

Recently, Whipple et al. (2017a) suggest a more general empirical relationship between erosion and k_s, based on different modelling laws:

$$\dot{e} = \alpha_w k_s^{f_w} \tag{1.27}$$

where α_w is linked to the erodibility properties (*e.g.* rock strength, fracture) and precipitation patterns (*e.g.* DiBiase et al., 2010; "Dominance of tectonics over climate in himalayan denudation" 2014; Kirby and Whipple, 2012; Scherler et al., 2014) and the exponent f_w is linked to interaction between erosion threshold and runoff variability (DiBiase and Whipple, 2011; Tucker, 2004). This formulation summarises the connection of erosion rates with channel steepness: positive correlation modulated by local intrinsic and extrinsic conditions.

1.2.4 Channel steepness as a proxy for tectonics

Erosion has been widely linked to tectonics for over a century (Davis, 1889; Gilbert, 1877; Lapparent and Lapparent, 1896), and authors have conducted quantitative studies using the morphology of a landscape to unravel displacement rates along faults (*e.g.* Lensen, 1964), demonstrating the links between

surface and deep processes (*e.g.* Willett, 1999). Amongst the tools used to link topography with tectonics, *sensu* active exhumation or surface uplift or timing and magnitude of past events, k_s has been a widely used tool that exploits the fact that river networks are the main engine of erosion in upland landscapes (*e.g.* F.J., 2017).

A number of seminal papers have developed, reviewed and challenged the use of k_s to unravel tectonics (*e.g.* Kirby and Whipple, 2012; Mudd, 2017; Whipple et al., 1999; Whipple, 2004; Wobus et al., 2006c). If one believes on the general formulation of the river evolution mass balance equation 1.23, then at topographic steady-state (*i.e.* $\frac{dz}{dt} = 0$) fluvial processes should perfectly balance the surface uplift generated by tectonic processes no matter which formulation of $\dot{e}$ or $\dot{d}$ (Willett and Brandon, 2002b). In a simplistic system following equation 1.24 with no threshold processes, channel steepness becomes:

$$k_s = \left[\frac{U(x)}{K(x)}\right]^{-n} \tag{1.28}$$

where $U(x)$ is the uplift rate in dimensions of length per time. This relationship predicts that k_s at steady-state, reflects a balance between surface uplift and local erosion, modulated by the n exponent. This observation has been also demonstrated for more complex formulations of $\dot{e}$ or $\dot{d}$ by Whipple et al. (1999).

Restricting the correlations between channel steepness and tectonics to steady-states would limit, or even eliminate, viable study sites, as steady-state landscapes often require stable conditions for unreasonable time to be achieved (*e.g.* Gasparini et al., 2007; Mudd, 2017; Whipple, 2004). Luckily, transient landscapes also hold information about tectonics, both where the landscape remains tectonically active or where the landscape is still equilibrating to past events (Kirby and Whipple, 2012). Both cases can also be analysed using the general mass-balance equation 1.23 without assuming specific formulations for $\dot{e}$ or $\dot{d}$, apart the reasonable assumption that they are both functions of discharge and channel gradient. Considering constant intrinsic conditions (*e.g.* lithology, upstream area, climate) at very short time step, any changes in base level linked to tectonics will generate contrasts in T_U at a discrete point. This contrast inherently increases local S

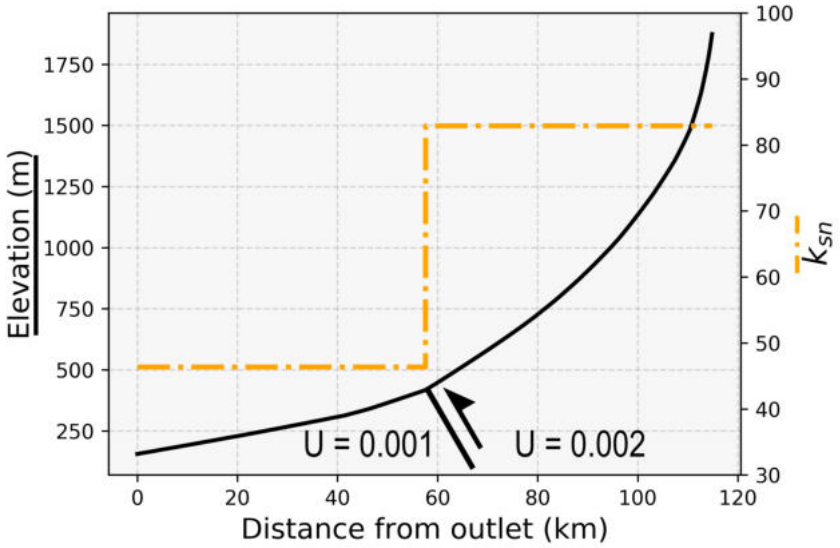

Figure 1.13: Erosional response to base level fall simulated with equation 1.24, with $\dot{e}_c = 0$, $n = 1.11$, $m = 0.5$, $K = 10^{-5}$ and $T_U = 0.001 m.yrs^{-1}$. a) illustrates the increase of erosion linked to the transient migrating reach through time on teh river long profile and b) represents the same river in χ - Elevation space, with k_{sn}. Note how k_{sn} and erosion are perfectly correlated. For the sake of illustrating the concept, equation is solved with a simple, explicit forward modelling scheme, with flow distance and drainage area extracted from the river described in Figure 1.1.

and/or Q and consequently increases erosion and/or reduces deposition at the immediate spatial and temporal vicinity of the tectonic contrast. This process sends tectonic signals upstream, changing the erosion and deposition state of the landscape and leaving morphological signatures. Inverting or retrieving these signals is therefore theoretically possible and this has been a keystone of geomorphological studies (*e.g.* Davis, 1889; Fox et al., 2014; Gilbert, 1877; Goren et al., 2014; Kirby and Whipple, 2012; Wobus et al., 2006c).

Unravelling tectonics from topography has indeed been an aspiration for many geomorphic studies. From the theoretical point of view, many studies (*e.g.* Whipple et al., 1999; Whipple, 2002; Wickert and Schildgen, 2019; Yuan et al., 2019) have been deriving the expression of k_s forced by tectonics from numerical models, deriving response time and magnitudes. These differ depending on many factors including sediment budget (*e.g.* Attal et al., 2011; Whipple, 2002; Wickert and Schildgen, 2019), local lithology (*e.g.* Campforts et al., 2019; Forte et al., 2016; Graf et al., 2017, this point will be developed in a later section), climatic (*e.g.*

Perron, 2017; Whittaker, 2012), stream piracy (*e.g.* Seagren and Schoenbohm, 2019; Whipple et al., 2017b) or model formulation (Lague, 2014). No matter which formulation is used, all the models demonstrate that reaches with different k_s can potentially be interpreted as sign of tectonics and highlight how crucial it is to be extracted (Kirby and Whipple, 2012).

Royden and Taylor Perron (2013) derive analytical solutions for the detachment-limited model and have highlighted the importance of detecting reaches with different k_s values, as well as their boundaries, to unravel meaningful tectonic signals from topography. They refer to these morphologies as "slope patches", which are defined as river segments with different k_s.

Although Royden and Taylor Perron (2013) confirm that k_s data could hold crucial tectonic information, they demonstrate that not all tectonic events will be retained: under some conditions slope patches can be overtaken and "erased" by adjacent slope patches. The evolution through time of the slope patches, and their potential to erase other slope patches, is controlled by the slope exponent of the stream power-laws. Royden and Taylor Perron (2013) demonstrate that if $n > 1$, concave-up knickpoints are preserved whereas concave-down knickpoints get consumed gradually. In contrast, when $n < 1$, only concave-down knickpoints are preserved, while concave up knickpoints get gradually stretched (Figure 1.14). Some authors (*e.g.* Fox et al., 2014; Goren et al., 2014) also suggested full numerical inversion of present-day topography to reconstruct rock uplift history in specific field site, but this approach requires many assumptions (discussed in the original manuscripts) and is difficult to generalise. They require, for example, the river network to be relatively static in map-view through time and the incision must be detachment limited.

Applications of the theory to real watersheds have lead to estimates of rock uplift. In one of the first studies correlating k_s to tectonic forcing, Kirby and Whipple (2001a) demonstrated that k_s in the Siwalik Hills (Himalaya, Nepal) reflected rock uplift rates estimated from independent data (Hurtrez et al., 1999). It requires however heavy calibration of detachment-limited constants and exponents. Lague and Davy (2003) demonstrated the same relationship, but suggested

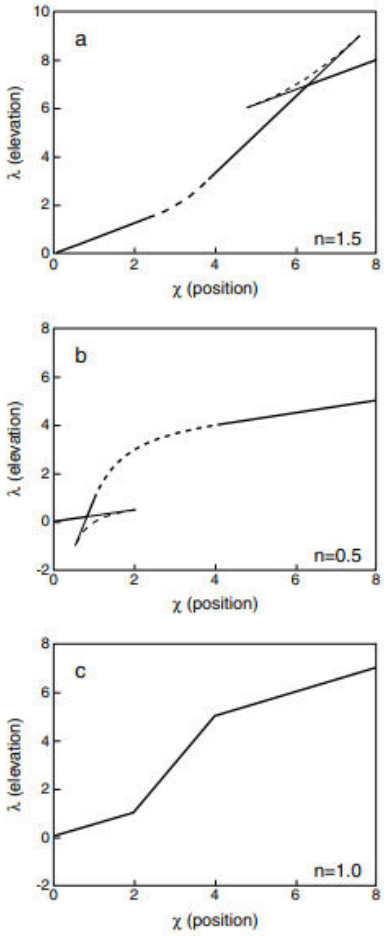

Figure 1.14: Illustration of slope patches and knickpoint through fluvial landscape evolution. Note the gradual alteration of the slope patches depending on n, the slope exponent of equation 1.24. λ is a dimensionless elevation used by the original author, full details and original figure from Royden and Taylor Perron (2013).

that calibration of the exponent should be constrained acknowledging geomorphic thresholds to translate meaningfully to erosion rates and rock uplift. This observation has been revisited by Kirby and Whipple (2012), who successfully reiterated such correlation on another segment of the Siwaliks Hills (Mohand anticline, India) and cross-correlated the results with incision rates derived from radio-carbon terrace dating and rock uplift derived from structural studies. Kirby and Whipple (2012) went on to demonstrate that k_s can be utilised to detect the active tectonics of the Main Frontal Thrust in the Himalaya, as well unravelling the timing and magnitude of fault displacements in the Saline Valley (United States of America) demonstrating a large spectrum of application correlating k_s to various tectonic processes.

Tectonics in transient landscapes requires calculation of k_s, as it sets the boundary conditions for hillslope processes. Identifying the different slope patches is therefore the prerequisite to relate to processes and forcings. For examples, Harkins et al. (2007) related k_s to rock uplift in the Tibetan Plateau (Tibet, People's Rebublic of China). They first identified a series of knickpoint along the main river and its tributaries separating two populations of channel steepness. k_s correlates well with the small variations of low erosion rates upstream of the knickpoints whereas it represents a balance between new uplift rates and waves of increased sediment fluxes downstream of the knickpoints.

Ouimet et al. (2009) reach similar conclusions in the Siwaliks Hills while demonstrating that hillslopes tend to converge toward a threshold, making fluvial geomorphology more adequate tool to unravel tectonics in this setting. This observation is shared in other setting as DiBiase et al. (2010) correlate short-scale tectonic gradient linked to the San Andrea fault (California, United States of America), to channel steepness and basin-averaged erosion rates while also demonstrating that hillslope processes failed to retain the same degree of tectonic information. Recent developments comparing hillslope morphologies with k_s (Clubb et al., 2020; Hurst et al., 2019) demonstrate that hillslope processes also retain tectonics information with a different response time and morphological expressions making the continuum river-hillslope providing complementary infor-

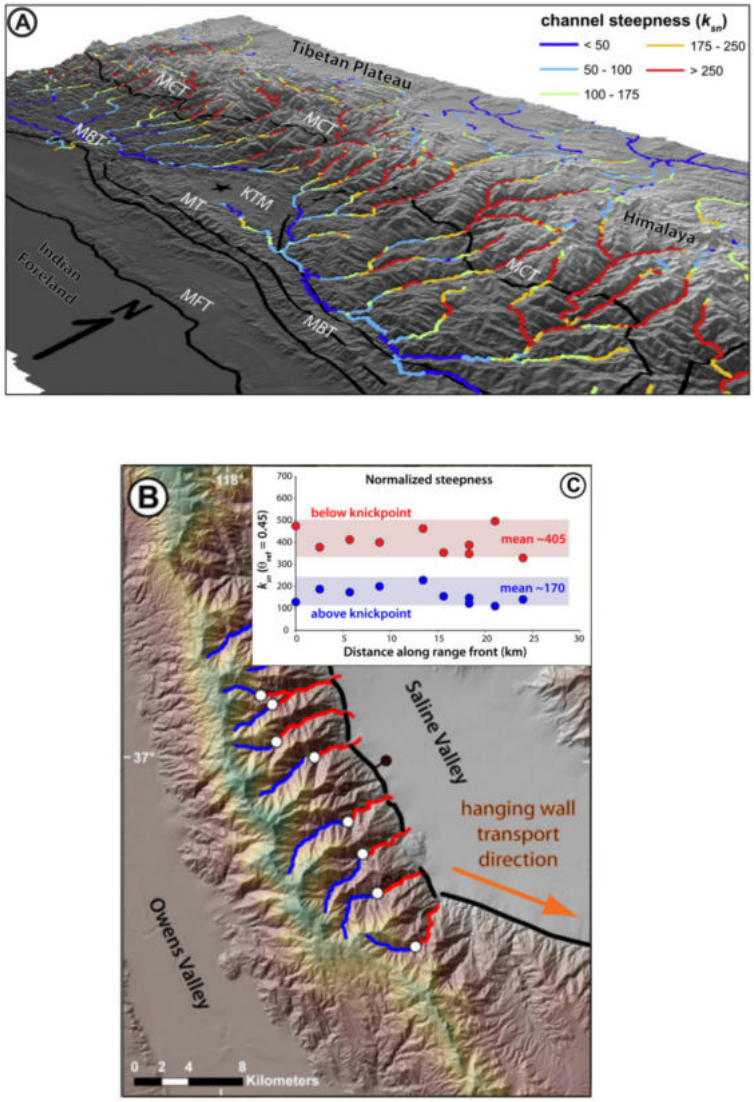

Figure 1.15: Tectonics from fluvial morphology, adapted from Kirby and Whipple (2012). A) Contrasts in k_{sn} in the Central Himalaya (Nepal, India) correlated with the Main Frontal Thrust (MFT) suggesting the activity of the fault. B) Transient signal migrating upward following the activity of the Saline Valley fault (United State of America). Knickpoints are separating two family of slope patches displayed in C).

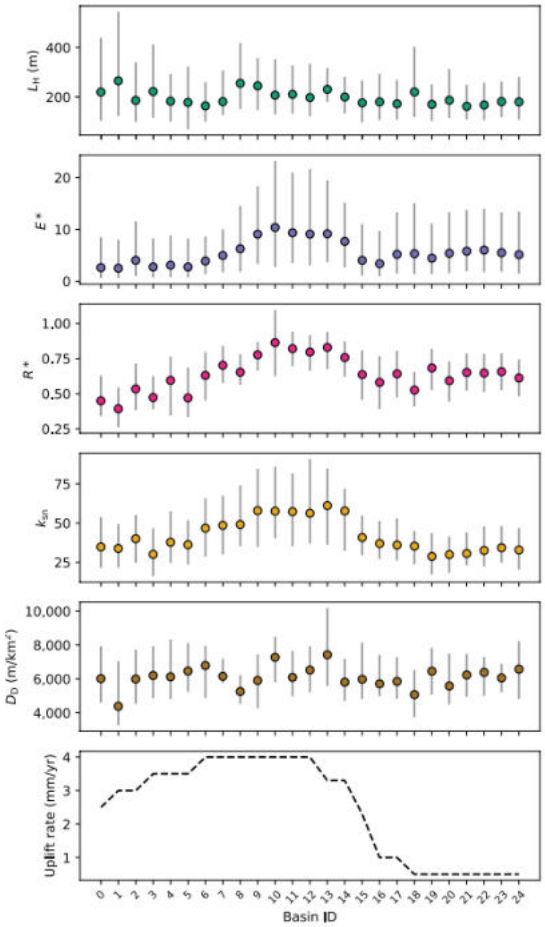

Figure 1.16: Geomorphometrics of watersheds near the Mendocino Triple Junction (California, United States of America). The Basin ID are sorted by Northing. D_D is drainage density; and R^*, E^* and L_H three metrics quantifying hillslope morphologies, respectively dimensionless relief, dimentionless erosion and hillslope length, full details can be found in Hurst et al. (2013). Note how in case, the hillslope metrics correlate with k_{sn} to express activate tectonics with similar global trends, and local variations in the response time. Figure adapted from Clubb et al. (2020).

mation or can provide an independent constrain to validate the tectonic nature of k_s contrasts.

1.2.5 Lithologic forcings on channel steepness

Tectonics are not the only forcing affecting channel steepness. Lithology is another factor that influences channel steepening. Consider two detachment-limited reaches with the same erosion rates. If the rock strength of one of the reach is higher than the other, stream power needs to increase to maintain the same erosion rates. If one believe the reasonable assumption that $\dot{e} = f(Q, S)$, then harder

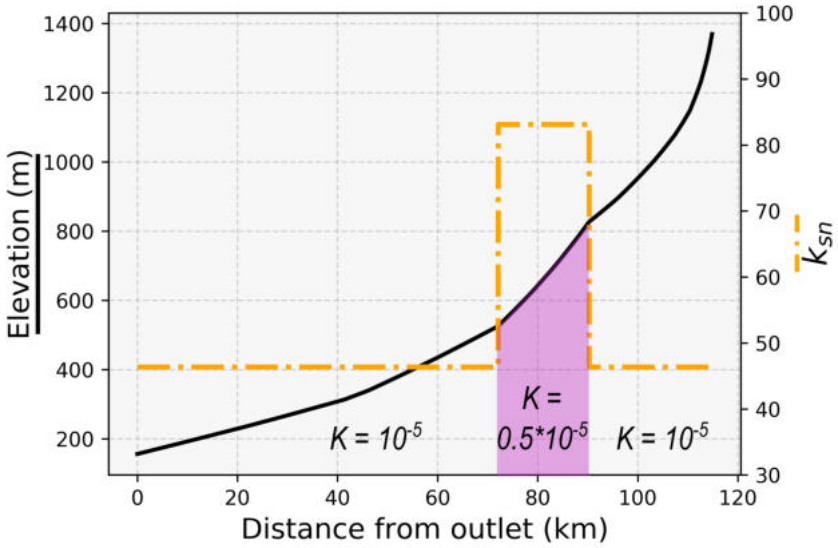

Figure 1.17: Theoretical expression of lithologic contrast, simulated with equation 1.24 and the setting from Figure 1.12, apart from the K values, displayed on the figure. k_{sn} here correlates with lithology.

lithologies will most probably result in an increase of channel steepness. In the basic formulation of the stream power law (equation 1.24), it translates in a reduction of the erodibility, the erosion efficiency parameter, and therefore of k_s *sensu* equation 1.26. This process is illustrated in Figure 1.20.

The role of lithology has been acknowledged by a wide range of studies, early ones using SL from equation 1.8: Goldrick and Bishop (1995) quantify steepening directly linked to lithologic forcing. Kirby et al. (2003) identified in the Tibetan Plateau (Tibet, People's Republic of China) that although the main driver of steep k_s patches was differential rock uplift, some steepened were at odds with the rest of the landscape and were therefore presumed to have harder lithology underlying the bed. Kirby et al. (2003) argue that the effect of lithology is not systematic, but more related to specific massifs with presumably particularly hard rocks.

Duvall (2004), in their work on coastal California (United States of America), demonstrated that meaningful interpretation of channel steepness into tectonics could not be made without acknowledging of lithologic variations, embedded amongst channel width and climatic variation in the erodibility K. They suggest that enforcing a constant K, and therefore assuming homogeneous lithology,

would lead to erroneous rates or calibration of the exponent n. k_s would still reflect erosion and tectonics in some places, but spurious tectonic interpretations could emerge in places where lithology plays a prominent role in driving channel steepness.

In their review of bedrock channels, Whipple et al. (2013) describe the role of lithology as relatively complex and difficult to generalise: it plays a role of dominant forcing in some cases (*e.g.* Bernard et al., 2019; Duvall, 2004; Strong et al., 2019) but can also get partially to completely overwritten by other forcings (*e.g.* DiBiase et al., 2010; Kirby et al., 2003). They also highlight that the expression of lithology is not restricted to the effect of rock strength but also of other characteristic varying spatially, *e.g.* fracture density, susceptibility to plucking. Finally, they suggested that the non-expression of lithology in certain studies could be linked to the cover effect of alluvium, which reduce drastically surface contact between the river and the actual rocks. A number of studies have acknowleded the joint occurrence of lithologic and tectonic forcing on channel steepness, and the most adopted method has been to identify and discriminate lithologically-related signals to interpret meaningful tectonics (Seagren and Schoenbohm, 2019).

Some entire landscape are even suggested to see lithology as the main forcing shaping their landforms. Bernard et al. (2019) demonstrated that the post-orogenic topography of the Pyrenees has been dominantly shaped by lithology. Hard internal granitoid massifs have been "pinning" the drainage divide while channel steepness correlates positively with lithologic variations. Gabet (2019) strongly contested hypothesis attributing channel steepness patterns to Cenozoic rock uplift in the Sierra Nevada (California, United State of America) by carefully relating all the slope patches and knickpoints with lithologic boundaries and field data, attributing all changes to the sole lithologic contrasts. Strong et al. (2019) demonstrated that lithology was either the main driver or the sole driver to explain the morphology of the Shillong plateau (India), where softer altered rocks are capping resistant hard rocks.

Erosion is inhibited by the lack of tools to erode from the fine and deep soil of the tops, while resistant newly exhumed rocks are hard to erode despite high

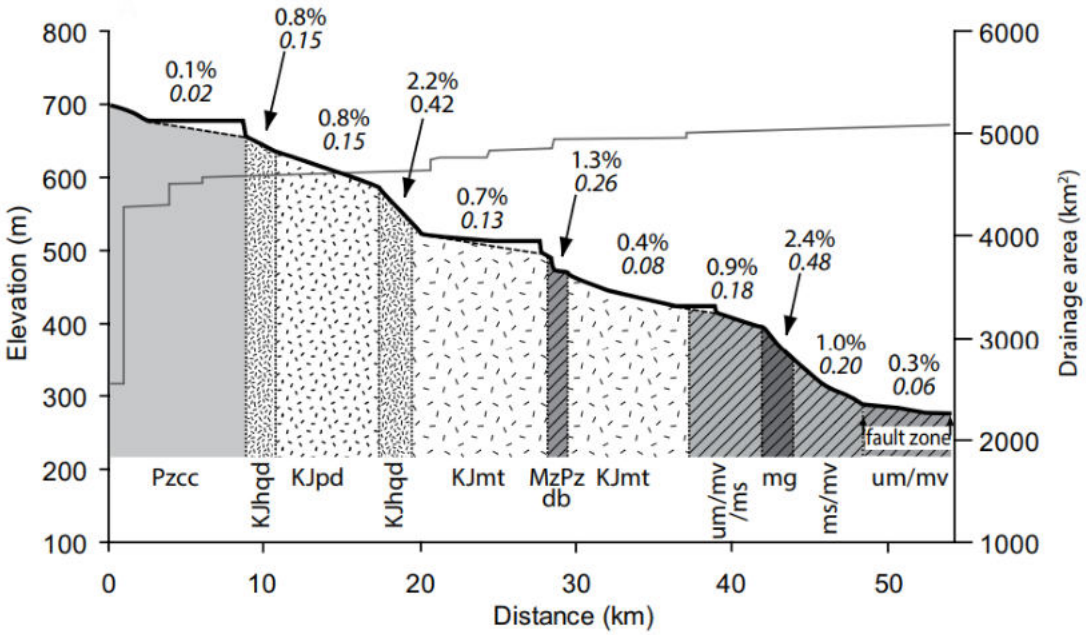

Figure 1.18: River profile from The Northern Sierra Nevada (California, United States of America) adapted from Gabet (2019). k_{sn} is written in italic and channel gradient is written in percentages. The authors suggest k_{sn} correlates with lithologic contrasts, highlighted here with different symbols.

precipitation, generating high plateau with very steep borders. Such behavior has been demonstrated using numerical modeling. For example Forte et al. (2016) implemented explicit 3D stratigraphic units within a landscape evolution model (Channel Hillslope Integrated Landscape Development (Tucker et al., 2001)) and demonstrate that lithologic contrasts were enough to generate patterns of differential erosion (and k_s by extension). Another modelling work suggesting the preponderant role of lithology in certain landscape is the work of Braun et al. (2014), where they suggest that eroding dense resistant rocks might enhance exhumation by decompression on the top of the more resistant lithology. But in many mountain ranges, faults are juxtaposing different rock types together, leaving an ambiguity on which forcings are actually express in the steepening (Figure 1.19). This point has not been explored, and Chapter 5 focuses on this specific problem.

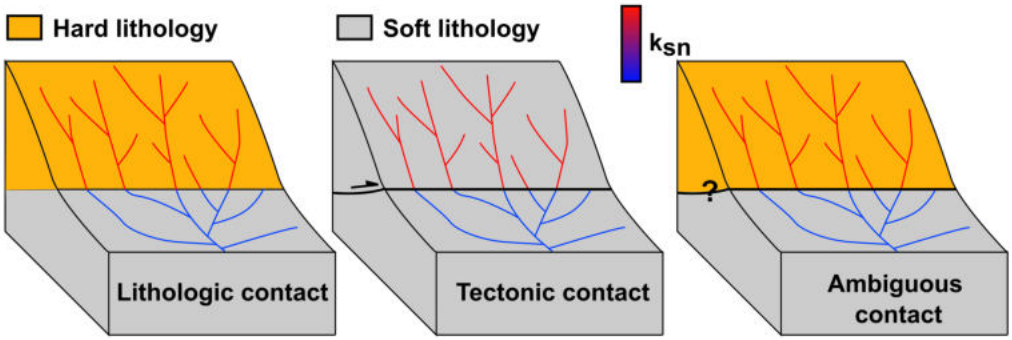

Figure 1.19: Illustration of the lithology versus tectonics paradox in cases where potentially active faults collapse spatially with a lithologic contact.

1.2.6 Other forcings on channel steepness

Lithology and tectonics are often considered to be the main forcings controlling k_s (Whipple et al., 2013), but they are not the sole ones. Sea level variations, in the same manner tectonic forcing, can cause steepened reaches to propagate upstream depending on the newly exposed topography. The morphological signature can be similar than the one retaining tectonic information (*e.g.* Crosby and Whipple, 2006).

Climate is also suspected to potentially play a role on it by controlling the discharge patterns but very few studies actually investigated the assumption that a common k_s should lead to more erosion in a wetter climate (Whipple et al., 2013), despite other modelling approaches demonstrating the role of climate in shaping the earth surface (Willett, 1999). In addition, works comparing modelling and topographic analysis suggest that the effect of climate and precipitation is highly variable, from unsignificant to highly nonlinear and case specific (DiBiase et al., 2010; DiBiase and Whipple, 2011; Scherler et al., 2014; Tucker, 2004) as demonstrated by equation 1.27.

Recent work based on numerical modelling, cosmo-radionuclides basin-average analysis and topographic analysis in the Andes (Campforts et al., 2019) suggests that k_s would record the effect of precipitation changes only if the timing of change would be sufficient. They also highlights that precipitation data is usually limited in time and hardly spatially estimable from the past records, making

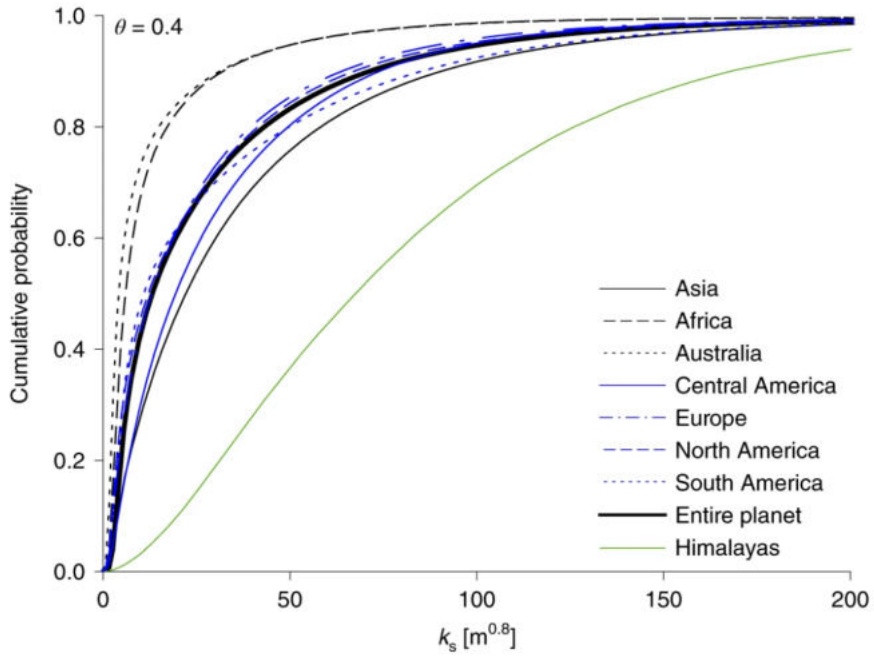

Figure 1.20: Worldwide compilation of k_s values from Hilley et al. (2019) illustrating a potential threshold on the values when reaching high steepness zones.

interpolations difficult. For a review about the role of climate in shaping overall topography, I direct the interested reader to Perron (2017) review.

Hilley et al. (2019) suggests a morphological limitation of the relationship between channel steepness and erosion. They combined a worldwide compilation of k_{sn} and demonstrated that all the data tended toward a maximum k_{sn} threshold which could not be exceeded. They suggest that in very steep landscape, the relationship becomes increasingly nonlinear and very sensitive to small changes in steepness explaining the threshold. However calculating worldwide k_{sn} implies that whichever θ_{ref} is chosen, it is assumed to be spatially invariant for the whole world. This assumption is challenged in chapter 4.

Another aspect affecting channel steepness is the channel width, which can also adapt to the same forcings as channel steepness (Whipple et al., 2013). Reduction of channel width can increase the flow depth and increase unit stream power without affecting channel slope. If k_s is calculated from drainage area, channel steepness does not record such a change, but can introduce a bias in the interpretation if changes are absorbed by changes in channel width. Hack (1957) demonstrated a power relationship between channel width and drainage

area while modelling studies suggest applying the effect of channel width into the erodibility, K.

Finally, k_s can be affected by changes in upstream area. Therefore stream piracy, where one basin takes drainage area from another (*sensu* Willett et al. (2014)), affects the downstream k_s. This process has been conceptually demonstrated with S–A plots (Seagren and Schoenbohm, 2019), and mentioned in few modelling-based studies (Giachetta and Willett, 2018c; Whipple et al., 2017b) but not quantified for a wide range of processes and field sites.

1.2.7 Variations in the concavity index

The concavity index, θ, describes the rate at which slope decreases as drainage are an increases in equation 1.16. If the normalised channel steepness approach is chosen, θ_{ref} becomes the normalisation parameter and is assumed over an area to calculate comparable k_{sn}. Drawing meaningful relations between morphology and forcings depends on that choice. Concavity index, however, can vary within a landscape. A number of studies suggested that for rivers close to steady state, the range in concavity index was relatively narrow between approximately 0.4 and 0.7 (*e.g.* Kirby and Whipple, 2012; Tucker and Whipple, 2002; Whipple et al., 2013; Whipple, 2004; Wobus et al., 2006c, and references therein), and much wider as basins get further from such state (Whipple et al., 2013). However, modelling behaviours of θ predict very different meanings when converting concavity index into processes or forcings, depending on which landscape evolution laws are taken into account (*e.g.* Tucker and Whipple, 2002; Wickert and Schildgen, 2019). Whipple et al. (2013), in their review of controls on channel morphology, state that concavity is relatively independent of climate, tectonics and lithology for near steady-state rivers. However they also suggest that this is not alwaysa the case, especially on transient system, but concavity does not systematically react the same way to a forcings from a field site to another suggesting a case by case basis to interpret it. This can also be difficult to relate to real landscape, as determining concavity indices can be done using different methods (*e.g.* Hergarten et al., 2016; Wobus et al., 2006c) based on the integral method or S–A plots.

They can have different morphological expressions. Chapter 4 is dedicated to θ and thoroughly explores the methodological aspect to extract concavity indices and the implications on other metrics.

1.2.8 Expression of forcings and processes through the χ coordinate

χ coordinate has been introduced to circumvent the limitation linked to slope–area methods (see Section 1.2.2 for full details about its definition). In their seminal paper, Perron and Royden (2013) developed the χ coordinate using equation 1.24 with no threshold components. As demonstrated with equation 1.22, it can be expressed without assuming any erosion law. First, the coordinate brings methodological improvements allowing (i) finer representation of k_{sn} as gradient of $z(\chi)$ plots, (ii) the representation of rivers of different size within the same referential and (iii) the constraining of concavity index. The latter is accomplished by finding the θ values making the $z(\chi)$ plots collinear, *i.e.* collapsing within the same referential, this part is explored in more details in Chapter 4. Second, if one assumes equation 1.24 with no threshold components as reasonable approximation of erosion processes, one can compare river long profiles in χ space with a direct approximation of their relative erosion power, hence expressed as the gradient of the transformed profiles. Steeper reaches correspond to either more erosion or lower erodibility. The χ coordinate is only valid for the fluvial section of the landscape, and Hergarten et al. (2016) suggest an extension of the latter to hillslopes; their method relies on a number of additional parameters, increasing the difficulties of calculating χ using their method.

Perron and Royden (2013) mostly described the use of χ in coordination with elevation data to express the S–A relationship within a clearer framework. χ indeed only accounts for drainage area and flow distance from a base level. Willett et al. (2014) suggest that the χ could be an effective proxy for tectonics via detection of drainage divide migration and reorganisation. The principle is linked to the area gain and loss *via* river capture (wherein divides "jump")

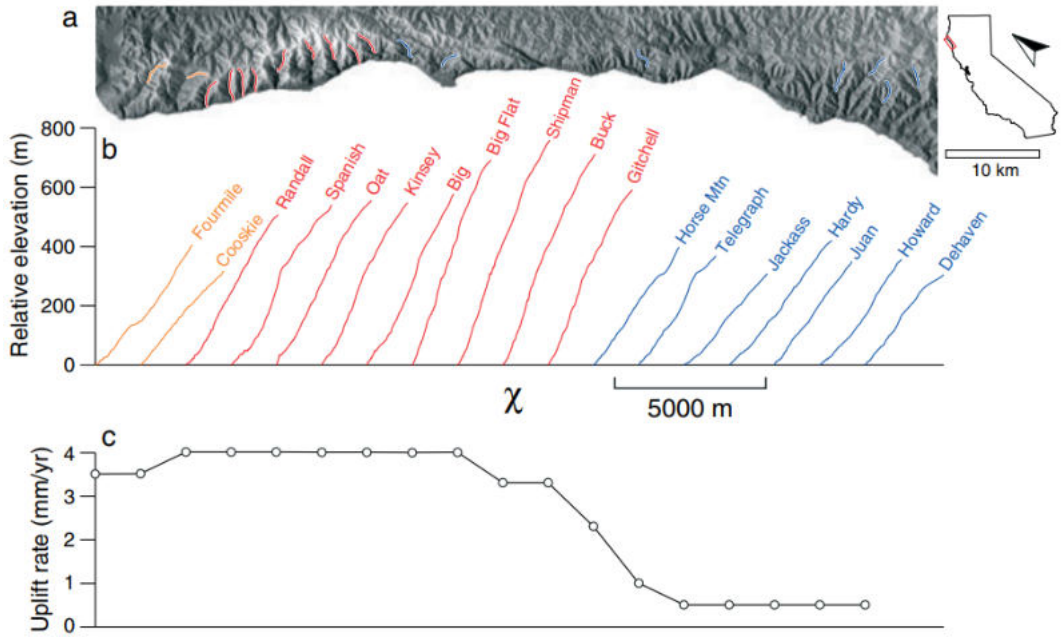

Figure 1.21: Transformed river profiles on the California coast near the Mendocino Trible Junction (United States of America). A) Location of the river profile. B) Transformed river profiles colored by qualitative groups of steepness. C) Surface uplift rates inferred from marine terrace dating. Perron and Royden (2013) suggested that the overall steepness

or gradual migration (continuous movement of the divides through time) which directly affect χ in the impacted area – *i.e.* the gained/lost area or the divide's vicinity. Hence, Willett et al. (2014) argue that contrasts in χ values across divides reflect instabilities in the divide position, low χ would therefore be a proof of an "aggressor" watershed migrating into a "victim" one depicting higher χ.

The theory of Willett et al. (2014) relies a on a number of assumptions. Explicitly, erodibility needs to be constant on both side of the divide and within the whole watershed, this implies the assumption of constant climate/precipitation, similar lithology and other intrinsic parameters (*e.g.* fractures, chemical weathering). Implicit assumption is that erosions and depositions laws, for fluvial and hillslope processes, are behaving the same way on both side of the divide. Finally it also assumes spatially constant concavity index, implications of the latter is explored in Chapter 4. Failing to justifying one of these assumption is expected to make that signal ambiguous.

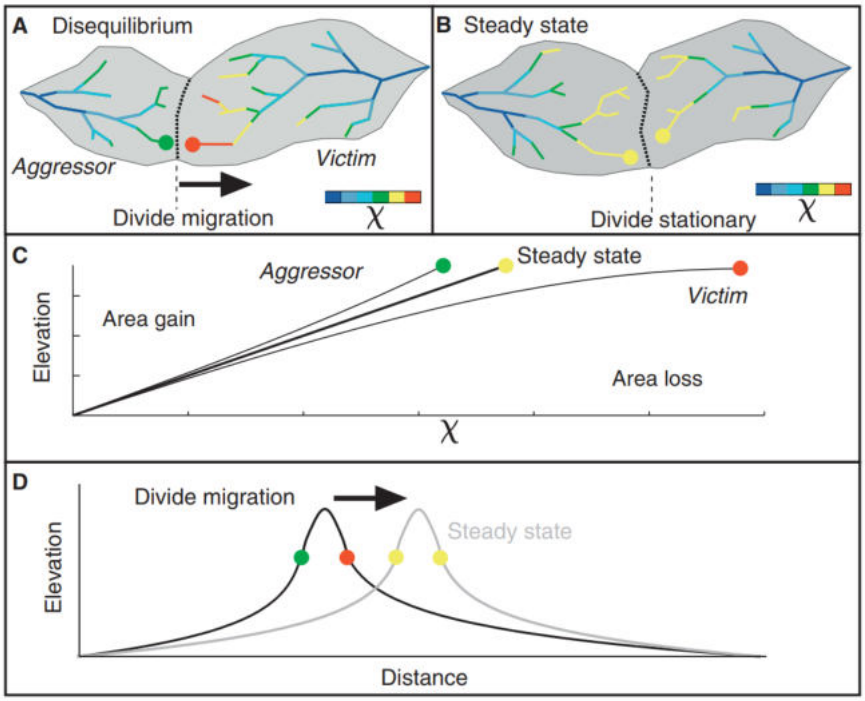

Figure 1.22: Conceptual principle behind using χ as a proxy for drainage reorganisation. A) χ contrast suggesting a divide in disequilibrium. B) Steady State basin, the divide does not migrate. C) Transformed river profile corresponding to A) and B). D) Divide migration to reequilibrate the coordinate.

Using variations in the χ coordinate across divides to detect divide migration has been widely applied (*e.g.* Giachetta and Willett, 2018c; Seagren and Schoenbohm, 2019; Winterberg and Willett, 2019), but suffers from some limitations. Forte and Whipple (2018) demonstrate that χ contrasts were not a effective as other metrics describing drainage stability, for example topographic gradient or k_s on both sides of the divide. They suggest that interpreting χ signature without encompassing elevation could be ambiguous. They also demonstrate the very high sensitivity of χ to the chosen base level x_b on equation 1.22. As χ integrates the inverse of drainage area normalised by concavity index, it is highly sensitive to the outlet location. Forte and Whipple (2018) show that calculating χ with different base levels in the Caucasus mountain range, all justified by their linkage to different processes and boundary (*e.g.* sea level, fixed elevation, mountain front), drastically change the contrasts and therefore the interpretation of drainage divide stability. Whipple et al. (2017a) also pointed out the ambiguity of the meaning of χ contrast in a modelling study demonstrating the numer-

ous causes potentially generating the contrast. They also concluded that only stream captures would leave a noticeable morphometric signature whereas gradual migration and small captures where less likely to systematically be retained in topography.

1.3 Thesis Outline

This thesis aims to build on the understanding of different controls on river channel steepness, concavity indices and the integral coordinate, χ. It focuses on different aspects: how to constrain them, what their limitations are and how they translate into processes. This work aims to challenge their application in heterogeneous landscapes where combined forcings are jointly affecting Flint's metrics.

However, being at the interface between the solid earth and the atmosphere, fluvial geomorphology is affected by a wide range of other forcings, for example lithology. The direct consequence is that different forcings can generate similar morphologies, leading to ambiguity in interpreting the genesis of morphology. This can lead to potentially spurious interpretations, where, for instance, a lithologic knickpoint could be interpreted as a product of non-existing rock uplift contrasts.

As discussed in the theoretical background, joint occurrence of different forcings in the landscape has been the object of a number of studies, with a trend to separate the signals into different influences and interpret the one believed to only reflect tectonics. Nonetheless, a proportion of upland landscapes show different forcings that occur at the same point in space. A striking example of this is the pernicious tendency of faults to juxtapose different rock-types.

This work aims to advance the field of fluvial geomorphology in two different ways. Firstly, I present novel methods that quantify concavity indices and slope patches. Methods are prerequisite keystones to interpretation, and developing objective characterisation of metrics is crucial to challenging their application across the globe. Secondly, I challenge the use of fluvial geomorphometrics to extract

meaningful tectonics in a heterogeneous landscapes that present high contrasts in lithology and rock uplift at the same location, the Eastern Carpathians. I demonstrate that careful, systematic extraction of fluvial geomorphometrics correlated with independent datasets allows circumventing the ambiguity of composite signals. The thesis is articulated as follow:

- Chapter 2 presents numerical methods used throughout the thesis. It covers (i) the choice of datasets, (ii) the choice of numerical tools on which new developments are built and (iii) the existing topographic analysis algorithms used within the different chapters.
- Chapter 3 presents a novel method to objectively extract the location of knickpoints and waterfalls: the slope patche boundaries. It suggests a range of metrics based on channel steepness to quantify their magnitude.
- Chapter 4 describes the implementation and applications of a method to investigate the spatial variations of concavity indices in upland landscapes with uncertainties. It explores spatial variation of this metrics in a wide variety of upland landscapes. The implication of calculating k_s and χ with a non optimal θ and the extent of the subsequent distortion are derived analytically and numerically.
- Chapter 5 applies existing and newly developed methods in fluvial geomorphology in the Eastern Carpathians, an lithologically heterogeneous landscape where different proxies suggesting contrasts in surface vertical motions, to constrain their extents.
- Chapter 6 discusses the overall results of the thesis. It integrates results in the broader geomorphological context and explores their implications. It also opens on ideas for future research on that topic.

Chapter 2

Geomorphometry from Digital Elevation Models

Early geomorphologists observed natural processes in the field, and used insights from fieldwork to propose relationships between topographic features and erosional processes that could be applied elsewhere. Field data of some form is always required to constrain models. However, the increasing availability of digital elevation models over the past few decades has allowed geomorphologist to test relationships derived from fieldwork at a regional, or even global scale. One can now systematically test hypothesises about fluvial morphology for whole watersheds, mountain ranges or even continents. In order to do so, the past few decades have seen the development of many algorithms for analysis of topographic data in support of extracting and analysing the geomorphometrics explored in the previous chapter, namely topographic analysis.

As with any numerical method, topographic analyses are dependant on the quality of the underlying data (in this case the DEM), but also on the algorithms themselves. This thesis uses numerical methods to utilise, develop and challenge topographic analysis for fluvial geomorphology. As most of this work relies on underlying numerical tools and methods, this chapter (i) describes the main existing datasets and numerical tools upon which I build the work and justifies the reasons these are used and (ii) explains the existing algorithms I use and the implication of these choices.

2.1 Availability of Digital Elevation Models

The now widespread availability of digital elevation models at ever increasing resolutions, is rapidly changing geomophology, considering the first global DEM appeared in late 1990s. Both satellite and aerial platforms are spurring a true revolution for geomorphology by offering contiguous data for the elevation of the whole earth surface. Development of multiple acquisition methods has led to worldwide cover, with, for many datasets, open data availability.

Tarolli and Mudd (2020) provide an extended review of the digital elevation models. I describe here the main datasets available for analysis at large scale. The first digital elevation model covering the whole world was ETOPO5 (Bamber et al., 1997), at 5 arc-minute resolution (approximately 10km at the equator) derived from a wide variety of national digital datasets. It was quickly followed by GTOPO30 (Gesch et al., 1999), a 30 arc-second resolution (approximately 1km at the equator) DEM acquired from a compilation of contour maps, national surveys and aerial photogrammetry.

Kilometric resolution is too coarse to capture typical fluvial morphologies, as most rivers of interest will be less than a kilometre wide. The first global-scale digital elevation model widely used to analyse rivers and other smaller scale features was SRTM (Farr et al., 2007), initially released at 90 metre resolution. SRTM was later released in an improved, void-filled 30 metre dataset (NASA-JPL, 2013). SRTM is satellite-derived from C-band Radar. The first 30 metre worldwide digital elevation model was however ASTER-GDEM (Abrams et al., 2010). Validation studies suggest the global quality of the ASTER-GDEM is inferior to SRTM (*e.g.* Gesch et al., 2016). More recently ALOS PRISM dataset released a newer 30 metre digital elevation model (Tadono et al., 2016) with a subsequent more detailed versions (Takaku et al., 2018), a coarser version of the commercial product AWS3D (5 metres resolution). Finally, TanDEM-X (Krieger et al., 2007, explains the data acquisition process pre-collection) released a 12 metre resolution digital elevation model from TerraSAR–X X band radar satellite, although this data is not open access and must be acquired through a proposal

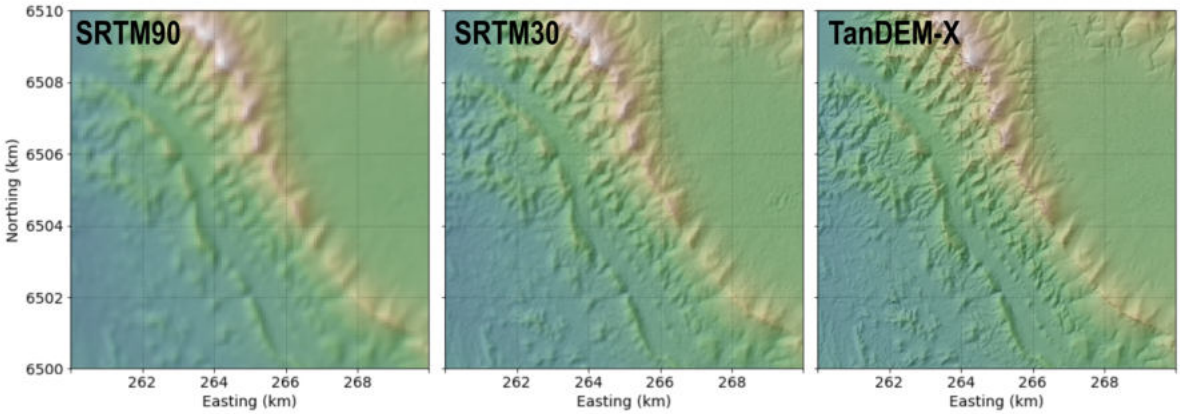

Figure 2.1: Digital elevation models for SRTM 30 metres precision, 90 metres precision and TanDEM-X (12 metres) for the Flinders Ranges (Australia, promotion sample available on https://tandemx-science.dlr.de/).

process.

Tarolli and Mudd (2020) review studies investigating the accuracy and overall quality of these Digital Elevation Models. TanDEM-X has been suggested to have the best vertical accuracy (Tarolli and Mudd, 2020, and references therein), although potentially inaccurate in very steep landscapes (Schwanghart and Scherler, 2017). For fluvial analysis, AW3D30 offers the best accuracy but SRTM also offer a reasonable quality. ASTER however has a systematic lower accuracy than other sources. For this thesis, we explored DEM consistency within each study. Chapter 3, aims to test a method over a wide range of data resolution and utilises a number of sources described in the chapter; Chapter 4 uses SRTM in order to facilitate extraction over sites scattered over the world; and Chapter 5 uses AW3D30. a comparison of SRTM 90 metres, 30 metres and TanDEM-X is illustrated in Figure 2.1.

I have only explored the Digital Elevation Models covering the whole Earth (or most parts of the Earth), but it is worth mentioning that a high number of regional or national Digital Elevation Models are also available depending where the case study is, for example the High Mountain Asia 8-metres DEM-Mosaic (Shean, 2017). In addition to satellite-derived datasets, lidar point clouds, obtained both from terrestrial and airborne instruments, are increasingly available. These offer various resolutions, which can be equal or better than 1 metre per pixel, depend-

ing on the density of data points. Such datasets are available through a wide array of national GIS portals as well as through data aggregating services like opentopgraphy.org. A full review on the availability of open-source datasets is presented in Tarolli and Mudd (2020).

2.2 Numerical framework to process the data

The first topographic metrics were calculated from contour maps (e.g. Ahnert, 1970; Hack, 1960), using topology of river networks (e.g. Strahler, 1957) or by direct field measurements. These approaches led to the establishment of the geomorphic laws and equations still in use by modern geomorphological studies described in Chapter 1. However such approaches were time-consuming and difficult to apply at large-scale due to the *quasi*-impossibility of automating the processes. The required measurement methods also involved direct user interventions, making observations difficult to reproduce. They also risked introducing human error during data acquisition and processing. These studies produced an amount of raw data that made direct interpretation tractable, *i.e.* without the need of reducing the dimensions of the dataset using data manipulations to extract signals (*exempli gratia* density plots, data binning, linear regressions, Principal Component Analysis).

This is at odds with recent studies that commonly represent large river networks with millions of data points (e.g. Giachetta and Willett, 2018b; Harel et al., 2016; Hilley et al., 2019, or Chapter 5 of this thesis). Section 2.1 demonstrated the a wide range of Digital Elevation Models at global and local scales are available for geomorphological studies. Their increasing spatial and temporal resolution is rapidly adding to the amount of data to process. Increased data availability has resulted in the challenge of being able to process the large amount of data in a meaningful, controlled, and reproducible way. This challenge has led to a rapid expansion of the tools available for this purpose.

Chapters 3 and 4 build on the idea of developing and applying methods aiming to systematically test geomorphic laws at all scales. Chapter 5 applies a range

of these methods to extract tectonic signals from a river network affected by a wide range of competing external and internal forcings. This thesis relies on the chosen underlying numerical framework. I therefore first introduce the existing numerical framework upon which the work is built. In this chapter I explain the technical reasons for these choices, the philosophical reasons behind them and a non-exhaustive list of considered alternatives.

2.2.1 Criteria for the numerical framework

I carefully based my choice of tools on the following criteria:

- Full reproducibility. The methods and results need to be entirely reproducible. To achieve this aim, tools I use must involve minimising manual user inputs, maximising objectivity in the algorithms and maximising the extent to which the data and tools may be shared. It follows from this that I use free, open-source data and software. I am particularly keen to avoid proprietary licences as they restrict the use of the tools to institutes that can afford them. I do not wish to block access to certain parts of the source code therefore leaving "black boxes" in the method used. The impact of paywalls on data reproducibility is explored by Tarolli and Mudd (2020).
- Modularity. The developed tools need to be flexible in term of usability and development. This implies (i) flexible user inputs to allow their integration in tool-chains of other frameworks, (ii) flexible inputs and outputs to allow the data to be pre- and post-processed softwares and (iii) well commented, documented and clear code structure to make possible its modification and integration in other frameworks.
- Performance. The processing and exploring of DEMs need to rely on reasonably efficient codes in order to (i) not to restrain the use to super-computers and (ii) optimising the computational complexity of algorithms to allow sensitivity analysis on the different parameters.
- Accessibility. The framework needs to ensure that developed tools are usable by the community. It involves ensuring (i) open source (see aforementioned reasons), (ii) the code does not require advance programming skills

to be utilised and (iii) extended and up to date documentation.

2.2.2 Base framework and tools for developing topographic analysis

I chose LSDTopoTools (Mudd et al., 2019b) as base framework for this PhD, as it fulfills all the aforementioned criteria. The framework is written in C++. C++ is a compiled coding language ensuring low-level controls on memory consumption and processor usage . "Low level" in this contexty means relatively close to the underlying computer architecture. It is object-oriented, which is a coding paradigm orientated around objects as entity with their owns attribute and methods able to interact with other objects. It allows the creation of efficient code structures as well as ensuring great flexibility and modularity. Finally C++ is completely open-source and free to use with a wide range of cross-platform compilers (*e.g.* g++, clang, MSVC). LSDTopoTools has been developed since the early 2010s and has an extended documentation (lsdtopotools.github.io/LSDTT_documentation/). The software is version controlled on the github platform and maintain by a team of developers from different research institutes.

LSDTopotools is host to the development of many topographic analysis algorithms (*e.g.* Clubb et al., 2014, 2019; Gailleton et al., 2019; Grieve et al., 2018; Mudd et al., 2014; Mudd, 2017) and of their application to real landscapes (*e.g.* Bernard et al., 2019; Clubb et al., 2020; Hurst et al., 2019; Strong et al., 2019). LSDTopoTools also has a python-based visualisation toolbox LSDMappingTools (Mudd et al., 2019a) which process the outputs of the first one. However, developing tools in C++ also has limitations. The ease of editing the tools, and to a lesser extent in using and installing the tools, is much lower than interpreted languages such as python or R, the most widely used for open-source research software. In addition, development time and integration of existing libraries is less straightforward, for instance reading and writing external data (*e.g.* Digital Elevation Models, or images) can be very tricky and reduces the flexibility of input format.

For conducting the research I therefore chose the following approach. I built all my tools within the LSDTopoTools framework, taking advantage of the existing algorithms and routine to process topographic data. I developed a python layer on the top of it using xtensor (https://quantstack.net/) to communicate in-memory between the two languages. Python is a dynamic interpreted language with a base coded in C. Users can therefore use the LSDTopoTools framework without needing knowledge of C++.

This framework, named **lsdtopytools**, allows users to combine efficient C++ code with the flexibility and wide library of tools available on python. I am using GDAL/rasterio (contributors, 2020; Gillies et al., 2019) for reading, writing and managing geographic projection; numpy (Van Der Walt et al., 2011) to process general operation (*i.e.* non specific to topographic analysis) on matrix-like data; Pandas (McKinney, 2010) for managing table-like data (*i.e.* input or output of data points); Matplotlib (Hunter, 2007) for visualisation; Scipy (Jones et al., 2015) for general algorithms (*e.g.* interpolation, statistics, signal processing); Numba (Lam et al., 2015) for writing small-scale optimised routing that have run times approaching C performances using LLVM engine; geopandas (including fiona and shapely) (Gillies et al., 2007; Snow et al., 2020) to process shapefile-type data (*i.e.* polygon, lines and point geographic data). The program is organised into three main packages: the LSDTopoTools package containing the original C++ code; lsdtt-xtensor-python, the python module containing the c++ object wrapping LSDTopoTools and exposing the main routines to python; and lsdtopytools, the python module containing all the python objects, routines and command-line interface to use LSDTopoTools. This approach allows (i) quick development of new routines through python and/or c++, (ii) taking advantage of python flexibility to provide many input and output options, (iii) the ability to quickly add user interfaces to new routines, (iv) taking advantage of the wide library of python packages to link the library to other tools. The framework is illustrated in Figure 2.2.

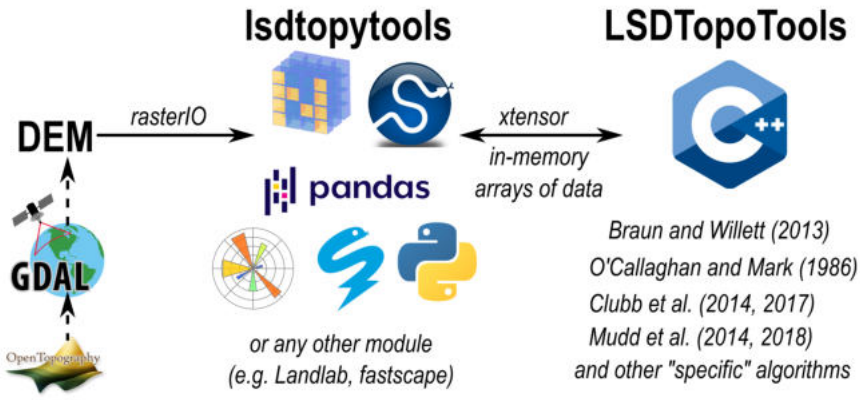

Figure 2.2: Framework utilised for the topographic analysis. Data is collected from open source dataset providers, and eventually prepossessed. Then the whole framework in integrated into a python module (lsdtopytools) making use of a wide range of existing ones and sending digital elevation models to C++ LSDTopoTools.

2.2.3 Existing tools

A number of numerical frameworks already exist, I explore in this subsection a non-exhaustive list of the main ones that have been considered through for this thesis.

First, traditional GISs are the most widely utilised tool to process and explore DEM and other raster data. They provide a user-friendly graphical interface, and many existing tool boxes for topographic analysis. Most of them are modular and allow an extension to be coded within their framework. The main examples of GISs include ArcGIS (https://www.arcgis.com/), a proprietary software in which some geomorphological extensions are installed (*e.g.* Queiroz et al., 2015, or stream profiler http://geomorphtools.geology.isu.edu/Tools/StPro/StPro.htm), and QGIS including GRASS and SAGA, a free and open-source equivalent framework (*e.g.* fluvial profiler, https://github.com/awickert/GRASS-fluvial-profiler). However as is the case for similar software, the graphical interface and the extreme flexibility of the tool make it slow to process large DEMs. The fact that extensions are embedded in a graphical framework makes the development of extensions less straightforward and limit the possibilities for optimisation. Any actions requiring manual input, *e.g.* manual selection of a parameters, decreases the reproducibil-

ity of the analysis and to a lesser extent its automation. In addition, ArcGIS is a proprietary tool which (i) does not reveal its source code introducing "black boxes" in the algorithm used and (ii) has a yearly cost for the base tool and each of its extensions making the tools less accessible than free and open software.

Alongside the GISs, a number of hard-coded frameworks and codes also exist. Some of these include script-based approaches and allow full reproducibility and optimisability. Perhaps the most widely used of these tools, TopoToolbox (Schwanghart and Scherler, 2014; Schwanghart and Kuhn, 2010), is a framework coded in the MATLAB proprietary language, alongside with C for some parts of the core. The framework is object oriented (*i.e.* a programming methods centered on objects providing "templates" of element with their own attributes and methods) and allows very high modularity and readability while providing extended tutorials and documentation. It has been used to develop a high number of algorithms (*e.g.* Schwanghart and Scherler, 2017) as well as extensions (*e.g.* Campforts et al., 2017; Forte and Whipple, 2018, 2019) focused on landscape evolution modelling and topographic analysis. Despite fulfilling most of the criteria aforementioned, TopoToolbox relies on the propietary software MATLAB. Even if the source code of TopoToolbox is available, the MATLAB part remains hidden. The code can be run without a license under certain conditions (Forte and Whipple, 2019), but no open-source alternative can allow the correct editing or usage of MATLAB code. The closest open source equivalent OCTAVE has the limitation of not including several key tooboxes.

Another tool worth mentioning is the python-based LandLab toolbox, first released by Hobley et al. (2017) and then expanded with many contributions. It offers a full open-source framework that relies on python modularity and C-underlying base to provide efficient tools via Cython (Behnel et al., 2011). A number of extensions have been developed (*e.g.* Adams et al., 2017; Strauch et al., 2018) and LandLab has extensive documentation. However, the code only includes a small number of topographic analysis algorithms, and it is optimised and designed for landscape evolution modelling. The framework is less adapted to developing topographic analysis.

Fastscape (Bovy and McBain, 2019) offers a similar python framework, based on xarray-simlab Bovy (2019). It is worth noting the existence of many other framework focused on hydrology, which could have been used to develop fluvial routines despite being sometimes too sophisticated for large-scale analysis. The most suitable candidate would have been RichDEM, a C++/python flow routing toolbox focused on extreme optimisation of preprocessing and accumulation algorithms (*e.g.* Barnes et al., 2014, 2019).

2.3 Numerical processing of Digital Elevation Models

Extracting geomorphometrics from river long profiles is not straightforward and requires the careful design of a processing tool chain involving many algorithms to go from Digital Elevation Model to k_s, θ or χ. Making this process computationally efficient is even more challenging.

One prerequisite is to extract the river network from the Digital Elevation Model, an exercise that in itself features many possible extraction algorithms. It requires the processing of at least basic hydromorphology such as drainage area or discharge, which can be affected by the quality of the Digital Elevation Model, and which may need to be preprocessed to ensure flow routing. Multiple algorithms exist for each of these steps, the choice will impact either the performance and/or the final result. This section explores the main existing algorithms utilised within this Thesis, describing the implications of the choices as well as alternatives.

2.3.1 Ensuring flow routing

Digital Elevation Models are inevitably noisy due to both data acquisition and geomorphic noise (e.g., the random array of boulders in a mountain channel, or short wavelength variations in rock hardness) (Tarolli and Mudd, 2020). The amplitude of this noise is not necessarily of huge scale and is very dependant on the data source, however it can artificially inhibit numerical flow calculations.

Indeed, if a internal node (*i.e.* a point representing a pixel which is not located at the edge of the digital elevation model) has no neighbour, it becomes ambiguous to determine how simulated water fluxes through this pixel (*e.g.* Barnes et al., 2014), which is required information to calculate flow direction and accumulation for a landscape. Topographic noise may artificially block the flow, beheading downstream regions from part of their true drainage area. Such a feature in the grid is referred as pit.

The most instinctive way to solve flow routing through the landscape is to model the evolution of flow depth in order to calculate how water will reroute naturally in the landscape (*e.g.* Davy et al., 2017), however it requires a lot of information and assumptions about the quantity of water, precipitation, infiltration or other hydraulic characteristics to be accurate which is a field of study by itself, not necessarily reflecting long-term processes (Whipple et al., 2013).

A number of solutions have been suggested to solve this problem (*e.g.* Barnes et al., 2014; Cordonnier et al., 2018; Schwanghart and Scherler, 2017; Soille and Gratin, 1994). The main categories of algorithms consist in either filling the depressions (*e.g.* Barnes et al., 2014) or carving the depressions (*e.g.* Lindsay, 2016).

The principle of filling pits within a Digital Elevation Model consists in increasing the elevation of any node within a depression to ensure an outlet. Many algorithms exist for this purpose. Barnes et al. (2014) reviews the existing algorithms and suggests Soille and Gratin (1994) was the first to introduce a filling algorithm. Barnes et al. (2014) also propose a new algorithm with linear complexity based on a priority queue to sort nodes, of which slightly modified versions (Barnes, 2016a; Zhou et al., 2016) are the most optimised in the literature. These algorithms are based on a queue, which start from the edges of the grid and process nodes sorted by their elevation. It finds the optimal path for a depression to spill out and apply the outlet elevation to all nodes within the pits. The differences between implementations lie in which method is used for the sorting, queuing, path finding and ignoring nodes which do not need to be processed.

For this Thesis, I utilise the algorithm described in Wang and Liu (2006)

which is of complexity $O(n \log_2[n])$ implemented within LSDTopoTools. As the algorithm produces the same result as the most optimised version, preprocessing flow routing is a one time process and the complexity of Wang and Liu (2006) is reasonable; I have chosen not to expend effort implementing faster algorithms.

Carving algorithms have the opposite approach to filling. They first identify the depressions, and "breach" a path from the bottom of the pit, *i.e.* the node with no down-slope neighbour, to the nearest outlet. We utilise the implementation of Lindsay (2016) for this thesis, which can be faster than filling depending on the pit geometry (Lindsay, 2016). Both algorithms can impose a minimum slope to the filled areas, which are added to the DEM to avoid flat areas.

Computation speed is not the main factor determining which algorithm to select. Each of the two methods may suit a particular landscape, depending on the topographic context. The methods can produce both "overfilling" and "overcarving". Filling and carving, with their respective caveats, are illustrated in Figure 2.3, 2.4 and 2.5.

Overcarving happens when topographic noise happens to show a very localised deep pit, *e.g.* a batch of few pixels few tens of metres bellow surrounding area. I have found that the ALOS World 3D 30m dataset, although quite accurate in mountains compared to SRTM (Tarolli and Mudd, 2020), is prone to localised pits: these tend to appear over bright objects such as metal roofs and sometimes at whitewater. Since the ALOS W3D30 DEM is derived from optical data, this problem suggest very bright pixels confuse the protogrammetric algorithms used to create this DEM. When a pit is present, the carving algorithm will generate an unrealistic trench to drain the pit. In general, I favoured carving over filling, as pits can be detected and manually filled, and once this is performed carving preserves more of the original topography. In Chapter 5, I also uses an hybrid method to carve most of the depressions but low surface deep artifact which get filled.

Overfilling occurs on very flat surfaces and narrow valleys, where a topographic dam (from noise or from an actual dam captured by the DEM) elevates the outlet of the area. This can result in filling of large upstream areas, hiding

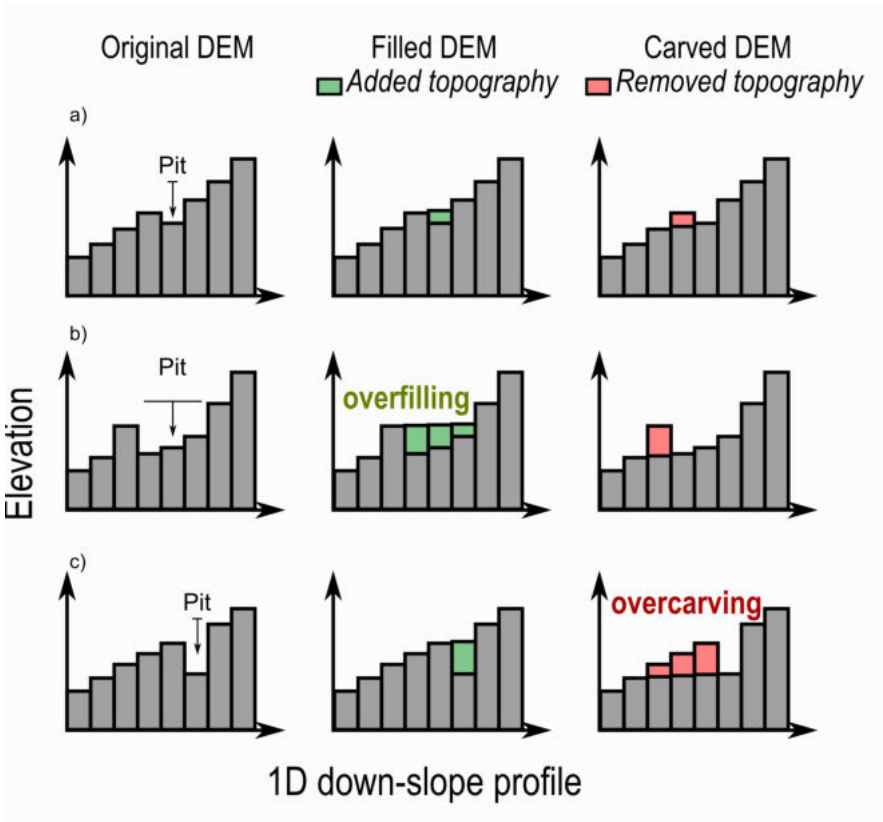

Figure 2.3: 1D conceptual topographic cross-sections illustrating 3 scenarios, (a,b, and c) highlighting how filling and carving algorithms alter the digital elevation model.

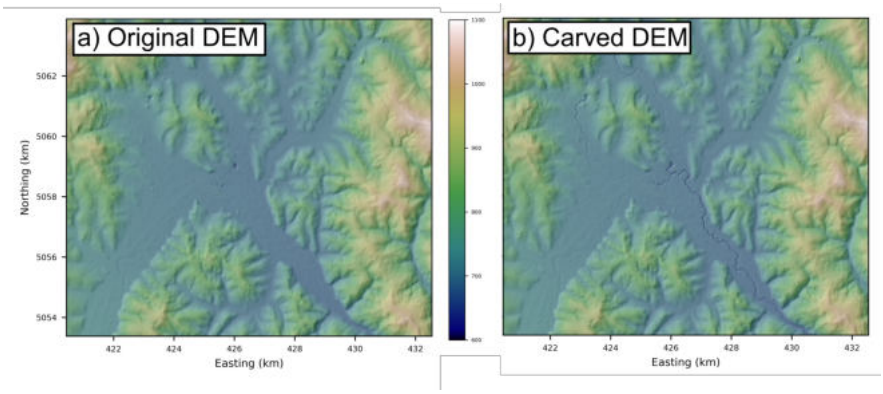

Figure 2.4: Carving algorithm caveat on a DEM. A small-surface pit trigger the carving of a deep trench and alters the flow routing in the area.

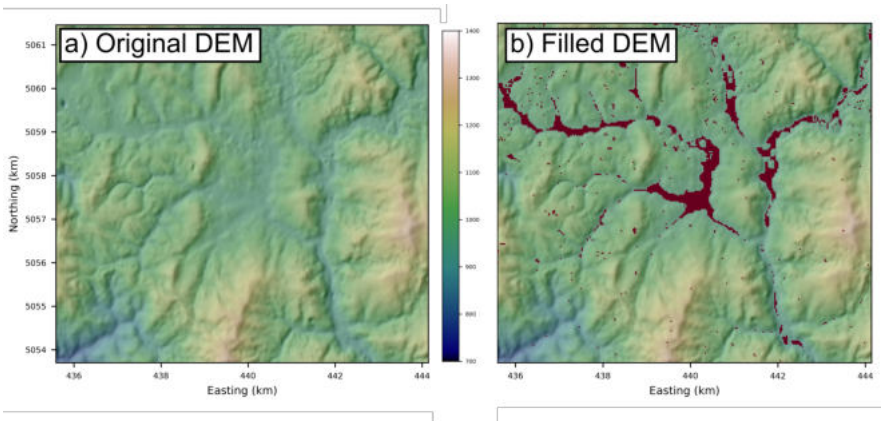

Figure 2.5: Filling algorithm caveat on a DEM. A "dam" triggers the filling of the whole upstream valley, the filled areas in red hide big portions of underlying topography.

topographic variations.

Recent developments have led to more sophisticated methods, which may be worth implementing in the future within topographic analysis suites. Schwanghart and Scherler (2017) developed within TopoToolbox (Schwanghart and Scherler, 2014) two statistical-based methods, namely quantile carving and CRS algorithms, which take the whole river network and makes use of non-parametric regression to correct the noise-affected sections. Another recent development is the use of graph theory to reroute the depression nodes in a correct order based on the topography. Two similar approaches have been developed to serve that purpose (Barnes et al., 2019; Cordonnier et al., 2018), these methods have two advantages: first it does not affect the topography circumventing the caveats linked to overfilling or overcarving while leaving extreme flexibility in potential

way to correct the topography; secondly they are extremely optimised showing both (i) a near-$O(n)$ complexity and (ii) already prepare the node structure for subsequent analysis.

2.3.2 Optimised node structure

Once the digital elevation model has been filled or carved, most algorithms that depend on flow routing rely on a carefully organised node structure for computational efficiency. For example, calculating drainage area or discharge at a node i needs to be done after all upstream ones to ensure correctness (*e.g.* O'Callaghan and Mark, 1984). A contrasting example is to calculate χ over a river network, which requires the accumulation of a value from base level to source and iterating though node in a particular order (Royden et al., 2000).

Prior to 2014, algorithms for flow ordering relied on sorting algorithms, which are notorious for their computational expense (Alturani et al., 2013). Braun and Willett (2013) were the first to derive a method specifically for processing Digital Elevation Models and ordering nodes that circumvented the for sorting algorithms. The method uses graph theory to organise nodes through a *stack* using the number of donors and the position of the receivers of each nodes. Donors, receivers and base level are calculated following a D8 routine (O'Callaghan and Mark, 1984), where each node has only one receiver and it is the one showing the steepest slope amongst the neighbouring down-slope nodes.

The resulting stack has many computational advantages. First, the computational expense is $O(n)$, which makes it particularly efficient for large rasters. Secondly, iterating through the node in the stack order ensures that every receiver node is processed before its donor nodes, without having to iterate through neighbours to check the ordering. Iterating through the stack in reverse order ensures that every donor node is processed before their receivers. Finally this approach allows users to segment the stack by extracting all nodes draining to an area with the total number of donors by node. All of these operations provide the prerequisite node structure to process efficiently most of the geomorphological routines. The main limitation of the method is that Braun and Willett (2013)'s

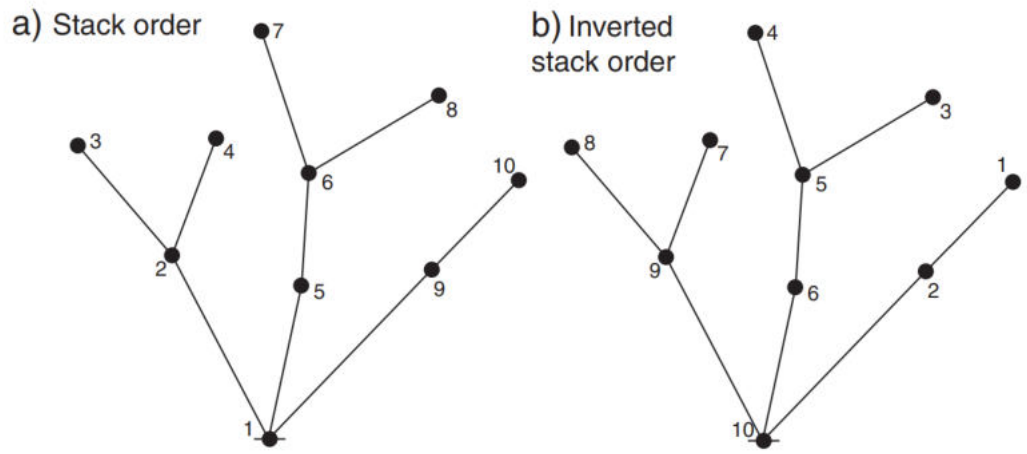

Figure 2.6: Illustration of the node structure from Braun and Willett (2013). The node order allows comprehensive iteration from base-level to top, and inverted stack order from top to bottom.

very efficient version only valid for single receiver, and is not compatible with multiple-flow frameworks (*e.g.* Tarboton, 1997). Alternative algorithms exist but there is a significant drop of performances as the number of edges (links from a node to others) is much higher if multiple receivers are allowed. In graph theory, the generic name of the algorithms organising a graph such as all the donors are processed before their receiver is "topological ordering".

2.3.3 Extracting river networks

Extracting a river network on the sole basis of landscape morphology has been examined by many geomorphological studies (*e.g.* Clubb et al., 2014; Grieve et al., 2016; O'Callaghan and Mark, 1984; Pelletier, 2013). A number of different principles have been invoked to find channel heads. The most common one, and the only one compatible with Digital Elevation Models with a resolution $< 12m$ (Grieve et al., 2016), is based on a critical drainage area for channel formation, or an estimate of critical discharge if precipitation data is available.

The first step consists in calculating flow routing through the landscape. Flow direction, donors and receivers have already been calculated in the previous step, flow accumulation can therefore be calculated by iterating through reverse stack order. The accumulation values, *i.e.* drainage area or precipitation per unit of

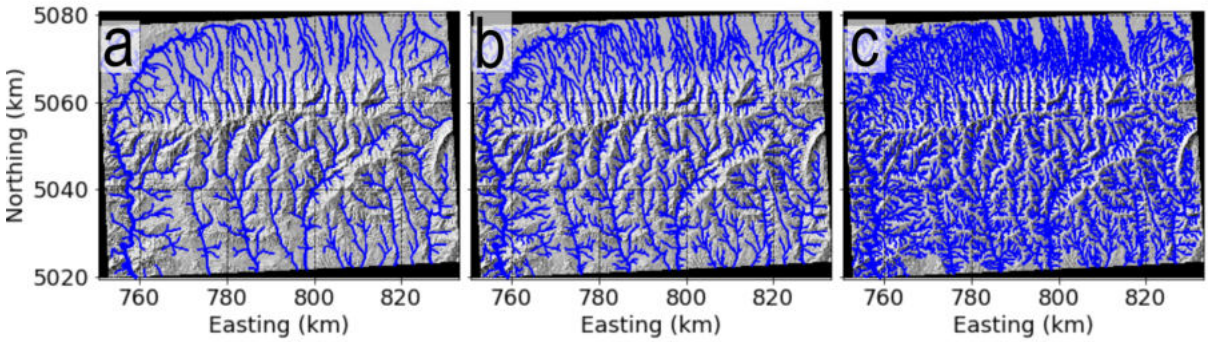

Figure 2.7: River network extracted with different drainage area thresholds, the values of drainage area at which the rivers are initiated. a) $4.5*10^5$, b) $1.8*10^6$ and c) $4.5*10^6$. The drainage density increases as the threshold decreases as less water is assumed to be required to initiate the rivers and therefore increase the number of presumed sources.

time per area, is (i) added to the node and (ii) transmitted to the receiver. Once the the stack is fully iterated, drainage area is available. Extracting rivers from this method only consists in applying a threshold drainage area to only keep the river node. The value of this threshold will determine the density of the extracted network, *i.e.* is the study focusing on small rivers or large ones.

Higher resolution Digital Elevation Models allow the use of more sophisticated methods, as determining optimal drainage area thresholds can be difficult, and potentially inaccurate because not all channel heads occur at the same drainage area (Clubb et al., 2014). For this thesis, three additional methods have been utilised. Pelletier (2013) suggested a two-parameter method, tested against synthetic and real landscapes. The method is based on tangential curvature and expected relative discharge in confined valley to determine channel head locations, which then can reconstruct a river network downstream. Clubb et al. (2014) developed a method using χ coordinate and tangential curvature to determine channel head named DrEICH (Figure 2.8), offering a process-based alternative to other purely morphological methods. Grieve et al. (2016) developed a method based on Passalacqua et al. (2010) and Pelletier (2013), using a Wiener filter to provide a non-parametric extraction method, not extremely sensitive to grid resolution.

The main limitation of all of these methods is that they rely on the choice of user defined parameters, which need to be constrained and or justify. There is no

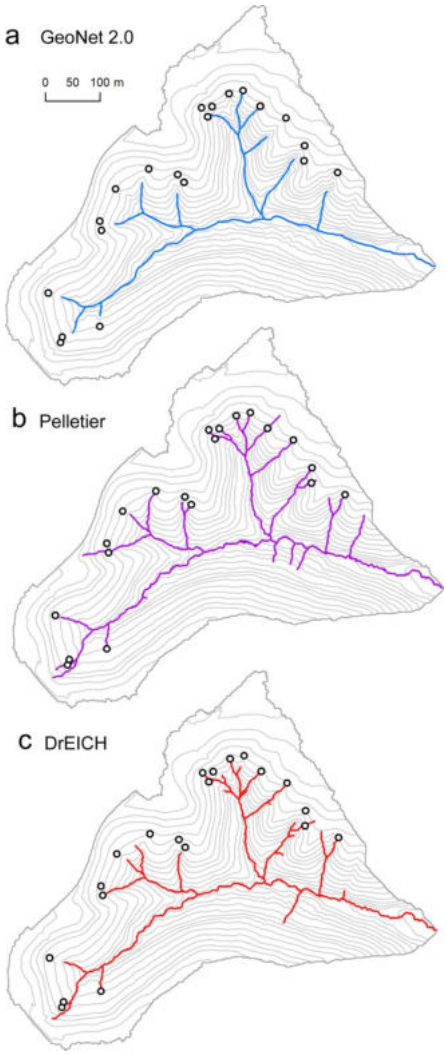

Figure 2.8: Channel heads extracted with different methods, the colored lines are the rivers extracted by the different algorithms and the circles are the river sources observed on field. Figure from Clubb et al. (2014).

general method to constrain them and they vary between landscapes. Artificially varying the density of the river network can affect the metrics extracted, as channel steepness is meaningless when extracted from hillslopes (Clubb et al., 2014; Kirby and Whipple, 2012; Whipple et al., 2013).

2.3.4 Constraining θ

To calculate χ, k_s or k_{sn}, the first step consists in calculating θ. I very briefly introduce the principal in this Subsection, as Chapter 4 is dedicated to this subject. Traditionally, constraining θ is done using linear regression of Slope–Area plots in log space (Wobus et al., 2006c). If equation 1.16 is converted into log space, we find:

$$\log_{10}[S] = -\theta \log_{10}[A] + \log_{10}[k_s] \tag{2.1}$$

allows the linearisation of the power-law relationship. θ can then be extracted using linear regression of the data points. This method often requires data pre-processing methods, such as binning or smoothing, which result in data loss (*e.g.* Mudd et al., 2018; Perron and Royden, 2013; Wobus et al., 2006c, and chapter Knickpoint and Concavity).

More recently, Perron and Royden (2013) first demonstrated the use of the integral method, whereby drainage area is integrated along flow distannce to result in a parameter called χ, to constrain θ. The principle is based on the fact that all tributaries are expected to be collinear in χ space, as indirectly suggested by earlier studies (Niemann et al., 2001; Playfair, 1802).

Mudd et al. (2018) presented different methods exploring ways to determine the value of θ which maximises collinearity in χ space and concluded that method based on a disorder metric is the most efficient and effective to quantify the colinearity (Goren et al., 2014; Hergarten et al., 2016). Chapter 4 expands on this method to explore spatial variations in concavity indices and its implication; the methods, its implications and advantages over S–A methods are developed there.

2.3.5 Calculating χ

Calculating χ requires user-defined parameters, *i.e.* subjective choices which require justification. Firstly, equation 1.21 demonstrates χ relies on the choice of the integration constant A_0, or "reference drainage area". For the majority of cases, we set this constant to 1, because this choice means that the gradient of the channel in χ–elevation space is the same as k_s (see equation 1.22). The implication of varying A_0 is explored in Chapter 3, and in Perron and Royden (2013). Secondly, χ values depend on the choice of x_b, the base level at which the integration starts. This point is explored by Forte and Whipple (2018), who demonstrated the effect of changing x_b at mountain range scale. Thirdly, as exposed in the previous subsection, χ depends on the choice of θ_{ref}.

Once these choices are made, χ is calculated numerically using the stack order from x_b to accumulate the value using trapezoidal approximation to approximate the integration:

$$\chi_i = \chi_{ri} + \left(\frac{A_0}{A_{ri}}^{\theta} + \frac{A_0}{A_i}^{\theta}\right)\frac{\Delta x}{2} \tag{2.2}$$

where i represents a river node i, ri is the receiver of i and Δx the flow distance between a node and its receiver $\Delta x = x_i - x_{ri}$.

2.3.6 Extracting k_s

Once θ is constrained and the χ coordinate calculated, one can further calculate k_s, or k_{sn}. Traditionally this was done using equation 2.1 (Wobus et al., 2006c), $\log[k_s]$ being the intercept of $\log[S]$ at $\log[A] = 0$. This method is available through a number of software packages (*e.g.* Forte and Whipple, 2019; Schwanghart and Scherler, 2014) that propose different methods to segment and bin S–A plots to extract k_{sn}. In Chapter 4, k_{sn} is also calculated with the Slope–Area method for comparing it to the integral one. Calculation follows Wobus et al. (2006a). For this thesis, all chapters use χ-based regression methods to calculate k_s. Gallen and Wegmann (2017) and Schwanghart and Scherler (2014) have methods providing linear regressions over a user-defined number of nodes to ex-

tract k_s from $\chi - z$ profiles. This method, although simple, has the drawback of smoothing over potentially sharp boundaries between slope patches (*sensu* Royden and Taylor Perron (2013)) and rely on a number of user inputs, reducing its reproducibility.

To circumvent this issue, Mudd et al. (2014) developed a segmentation algorithm that aimed to objectively segment the $\chi - z$ profiles. The segmentation process should ideally fulfill two conditions: (i) each segment should minimise the linear regression error R^2 to accurately approximate the river profile while (ii) providing a relevant number of segments representing the slope patches. The first condition is easier to fulfill with a high number of segments, as ultimately linear regressions with very few nodes have a much higher R^2, but this is in tension with the second condition which requires a reasonably low number. Note that each rivers is processed separately, as opposed to the whole basin at the same time like slope area method, to ensure that each slope patch is representing local conditions.

To balance the two conditions, Mudd et al. (2014) set a multi-steps algorithms that separates data into the most likely combination of piecewise linear segments. First, the method partitions a given set of nodes in the profile using a method described in Walker and Skiena (1992), providing all possible sets of segments for this particular subset of nodes within the transformed profile. Secondly, it calculates the slope, intercept and R^2 of the linear regression of each possible segments. Thirdly, the most-likely combination of segments is selected using a criteria originally described in Akaike (1974) and later modified by Hurvich and Tsai (1989):

$$AICc = 2(k_{AIC} - \log[MLE] + \frac{k_{AIC}(k_{AIC}+1)}{N - k_{AIC} - 1}) \tag{2.3}$$

where

$$MLE = \prod_{i=1}^{N} \frac{1}{\sqrt{2\pi}\sigma} exp[-\frac{r_i^2}{2\sigma^2}] \tag{2.4}$$

k_{AIC} is the number of parameters per simulations (*is est* the intercept and the

slope of each segments, then the number of segments times 2), N is the total number of node by segments and σ the standard deviation of the the elevation nodes within the segment. $AICc$ penalises overfitting with too many segments (this is the purpose of the $AICc$, and also penalised poor fits of individual segments. While this method is able to fulfill the aforementioned criteria for successful segmentation, it has its limititations. The main limitation of the Mudd et al. (2014) is that the computational expense increases non-linearly with the number of nodes within the subset and becomes difficult to use when the number exceeds 100 (Mudd et al., 2014): in fact the computational expense goes as the factorial of number of nodes in the subset, meaning even 200 nodes becomes computationally impossible. To alleviate this problem (Mudd et al., 2014) implemented a Monte Carlo iterative scheme, which skips a given number of random nodes at each iteration with the intention of making each subset unique and covering more distance along the profile. The whole process of partitioning and selecting the most-likely combination is repeated at each iteration, and the final k_s value of each node is the averaged values of each iteration in which the node has been taken in account.

The imitations of the method, beyond computational expense, are mainly linked to the need of constraining its parameters. The exact effect of each parameters is developed in Chapter 3. The main element to constrain is the size of the segments, which is influenced by (i) the number of nodes skipped in averaged during each iterations and (ii) the number of nodes by subsets. However there is not a best practice as this aspect depends on the context in which k_{sn} is calculated (*i.e.* is the study investigating large scale variations in channel steepness, or detailed slope patches) and on the quality and resolution of the Digital Elevation Model.

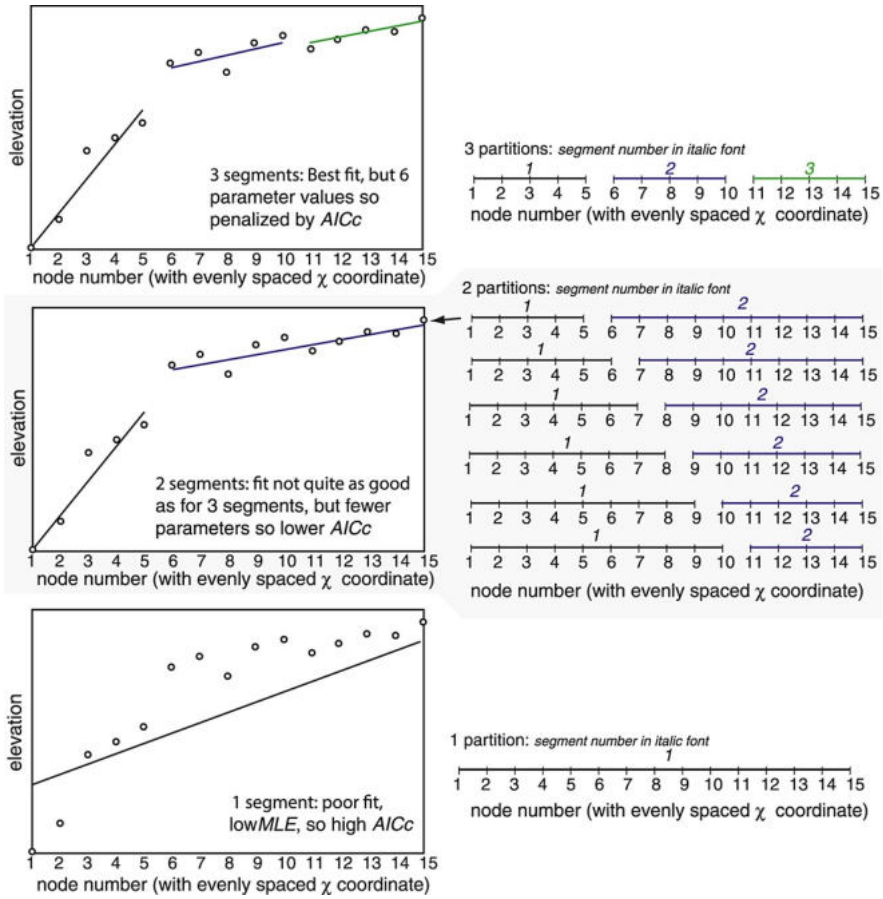

Figure 2.9: Illustration of the partitioning process to calculate k_{sn} from χ–Elevation profile. It illustrates the co-balancing of the AICc and the MLE to determine the optimal segments. Figure from Mudd et al. (2014).

Chapter 3

A segmentation approach for the reproducible extraction and quantification of knickpoints from river long profiles

The work presented in this chapter was published in ESURF:

Gailleton, B., Mudd, S. M., Clubb, F. J., Peifer, D., and Hurst, M. D.: A segmentation approach for the reproducible extraction and quantification of knickpoints from river long profiles, Earth Surf. Dynam., 7, 211–230, https://doi.org/10.5194/esurf-7-211-2019, 2019.

This research was conducted in collaboration with the named co-authors, who helped to edit the final manuscript and contributed to software development. I wrote the topographic analysis algorithms, performed the analyses, created the figures, and wrote the manuscript.

Abstract

Changes in the steepness of river profiles or abrupt vertical steps (i.e. waterfalls) are thought to be indicative of changes in erosion rates, lithology, or other factors that affect landscape evolution. These changes are referred to as knickpoints or knickzones and are pervasive in bedrock river systems. Such features are thought to reveal information about landscape evolution and patterns of erosion, and therefore their locations are often reported in the geomorphic literature. It is imperative that studies reporting knickpoints and knickzones use a reproducible method of quantifying their locations, as their number and spatial distribution play an important role in interpreting tectonically active landscapes. In this contribution we introduce a reproducible knickpoint and knickzone extraction algorithm that uses river profiles transformed by integrating drainage area along channel length (the so-called integral or χ method). The profile is then statistically segmented and the differing slopes and step changes in elevations of these segments are used to identify knickpoints and knickzones, and their relative magnitudes. The output locations of identified knickpoints and knickzones compare favourably with human mapping: we test the method on Santa Cruz Island, CA, using previously reported knickzones and also test the method against a new dataset from the Quadrilátero Ferrífero in Brazil. The algorithm allows extraction of varying knickpoint morphologies, including stepped, positive slope-breaks (concave upward) and negative slope-break knickpoints. We identify parameters that most affect the resulting knickpoint and knickzone locations, and provide guidance for both usage and outputs of the method to produce reproducible knickpoint datasets.

3.1 Introduction

Landscapes are shaped by competition between crustal processes such as tectonic plate motion or dynamic topography and deposition or erosion at the Earth's surface. This competition, if unperturbed, tends toward topographic steady-state where vertical motions are counterbalanced by erosion (e.g., Hack, 1960; Willett

and Brandon, 2002b). In unglaciated landscapes, the main driver of erosion is the river system (Ahnert, 1970), which incises the landscape to remove and transport material from uplands to active basins. The analysis of river long profiles has been a key method to interpret landscape evolution (e.g., Wobus et al., 2006a), from the early recognition of graded rivers (e.g., Gilbert, 1877) to the generalised recognition that river profiles reflect varying erosion processes (e.g., Dietrich et al., 2003; Hack, 1960; Howard, 1965; Howard et al., 1994; Kirby and Whipple, 2012; Mackin, 1948).

In a river system, topographic steady state requires spatially stable rock uplift and climatic conditions over a long period of time (Willett and Brandon, 2002b). In most landscapes, however, these conditions are unlikely (Baldwin et al., 2003). Many processes have been suggested to result in both spatial and temporal variations in uplift rate, such as varying tectonic stress (e.g., Kirby and Whipple, 2012), complex mantle processes inducing vertical motions (e.g., Braun, 2010; Faccenna and Becker, 2010), uplift driven by differential rock density (Braun et al., 2014) and base level variations linked to eustatic variations (e.g., Lambeck and Chappell, 2001; Powell, 1875; Schumann et al., 2016). River systems affected by these processes respond by transmitting signals upstream through the channel network (e.g., Royden and Taylor Perron, 2013; Whipple et al., 1999), eventually driving drainage network reorganisation resulting in additional transient signals (e.g., Castelltort et al., 2012; Mather, 2000; Mudd, 2017; Whipple et al., 2017a; Willett et al., 2014). Moreover, river profiles are also affected by intrinsic landscape properties, such as fracture density (e.g Whipple, 2002) or differential lithology (e.g., Forte et al., 2016; Stock and Montgomery, 1999) which can also lead to morphological adjustment of the channel (e.g., Kirby and Whipple, 2012). The most direct and widely observed expression of river adjustment to transient or intrinsic perturbations is a discrete change in river gradient, commonly referred as a “knickpoint”.

Changes in channel gradient linked to different lithologies have been recognised in geomorphological studies for centuries. Lapparent and Lapparent (1896) suggested that these changes may represent “successive reaches” with different

base levels, hypothesising that these reaches somehow migrate upstream. Davis (1889) recognised the tectonic genesis of some of these signals, describing how landscapes experience erosion cycles with periods of "rejuvenation" followed by periods of gradual adjustment, and thus transience. However, these early studies did not name such morphologies as distinct entities. The term "knickpoint" was first introduced into the geomorphological literature by Knopf (1924), borrowing the word from chemical sciences to "denote an abrupt change in direction from a gentle concave curve to a curve that is convex upward" (p.636).

Based on earlier observations on the topography and geology of the Appalachians (e.g., Barrell, 1920; Bascom, 1921), Knopf (1924) described a knickpoint as a migrating steepened boundary between two river reaches. She went on to state that the downstream reach should flow with a gradient determined by the present day balance between uplift and erosion, and the upstream reach should flow with a gradient representing an older such balance. Recognition of knickpoints and their significance in transient landscapes has driven much research into interpreting topography (e.g., Abbühl et al., 2011; Crosby and Whipple, 2006; Kirby and Whipple, 2012; Wobus et al., 2006a), as well as using river profiles to extract past uplift histories (e.g., Pritchard et al., 2009).

The diverse nature of knickpoint formation means that these features have been used to investigate many geomorphological problems. For example, retreat rates have been used to link knickpoints with tectonic events and faulting (e.g Attal et al., 2011; Attal et al., 2008; Whittaker, 2012) or climatically triggered base-level fall (e.g., Baynes et al., 2015; Crosby and Whipple, 2006; Neely et al., 2017). Although migrating knickpoints are commonly associated with base level variations, Haviv et al. (2010) highlighted the role of differential lithologies in retreat rates of vertical knickpoints within tectonically and climatically stable landscapes. Furthermore, Scheingross and Lamb (2016) and Scheingross et al. (2017) noted the importance of sediment supply and hydraulic conditions in waterfall retreat, providing a quantitative interpretation of the early observations of Lapparent and Lapparent (1896) on waterfall migration. Cook et al. (2013) observed an important correlation between knickpoint retreat and bedload transport, fur-

ther highlighting the importance of sediment transport. Bishop and Goldrick (2010) demonstrated that considering the role of resistant lithologies is crucial when studying landscape evolution, as they can considerably slow down landscape response time to transient signals. Other studies have linked knickpoints directly to landscape characteristics such as heterogeneous lithology (e.g., Duvall, 2004; Kirby et al., 2003; Stock and Montgomery, 1999; Tucker and Slingerland, 1996). Recent analogue experiments on knickpoint retreat (e.g., Baynes et al., 2018) have highlighted the inter-connectivity of all these processes and the need to consider both internal and external landscape characteristics.

These examples demonstrate the importance but also the diversity of transient and lithologic signals in landscapes, and highlight that different processes can generate remarkably similar channel morphology. It is therefore crucial to define knickpoints morphologically before drawing interpretations about their significance in term of processes or genesis. In this contribution, we aim to provide a method for reproducibly and systematically extracting knickpoints within real landscapes based on river profile morphology.

3.1.1 Knickpoint morphology and detection

Morphological description

Knickpoints can be defined as discrete changes in river gradient (Whipple et al., 1999). Haviv et al. (2010) proposed two end-member knickpoints: break-in-slope knickpoints, expressed by an abrupt change in river gradient; and break-in-elevation knickpoints, characterized by step in the elevation as a waterfall with similar gradient on both sides of the knickpoint. These knickpoints are now commonly referred as slope-break knickpoints and vertical-step knickpoints (e.g., Kirby and Whipple, 2012; Neely et al., 2017). Kirby and Whipple (2012) suggest that although vertical-step knickpoints tend to be linked to discrete heterogeneities along the river profile (e.g., caused by geological boundaries), both morphologies can be either fixed or mobile and each style of knickpoint may be generated by a range of processes.

As discussed in Goldrick and Bishop (2007) and Kirby and Whipple (2012), both morphologies can be detected using a slope–area plot (Figure 3.1) or a slope–distance plot. It has long been observed that channel gradients vary systematically as a function of drainage area. For example, Gilbert (1877) stated that "In general we may say that, *ceteris paribus*, declivity bears an inverse relation to quantity of water (p.114)." How do we then find anomalous channel gradients? In the mid-twentieth century, authors such as Hack (1957) and Morisawa (1962) found systematic, quantitative relationships between channel gradient and drainage area, often used as a proxy for discharge. Morisawa (1962) and later Flint (1974) recognised that channel gradients often declined systematically downstream in a trend that could be described by a power law:

$$S = k_s A^{-\theta}, \tag{3.1}$$

where θ is referred to as the concavity index since it describes how concave a profile is: the higher the value, the more rapidly a channel's gradient decreases downstream. The term k_s is called the steepness index, as it sets the overall gradient of the channel, and a number of authors have noted that k_s frequently scales with erosion rate in lithologically homogeneous landscapes (e.g., DiBiase et al., 2010; Harel et al., 2016; Mandal et al., 2015; Ouimet et al., 2009; Scherler et al., 2014). A knickpoint might manifest itself as an abrupt change in slope–area scaling, and lead to local variations in k_s (Figure 3.1a).

However, using slope–area data derived from digital elevation models (DEMs) suffers from noise in channel slopes, leading to scattering of gradient data, as discussed in Perron and Royden (2013). Wobus et al. (2006a) proposed methods to reduce the effect of noise and extract trends from slope–area plots. These recommendations include regular sampling of elevations to extrapolate artefact-free contour lines or logarithmic binning by drainage area. Smoothing induces inexorable data loss and may result in difficulties detecting subtle, but important features such as knickpoints (Figure 3.1b).

Alternatively, we can integrate equation (3.1), since $S = dz/dx$ where z is elevation and x is distance along the channel (e.g., Whipple et al., 2017b), resulting

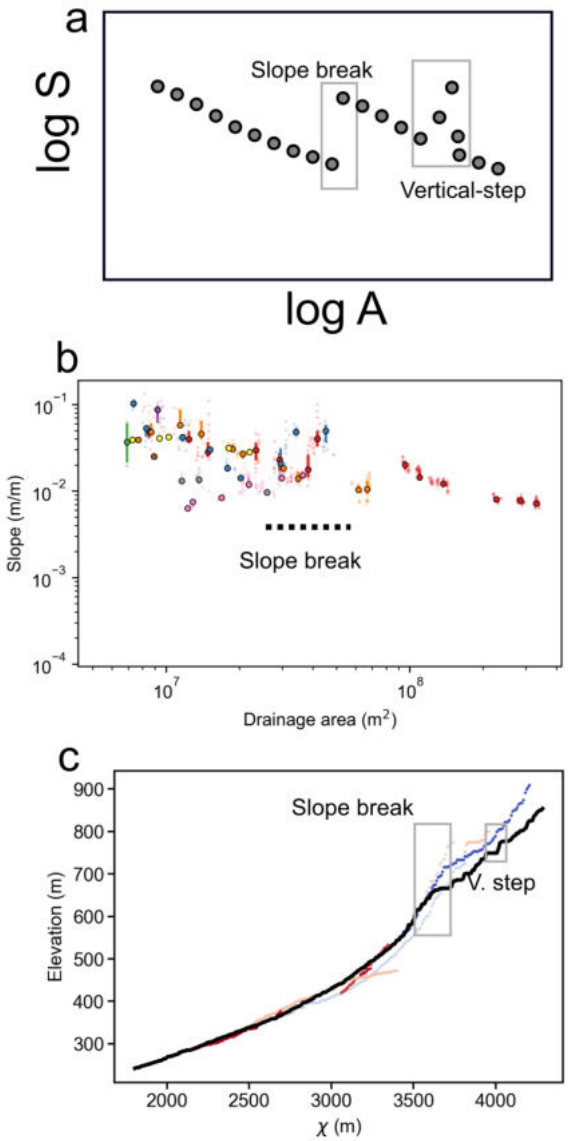

Figure 3.1: Different methods to detect knickpoints. (a) Cartoon showing how vertical-step and slope-break knickpoints appear in slope–area plots, adapted from Kirby and Whipple (2012). (b) A slope–area plot derived from SRTM 30 metres resolution data in Romania; the catchment's outlet coordinates are 45.252842, 26.375697 (WGS84). Different colours represent different tributaries, small '+' symbols are individual data points and circles are logarithmically binned data. A single slope-break knickpoint can be interpreted but minor knickpoints are more difficult to extract. (c) The same basin represented in a χ–elevation plot, using $\theta = 0.15$.

in

$$z(x) = z(x_b) + \left(\frac{k_s}{{A_0}^\theta}\right) \int_{x_b}^{x} \left(\frac{A_0}{A(x)}\right)^\theta dx, \tag{3.2}$$

where A_0 is a reference drainage area, introduced to nondimensionalise the area term within the integral in equation (4.3). We can then define a longitudinal coordinate, χ (Royden et al., 2000):

$$\chi = \int_{x_b}^{x} \left(\frac{A_0}{A(x)} \right)^{\theta} dx. \tag{3.3}$$

χ has dimensions of length, and is defined such that at any point in the channel

$$z(x) = z(x_b) + \left(\frac{k_s}{{A_0}^{\theta}} \right) \chi. \tag{3.4}$$

The χ approach to represent normalised long profiles (equations (4.5) and (4.4)) can serve as an alternative method to explore the slope–area relationship within a drainage network. The χ coordinate integrates information about drainage area, while requiring less smoothing and lumping than $\log(S)$–$\log(A)$ plots (Figure 3.1c). This approach has been widely used in recent studies (e.g., Moodie et al., 2017; Mouchené et al., 2017; Mudd et al., 2014; Neely et al., 2017; Perron and Royden, 2013; Whipple et al., 2017a; Willett et al., 2014).

Existing algorithms

Traditional knickpoint identification from DEMs relied upon user-based selection along river long profiles (e.g., Hayakawa and Oguchi, 2006; Wobus et al., 2006a). Several computational methods have been proposed for extracting knickpoints from DEM-derived datasets. The first (semi-)automated methods taking advantage of digital topographic data used long-profile geometry to isolate knickpoints or knickzones. Hayakawa and Oguchi (2006) proposed a semi-automated extraction method based on decreasing of gradient with increasing length. This method involved the use of ArcGIS and spreadsheet software to process the outputs for each river. Recognising the need for automated regional knickpoint mapping methods in geomorphological studies, Gonga-Saholiariliva et al. (2011) proposed an automated algorithm to map abrupt changes in river gradient using slope, profile, and planview curvature. Gallen et al. (2013) used systematic changes in profile convexity over given thresholds ($>$ 20 metres in elevation drop, coupled

with a slope threshold ≥ 0.1) to isolate knickpoints in fluvially-dominated channels with the aim of reconstructing rejuvenation events, both climatically and tectonically driven, in the southern Appalachians. A similar method has been implemented in ArcGIS by Queiroz et al. (2015). More recently, Zahra et al. (2017) published an ArcGIS toolset (called KET) that automates and optimizes the Hayakawa and Oguchi (2006) method. These methods are based of the direct use of channel elevation, gradient and curvature, and so are susceptible to previously described limitations related to noise. Furthermore, the Hayakawa and Oguchi (2006) method does not incorporate drainage area information, which is an important parameter to consider when studying knickpoints over large spatial scales, or when interpreting the retreat rates of these features.

Another set of methods exploit the use of k_s from equation 3.1 (or k_{sn} when calculated using a fixed value of θ) to extract knickpoints from slope-area plots, as reviewed by Neely et al. (2017). These methods suffer from limitations linked to slope-area scattering, noise sensitivity and difficulty in precisely locating knickpoints because of the stepped nature of drainage area (increasing instantaneously downstream when a new tributary reaches the river channel). To ameliorate problems with noise and data scattering, Bennett et al. (2016) devised a method that first calculates k_{sn} on channel profiles smoothed using the algorithm of Schwanghart and Scherler (2014). This derives k_{sn} either from regression of slope–area plots, or using the first-order derivative of χ plots. The method selects a knickpoint where the ratio between downstream and upstream k_{sn}, averaged with two 2-km long serial windows, exceeds a factor of two.

Neely et al. (2017) developed an algorithm focused on knickzone detection (KZ-picker). Knickzones are selected from normalized profiles (using the approach of Perron and Royden (2013)) by comparison with a reference profile, calculated for a defined concavity index (θ in equation 3.1). This reference profile is a line in χ–elevation space between the outlet and headwaters of the channel, and knickzones are then defined based on the deviation of the χ profile from the reference. After initial detection, knickzones are quantified by their relief (elevation drop) and adjusted using several filters or lumping-window parameters. This

method is well adapted to detect knickzones that are composed of a base and a lip separating a steepened reach. Example of output produced by this algorithm and compared to our is presented in section (3.5.4).

Another method for extracting knickpoints has recently been implemented using TopoToolbox (Schwanghart and Scherler, 2014). Albeit unpublished, the code is available and also aims to reproducibly extract knickpoint locations from river profiles. It selects knickpoints by creating reference channel profiles that are concave up and then selecting knickpoints where the actual channels are the most different from the reference channels. Although not based on the slope–area relationship, this method is perhaps the closest algorithmic attempt to match the knickpoint definition of early workers (e.g., Knopf, 1924). A sensitivity parameter defines the number of iterations and indirectly the number of knickpoints detected. After knickpoint extraction, a value is attributed to each identified knickpoint quantifying the divergence of the long profile from the reference profile. We discuss the similarities and differences of this method compared to our method in Section 3.6.

Motivation for a new method

Despite the large number of past approaches to selecting knickpoints, we have developed a new method because i) many authors still select knickpoints based on qualitative interpretation of channel long profiles or slope–area data and we desired an open source, reproducible method that has no reliance on proprietary software such as ArcGIS (e.g., Hayakawa and Oguchi, 2006) or MATLAB (e.g., Neely et al., 2017; Schwanghart and Scherler, 2014); ii) channel erosion is modelled to scale with discharge, and therefore we wished to use a method that includes discharge (or its proxy drainage area); iii) existing slope–area approaches make it difficult to pinpoint knickpoint locations (Figure 3.1), and therefore we choose to use a χ-based approach; iv) we wished to develop a method that not only selected knickpoint locations but included metrics of changes in normalised channel steepness, as that metric is frequently used in tectonic geomorphology and v) we aimed to create a method allowing the differentiation between different

knickpoints morphologies (e.g., slope-break vs vertical-step).

Although the newest methods (Neely et al., 2017; Schwanghart and Scherler, 2014) meet a subset of these criteria, they both only describe a specific morphology of knickpoint/knickzone and use indirect methods to quantify their magnitude (e.g. derived from the comparison with a reference profile). Our aim here is to provide a method that selects locations, styles (e.g. vertical step, slope-break), and magnitudes (e.g. main features or secondary ones) of knickpoints and knickzones that is free of manual selection in order to complement these existing methods that are more focused on identifying locations of a particular style of knickpoints and knickzones (e.g. waterfall).

We provide comparisons with two existing methods in section 3.5.4. These have been chosen for the following reasons: i) the knickpoint-extracting algorithms are open-source (with the limitation of MATLAB licenses), ii) the methods are objective, reproducible and provides a quantification of knickpoint magnitude in order to compare it with our and iii) (Schwanghart and Scherler, 2014) is purely based on channel morphology while (Neely et al., 2017) uses the slope–area relationship and χ thus providing a reasonable comparison of our algorithm with the range of existing methods.

3.2 Methods

An overview of our knickpoint identification method can be found in figure 3.2.

3.2.1 DEM preprocessing and river network extraction

Firstly, we fill the DEM using the filling algorithm of Wang and Liu (2006), to make sure that each cell has a flow direction and to avoid internal basins generated by DEM noise (e.g., Barnes et al., 2014). This approach is suitable for cases where no feature is spuriously damming the DEM. Spurious damming can occur when vegetation, bridges, or other features lead to high elevations over the channel when in fact the channel sits at a lower elevation. The filling process will create flat surfaces behind such spurious dams and will therefore hinder channel

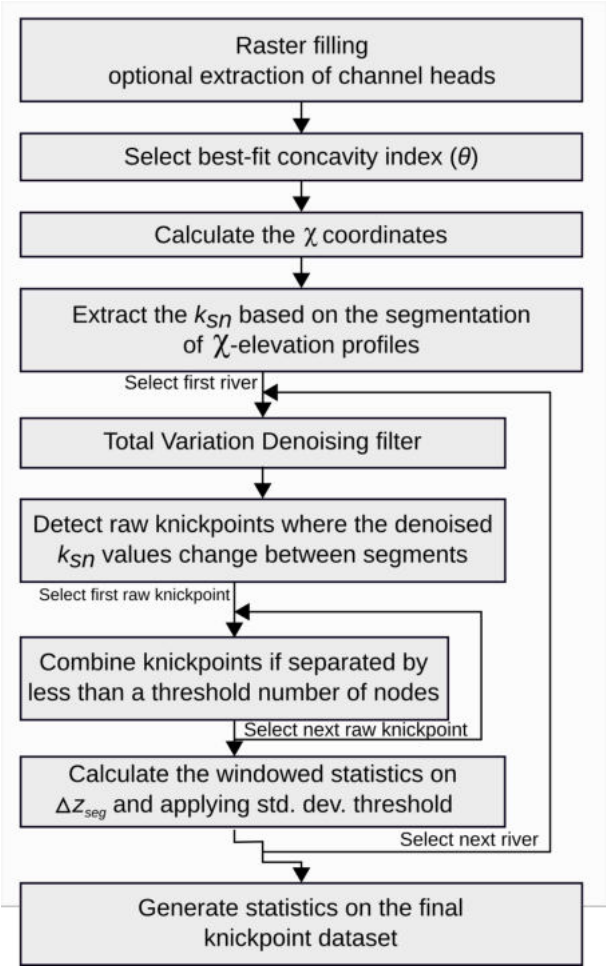

Figure 3.2: Flowchart of the knickpoint detection algorithm.

profile analysis.

If features that lead to spurious damming are present, we give users the option to use a breaching or carving algorithm. This excavates through spurious dams to avoid overfilling. The depression-breaching algorithm in our code is that created by Lindsay (e.g., 2016) and adapted from Barnes (2016b) within our method. It is also possible to supply the algorithm with preprocessed DEMs (e.g., Schwanghart and Scherler, 2017).

From the preprocessed, carved, or filled DEM, we provide several methods of extracting the river network, including the DrEICH method (Clubb et al., 2014); a curvature method proposed by Pelletier (2013); and a method that uses a Wiener filter (Wiener, 1949) that combines elements of the methods of Pelletier (2013) and Passalacqua et al. (2010) first implemented by Grieve et

al. (2016) and F.J. (2017); Grieve et al. (2016) found this latter method least sensitive to DEM resolution. Finally, we include extraction based on a drainage area threshold, more suitable for low-resolution DEMs (e.g., SRTM, ASTER) or large-scale studies where the location of channel heads is less important. We also ensure during the preprocessing that no catchments are beheaded by the edge of the DEM, as the χ coordinate is a function of drainage area and therefore incomplete basins will have incorrect χ values.

3.2.2 k_{sn} extraction

Following channel extraction, we then calculate the χ coordinate for the resulting network. A key parameter that must be constrained prior to calculation of χ is the concavity index (θ). Changing the concavity index significantly affects values of the the χ coordinate (e.g., Gasparini and Whipple, 2014; Kirby and Whipple, 2012; Mudd et al., 2018) and therefore subsequent knickpoint extraction. We select the concavity index using a method developed by Mudd et al. (2018). This method calculates the χ coordinates for a range of concavities within each watershed, and determines the most likely concavity index by directly comparing the collinearity of points on each tributary with the trunk channel (Mudd et al., 2018; Perron and Royden, 2013). This approach does not assume linearity in χ–elevation space, and therefore is applicable in transient landscapes (Mudd et al., 2018).

Once we determine θ values for each basin, we calculate χ and then use χ–elevation profiles to determine changes in k_{sn}, which is the gradient of the χ–elevation profile when we set $A_0 = 1$ (see equation 4.3). Theoretical work by Royden and Taylor Perron (2013) suggested that in eroding landscapes changes in erosion rates would be represented by changes in χ–elevation gradient between segments of channels that would be linear in χ–elevation space, which Royden and Taylor Perron (2013) called slope patches. Mudd et al. (2014) devised a statistical method that identified the most likely linear segments in χ–elevation space. This technique searched all possible combinations of channel pixels and used the corrected Akaike Information Criterion (AICc) (Akaike, 1974; Hurvich

and Tsai, 1989) to balance goodness of fit of linear segments against over-fitting the data. Here we use this same algorithm to search for breaks in slope within the profile corresponding to knickpoint locations.

Knickpoints will manifest themselves as changes in the slope of these patches, equivalent to the slope-break knickpoints of Kirby and Whipple (2012), whereas knickzones will be represented by patches with locally high gradients. That is, knickpoints and knickzones result in either changes in or locally high values of k_s (or k_{sn} if calculated with a fixed concavity index). The segmentation algorithm casts the profile as a series of linear segments, and each segment has a gradient and an intercept. The gradient reflects k_s of the segment and the intercept can be used to detect vertical-step knickpoints, as it detects elevation jumps between adjacent slope patches.

The method developed by Mudd et al. (2014) subsamples underlying topographic data iteratively: on each iteration nodes from the channel network are chosen randomly and segmentation is applied to this subset of nodes. The number of iterations is called n_{MC}. This iterative approach was taken because it significantly reduces the sensitivity of the results to user parameters (Mudd et al., 2014). The computational expense of the segmentation scales highly nonlinearly with the number of nodes so channel profiles are broken into subsections of length n_{tg} (called the "Target Nodes" in Mudd et al. (2014)). The sampling of the underlying data on each iteration is random: after each sample nodes are "skipped" randomly, the number of nodes skipped varies with a uniform distribution from zero to twice a parameter n_{sk} such that the mean "skip" is n_{sk}. We explore the sensitivity of the method to these parameters in the discussion.

The final k_{sn} values are an average of many iterations using different channel profiles subsampled from the raw data, as are intercepts of local segments. These averaged values are used to build segmented elevation. Each node then represents an average of the best-fit segments for every iteration of the segmentation routine (Figure 3.3a):

$$z_{segi} = M_{\chi i} * \chi_i + b_{\chi i}, \tag{3.5}$$

where i is the given node, z_{seg} its elevation on the segment, M_χ the average gradient of the segments and b_χ the averaged intercept of the segments. M_χ can be expressed with the following equation:

$$M_\chi = (\frac{E}{K * A_0^m})^{1/n}, \tag{3.6}$$

We note here that M_χ is the same as k_{sn} if χ is calculated using $A_0 = 1\text{m}^2$.

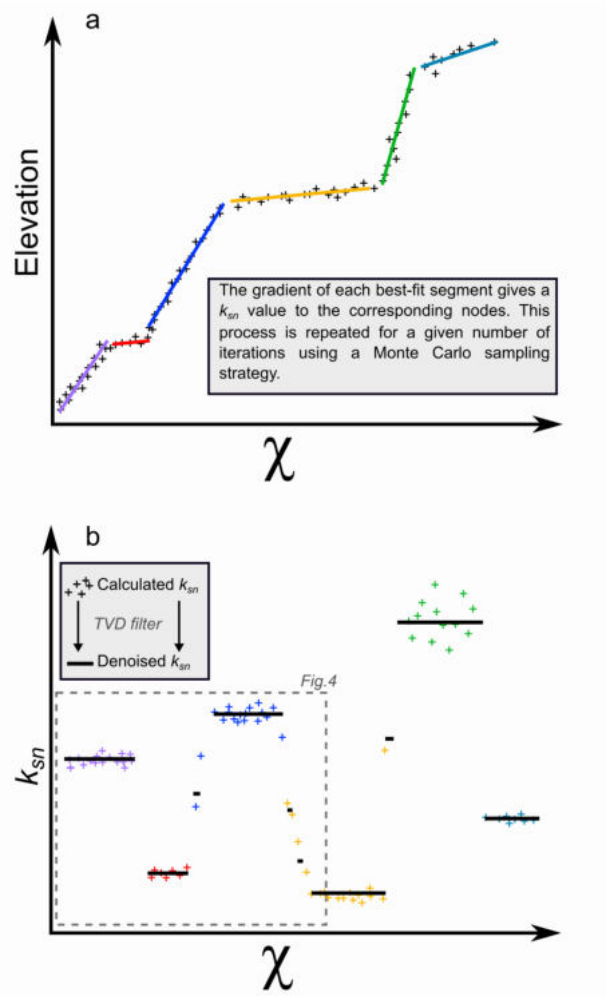

Figure 3.3: Extraction of normalised channel steepness (k_{sn}) from a river profile. (a) Example of best-fit segmentation (Mudd et al., 2014) where '+' symbols are individual data points and the coloured lines are the segments. (b) The associated plot of k_{sn} plotted as a function of χ coordinate. The segmentation output results in some noise due to iterative sampling of the channel network ('+' symbols). Total Variation Denoising filter (Condat, 2013) is then applied on the signal to extract the main variations in k_{sn}.

3.2.3 Knickpoint extraction from k_{sn} data

Change point detection

Change point detection is a common technique used within many fields (e.g., time series analysis) and a number of statistical tools have been developed to identify change points, reviewed and described by Truong et al. (2018). In our case, the signal (k_{sn}) is by definition piecewise stationary, and abrupt changes occur between each segment (*i.e.*, knickpoints). Change point detection algorithms aim to estimate and isolate the exact location of these boundaries between stationary patches. Method choice depends on the nature of the original dataset (*e.g.,* noise intensity) and the number of changes we aim to extract (*e.g.,* predetermined or unknown). In our case, although the segmentation algorithm of Mudd et al. (2014) can result in very sharp segment boundaries, in many cases the transitions between segments is fuzzy. We therefore have an unknown number of change points to detect from a variably noisy signal. We therefore choose to use a signal processing filter (Condat, 2013) to flatten the piecewise k_{sn} patches and discretise all potential change points. This algorithm identifies where k_{sn} and elevation are statistically varying the most within any transition zones. It also combines segments that have very small changes in k_{sn} relative to the noise in the data (Figure 3.3b).

We denoise the data using a one dimensional Total Variation Denoising (TVD), a signal processing filter adapted from a optimized algorithm by Condat (2013) solving the following equation:

$$\underset{x\in\Re^N}{minimize}\frac{1}{2}\sum_{k=1}^{N}|y[k]-x[k]|^2+\lambda\sum_{k=1}^{N-1}|x[k+1]-x[k]|\,, \tag{3.7}$$

where N represents the number of samples (nodes) per population (in this case a river channel from source to next higher-order stream, or the outlet), y represents the raw signal $y_1, y_2, y_3, ...y_N$, in this case k_{sn} ordered by ascending χ within each river, x the denoised signal $x_1, x_2, x_3, ...x_N$, referred as denoised k_{sn}, and λ is a regularization parameter (Condat, 2013). This method minimises variations, where the parameter λ must be real and greater than zero. Greater

λ values result in less variation in the processed signal, and $\lambda \to +\infty$ results in no variation in the processed signal whatsoever. The selection and sensitivity of this parameter is discussed in Section 3.5.1.

After denoising the data, our method then iterates through all nodes in each channel and identifies change points as any variation in the denoised k_{sn} data. These represent first-order knickpoints that we quantify by their change in denoised k_{sn}, which we call Δk_{sn}. Δk_{sn} is a quantitative measure of the magnitude of the slope-break component of the knickpoint (Figure 3.4a). We refer to change points as knickpoints in the rest of the manuscript.

Combining knickpoints

Denoised k_{sn} data can still contain closely clustered steps in k_{sn} values, which may in fact represent a single knickpoint. We therefore use an algorithm to determine which of these clusters can be combined. Iterating through each river, the algorithm tests the neighbouring nodes of each raw knickpoint in a window that we call the "combining window". If two knickpoints in the denoised k_{sn} data are within the combining window and both have the same sign of Δk_{sn}, the two knickpoints are merged and their magnitude summed. This process is repeated using newly merged knickpoints until no nodes are within the combining window, or until a change in knickpoint sign (Figure 3.4b). The combined knickpoint is then centred between the combined nodes. The width of the combining window (which we denote r_{comb}, and is defined by a number of nodes rather than a flow distance) is a user-defined parameter, the selection of which we address in Section 3.5.1.

Vertical-step knickpoint detection

Small variations between segments with similar k_{sn} values may be ignored by denoising, which may seem trivial if the aim is to isolate the main variations in channel steepness. However, this may lead to vertical-step knickpoints being missed if channel segments above and below the vertical-step knickpoint have similar k_{sn} values despite a jump in z_{seg}. We therefore use a second approach

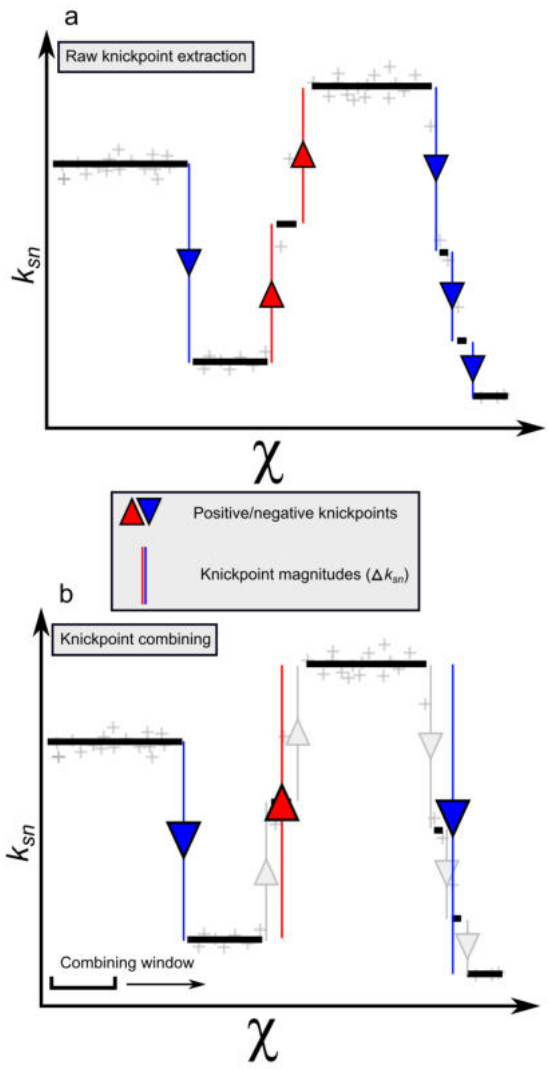

Figure 3.4: Knickpoint extraction from the denoised k_{sn} profiles. (a) The first step extracts all variations of k_{sn}, quantifying each with Δk_{sn}, which we call the "raw" knickpoint dataset. Negative and positive changes represents decreases or increases of k_{sn}, respectively. (b) After detection of changes in k_{sn}, knickpoints are combined. All knickpoints within a node window will be combined, summing their values (i.e., a sum of Δk_{sn}. This process is repeated as long as the subsequent raw knickpoint is within a node window and as long as the polarity (*i.e.*, if it is negative or positive) does not change.

to extract knickpoints, allowing us to identify both slope-break and vertical-step knickpoints.

The algorithm calculates changes in z_{seg} using equation (3.5) in order to isolate the main jumps in profile elevation. We differentiate this value along the river nodes (Δz_{seg}) to detrend the elevation signal and focus on the stepped vari-

ations. For each node in the channel, the mean and standard deviation of Δz_{seg} is calculated within a window of surrounding nodes; the window width in nodes is called r_W. The nodes within the first and last half-windows are calculated using respectively the first and last window. Δz_{seg} is then compared to the standard deviation of the nodes within the corresponding window multiplied by a coefficient (which we call T_σ), and the node is selected as a vertical-step knickpoint if Δz_{seg} is greater (Figure 3.5b). This approach ensures that the selected vertical-step knickpoints show an anomalous increase in elevation. The selection of the window width and the coefficient are discussed in Section 3.5.1. We can then use Δz_{seg} as a quantitative measure of the size of each vertical-step knickpoint.

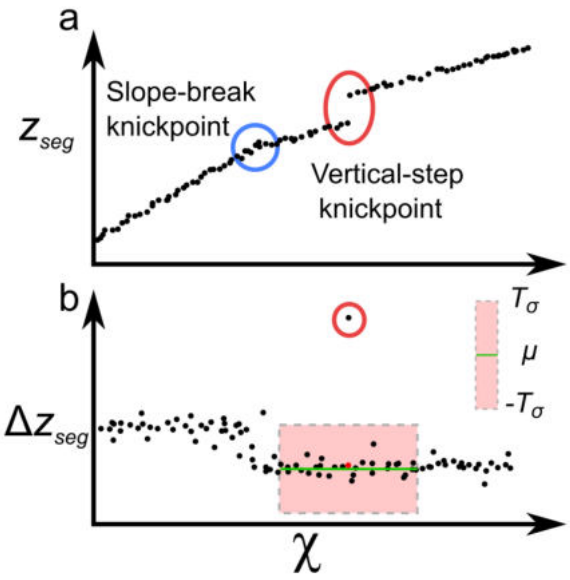

Figure 3.5: Extraction of knickpoints from the segmented elevation (equation 3.5). (a) Expression of a vertical-step knickpoint in a $\chi - z_{seg}$ profile compared to a slope-break knickpoint. (b) Representation of the identification window and the corresponding standard deviation around the reference node (in red). μ is the mean and T_σ the coefficient applied to the standard deviation. This process is repeated for each node. Reference nodes outside their own window are considered to be outliers.

3.2.4 Accuracy metrics

The accuracy of the method is assessed using a true positive (TP), false positive (FP) and false negative (FN) approach. This comparison method is often use to test algorithm performances on point data, such as channel heads (e.g., Clubb et

al., 2014; Orlandini et al., 2011) or knickzone locations (e.g., Neely et al., 2017). We test the algorithm with these accuracy metrics using two sites where locations of hand-picked knickpoints based on field observations and river profiles are available. Knickpoints were identified at Santa Cruz Island (California, USA) by Neely et al. (2017), and we introduce a new dataset in the Quadrilátero Ferrífero, Minas Gerais, Brazil.

We define as TP a reference knickpoint detected by the algorithm, as FP a knickpoint detected by the algorithm that is not a reference knickpoint, and as FN reference knickpoints not detected by the algorithm. Neely et al. (2017) proposes a fourth kind of prediction called "mixed" to assess the knickzone base and lip detection, where only one of the two knickzone boundaries is detected. We chose not to use this approach as we define a knickpoint as a point location showing an increase or decrease of k_{sn} or Δz_{seg}, which is more applicable to varying knickpoint morphologies. The definition of the different knickpoint predictions allows the calculation of sensitivity, s, reliability, r, and metrics. We also add an overall quality metric, q, described in Heipke et al. (1997). The sensitivity can be expressed as:

$$s = \frac{\sum TP}{\sum TP + \sum FN}, \tag{3.8}$$

where $\sum TP$ and $\sum FN$ are the sum of TP and FN. This metric measures the method's ability to detect knickpoint that a user would have manually picked. $s = 1$ implies the detection of all the locations of reference knickpoints. The reliability can be expressed as:

$$r = \frac{\sum TP}{\sum TP + \sum FP}, \tag{3.9}$$

where $\sum TP$ and $\sum FP$ are the sum of TP and FP. This metric measures the occurrences where the method identifying knickpoints that a user would not have picked. The overall quality metric can be expressed as:

$$q = \frac{\sum TP}{\sum TP + \sum FP + \sum FN}. \tag{3.10}$$

A q value of unity implies perfect agreement between algorithmically and hand-picked knickpoints. We focus on these metrics instead of the knickpoint magnitude, as it is more difficult to predict and is dependent on many parameters within the extraction of the Δk_{sn} values.

3.3 Test locations

In order to test the performance of our method, we extract knickpoints from two field sites with independently-mapped knickpoint and knickzone locations. The first of these sites is Smugglers Basin on Santa Cruz Island (California, US), where knickpoints and knickzones were mapped by Neely et al. (2017) using a combination of fieldwork and supervised selection from river long profiles. Smugglers basin is undergoing transient adjustment to climatic and tectonic signals (Neely et al., 2017). The second field site is located in the Quadrilátero Ferrífero (Minas Gerais, Brazil), where we present a new dataset of extracted knickpoint and knickzone locations from field observations and river profiles. Quadrilátero Ferrífero represents a more stable site in term of climate and tectonics (e.g., Dorr, 1969; Salgado et al., 2008), and therefore knickpoints in this landscape have been linked instead to changes in lithology.

3.3.1 Santa Cruz Island, USA

The first calibration test site is the headwaters of the Smugglers Cove catchment, located in the SE of Santa Cruz Island, the largest of the California Channel Islands (California, USA). Lidar data at 1 m resolution are available in the basin via the 2010 US Geological Survey Channel Islands lidar Collection, available from OpenTopography (opentopography.org).

The basin has a total relief of approximately 550 m and drains to the Pacific Ocean. Previous work has estimated uplift rates of $\approx$1 mm yr^{-1} using dated terraces and fault activity (e.g., Muhs et al., 2014; Pinter et al., 1998), and the site has experienced regional sea-level variations (e.g., Pinter et al., 2018; Schumann et al., 2016). This, along with bedrock heterogeneity, has led to numerous knick-

zones in the catchment which have been mapped and tested against a previous knickzone extraction algorithm by Neely et al. (2017). 18 knickzone bases and lips have been reported based on topographic expression and field observations across the whole catchment. As the Neely et al. (2017) algorithm is targeted specifically at knickzones, we compare the mapped knickzone bases and lips with those picked by our algorithm. Knickzone bases and lips are the equivalent of increases and decreases in k_{sn}, respectively.

We extracted channel heads using a curvature-based method of channel extraction, following Pelletier (2013) and Grieve et al. (2016). This method has an estimated accuracy of ≈10 metres horizontally along drainage paths (Clubb et al., 2014). Before extracting channel steepness, we calculated the best fit concavity index for the basin by maximising collinearity between the main stem channel and the tributaries in χ–elevation space, using the bootstrapping method of Mudd et al. (2018): the best-fit θ at the site is 0.25.

3.3.2 Quadrilátero Ferrífero, Minas Gerais, Brazil

The second calibration test site is located in the eastern part of the Quadrilátero Ferrífero (QF, Brazil), in a basin draining the Caraça Range (Figure 3.8). The QF is an area of relatively high elevation in southeastern Brazil, and the Caraça Range is its most pronounced topographic feature with a maximum elevation of ≈2100 m and maximum relief of ≈1500 m. Tectonic activity is thought to have ceased by ≈500 Ma (e.g., Alkmim and Marshak, 1998; Chemale et al., 1994; Dorr, 1969). Upstream areas are primarily underlain by resistant rocks (e.g., quartzites and banded iron formations), whereas less resistant rocks often underlie downstream areas (e.g., schists and phyllites). The association of mountainous topography and long-term tectonic stability have led to controversy in the post-orogenic evolution of the QF (Bezerra and Peifer Bezerra, 2018). The most accepted hypothesis is that differential denudation of lithologies with different resistance to denudation has led to a geomorphic differentiation where the uplands, underlain by strong rocks, are high because they have been denuded less and more slowly than their surroundings (e.g., Bezerra and Peifer Bezerra, 2018; Harder and Chamberlin,

1915; James, 1933; Salgado et al., 2008; Varajão, 1991). An alternative hypothesis is that the relief of the QF results from a complicated history of geographic cycles interrupted by epeirogenic uplift (e.g., Barbosa, 1980; Dorr, 1969; King, 1956).

Knickpoints are common features in the rivers flowing away from the Caraça Range (Figure 3.8). These rivers have headwaters at high elevations (≈2000 m), and their long profiles display many convexities associated with substantial elevation drops (up to 1.4 km of descent over ≈15 km of downstream distance), and steep channel and hillslope gradients. These rivers flow over quartzite terrains, yet transitioning in their distal part to schists (see Supplementary Materials 5.2). The origin of these knickpoints is unresolved, being possibly the result of spatial variations in rock resistance, or alternatively resulting from transient uplift signals that have failed to progress beyond quartzite units (Bezerra and Peifer Bezerra, 2018). We used a TanDEM-X DEM with 12 m resolution to extract knickpoints from the QF. Before extracting channel steepness, we estimated the best fit concavity index as 0.15 using the methods presented in Mudd et al. (2018).

3.4 Results

3.4.1 Performance at Santa Cruz Island

We carried out knickpoint extraction on Santa Cruz Island initially with parameters detailed in Table 3.2; the full parameter file is available in the Supplementary Materials. As explained in Section 3.2, extraction prior to post-processing thinning generates a dense dataset of knickpoints both within and outside knickzones identified by the calibration dataset (see Supplementary Materials 5.1). Therefore, we apply a threshold approach to thin the dataset by removing small knickpoints. We set cut-off values of $|\Delta k_{sn}| > 0.8$ and $\Delta z_{seg} > 2.1$, where knickpoints smaller than these thresholds are ignored. These values are set for this case study with the specific aim to isolate the main knickpoints while matching with the calibration dataset. This approach is fully reproducible and does not involve manual picking of knickpoints.

Our thinning procedure reduced the number of slope-break knickpoints from

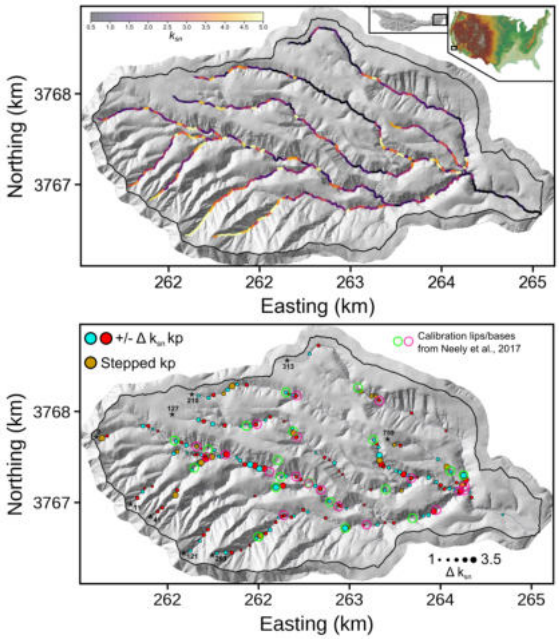

Figure 3.6: The test location on Santa Cruz Island, CA, USA. (a) Map of channel network extracted with the Pelletier method (Pelletier, 2013), and is coloured by k_{sn} value calculated with Mudd et al. (2014). (b) Extracted knickpoints plotted after thinning the dataset as described in Section 3.4.1. The purple and green circles respectively represent the calibration knickzones' bases and lips with the 50m radius used for assessing algorithm performances. Stars and associated numbers are source numbers, which can be compared to Figure 3.7. Topographic data is 1 meter precision lidar DEM (see Supplementary Materials 1 for metadata), reprojected in WGS84 UTM zone 11N.

398 to 160; and the number of vertical-step knickpoints from 40 to 17. This is a relatively high number of knickpoints compared to the calibration bases and lips (18 pairs). However, this disparity can partly be explained by the differences in methods: our algorithm details discrete changes in channel morphology whereas the calibration knickzones are identified over longer channel reaches. Therefore, one mapped knickzone may contain several algorithmically identified knickpoints.

Neely et al. (2017) propose an error radius of 50 metres around each base and lip in order to test the performance of their algorithm: we used the same approach when comparing our extracted knickpoints to the calibration data. A TP is determined as any knickpoint within the calibration knickzone or the corresponding 50 m radius. A FP is determined as any knickpoint which does not lie within this radius, and a FN is determined as a base or a lip which is not identified by our algorithm. The reliability, sensitivity, and overall quality metrics

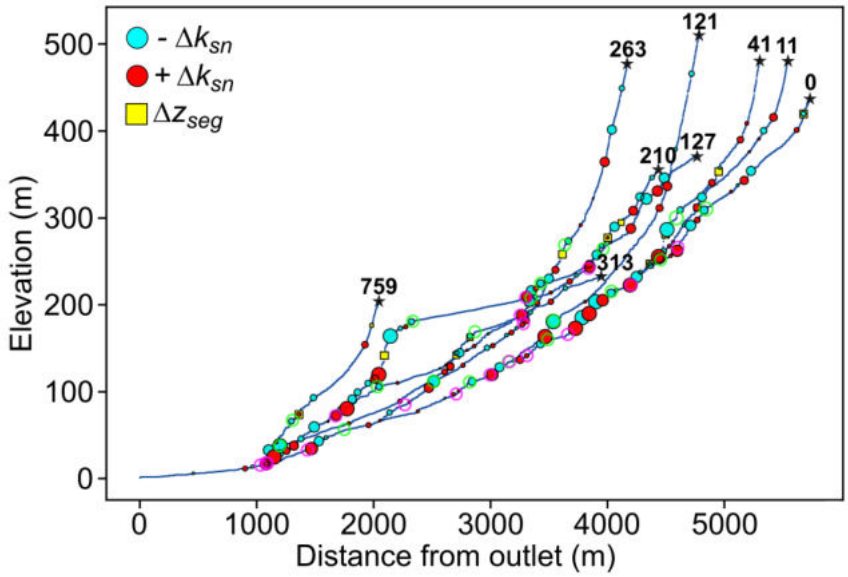

Figure 3.7: Knickpoints extraction for Santa Cruz Island, CA, USA shown for the channel long profiles. These are the same knickpoints depicted in Figure 3.6b. The stars and associated numbers correspond to the source numbers, and green and mauve circles correspond to the lips and bases of mapped knickpoints from Neely et al. (2017).

are presented in Table 3.1. High sensitivity ($s = 0.93$) but lower reliability ($r = 0.53$) and overall quality ($q = 0.51$) suggest that the algorithm detect the bulk of human selected knickpoints, but also a significant amount of other knickpoint features. The implications of these results are discussed below.

Table 3.1: Accuracy metrics for calibration site I (Smugglers Catchment, California, USA)

Source key	TP	FP	FN	Total detected
0	26	15	4	41
11	0	15	0	15
41	4	5	0	9
121	2	5	1	7
127	17	15	1	32
210	17	9	0	26
263	11	13	0	24
313	10	4	1	14
759	4	5	0	9
Total	91	81	7	177

$s = 0.93$, $r = 0.53$ and $q = 0.51$

Table 3.2: Parameter values used for the two field sites. Differences in parameter values between the two sites is due to differing DEM resolution (1 metre for Santa Cruz Island, and 12 metres for the Ribeirão Caraça). Sensitivity to these parameters is described in Section 3.4.3. Note that although the parameter values have been carefully optimized for knickpoint analysis, we suggest the below values as defaults for each of these two data resolutions in order to allow a rapid initial knickpoint extraction for other landscapes.

Parameter name	Santa Cruz Island, USA	Ribeirão Caraça, Brazil
n_{tg}	30	50
n_{sk}	1	1
n_{MC}	100	100
λ	1.7	0.3
r_{comb}	10	30
T_σ	7	7
r_W	120	100

3.4.2 Performance at Quadrilátero Ferrífero, Minas Gerais, Brazil

The application of our method in the Ribeirão Caraça basin resulted in a dense dataset of knickpoints (n = 252); see Table 3.2 for parameter values and the supplementary materials for full parameter file. To thin this dataset, we removed knickpoints with attributes lower than the cut-off values of $|\Delta k_{sn}| > 0.8$ and $\Delta z_{seg} > 2.1$ for the slope-break and vertical-step knickpoints respectively. This filtering procedure decreased the number of slope-break knickpoints from 252 to 108, whereas the number of vertical-step knickpoints diminished from 44 to 23. We tested the performance of our method compared to human-selected knickpoints for the Ribeirão Caraça basin using the metrics TP, FP and FN (Table 3.3). We used the same error radius as was used on Santa Cruz Island for consistency. These metrics (see Section 3.2.4) indicate that the sensitivity of our method is high for the Ribeirão Caraça basin ($s = 0.89$), and thus the bulk of human-selected knickpoints are captured by our algorithm. On the other hand, the reliability ($r = 0.60$) and the overall quality ($q = 0.56$) are lower because the number of false positives is high, indicating that our algorithm determines a relatively high number of knickpoints compared to human selection. In summary, our algorithm captures knickpoints that are visually selected for the Ribeirão Caraça basin, as well as many knickpoints that are not recognised by traditional field mapping of knickpoints, but are morphologically similar, as defined by our algorithm.

3.4.3 Sensitivity to algorithm parameters

One important parameter in our method of knickpoint detection is the concavity index (θ). The concavity index controls the magnitude of k_{sn} because it determines the values of χ (equation 3.6), and a higher concavity index will produce higher k_{sn} values for the same channel. We ran the algorithm on Santa Cruz Island for θ values ranging from 0.05 to 0.95, in steps of 0.05.

Because the value of θ affects k_{sn} order of magnitude, λ must be adapted to

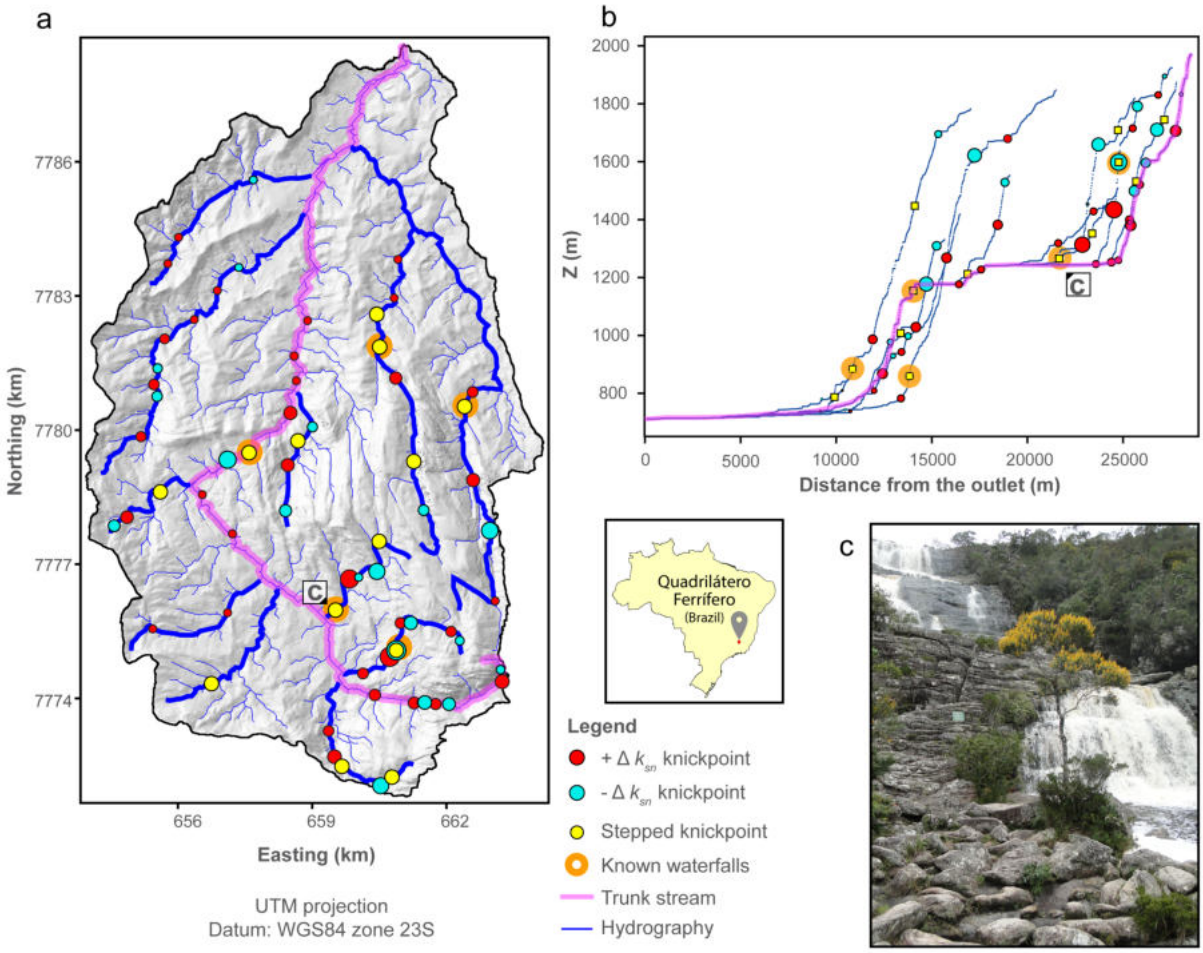

Figure 3.8: Knickpoint extraction on the Ribeirão Caraça basin (Caraça Range, QF, Brazil). (A) Map of knickpoints extracted with the algorithm after thinning the dataset as described in Section 3.4.2. Most of the calibration knickpoints are expressed by a succession of knickpoints detailing along-channel increases/decreases in k_{sn}. Streams depicted in B are shown as thick blue lines. (B) Longitudinal profile of the trunk stream (the Ribeirão Caraça river) highlighting the performance of the algorithm in picking along-channel breaks in steepness. (C) Example of known waterfall (*i.e.*, waterfall with a name) in the field; in this case, the Cascatinha waterfall. This waterfall features an elevation break of 40 m. Other known waterfalls include the Cascatona, Bocaina, Brumadinho, and Quebra-ossos waterfalls.

keep denoising the signal. We therefore tested a wide range of λ values for each θ value. From these tests (see Supplementary Materials 4.1) we determined default λ values appropriate for a range of θ values. These default values are implemented internally in the code, but can be modified if needed. Sensitivity of knickpoint locations to θ using default λ values are presented in Figure 3.9. This analysis shows that the general spread of the data, represented by its z_{score} (difference between the data point and the mean normalised by the standard deviation), is

Table 3.3: Accuracy metrics for calibration site II (Ribeirão Caraça basin, Caraça Range, QF, Brazil)

Source key	TP	FP	FN	Total detected
0	17	13	2	32
1	6	5	1	12
5	9	1	0	10
22	4	2	0	6
37	3	2	1	6
56	4	2	1	8
88	9	7	1	17
114	5	2	1	9
139	8	5	0	14
151	4	4	1	10
252	6	8	0	15
Total	75	51	8	139

$s = 0.89$, $r = 0.60$ and $q = 0.56$

not significantly impacted by different θ values. However, the relative magnitude of each knickpoint, measured by changes in k_{sn}, depends on the chosen value of θ. Therefore, if the intention of the user is to find the spatial distribution of the largest knickpoints then it is essential that θ is picked with care (see Supplementary Materials 4.2 for more illustrations of that).

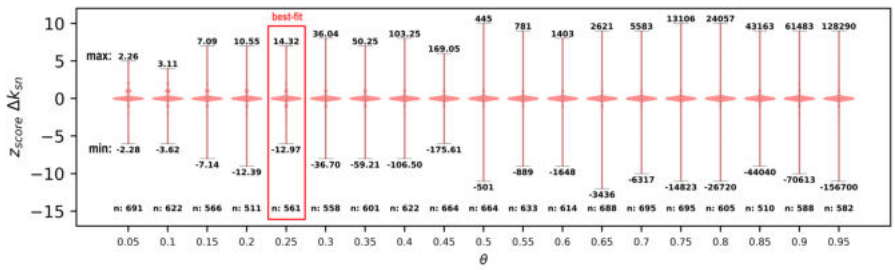

Figure 3.9: Sensitivity of the knickpoint extraction to the concavity index (θ). As different values of θ result in different values of k_{sn}, we use a normalised z_{score} (*i.e.* the difference to the mean normalised by the standard deviation) to compare the overall spread of Δk_{sn}. The plot shows probability distributions of the z_{score} of Δk_{sn} represented by violin plots calculated with a Kernel Density Estimation (bandwith = 0.20). The outliers and their relative magnitudes are affected by this parameter, whereas the general data distribution remains similar. The 'min' and 'max' stated above and below the violin plots respectively represents the minimum and maximum ΔM_χ for each run.

Because k_{sn} values are sensitive to the value of the concavity index, θ, it is important to note that basins with different θ values should be analysed separately to isolate knickpoint locations. Δk_{sn} values are therefore also dependent on the

value of θ and so relative magnitudes of knickpoints and knickzones should only be compared amongst basins with the same θ value. On the other hand, the locations of knickpoints and knickzones are relatively insensitive to θ so the method can be used to determine the spatial distribution of knickpoints across large areas even in the event that the concavity index may vary spatially.

The extraction of channel steepness will also be influenced by parameters in the segment fitting algorithm (Mudd et al., 2014): the number of target nodes (noted n_{tg}) and the average number of nodes skipped (noted n_{sk}). We therefore ran sensitivity analyses on these parameters testing every combination for the following ranges of values: from 5 to 120 n_{tg}, and values of 1 to 4 for n_{sk} parameter. Our results show that both of these parameters affect the segment lengths. Increasing either the number of n_{tg} or the n_{sk} parameter leads to longer segments (see Supplementary Materials 4.3 for more details). This affects the number of knickpoints detected. We also tested the number of Monte-Carlo iterations (n_{MC}) processed for each segment from 5 to 500, and find that the results become insensitive to n_{MC} when $n_{MC} > 50$.

The results of the vertical-step knickpoint detection can change with the size of moving window that detects sudden changes in z_{seg} compared to neighbouring nodes (Section 3.2). We tested the following combination of parameters for vertical-step knickpoint detection: r_W from 10 to 200 nodes, over intervals of 10 nodes; and T_σ from 5 to 10 over intervals of 0.5. Our results show that the extraction is insensitive to r_W above a threshold minimum value, around 80 in our case. Below this value, the algorithm begins to identify steep channels as a succession of steps and will detect each node in the steep section as a knickpoint. We find that the number of extracted knickpoints becomes much higher if $T_\sigma < 6$, whereas $T_\sigma > 8$ results in very few knickpoints being detected. We therefore suggest selecting a value of $6 \leq T_\sigma \leq 8$.

The resolution of the DEM may also affect the location of extracted knickpoints and knickzones. We conducted a sensitivity analysis on raster resolution by resampling the original 1 m lidar-derived DEM into coarser grids to represent common available resolutions of 5 m (e.g., NED or NetMap), 10 m (e.g., NED

or TanDEMX) and 30 m (ASTER or SRTM). Our results (see Supplementary Materials 4.7) show a decreasing number of detected knickpoints at coarser grid resolutions. This is directly linked to the amount of nodes in each river profile: as the resolution decreases, the number of nodes per river also decreases, meaning that less segments are used to extract k_{sn}. Therefore, less knickpoints are detected as knickpoints tend to be located near the segment boundaries. Furthermore, with lower resolution grids the knickpoints that are detected tend to represent larger-scale variations in the channel profile. Vertical-step knickpoints also tend to be identified as steepened reaches rather than purely vertical regions of the channel profile, as the grid resolution prohibits identification of small waterfalls. In order to show an overview of the algorithm performance in different field sites and DEM datasets, we extracted knickpoints from an additional test site using a 30 m DEM derived from SRTM (Supplementary Materials, Figure S21).

3.5 Discussion

3.5.1 Selecting parameter values

Ideally our method for knickpoint detection could proceed without any human supervision. Due the the method's sensitivity to grid resolution, roughness, as well as the intrinsically heterogeneous nature of landscapes, the method does however retain some user-defined parameters. The sensitivity analysis performed on the Santa Cruz Island data (Section 3.4.3) indicates which of these must be selected with care.

We found that changing the concavity index does not change the location of the knickpoints substantially, but it does control their relative magnitude (Section 3.4.3), and therefore if the user is interested in knickpoint magnitude than θ should be selected carefully (e.g., Mudd et al., 2018). Parameters linked to segmenting the χ–elevation profiles (Mudd et al., 2014) that affect results are the n_{tg} and n_{sk} parameters (Section 3.4.3). Increasing both of these increases the length of the segments, where setting these parameters to smaller values result

in a large number of detected changes in k_{sn} which must thereafter be thinned. The one potential advantage of smaller segments is that more vertical-step knickpoints can be detected (i.e., waterfalls). Smaller segments also affect the relative values of knickpoint magnitude because short, steep reaches can be extracted and will generate high magnitude Δk_{sn} knickpoints. If high values for the n_{tg} and n_{sk} parameters are used, the resulting knickpoint dataset will be sparser but will not necessarily detect local changes of k_{sn} due to local layers of hard rock layer or a change in erosion process, for example. Larger segments are also less sensitive to topographic noise. After running sensitivity analyses, we recommend default parameters of $n_{tg} = 80$ and $n_{sk} = 1$.

Once segmentation is performed, we use the TVD routines to isolate changes in k_{sn}, which require an additional parameter (λ) to control the degree of denoising (equation 3.7). As the relative magnitude of k_{sn} is controlled by the θ value, we also determine the λ value for each value of θ that best isolates changes in k_{sn} based on our sensitivity analysis (Section 3.4.3). However, some landscapes that are either very gentle or steep may require changes to the λ value: low-relief landscapes may require a smaller λ value whereas the opposite is true for steep landscapes. The user can check the efficacy of the selected λ value by plotting k_{sn} and denoised k_{sn} against χ or the flow distance. Guidance on selection of λ is described in greater detail in Supplementary Materials Section 4.1.

We also explored the possibility of using the TVD routine to denoise the river profile before extracting knickpoints in order to avoid dependency on the θ parameter. We applied the denoising routine on $\Delta elevation$ in order to reduce the amount of variation. The intensity λ of denoising has to be manually selected and controls the amount of change from original data. Results from these tests are available in the Supplementary Materials (Figures S18-S20). We found that additional denoising is still required during the Monte Carlo segment determination of Mudd et al. (2014). We suggest that prior smoothing of river profiles needs to be carefully considered, as it unavoidably leads to some modification of the existing profile. Users of our software may, if they wish, apply a technique for denoising river profiles prior to applying our method (e.g. Schwanghart and

Scherler, 2017).

The width of the combining window can also be an important factor. As explained in Section 3.2, segment boundaries can still be fuzzy after the denoising process, generating successions of low-magnitude slope-break knickpoints. The combining window solves this issue by merging adjacent knickpoints within a certain radius. However, underestimating r_{comb} could result in retaining some of these low-magnitude knickpoints. Overestimating its size would possibly result in shifted knickpoint locations and misrepresentation of their magnitude if unrelated knickpoints are merged. In the case where the DEM resolution is high enough to represent a close succession of knickpoints, we recommend carefully choosing a combining window smaller than the spacing between these features in order to avoid merging them.

Vertical-step knickpoint detection is controlled by two parameters: the window radius (r_W) and the standard deviation threshold for detecting anomalies (T_σ). Section 3.4.3 details the combined sensitivity analysis on these parameters and allows us to determine a set of values suitable for this analysis. However, if the user's specific aim to detect vertical-step knickpoints (assuming that the DEM precision allows it), we recommend that users precisely constrain the standard deviation coefficient, the window size and the segment size, in order to make sure that vertical-step knickpoints are extracted rather than slope-break.

Although parameters in the method may be tuned and therefore the method can be supervised, it is reproducible. Workers using the method can report on the parameter values used and others can use these to reproduce the original results. One advantage of these adjustable parameters is that users can visually inspect outputs and change parameters such that the algorithm selects "obvious" knickpoints. However, we emphasize that this is not hand picking of knickpoints: the algorithm output is a dense dataset of knickpoints. While sorting the dataset, once a threshold or statistical criteria is selected, all knickpoints and knickzones matching the selection are chosen. This means that one cannot eliminate knickpoints that qualitatively appear to be in the "wrong" place. As highlighted in Figure 3.7, human selected knickpoints and knickzones frequently produce biased

knickpoint datasets that both include and exclude knickpoints and knickzones that have the same magnitude. We note that because the segmentation algorithm uses a Monte Carlo sampling routine (Mudd et al., 2014) there may be minor differences in results between two users, but by using a reasonable n_{MC} ($>$50) the results from one run to the next are nearly identical.

3.5.2 Quantification and selection of knickpoints

The aim of extracting knickpoints is mainly to link knickpoint location and magnitude to a specific event resulting in landscape transience (e.g., Crosby and Whipple, 2006). Therefore, an important step is to isolate the most significant knickpoint features from the dense raw dataset in order to interpret landscape evolution, which can be done using knickpoint magnitude. Knickpoint magnitude may be affected by the calculation of k_{sn} using the gradient of segments in χ–elevation space. Depending on the relief, and particularly with a high value of θ, the absolute values of χ coordinates and associated elevation can differ by an order of magnitude. If the values of χ are low compared to the values for elevation, any changes in elevation at a knickpoint will result in a much higher segment gradient than if the χ values are of a similar magnitude as the elevation. This can result in the exaggeration of knickpoint magnitude in high relief landscapes, for example, where it is more likely that χ values will be lower than the elevation values and eventually results in a bias during the sorting. We therefore suggest that, in such cases, A_0 from equation 4.4 should be set such that the value of the χ coordinate is the same order of magnitude as the elevation. However, if $A_0 \neq 1$, then the gradient of the segment corresponds to M_χ in equation 3.6, rather than to k_{sn}. We wish to emphasise that this does not change the relative ordering between knickpoints. We illustrate this relationship by running a simple sensitivity analysis on the Santa Cruz Island dataset, with a range of A_0 varying from 1 to 500 (Figure 3.10). This sensitivity analysis shows that, as A_0 is increased, the extreme values of Δk_{sn} within the dataset are reduced, so that the effect of low absolute χ values on the gradient calculation is diminished. As for θ (see section 3.4.3), knickpoint absolute magnitude (*i.e.,* the direct value of Δk_{sn} and Δz_{seg})

cannot be compared if calculated with different A_0 from equation 4.4. However the location of the isolated main knickpoints can still be compared.

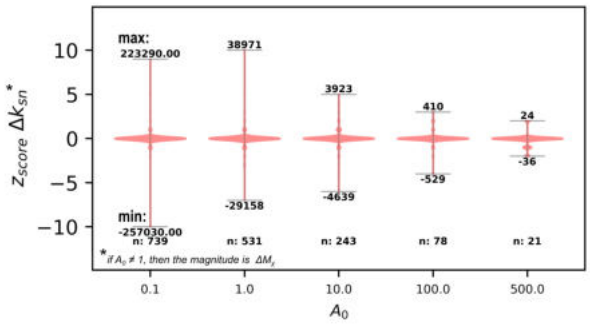

Figure 3.10: The effect of varying A_0 on knickpoint extraction (equation 4.4). The reference area (A_0) will affect knickpoint magnitude and can be increased to reduce exaggerations in χ-elevation gradients. Changing A_0 does not affect the relative order of knickpoints: the largest knickpoints remains the largest for all values of A_0. Increasing A_0, however, reduces the spread in the z_{score} of the changes in channel steepness. This value has to be set only if necessary (e.g., if the high-gradient effect is important): $A_0 \neq 1$ implies that the magnitude is not Δk_{sn} but ΔM_χ from equation 3.6. Moreover, overestimating A_0 can mask knickpoints that would be detected with $A_0 = 1$ m^2. The 'min' and 'max' stated above and below the violin plots represent the minimum and maximum ΔM_χ for each run.

Our sensitivity analyses suggest that two different approaches may be used to select knickpoints. The first of these is that a single θ and A_0 can be fixed for an entire landscape: the knickpoint magnitudes can directly be used to isolate the main knickpoint locations and relative importance. However, this approach may lead to some errors due to inevitable landscape heterogeneity over larger scales. The second approach is to calculate θ and A_0 values separately for individual basins, which allows knickpoints to be extracted with greater precision than if a single value is set for the entire landscape. However, this approach means that the knickpoint extraction has to be processed independently for each catchment, and only the location (e.g., latitude, longitude, elevation) are comparable between different catchments. Which approach is taken is dependent on the aims of each particular study, and should be carefully considered on a case-by-case basis.

3.5.3 Knickpoint and knickzone morphology

Along with the calculation of knickpoint magnitude, our algorithm allows the characterisation of knickpoint morphology. We can identify different knickpoint or knickzone types by i) identifying locations where k_{sn} increases downstream (positive slope break knickpoints); or ii) identifying locations where k_{sn} decreases (negative slope break knickpoints); and iii) identifying locations where a sudden change in elevation occurs (vertical step knickpoints). This approach is suitable to identify the most common morphologies described in the literature (e.g Haviv et al., 2010; Kirby and Whipple, 2012). However, we wish to emphasise that this algorithm can also be used to focus on one particular knickpoint morphology. For example, the classical convex-upwards knickpoint expression (e.g., Knopf, 1924) can be isolated by only displaying the knickpoints with a drop of Δk_{sn} (Figure 3.11b). In order to examine steepened reaches or knickzones, we can also isolate locations where Δk_{sn} increases. Finally, waterfall detection can be achieved, if the resolution of the DEM allows it, by focusing on locations with a jump in z_{seg}. We provide all these different knickpoint types for the Smugglers Catchment in the Supplementary Materials (Figure S12).

3.5.4 Comparison with other knickpoint extraction techniques

For each of our two study sites, we have presented performance metrics of our method compared to knickpoints selected by humans. We find that our method has a high sensitivity, meaning that nearly all human-identified knickpoints were selected by the algorithm, but a lower reliability. This suggests that our algorithm also identifies many changes in channel steepness which are not selected as knickpoints through field mapping techniques. This raises the question of whether algorithmic selection of knickpoints is more or less trustworthy than those selected by humans.

Knickpoints identified for geomorphic studies should be reproducible, in that two workers should be able to select the same locations and magnitudes from

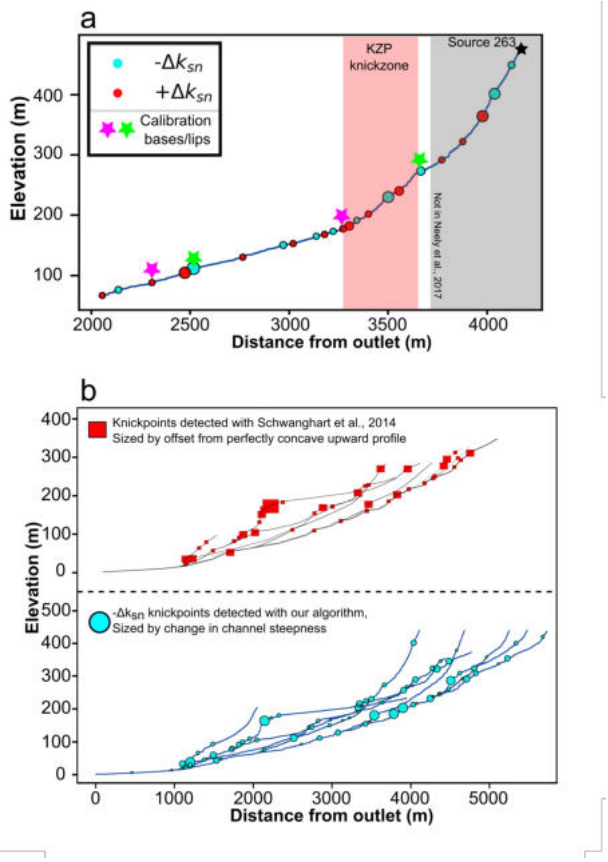

Figure 3.11: Comparison of results on the Smugglers catchment from our algorithm and the most recent similar ones. (a) Results for a single source from KZPicker (Neely et al., 2017) and our results. The results from Neely et al. (2017) are directly taken from their study to ensure objectivity. Only the slope-break knickpoints are displayed to make the comparison valid. (b) Basin-wide comparison between our algorithm outputs and the one recently implemented in Schwanghart and Scherler (2014) using tolerance = 5. We only display the knickpoints showing a decrease of k_{sn}, in order to provide a relevant comparison with the knickpoints morphology detected by Schwanghart and Scherler (2014). Differences in channel length are due to different methods for extracting channel heads between the two techniques.

the same river profile. This is challenging when mapping features in the field, as different workers may have different criteria for what constitutes a knickpoint. Furthermore, knickpoint selection should be objective: the same morphological criteria should be used to identify all features in the dataset. A common problem with field mapping by humans is that some specific features are picked in order to interpret a signal, whereas others with a similar morphology may be omitted. Our approach allows the production of an objective dataset of knickpoint locations and magnitudes that can be later correlated by the user with process-based

interpretations. Algorithmic extraction also allows coverage of much larger areas compared to field mapping, that can later be calibrated with additional data (e.g., Crosby and Whipple, 2006). As illustrated by our accuracy metrics, our algorithm produces dataset significantly denser than hand picked knickpoints. However it is possible to thin the number of knickpoints by applying thresholds metric values selected based on statistical criteria, and making the number of identified features similar to human-picked datasets. Such a process is objective in the sense that no hand selection is involved: only the morphology drives the thinning.

To provide a full assessment of our methods, we compare its output to the one generated two other algorithms as explained in section 3.1.1: TopoToolbox (Schwanghart and Scherler, 2014); and KZ-picker (Neely et al., 2017). Figure 3.11a expresses the differences between KZ-picker and our algorithm for a single channel, where KZ-picker identifies the main knickzone (in red) and quantifies its magnitude by the difference in elevation between the toe and lip of the knickzone. The purpose of the KZ-picker is to find broad zones of steepened channels and is less granular than our method (e.g., Section 3.4.1). It is also not constructed to identify discrete vertical-step knickpoints. Because the raw output from our algorithm is however denser than the KZ-picker, main knickpoints from our algorithm require more sorting based on their magnitudes which results in extra steps to explore the data.

Figure 3.11b provides a basin-wide comparison of our outputs with those from TopoToolbox (Schwanghart and Scherler, 2014), with a tolerance parameter of the TopoToolbox method fixed to 5. In order to ensure that the comparison is valid we only compare it to our negative Δk_{sn} knickpoints, which should quantify similar features. The TopoToolbox method effectively identifies the main knickpoints expressed by the difference to an idealised profile that is concave-up. However, reducing the tolerance parameter increases the number of knickpoints detected (e.g., 10: 12 knickpoints, 5: 44 knickpoints, 1: 343 and 0.1: 2234) meaning that the TopoToolbox method can result in a network of knickpoints that has a similar density to our method. However the TopoToolbox method relies on

profiles in elevation plotted against flow distance and so further processing is required to analyse changes in channel steepness using this method. Because selection of knickpoints in this method is not normalised for drainage area, the largest knickpoints selected may not correspond to the largest changes in channel steepness. However it has fewer parameters and is more computationally efficient than our method.

While the KZ-picker and the TopoToolbox methods are well adapted for identifying specific types of knickpoint, neither allows the separate identification and quantification of positive slope-break, negative slope-break, and vertical-step knickpoints. Each method produces slightly different data products that can be used to interpret different components of the channel network, making these methods complementary.

Finally, we chose to build our change point detection method using the TVD routine (Condat, 2013). However, as explained in Section 3.2, alternative methods could be used. The algorithm therefore provides the raw data before the TVD routine, meaning that this data can be ingested by other change point detection techniques, *e.g.,* the methods reviewed in Truong et al. (2018) and its associated open-source code.

3.6 Conclusion

We have developed a new method for extracting knickpoints and knickzones from topographic data. Our method extracts slope-break knickpoint locations using changes in channel steepness k_{sn}, calculated by combining a statistical method for segmenting channels into reaches of different channel steepness (Mudd et al., 2014) and a recently introduced denoising technique (Condat, 2013). The method also identifies vertical-step knickpoints by searching for breaks in elevation between channel segments of similar channel steepness. Our algorithms provide a dense dataset of objectively extracted knickpoint locations, along with the relative magnitude of each knickpoint defined by either the change in channel steepness (for slope-break knickpoints) or the jump in elevation (for vertical-step

knickpoints) to quantify knickpoints morphologies.

We tested our algorithm on two datasets where knickpoints were independently field mapped, and found that our method successfully extracted the human-identified knickpoints in the vast majority of cases. In general the method identifies more knickpoints compared to field mapping, as illustrated by our accuracy metrics, especially in the case of knickzones where one broad steepened reach may result in multiple discrete segments in χ-elevation space. We provide tools for sorting and thinning the dense dataset in order to isolate the most significant breaks in the channel profile without involving any human-based selection. Resulting knickpoints can be compared with lithological, climatic, or tectonic datasets. Our method therefore provides an objective, systematic and reproducible technique for quantifying knickpoints and knickzones, which can then be used to inform process-based interpretations of landscape evolution.

Chapter 4

Impact of changing concavity indices on channel steepness and divide migration metrics

The work presented in this chapter is to be submitted in JGR-Earth Surface in collaboration with Mudd S.M., Grieve S.W.D., Clubb F.J. and Hurst M.D. This research was conducted in collaboration with the named co-authors, who helped to edit the manuscript and contributed to software development and data processing. I wrote the topographic analysis algorithms, performed the analyses, created the figures, and wrote the manuscript. SMM edited the manuscript, performed some of the analysis for table 4.1 and edited the analytical solutions; SWDG edited the manuscript and performed analysis for table 4.1; FJC edited the manuscript and figures and performed analysis for table 4.1; and MDH edited the manuscript and figures.

Abstract

The concavity index, θ, describes how quickly river channel gradient changes as one moves downstream. It is used in calculations of normalized channel steepness index, k_{sn}, a metric for comparing the relative steepness of channels with different drainage area. It is also used in calculating a transformed longitudinal coordinate, χ, that incorporates drainage area or discharge, which has been employed to search for migrating drainage divides. We explore the variability in θ across multiple landscapes, and introduce new methods to quantify its variability. We describe the degree to which both k_{sn} and χ can be distorted in both space and by magnitude if θ is assigned a value not appropriate for a particular drainage basin. Changes in θ of 0.1 or less are unlikely to affect the spatial distribution and relative magnitude of k_{sn} values, but larger changes can change the spatial distribution of k_{sn} and in some cases invert relative steepness: relatively steep areas become relatively gentle areas as quantified by k_{sn}. These inversions are sensitive to drainage area: knickpoints that do not occur at large tributary junctions will exist regardless of the selection of θ. We show that the median of most likely θ across a wide range of mountainous and upland environments, based on a network disorder metric, is 0.425, with first and third quartile values of 0.225 and 0.575. This wide range of variability suggests workers should not assume θ based on global studies but should instead calculate a representative θ and exclude basins for which this value is a poor fit. Finally, we demonstrate that the χ coordinate is sensitive to varying values of θ, and given the spatial heterogeneity of θ, comparison of χ values across drainage divides with heterogeneous lithology should be employed with extreme caution.

4.1 Introduction

For over a century, geoscientists have recognised the potential of fluvial geomorphology to unravel links between landscape evolution and external forcing (e.g. Davis, 1889; Gilbert, 1880). In his review of physical geography at the time, Lapparent and Lapparent (1896) outlined a number of basic observations under-

pinning modern geomorphology: the systematic concave up shape of river long profiles, the hypothesis that erosion is correlated with channel gradient, and the influence of lithologic contrasts and inherited tectonic structures on river profile form. The geometry of river profiles later became one of the key tools for geoscientists in the first half of the 20^{th} century for interpreting landscapes (e.g Knopf, 1924).

If you believe that channel gradient encodes information about erosion rates, lithology, or other factors, you are faced with a fundamental problem: the concave nature of a typical river obscures relative steepness, as channel gradient has the pernicious tendency to increase towards the headwaters of a catchment. That is, how can one tell if a headwater channel is steeper, in a way that is meaningful for interpreting landscape evolution, than a section of the river some distance downstream? Some normalization is therefore required to compare river sections with different drainage areas. Morisawa (1962) noted a power law relationship between gradient and drainage area, which led to a means of normalizing river gradients. Flint (1974) formalized these observations into the slope–area relationship with a concavity index (θ), which describes how quickly river gradient decreases with drainage area, and a steepness index (k_s) that describes the relative steepness of a reach regardless of its drainage area:

$$S = k_s A^{-\theta} \tag{4.1}$$

where S is the gradient of elevation along the channel ($S = dz/dx$ where z is the elevation and x the flow distance); and A is the drainage area. The steepness index, in particular, has been widely used in geomorphology because of its observed positive correlation with erosion rates (e.g., Cyr et al., 2010; DiBiase et al., 2010; Harel et al., 2016; Kirby and Whipple, 2012; Mandal et al., 2015; Ouimet et al., 2009; Safran et al., 2005; Scherler et al., 2014). The value of steepness index derived from drainage area and gradient depends on the value of the concavity index, so in order to compare different channels, the steepness index is typically calculated with a single value of θ, resulting in a "normalized" steepness index (k_{sn}) (Wobus et al., 2006c). Despite the importance of constraining θ for calcu-

lating channel steepness, it is often assumed in many studies that $0.4 < \theta < 0.6$ (e.g. Kirby and Whipple, 2012; Tucker and Whipple, 2002; Whipple, 2004).

Numerous authors have attempted to extract concavity indices from topographic data. For example, Tucker and Whipple (2002) compiled concavity indices using slope–area regression from ten previous studies, aggregating 27 different sites, and found concavity indices ranging from 0.11–1.13. Whipple (2004) argued that if you limit extraction of the concavity index to bedrock rivers with homogeneous substrates, homogeneous uplift fields and time invariant uplift, the range of concavity indices converges to a range between 0.4–0.7.

Whipple (2004) went on to articulate circumstances in which concavity indices may fall outside this range. They argued that low concavity indices ($<$0.4) can result from drainage basins influenced by debris flows (e.g. Stock and Dietrich, 2003) or from downstream increases in incision rate or rock strength (Kirby and Whipple, 2001b). Alluvial rivers can also have low concavity values: Gasparini et al. (2004) used a numerical model to predict that finer sediment could result in low concavity values ($<$0.4) when either grain size was less than 100 mm in homogeneous sediment or if there was a high percentage of sand in mixed gravel and sand rivers. Whipple (2004) suggested that high concavities ($>$0.7) could result from downstream transitions to full alluvial conditions with bedrock reaches in headwaters, and also noted the findings of Kirby and Whipple (2001b) that high concavity can result from downstream increases in rock strength or incision rate. Extreme concavity values ($>$1.0) can also result from large knickpoints (e.g. Schoenbohm et al., 2004).

In this contribution, we aim to question this assumption that a narrow range of θ values is appropriate for the majority of Earth's landscapes. To do this, we attempt to constrain the range of concavity indices present both within and between a wide range of different field sites. We then examine the impact of using a poorly-constrained concavity value on estimates of k_{sn} and the metric χ, which integrates drainage area along channels and has been used to detect drainage dived migration (Willett et al., 2014). We also compare different methods of estimating the most likely values of θ and refine existing methods of quantifying

the uncertainty in choosing a most likely value of θ.

4.2 Determining the concavity index

4.2.1 Concavity index derived from slope–area data

A common approach to deriving fluvial profile concavity is to transform equation 4.1 into logarithmic space:

$$\log[S] = \log[k_s] * -\theta \log[A] \tag{4.2}$$

where θ is the gradient of $\log[A] - -\log[S]$ plots and k_s the intercept where $\log[A] = 0$ (i.e., where $A = 1m^2$ if areas are reported in square meters). This logarithmic slope–area method has been widely used to determine both concavity and channel steepness (e.g. Kirby and Whipple, 2012; Whipple et al., 2013; Wobus et al., 2006c).

However, the use of raw S–A data has limitations: the seminal Wobus et al. (2006c) paper includes the word "pitfalls" in the title. DEM data is inherently noisy (e.g Perron and Royden, 2013; Wobus et al., 2006c), either because of natural noise in river profiles or due to errors in the acquisition methods (e.g. airborne lidar or satellite), and taking the gradient of noisy data amplifies that noise (e.g. Perron and Royden, 2013). In addition, tributaries result in large jumps in drainage area, resulting in major gaps along the A axis. Between tributaries drainage area increases slowly, but channel gradient can vary dramatically due to heterogeneity in local river bed conditions. This means that some form of averaging or binning must be used on the raw slope–area data in order to extract k_s and θ values.

We illustrate difficulties in extracting the concavity and steepness indices from S–A in Figure 4.1. This figure contrasts a theoretical case (panel **a**) with real data that considers the basin as a whole (panel **b**), each different tributary channel (panel **c**), or solely the main stem channel (panel **d**). Values of θ can vary substantially in the same drainage basin depending on the S–A data used, as

shown by the histograms of best-fit populations of θ within the inset plots in panels **b,c,d**. This does not suggest that S–A data is unsuitable for extracting landscape metrics: steepness indices derived from this method have been shown to correlate well with other landscape properties such as erosion rates and tectonic activity in a range of contexts (e.g. Kirby and Whipple, 2012). However it highlights the potential difficulties and uncertainties in using this technique to extract θ or k_s, particularly across large areas where θ might vary spatially.

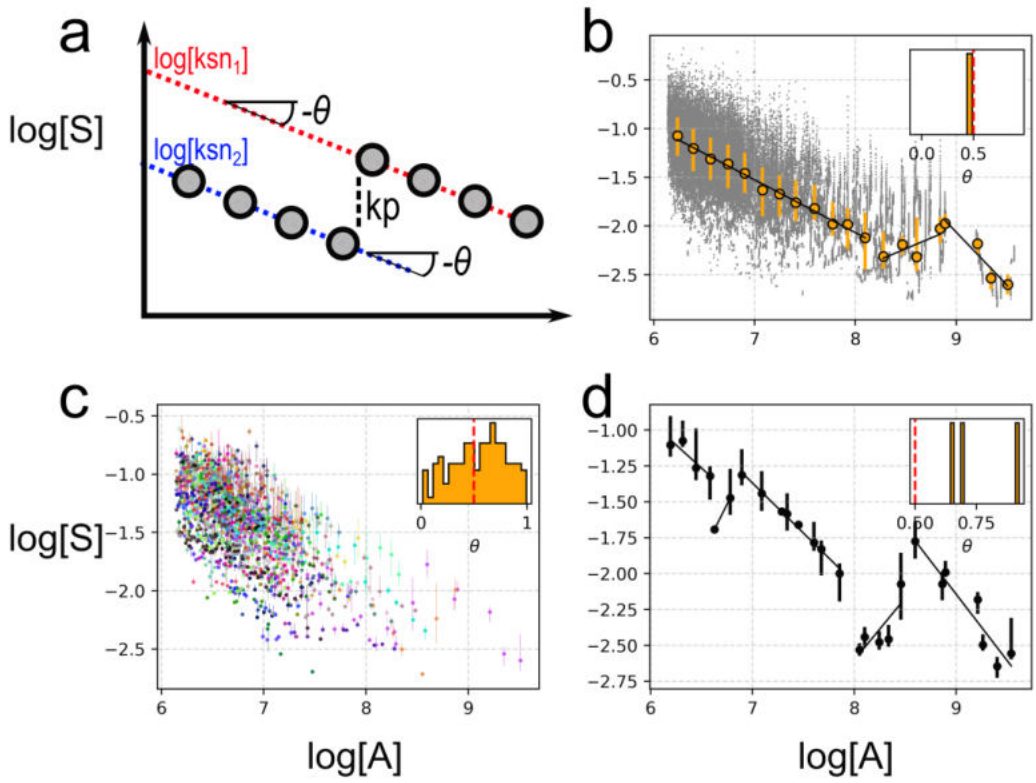

Figure 4.1: Example slope–area plots. **a.** An idealized channel with slope and area following equation 4.1. θ is uniform and a clear knickpoint separates two populations of k_{sn}. **b.** Slope–area data from a real watershed (the Buzău river in Romania, 3000 km^2, outlet coordinates latitude 45.20 and longitude 26.75 in WGS84). Each grey point represents gradient calculated over a vertical window of 20 meters; data derived from the ALOS World 3D 30 dataset. Note the noise and irregularity of data spacing along the axes. In orange, data is binned by drainage area and concavity is calculated using a segmentation algorithm described in Mudd et al. (2014). Only one of the resulting segments has a concavity between 0 and 1: the inset in panels **b,c, and d** show histograms of concavity values between 0 and 1 based on segmentation of S–A data. Panel **c.** shows slope–area data binned by drainage area for all tributaries of the same watershed. The population of θ is obtained by using the segmentation of slope–area data in each each tributary. Panel **d.** shows data data for the main stem channel only.

4.2.2 Concavity index from the integral approach

These problems with the slope–area approach have led to the development of alternative methods in recent years. One such technique is to integrate drainage area along flow distance, which was first suggested by Royden et al. (2000) and further developed in Perron and Royden (2013) as a way to circumvent uncertain-

ties associated with calculating gradient from noisy topographic data. Following Whipple et al. (2017b) we can integrate equation 4.1, resulting in

$$z(x) = z(x_b) + \left(\frac{k_s}{{A_0}^\theta}\right) \int_{x_b}^{x} \left(\frac{A_0}{A(x)}\right)^\theta dx, \tag{4.3}$$

where A_0 is a reference drainage area, introduced to nondimensionalize the area term within the integral in equation (4.3). We can then define a longitudinal coordinate, χ:

$$\chi = \int_{x_b}^{x} \left(\frac{A_0}{A(x)}\right)^\theta dx. \tag{4.4}$$

The coordinate χ has dimensions of length, and is defined such that at any point in the channel:

$$z(x) = z(x_b) + \left(\frac{k_s}{{A_0}^\theta}\right)\chi. \tag{4.5}$$

Equation 4.5 has two key predictions: firstly, assuming that k_s and θ are spatially constant, there will be a linear relationship between χ and elevation for a single channel; and secondly, that tributaries will be collinear with the main stem. If the linearity prediction is true, θ can be calculated for a river by iterating through a range of θ values for a given network and selecting the value with a best-fit linear relationship between χ and elevation (Perron and Royden, 2013). In many real landscapes which are undergoing transient adjustment, however, k_s may vary spatially. Alternative approaches have attempted to fit a number of linear segments to χ-elevation data to circumvent this problem (Mudd et al., 2014).

The collinearity prediction provides a second independent metric of calculating the concavity index (θ) that does not assume that river profiles are linear in χ-elevation space. Instead it assumes that a point anywhere on the channel network with the same χ value will have the same elevation. This has been used as the basis for a number of techniques which calculate the concavity index by minimising the scatter between points on tributaries with the main stem channel

(Goren et al., 2014; Hergarten et al., 2016; Mudd et al., 2018). The collinearity test would be rather restrictive, however, if it were limited to landscapes where k_s were uniform. Royden and Taylor Perron (2013) used solutions of the stream power law to show that collinearity holds even if there are perturbations to the erosion rate that propagate upstream through the channel network. The stream power law has many assumptions (e.g. Lague, 2014), but we can alternatively use geometric relationships to show that collinearity is indicative of the most likely concavity index without invoking stream power.

Two centuries ago, Playfair (1802) observed that tributary junctions often featured channels joining at a common elevation: waterfalls are not systematically present at tributary junctions. This must mean that the two contributing streams need to have eroded at the same rate as the river just downstream of the junction. Niemann et al. (2001) expanded on this geometric observation and derived an expression for the migration rate of a local channel steepening or knickpoint (called its celerity, Ce_h [L/T]) of:

$$Ce_h = \frac{1}{S_2 - S_1}\Delta E, \tag{4.6}$$

where S_1 is the channel slope prior to disturbance, S_2 is the channel slope after disturbance (e.g., due to a change in incision rate E), and ΔE is the difference between the incision rate before and after disturbance (which can be equated to uplift rates U_1 and U_2 in units of length per time, $\Delta E = U_2 - U_1$). Following Wobus et al. (2006c) we can introduce drainage area into equation (4.6) by replacing the slope terms using equation (4.1).

$$Ce_h = \frac{U_2 - U_1}{k_{s2} - k_{s1}}A^{\theta}. \tag{4.7}$$

Once Ce_h is known, we can calculate the vertical celerity (Ce_v) which is simply the horizontal celerity multiplied by the local slope after disturbance S_2 (Wobus et al., 2006c). The vertical celerity of a disturbance to the channel network is independent of drainage area:

$$Ce_v = \frac{U_2 - U_1}{k_{s2} - k_{s1}} k_{s2}. \tag{4.8}$$

Equation (4.8) implies that, under conditions of spatially homogeneous uplift and constant erodibility (i.e., channels with the same slope and drainage area erode at the same rate), then changes in slope will propagate vertically in elevation at a constant rate. If we begin with a landscape with constant k_s as described in equation 4.5 that has a collinear channel network, and propagate changes in slope at a constant vertical celerity, the network will remain collinear even if k_s becomes spatially heterogeneous.

4.2.3 Can we know if a concavity index is "correct"?

The calculations of concavity index presented above are based on models of detachment-limited incision. A number of authors have also attempted to derive the concavity index from transport-limited models (e.g., Whipple and Tucker, 1999; Wickert and Schildgen, 2019). Although these models are a promising approach for understanding the fluvial concavity index, it is currently challenging to test these predictions by quantifying the correct concavity index from field observations.

An alternative approach is to create simulated topography using a model that bears some resemblance to measured incision processes, impose a concavity index upon this model, and then test if the topographic methods are able to correctly extract the imposed concavity index (e.g. Mudd et al., 2018). In spatially homogeneous, steady state landscapes, both methods could extract the correct concavity index, which is unsurprising since this situation just produces a topographic surface exactly obeying equation 4.1. If the modelled landscapes were perturbed by changing uplift rates, or variations in erodibility, then Mudd et al. (2018) found that the slope–area method could not reliably be used to identify the imposed concavity index. In contrast, Mudd et al. (2018) found the collinearity approach could identify the imposed concavity index under spatial and temporal heterogeneity that might be found in a natural landscape. Therefore, for the rest of this

paper, we primarily focus on extracting the concavity index using the collinearity method.

4.3 Impact of varying concavity on the channel steepness index

The channel steepness index set out equation 4.1 (k_s) depends on the concavity index, meaning that a reference value of θ (θ_{ref}) must be set to compare k_s values across multiple basins (Wobus et al., 2006c). This results in "normalized" values of the steepness index, k_{sn}. Values of the normalized steepness index, k_{sn}, have been widely correlated with either uplift rates, inferred from a range of indicators such as dated terraces (e.g., Snyder et al., 2000), or erosion rates, usually inferred from the concentrations of in-situ cosmogenic nuclides such as ^{10}Be (e.g., Lal, 1991). In many such studies, there is a clear positive correlation between k_{sn} and inferred erosion and uplift rates (e.g., Cyr et al., 2010; DiBiase et al., 2010; Harel et al., 2016; Kirby and Whipple, 2001b; Mandal et al., 2015; Ouimet et al., 2009; Safran et al., 2005; Scherler et al., 2014). Broadly speaking, these results indicate that steeper channels do reflect faster erosion rates, if one controls for other factors such as lithology.

If we believe that channel steepness can serve as a proxy for erosion rates, and that erosion rates are correlated with uplift rates, then it follows that channel steepness may be a powerful tool for detecting spatial variations in tectonic activity (e.g. Kirby and Whipple, 2012). However, k_{sn} is a function of the concavity index. If we choose the incorrect value of the concavity index, what is the potential for misinterpreting the spatial distribution of relative channel steepness, and therefore uplift patterns?

Figure 4.2 depicts scenarios where changing the value of the concavity index will result in substantially different interpretations of the spatial variation in channel steepness. Figure 4.2a illustrates a catchment with spatial heterogeneity in θ. If one θ is used for the entire catchment this can lead to dramatic differences in the calculated k_{sn} values. This behavior is also expected in χ space, as shown in

Figure 4.2b, where the steep slope patches, which are interpreted as representing faster erosion, appear in different locations depending on the value of θ. Panels **c.** and **d.** also highlight how, depending on the choice of θ, one might find two clearly separated values of k_{sn} within the channel network or a range of values (see inset in panel **c.**).

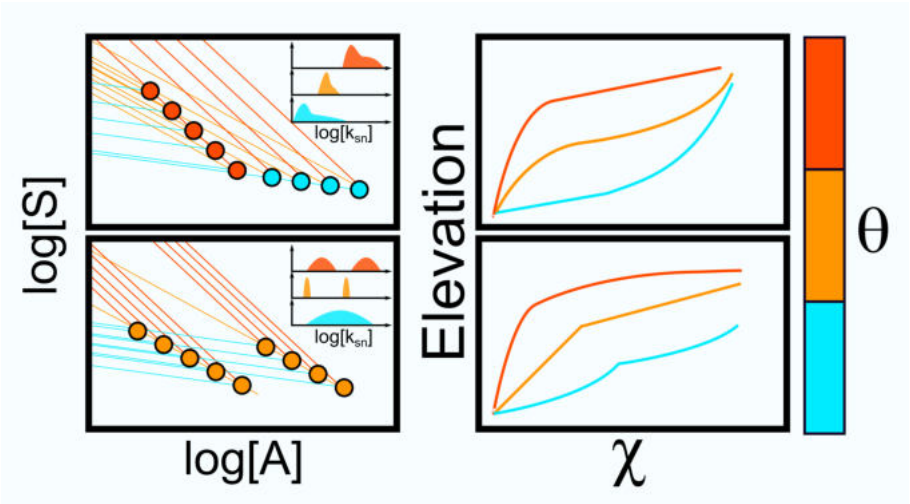

Figure 4.2: Schematic diagram exploring ways in which changing the values of the concavity index lead to differing interpretations of tectonics or erosion based on channel steepness index. Blue, orange and red colors represent low, medium and high concavities, respectively. The left column depicts S–A data for two idealized catchments and the right column shows the corresponding χ-elevation plots. The value of k_{sn} for each point in these basins will be determined by the point at which the lines intersect with the vertical axis at $\log[A] = 0$. Catchment 1 (top row) represents a catchment with spatial variation in concavity from a low-concavity outlet to high-concavity headwaters. Selecting one index for the entire catchment will alter the distribution of k_{sn} values as shown in the inset plots. Catchment 2 (bottom row) represents a catchment with one concavity but spatial variation in k_s. This spatial variation in k_s will only be detected if the correct concavity value is chosen.

Conceptual diagrams such as Figure 4.2 highlight the uncertainties in k_{sn} that are generated by uncertainties in θ. However, it is not straightforward to predict where these distortions will be greatest. One issue is that the relationship between k_{sn} and θ is non-linear: the order of magnitude of the steepness values for different values of θ are not directly comparable. In addition, the noise of S data and sparsity of A data, caused by jumps in A at junctions, require the use of data-loss methods such as binning (e.g. Wobus et al., 2006c). This disconnects single points in a channel from S–A data and therefore hinders our ability to

check binned values against field knowledge. Although the χ transformation offers a means to circumvent some of these issues (Perron and Royden, 2013), it is calculated with a fixed θ value, meaning that landscape–scale χ transformations may be distorted by the choice of θ (Figures 4.2b and d. Our study is focused on assessing the extent of this distortion and proposing metrics to estimate which θ value will least distort values of k_{sn}.

4.4 Methods

4.4.1 Quantifying concavity using disorder

We begin by looking at the uncertainty in θ for a single basin. We use the disorder metric, first suggested by Goren et al. (2014), that is a measure of how far tributaries depart from the main stem river and amongst themselves in χ–elevation space (e.g. Goren et al., 2014; Hergarten et al., 2016; Mudd et al., 2018; Shelef et al., 2018). Our implementation follows the method of Hergarten et al. (2016). It ranks every point in the channel network by increasing elevation, and then checks to see if the associated χ coordinates are similarly ranked (or not):

$$R = \sum_{i=1}^{N} \left| \chi_{s,i+1} - \chi_{s,i} \right|, \tag{4.9}$$

where the the subscript s, i represents the sorted i^{th} χ coordinate that has been sorted by its elevation. This sum, R, is minimal if elevation and χ are related monotonically. However it scales with the absolute values of χ, which are sensitive to the concavity index (see equation 4.4), so following Hergarten et al. (2016) we scale the disorder metric, D, by the maximum value of χ in the tributary network (χ_{max}):

$$D = \frac{1}{\chi_{max}} \left(\sum_{i=1}^{N} \left| \chi_{s,i+1} - \chi_{s,i} \right| - \chi_{max} \right). \tag{4.10}$$

The most likely concavity index is that which results in the lowest value of D for the river network: a perfectly collinear population of points would have $D = 0$

(Hergarten et al., 2016). To constrain uncertainty, Mudd et al. (2018) created subset networks formed from the trunk stream and every possible combination of three tributaries (Figure 4.3). The minimum D value was calculated for all of these combinations by iterating over θ values, creating a population of best fit concavity index values from all the combinations. The median and interquartile range were then reported.

Several authors have shown this method is effective in identifying the most likely concavity index for a watershed (Hergarten et al., 2016; Mudd et al., 2018). However, as explained in section 4.3, one may be compelled to use a different value of θ for a particular watershed, for example if one is comparing values of normalized channel steepness and needs to apply a constant θ value across the landscape to generate k_{sn} data. We would like to know how well this fixed value of θ performs for multiple basins. We have therefore adapted the disorder approach to quantify sensitivity to changing θ. For every combination of tributaries, we calculate a value of D for a range of θ values. We then normalise each value of D by the maximum disorder value (D_{max}) from that range:

$$D^* = \frac{D}{D_{max}} \tag{4.11}$$

This results in a population of D^* values for every value of θ, and these values vary between 0 and 1 (Figure 4.3). If the dataset is perfectly collinear, then D will equal 0 (Hergarten et al., 2016), so normalizing by D_{max} means D^* spans from the maximum disorder to perfectly collinear channel networks. We can then quantify the median and lower quartile of D^* as a function of θ, and from these derive estimates of the most likely θ value as well as some indication of how well constrained this value is. If the best fit concavity index is well constrained, the D^* values will have a sharply defined minimum, whereas a poorly defined value will have a very broad range of D^* values as illustrated in Figure 4.3c. We calculate D^* to provide metrics reflecting how well constrained θ is for a given watershed.

Finding the value that minimises the disorder might suggest the most likely value for a watershed. However it is also important to quantify the goodness of this value, *i.e.* if a range of values would result in similar disorder metrics,

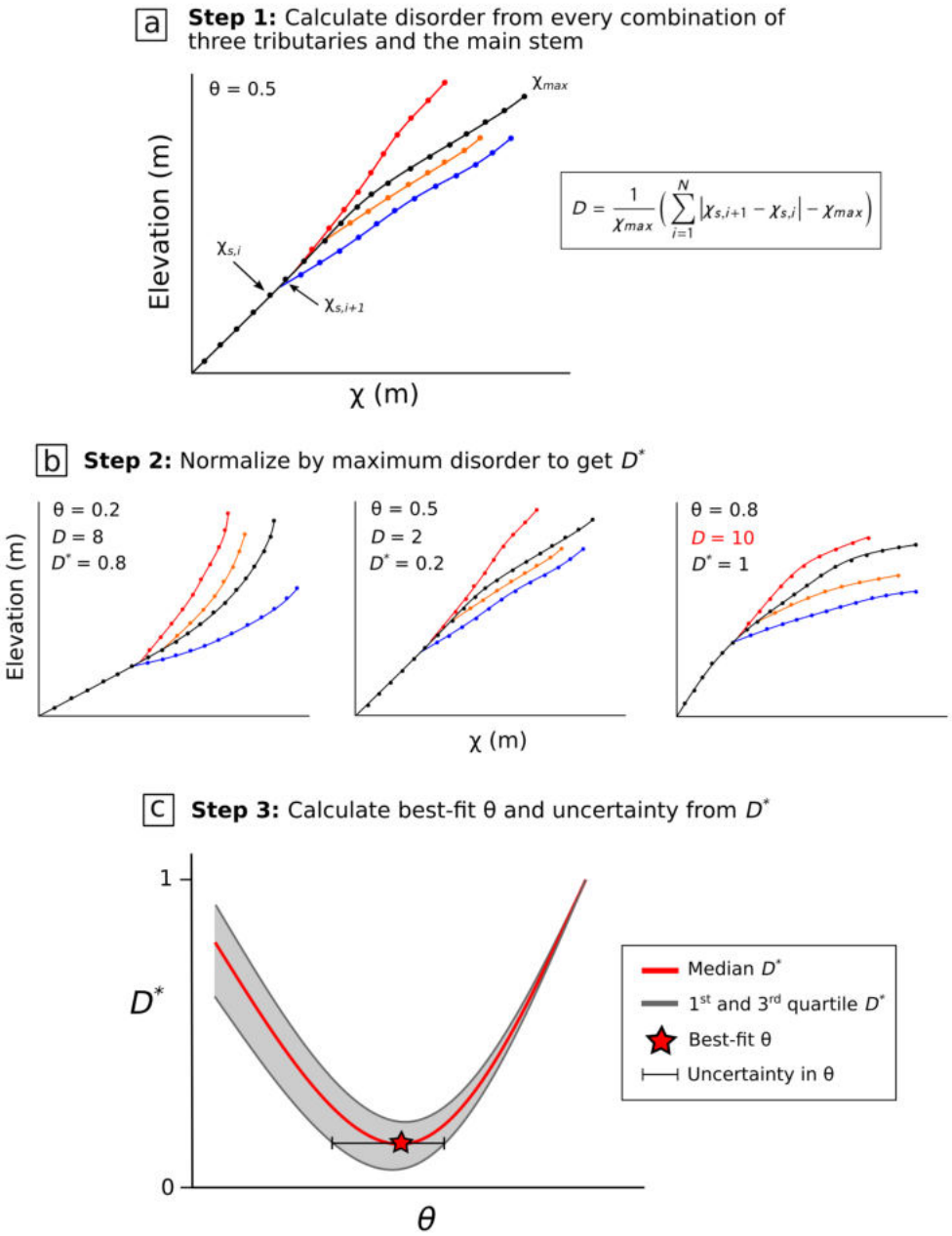

Figure 4.3: Conceptual illustration of the disorder calculation method.

or alternatively if small changes to the value of θ would lead to much greater disorder. We therefore developed a further metric for quantifying the uncertainty of θ within a watershed. The most likely value of θ is defined by the minimum value of median D^* from all combinations of tributaries extracted for each value of θ. Alongside the median we also calculate the first quartile: these values are lower than the median for each value of θ, so we draw a horizontal line from the minimum of the median D^* values and mark where this intersects with the first quartile D^* values at both lesser and greater values of θ (Figure 4.4, panels **a,d**). We then define the uncertainty range, $R\theta$, as the distance between these two points (max_{Q1} and min_{Q1}):

$$R_\theta = max_{Q1} - min_{Q1} \tag{4.12}$$

Lower values R_θ mean that there is less uncertainty on the best-fit θ (Figure 4.4). We can further assess the goodness of fit for θ for entire landscapes by calculating the cumulative distribution (CDF) of R_θ values across multiple basins. The shape of the cumulative distribution is a direct proxy of the cleanness of the best-fits: a steep CDF with low values would mean that the majority of basins had relatively low uncertainties on θ, whereas a more gradually increasing CDF would indicate that the landscape exhibits a wider range of uncertainty on θ.

The technique outlined above allows us to calculate the best-fit theta value for one particular basin. However, D^* is less useful if we wish to constrain the most likely value of θ across multiple watersheds, as different basins will have a different minimum value. Therefore, we also calculate a disorder metric normalized by the range of disorders within a basin, which we call D^*_r:

$$D^*_r = \frac{D - D_{min}}{D_{max} - D_{min}} \tag{4.13}$$

We can calculate D^*_r for the reference value of θ (θ_{ref}) across every basin in the landscape. If the best-fit θ for a particular basin is equal to θ_{ref}, then D^*_r for that basin will be 0. We can therefore interrogate the distribution of D^*_r values for the landscape to determine how well-constrained θ_{ref} is, and therefore how

reliable our estimates of normalized channel steepness will be.

4.4.2 Quantifying spatial variations of θ using S–A

The disorder metric outlined in Section 4.4.1 relies on comparing the main stem channel with a number of tributaries. In some cases, either where basins have very few tributaries, or if concavity along a specific channel is of interest this method is not applicable. In these cases we use slope–area plots to quantify spatial variations in θ, as illustrated for the Danube case study (Section 4.5.4). We calculate the slope of the main channel using a fixed elevation drop of 5 meters. We wish to look at broad patterns in concavity so we segment the river into reaches based on their geological and/or geographical settings, *e.g.* by sedimentary basin or upland area. In each subjectively defined reach, we apply an iterative Monte Carlo sampling scheme to randomly select 80% of the points within the reach and perform linear regressions to determine a population of θ values for each reach.

4.5 Concavity across scales

We use the collinearity method outlined in Section 4.4.1 to investigate concavity across a wide range of different scales, ranging from individual drainage basins to entire mountain ranges. We aim to explore how variable concavity is spatially across different regions and test our ability to constrain a representative θ that can be used in channel steepness calculations.

4.5.1 Individual drainage basins

As a first step, we illustrate the collinearity method with two small watersheds in different geological contexts (Fig. 4.4). The aim of using D^* is to not only determine the best-fit values for a given watershed, but also to determine how "wrong" other values are. This is necessary because normalized steepness values (k_{sn}) are frequently calculated, which inevitably results in channel steepness val-

ues being calculated using values of θ which are inappropriate for an individual basin.

The first example site (Figure 4.4a,b,c) is in the Loess Plateau (China). It features a relatively homogeneous substrate and relatively homogeneous concavity indices estimated from previous studies (e.g. Mudd et al., 2018; Zhang et al., 2020). The density map in Fig. 4.4a shows D^* values for each value of θ tested, and for each combination of tributaries tested in the watershed. Higher densities (e.g., bright colours) mean that many of the tributary combinations returned that value of D^*. Median values minimising D^* suggest a most likely θ value of 0.425. A χ–elevation plot made using this concavity (Figure 4.4b) shows a linear channel profile, suggesting a channel with homogeneous substrate and a constant erosion rate (Perron and Royden, 2013).

Figure 4.4c displays transformed river profiles for different θ with a normalised $\chi^* = \frac{\chi}{\chi_{max}}$ to plot the two populations of χ on the same horizontal scale. Both of these θ values lead to substantial divergence from the linear profile in panel **b**. If the θ values in panel **c** were used to determine k_{sn}, one would predict a wide range of channel steepnesses. Low values of θ result in tributaries that have higher values of k_{sn} than the main stem (i.e., they are steeper in χ–elevation space), whereas tributaries have lower values of k_{sn} than the main stem if θ is large. We also observe that the black dataset using $\theta = 0.15$ is closer to collinearity than the red dataset using $\theta = 0.85$ as predicted by its lower disorder value.

The second test site is a watershed located in the South-Eastern Carpathians (the outlet is 5 km NW of Buzau, Romania). The landscape is marked by spatial variations in uplift and subsidence, heterogeneous lithology (Maţenco and Matenco, 2017, and references therein), and shows strong evidence of stream piracy (e.g. Borgh, 2013a). Figure 4.4d presents a density plot of D^* values that feature more scatter than those of the Loess Plateau. However, the most likely θ, which here is 0.275, can still be determined from the minimum value of D^*. Figure 4.4e demonstrates that the method still isolates the value of θ which maximises collinearity despite prominent breaks-in-slope, a small number of outlier tributaries, and many competing forcings. If we compare the χ–elevation profiles

in Figure 4.4f, we see that the profiles with a high value of θ are much more scattered than those with a low value of θ, which reflects the relative spread of D^* at these θ values depicted in the density plot in Figure 4.4d.

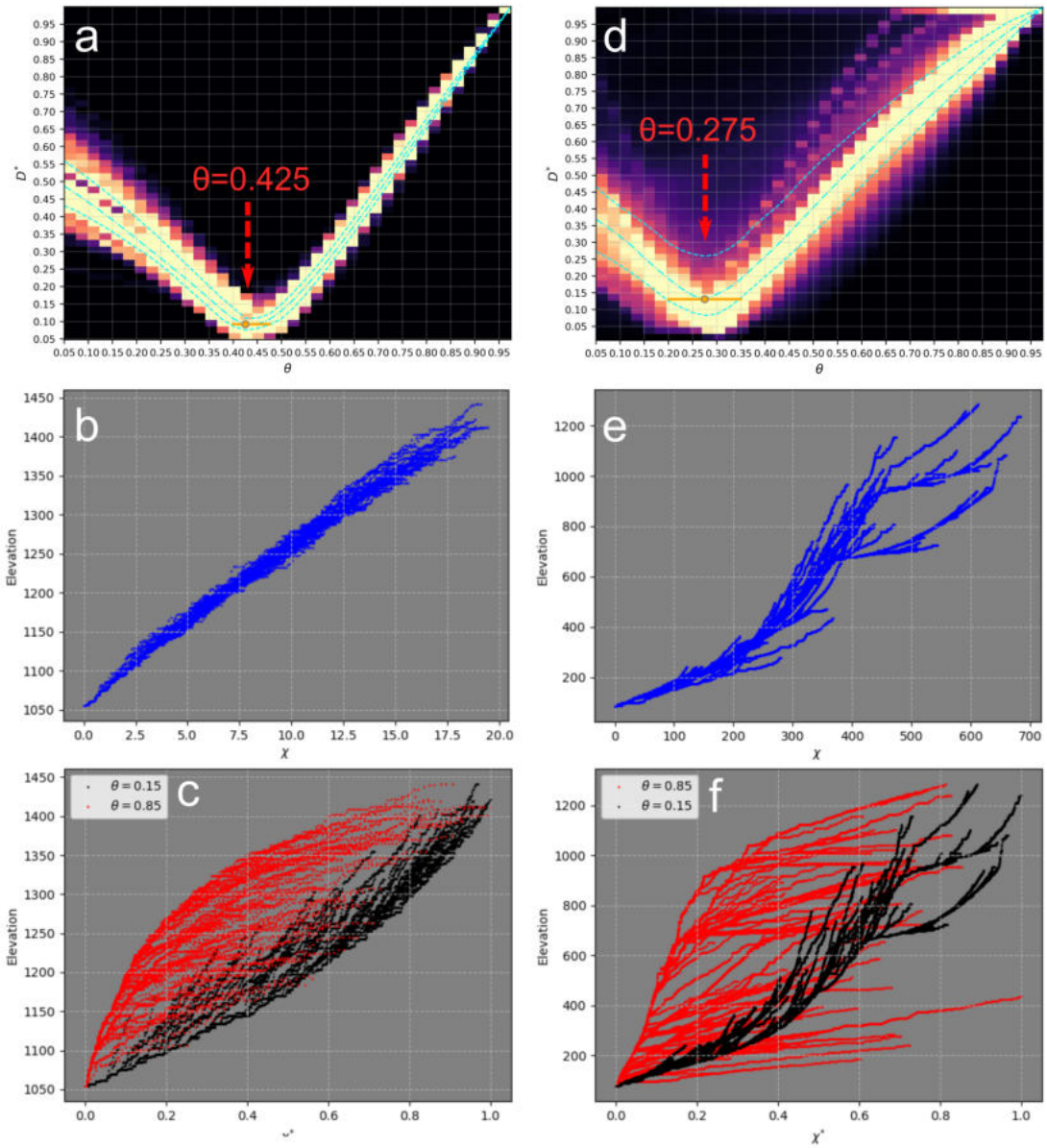

Figure 4.4: θ best-fit for single watershed in the Loess Plateau (a,b and c) and for the Buzau river (d,e and f) in the South-Eastern Carpathians. a) and d) Density plots of the D^* for each combination of watersheds function of θ. It suggest $\theta_{opt} = 0.425$ with a sharp and clear minimum for the Loess Plateau and $\theta_{opt} = 0.275$ for Buzau. b) and e) χ-Elevation profile for the river at calculated with optimal θ. Note the collinearity of the profiles. c) and f) Nondimensionalised $\chi^* = \frac{\chi}{\chi_{max}}$ calculated with non-optimal θs. Note the high scatter compare to their optimised counterparts.

4.5.2 Distribution of θ across mountain ranges

A mountain range or discrete upland area is a convenient unit of study in geomorphology (e.g. Gilbert, 1880). To illustrate variations in the concavity index across mountain ranges, we apply our method to a range of sites showing different tectonic and lithological characteristics, as well as a range of scales: The San Gabriel mountains (CA, USA), the Cordillera Central of Ilocos Norte (Luzon Island, Philippines), the Eastern Carpathians (Ukraine, Romania and Republic of Moldova), and the Himalayas. For each test site, we extract all watersheds within the landscape with drainage areas from 50 km^2 to 1000 km^2. We remove nested watersheds to avoid including the same channels multiple times. This range in drainage area provides a good balance between basins that have a number of tributaries with which to measure collinearity, and basins having a limited amount of internal heterogeneity such as faults, lithologic contacts or climate gradients.

San Gabriel mountains

The San Gabriel mountains sit within the tectonically active Transverse Ranges in Southern California (USA) (e.g Lindvall and Rubin, 2008). DiBiase et al. (2010) quantified the erosion rates in the area using basin-wide cosmogenic radionuclides (CRN) and observed positive correlations between erosion rates and k_{sn} in the region. Using linear regressions on binned S–A plots, they suggested θ=0.45. We apply our methodology to the same field area (Figure 4.5). Figure 4.5a shows the spatial distribution of most likely values of θ, *i.e* θ value minimising D^* for each basin, across the landscape. Figure 4.5b suggests relatively low values of the concavity index with most falling between 0.25 and 0.4. Figure 4.5c shows that more that 60% of the basins have an $R\theta$ below 0.2, meaning their best-fit is narrow and relatively well-defined, with some basins even showing $R\theta$ close to 0.

A strategy to select a representative θ value depends on the watershed of interest. In our case, if we are interested in all the basins on Figure 4.5, we suggest selecting $\theta = 0.3$ to minimise distortion. Figure 4.6 can be used to assess which basins will be most disordered, that is, have the highest D^* value for a particular θ value. One might have less confidence in k_{sn} values extracted from

basins that are highly disordered in Figure 4.6 when using the regional θ value.

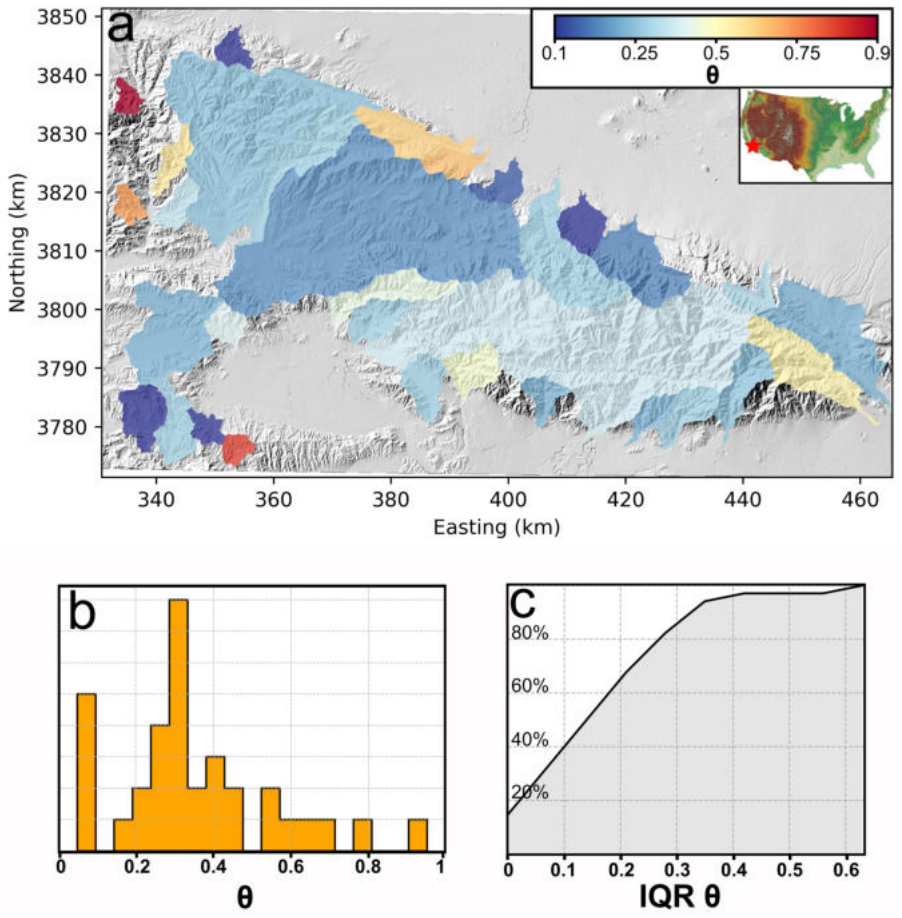

Figure 4.5: Analysis of the spatial variations in concavity index of the San Gabriel mountains and surroundings. a) Map of best fit θ in the area. Note the relative uniformity of the the best fit value of θ. b) Distribution of the best-fit values. The high concentration of $\theta = 0.05$ is linked to the fact that this is the minimum value considered and encompasses all best-fits lower than this. c) Cumulative distribution plot of $R\theta$. This plot shows that 80% of the watersheds have $R\theta$ values less than 0.3.

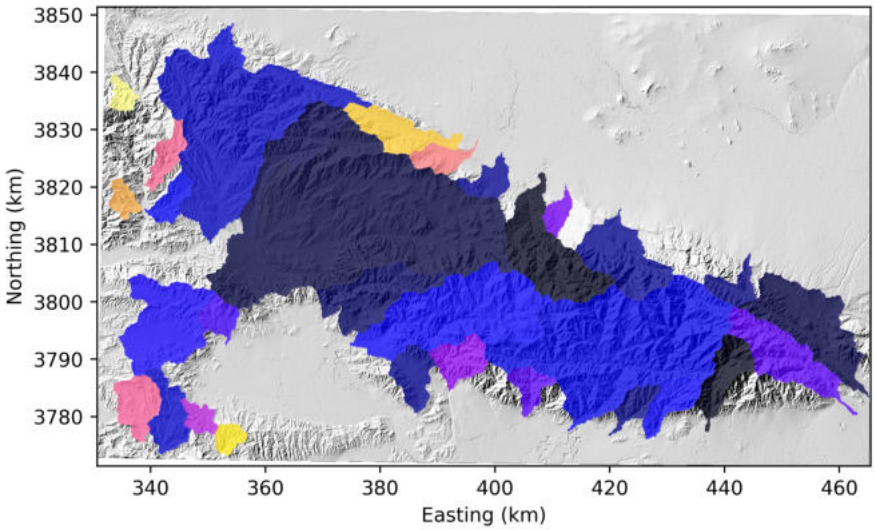

Figure 4.6: D^* values for each watershed for $\theta = 0.3$. Low values, close to 0 in dark, reflect basins that have very low disorder with this value of θ, whereas basins with higher D^* values are much more disordered. Comparison with Figure 4.5 allows one to identify basins that are highly disordered because they do not share the regional best-fit θ (e.g., the basin in the SE corner of the study area), but it can also identify basins that have a similar best fit θ to the regional value, but are still somewhat disordered (e.g., the basin with an outlet on the southern side of the study area with an Easting of just over 340 km).

Cordillera Central of Ilocos Norte, Philippines

The second test site is the Cordillera Central of Ilocos Norte, in the northern part of Luzon island, Philippines. The island is bordered by doubly vergent subduction zones, one to both the east and west of the island. This tectonic forcing has led to the partition of the island by a network of active faults: the Philippine fault system features shearing, compressive, and extensional faults (e.g. Aurelio et al., 2009; Ringenbach et al., 1992). The analysis of the spatial distribution of concavity indices (Figure 4.7a) contrasts with the result from the San Gabriel mountains: it is much more heterogeneous. The most represented value of θ for the range is 0.45 (Figure 4.7b), but the mountains feature basins with most likely θ values that vary between 0.05 and 0.65, and there is no dominant value or range of values amongst the most likely θ values (Figure 4.7b).

This heterogeneity is observable from other perspectives: Figure 4.7c shows the $R\theta$ values of the range. The curve rises much more gradually than that of Figure 4.5c. Only 30% of the basins have an $R\theta < 0.2$ and 20% of them have an $R\theta > 0.4$, suggesting large uncertainties in the most likely value of θ.

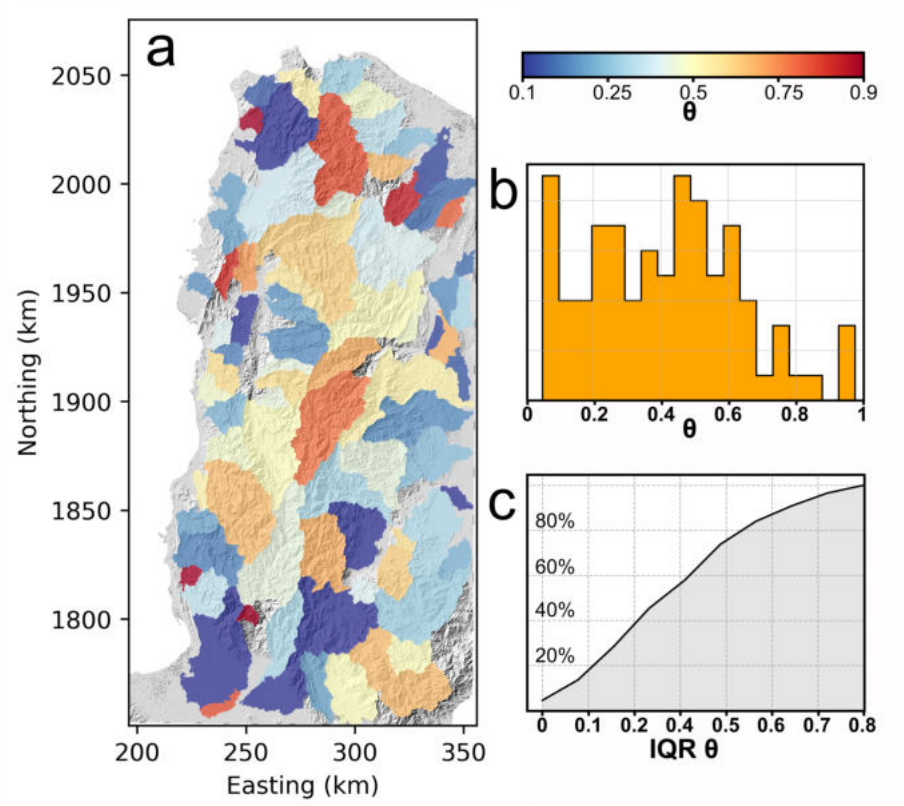

Figure 4.7: Summary of θ best-fit analysis for Luzon field site (Phillipines). a) Spatial distribution of the best-fits for each watershed showing striking heterogeneity across the region. b) Distribution of θ values compiled for all watersheds: there is no clear peak in the best-fit θ. c) Cumulative density plot of the uncertainty $R\theta$. The low steepness of the curve shows the spatial heterogeneity in best-fit θ.

The Eastern Carpathians

The Eastern Carpathians system is part of the eastern continuation of the Alpine orogeny, and is more lithologically heterogeneous than the previous two sites. In their review of the regional tectonics and its topographic expression, Mațenco and Matenco (2017) (and references therein) highlighted several domains which evolved differently, ultimately controlling emergent features of the topography. The different domains are shown in Figure 4.8a): (i) the Southern Carpathians, composed of resistant magmatic and metamorphic rocks with Mesozoic last

significant exhumation events; (ii) the Eastern Carpathians, composed of sedimentary rocks of variable strength and fewer magmato-metamorphic massifs, with exhumation history from late Miocene to present in localised sections; (iii) The Transylvanian Basin, an uplifted back-arc basin with potential drainage reorganisation (Borgh, 2013a); (iv) The Getic and Focsani depressions, made of alluvial fans from the Southern Carpathians and subsidence of the active part of the Eastern Carpathians; and (v) the European Foreland, the foreland basin of the Eastern Carpathians and part of the European Shield (Mațenco and Matenco, 2017, and references therein).

Figure 4.8 presents a summary of the concavity index distribution within the Romanian Carpathians. Figure 4.8b shows the most likely values of θ are widely distributed, but the distribution is centered around 0.625, excluding a large number of values with a best fit θ of <0.05. Figure 4.8c suggests that the different domains behave differently. The Getic and Focsani depressions primarily feature low concavities, between 0.2 and 0.4. Basins in the Southern Carpathians feature low to medium concavity with a wide range of low values between 0.1 and 0.5. The Transylvanian basin and the Eastern Carpathians present similar trends with best-fits centered on 0.5, although the relatively flat distributions suggest a less well constrained best-fit. The European Foreland, in contrast, has high θ values, > 0.6.

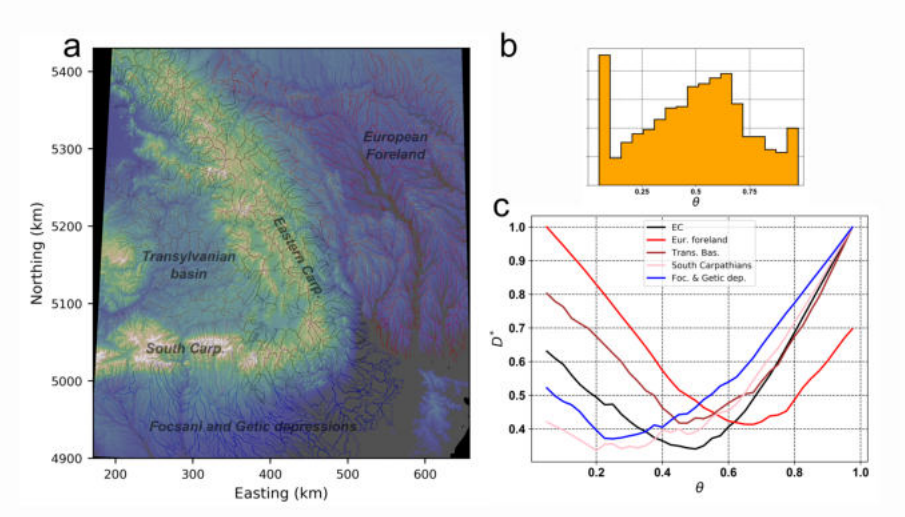

Figure 4.8: Concavity results from the Eastern Carpathians. a) Watershed between $5e^7m^2$ and $1e^9m^2$ extracted colored by domain corresponding to the legend on c. The base map and subsequent units are in WGS84 UTM35N. b) Best-fit concavity across the field site. Note the peak of low values representing values lesser or equal to 0.05. c) Median profiles of the median D^* for each of the watershed by zones. Global trend can be isolated with significantly different minimums for the different area. The colors correspond to the basin outlined in a) and described in the legend.

The Himalayan system

We also illustrate the spatial distribution of concavity in the central Himalayan system. We include in this analysis the main basins draining the range, outlined in black in Figure 4.9a, and their surrounding smaller basins on the Tibetan plateau and the Gangetic plain.

Himalayan River networks have been widely studied (e.g. Clark et al., 2004; Gupta, 1997; Lavé and Avouac, 2001; Seeber and Gornitz, 1983). Due to the heterogeneous nature of the range's lithology and tectonics (e.g., Yin, 2006), as well as strong gradients in precipitation and discharge (Bookhagen and Burbank, 2010), we might expect strong variations in θ values: the Himalayas do not disappoint in this regard (Figure 4.9).

Within the mountain belt, the most likely θ values are centred roughly around 0.45, but large numbers of basins have most likely values between 0.05 to 0.7. Subtle patterns may be recognised; for example the patch of high concavity at Easting 750 km - Northing 3250 km, or the strip of low concavity just north of

the basins outlined in black; but apart from systematically low concavity in the plains, no clear signal emerges. This suggests caution should be used in applying a single value of θ across the range when exploring channel steepness.

We also analysed the large scale expression of θ within the major basins, outlined in black, that average the effect of more factors than smaller basins (Figure 4.9c). Most of the large basins have a global θ in between 0.2 and 0.4 with large uncertainties. One basin features a very high concavity, at odds with Figure 4.9a, suggesting that large-scale expression of concavity might hide local heterogeneities.

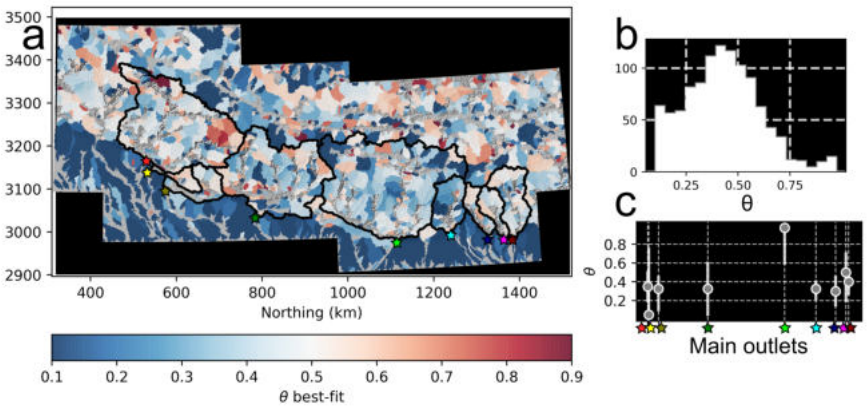

Figure 4.9: Distribution of θ across the Central Himalaya. a) Spatial distribution of the best-fit θ for all watersheds in a range of drainage area from $5e^7$ to $1e^9$ metre square. The black outlines are representing the main basins draining to the mountain front. The stars are their outlets and refer to figure c. b) global distribution of all the best fits in the study area. Note that the very low values (0.05) have been omitted here for the sake of clarity.

4.5.3 Variability in the concavity index across multiple basins

To give a broader picture of variation in the value of θ across many different landscapes, selected to represent a broad range of climate, lithology and tectonic activity. We have avoided depositional areas (*e.g.*, sedimentary basins and alluvial fans) because these areas cannot be expected to adhere to Playfair's Law, which serves as the basis for our reliance on the disorder metric (see Section 4.4.1).

Our compilation was constructed by extracting all basins in each landscape with drainage areas from 50 km^2 to 1000 km^2. As in all previous examples, we

remove nested basins and we avoid analysis of any basin which is on the edge of the DEM, as these may have incorrect drainage areas.

Our compilation of basins includes 5033 basin analysed for most likely θ across a diverse range of landscapes. The median value across all these basins is 0.425, which is consistent with previous studies based on slope–area data (e.g. Tucker and Whipple, 2002). This central tendency, however, masks a very large degree of heterogeneity. The first and third quartile of most likely θ values are 0.225 and 0.575. We note that our table makes no effort to isolate bedrock channels, and we may expect greater heterogeneity if the study area includes both alluvial and bedrock rivers (e.g., Whipple, 2004).

The table includes metrics of the range of uncertainties across multiple landscapes. We hope this serves as a benchmark for authors to determine how "messy" their landscape is in a global context. The first and third quartiles for R_θ across all 5033 basins is 0.175 and 0.375, respectively. Therefore, basins with an R_θ value of 0.175 or less have a sharply defined θ compared to most basins, whereas basins with an R_θ above 0.375 are particularly disordered: in these basins it is virtually impossible to constrain the correct value of θ.

4.5.4 Variability along continental-scale rivers: the Danube

Our previous test sites aimed to show the variation of concavity across different scales of field site. However there is still a particular case that has not been investigated: continental-scale rivers. Here we do not aim to extract concavity values over sets of basins, but rather over a large river crossing a continent. Exploring θ over a large river is particularly important for χ, because the χ coordinate integrates discharge data from base-level to top. Thus, χ values at basin headwaters are sensitive to poorly fit values of θ downstream (Forte and Whipple, 2018).

The Danube is the second longest river in Europe which flows for approximately 2,860 km, connecting the Alps to the Black Sea. It acts as a major source-to-sink component of the Alpine-Pannonian-Getic-Black-sea system and sets boundary condition for the erosion of the North-Eastern Alps (Matenco et

Table 4.1: Concavity indices across selected landscapes. At each site we analyse a number of basins and report the median, and first and third quartiles of the most likely θ values amongst the basins. We also report the median and first and third quartiles for the range of uncertainty (R_θ) for individual basins. Maps showing exact locations of study areas and spatial distributions of θ and R_{theta} can be found in the Supplemental Materials.

Site Name	N Basins	Median θ	Q1 θ	Q3 θ	Median R_θ	Q1 R_θ	Q3 R_θ
Chilean Andes	65	0.475	0.225	0.625	0.275	0.125	0.4
North Arkansas	11	0.65	0.525	0.663	0.3	0.2	0.412
Bureya Massif	75	0.45	0.325	0.55	0.225	0.175	0.325
Eastern Carpathians	876	0.5	0.325	0.65	0.275	0.175	0.375
Caucas Mountains	366	0.362	0.175	0.5	0.25	0.15	0.35
Sierra Madre, Mexico	94	0.45	0.306	0.525	0.25	0.131	0.375
Corsica	30	0.388	0.256	0.425	0.288	0.225	0.444
Ethiopian Highlands	111	0.3	0.2	0.4	0.175	0.125	0.275
Jebal Barez, Iran	54	0.2	0.106	0.275	0.175	0.125	0.25
Lesotho	78	0.475	0.35	0.569	0.175	0.1	0.275
Luzon	88	0.425	0.225	0.575	0.338	0.225	0.475
Edge of Mongolian Plateau	107	0.45	0.35	0.525	0.225	0.125	0.338
Basins along Nujang River	71	0.45	0.325	0.625	0.275	0.175	0.425
Oregon Coast Ranges	26	0.538	0.338	0.75	0.25	0.175	0.3
San Gabriel Mountains	34	0.325	0.275	0.444	0.212	0.125	0.3
Southern Altai Mountains	551	0.35	0.175	0.525	0.25	0.15	0.4
Southern Brazil	102	0.475	0.4	0.55	0.225	0.15	0.275
Western South Africa	634	0.25	0.125	0.425	0.225	0.15	0.35
Southern Wisconsin	60	0.562	0.45	0.625	0.2	0.144	0.325
Yemen	52	0.4	0.275	0.506	0.175	0.125	0.256
Atlas Mountains	26	0.4	0.275	0.5	0.225	0.175	0.325
Dolomites	28	0.538	0.35	0.756	0.338	0.225	0.5
Hida Mountains	51	0.5	0.3	0.575	0.3	0.225	0.438
Himalayas	645	0.4	0.25	0.525	0.275	0.175	0.4
Allegheny Plateau	118	0.7	0.556	0.819	0.25	0.175	0.394
Northern Appalachians, USA	177	0.525	0.4	0.675	0.35	0.225	0.45
Southern Appalachians, USA	277	0.5	0.3	0.625	0.35	0.225	0.45
Olympic Mountains	33	0.575	0.4	0.675	0.325	0.2	0.425
Pyrenees	61	0.475	0.3	0.575	0.325	0.225	0.4
Taiwan	97	0.45	0.15	0.575	0.275	0.2	0.375
Tien Shan	40	0.612	0.5	0.756	0.325	0.25	0.481
Zagros Mountains	49	0.475	0.3	0.625	0.25	0.125	0.4

al., 2013). It also crosses several sedimentary basins which are separated by gateways, each having a history of opening and closing through geological time (e.g. Leever et al., 2011; Leever et al., 2010).

We extracted the Danube river long profile using a pre-conditioned DEM from the HydroShed (Lehner et al., 2008), and segmented the profile by very general domains: i) the Danube delta and crossing of the Northern Dobruja range (Eastern Romania, in dark blue in figure 4.10); ii) the Dacic depression, foreland of the South Carpathians (light blue in figure 4.10); (iii) the Iron Gates, the gateway between the Dacic depression and the Pannonian Basin (green in figure 4.10); (iv) the Pannonian Basin (orange in figure 4.10) and the Alpine Danube (red on figure 4.10). Processing of concavity along the river suggest systematically low concavity on most of the sedimentary basins (between -0.15 and 0.15). The Iron gate area and the Alpine Danube show higher concavity around 0.3.

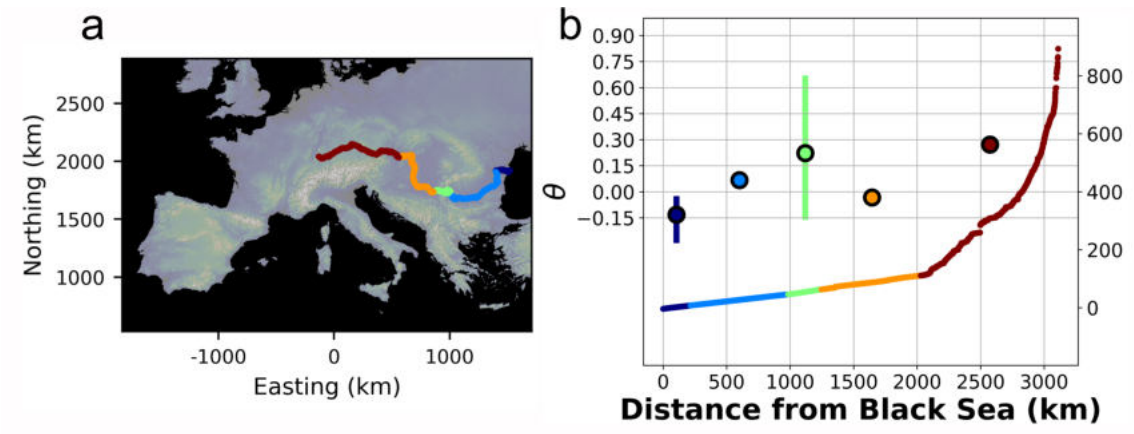

Figure 4.10: a) Map of the Danube River's course, coloured by domains discussed in the text. Raster preconditioned by Hydroshed (Lehner et al., 2008) and projected in Lambert Conformal Conic. b) Long profile of the Danube river, with θ for each river domain. Note the overall low concavity on θ for most of the lowlands.

4.6 Distortion of k_{sn} and χ values linked to variations in θ

We have demonstrated the variability of θ values at a wide range of scales. When studying a field site, no matter the scale of the area, one needs to assume a

reference θ for the study in order to use k_{sn} or χ. This forces the worker to calculate k_{sn} with θ values that may not be the most likely for some of the watersheds. Therefore, we now move on to explore how changing values of θ will affect k_{sn} and χ values, and consequently our interpretation of landscape metrics. We first investigate analytical expressions of the distortion, and then illustrate the distortion using real landscapes.

4.6.1 Distortion of k_{sn}

Interpreting k_{sn} in a meaningful manner involves focusing on the contrasts between the slope patches, sensu Royden and Taylor Perron (2013) across a field site. Indeed, local contrasts in k_{sn}, *i.e.* a knickpoint, are commonly interpreted as driven by phenomenon such as climatically driven base-level drop (e.g. Crosby and Whipple, 2006) or tectonincally driven changes in uplift or fault throw rates (e.g Kirby and Whipple, 2012). If contrasts between two slope patches are exaggerated, attenuated, inverted, annihilated or artificially created, spurious patterns carry a real risk for misinterpretation.

Analytical formulation of k_{sn} distortion

We consider two points in a channel network, labelled with subscripts M and N, that are characterised by their slope and drainage area (S_M, A_M) and (S_N, A_N). Their k_{sn} values (expressed as k_M and k_N can be expressed rearranging equation 4.1 as follows:

$$k_M = S_M A_M^{\theta_{ref}} \tag{4.14}$$

and

$$k_N = S_N A_N^{\theta_{ref}} \tag{4.15}$$

We can calculate the ratio of k_{sn} for these data points, which we call r_k, that is valid for a given θ:

$$r_{k,\theta} = \frac{S_M A_M^\theta}{S_N A_N^\theta} \tag{4.16}$$

Which we recast with a slope ratio, r_S, and an area ratio, r_A:

$$r_{k,\theta} = r_S r_A^\theta \tag{4.17}$$

Where $r_S = \frac{S_M}{S_N}$ and $r_A = \frac{A_M}{A_N}$. To assess the distortion linked to changing the value of θ, we aim to express the ratio r_k as a function of $\Delta\theta$, with $\Delta\theta$ defined as:

$$\Delta\theta = \theta_2 - \theta_1 \tag{4.18}$$

with θ_1 and θ_2 are the different concavities used. A logarithmic transformation can simplify comparison of the two k_sn values:

$$\ln[r_{k,\theta_2}] - \ln[r_{k,\theta_1}] = \ln[r_S] + \theta_2 \ln[r_A] - \ln[r_S] - \theta_1 \ln[r_A] \tag{4.19}$$

The slope ratios cancel because these are not affected by θ:

$$\ln[r_{k,\theta_2}] - \ln[r_{k,\theta_1}] = \Delta\theta \ln[r_A] \tag{4.20}$$

We can define a factor that quantifies the distortion ratio between the two k_{sn} values as we vary θ, which we call the distortion factor, β_r:

$$\beta_r(\Delta\theta) = \frac{r_{k,\theta_2}}{r_{k,\theta_1}} = r_A^{\Delta\theta} \tag{4.21}$$

Examples of k_{sn} distortion in real landscapes

We first illustrate distortion of k_{sn} with the test sites used in Figure 4.4. Figure 4.11 shows the extent of k_{sn} distortion for different hypothetical cases where θ is set at a value that differs from the most likely value. We normalise all the k_{sn} values by their range of values, noted k^*_{sn}, to circumvent the differences in magnitude between the different values of θ. We display their median basin-wide distribution, binned by distance from their respective outlets.

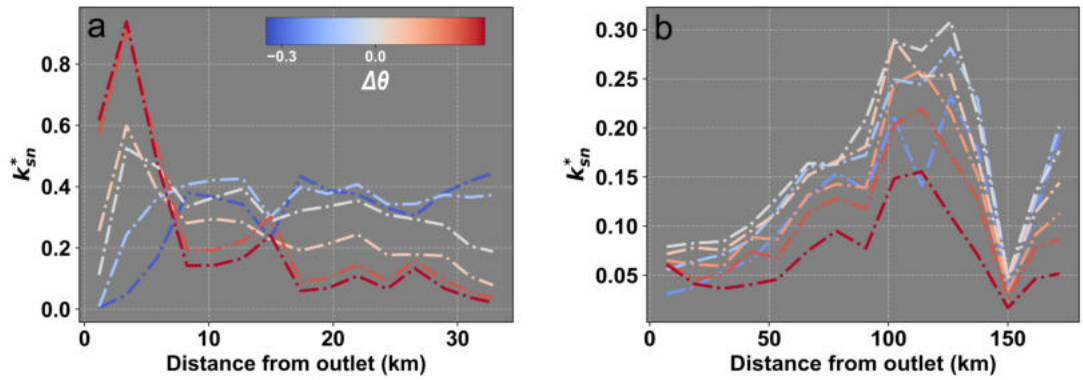

Figure 4.11: a) Distribution of k^*_{sn} – *i.e.* normalised to range – for a range of θ along the watershed investigated in section 4.5.1a) (Loess Plateau, People's Republic of China). The different colours correspond to $\Delta\theta$ from the best fit $\theta = 0.425$. b) Distribution of k^*_{sn} for a range of θ along the watershed investigated in section 4.5.1d) (Buzau river, Romania). The different colours correspond to $\Delta\theta$ from the best fit $\theta = 0.275$.

Figure 4.11 gives an insight of the possible distortion at the scale of a single watershed. At optimal $\theta_{opt} = 0.425$ for the first field site (see section 4.5.1), figure 4.11a depicts a k_{sn} profile showing an initial increase of k_{sn} in the first 8 kilometres followed by a slight decrease in median value the rest of the profile. Using $\theta > \theta_{opt}$ gradually inverts this contrast by over-estimating k_{sn} in the first section of the profile. The normally decreasing part of the profile is gradually over-estimated. On the other hand, using $\theta < \theta_{opt}$ exaggerates the contrast between the lowest values near the outlet and the rest of the profile. The slightly decreasing pattern becomes flat or even increasing for very low θ.

The second and more heterogeneous field site (Buzau, Romania, see section 4.5.1, $\theta_{opt} = 0.275$), shows a gradual increase of k_{sn} followed by a sharp decrease near the headwaters of the network (figure 4.11b). Changing the value of θ at this site does not change the overall pattern of channel steepness, however overestimates of θ result in a flattening of the contrasts. We also extracted illustrative k_{sn} distortion across multiple basins within the Luzon field site (Figure 4.12, see Section 4.6 for context). A number of potentially spurious patterns emerge with the use of different θ values to calculate k_{sn}. In this site, higher values of θ result in the largest proportion of high values of steepness in the range.

The zone of high k_{sn} values in Figure 4.12c is more extensive than the one in Figure 4.12a. Another systematic observation at higher θ, is that channels with more drainage areas feature higher values. We determined an area of interest outlined in light green (to not interact with the k_{sn} color scheme) in Figure 4.12a, b and c in order to illustrate more thoroughly some aspects of the distortion. The green area includes a number of sub-basins draining to a low-relief area. At $\theta = 0.2$, the larger channels have low steepness values, and the northern section of the range has generally higher k_{sn} than the eastern section of the range. The plain has systematically low steepness and no sharp contrasts in k_{sn} are visible. When $\theta = 0.45$, river steepnesses increases. Contrasts between the different sections are less pronounced but a few steeper areas do appear. At $\theta = 0.7$, some of the larger rivers become steeper than the surrounding terrain. A number of sharp k_{sn} patches appear.

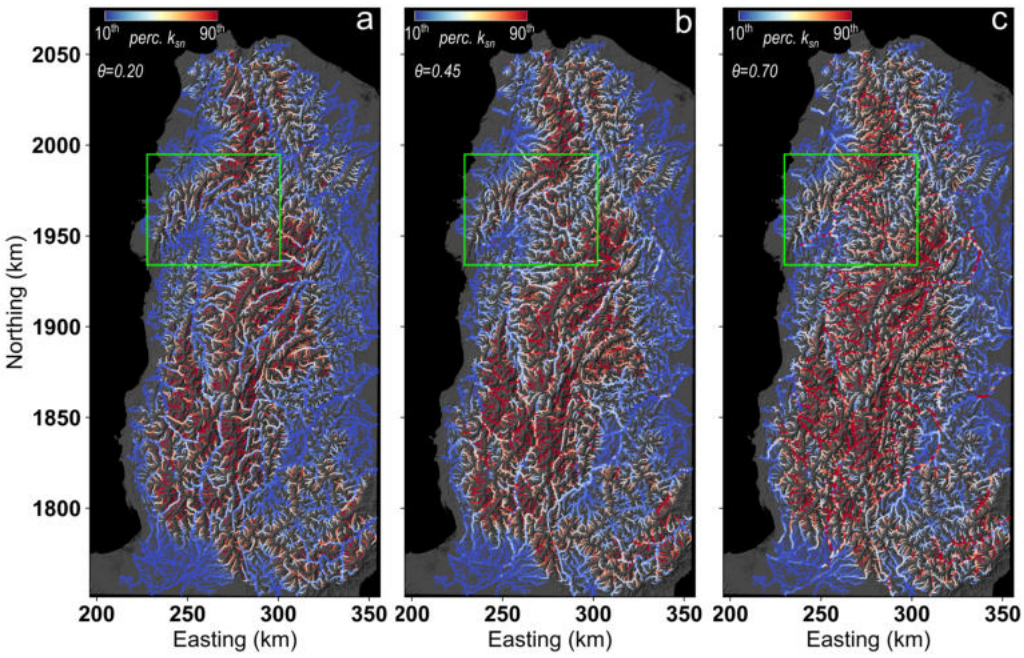

Figure 4.12: River network in the Luzon island (Philippines) coloured by k_{sn} values for different θ. In order to produce comparable results, the minimum and maximum colours are set to respectively the 10^{th} and the 90^{th} percentile of each k_{sn} populations. θ values have been picked in order to represent the general distribution of best-fits (see Figure 4.7): 0.20 for a), 0.45 for b) and 0.70 for c). River points are sized by $log[A]$ and largest A are plotted on top.

Subsequent implications and predictions

Equation 4.21 highlights a number potential biases in k_{sn} values when calculated with non-optimal θ. Figure 4.13 presents the analytical solution to the distortion β_r, which has the amusing property of looking like a bow tie.

Interpreting this bow tie may be slightly confusing, since β_r is a ratio of ratios. Let us let first give a more concrete example: consider a landscape where, at a given value of θ all the values of k_{sn} are the same. This means that r_{k,θ_1} must always equal unity and that β_r will be equal to the ratio in channel steepness between two points with a drainage area threshold r_A. If the θ value is reduced, then channel reaches with a larger drainage area will have a smaller k_s value than those with smaller drainage area. If the θ value is increased, then it is the reaches with larger drainage area that will increase their k_s values relative to smaller channels.

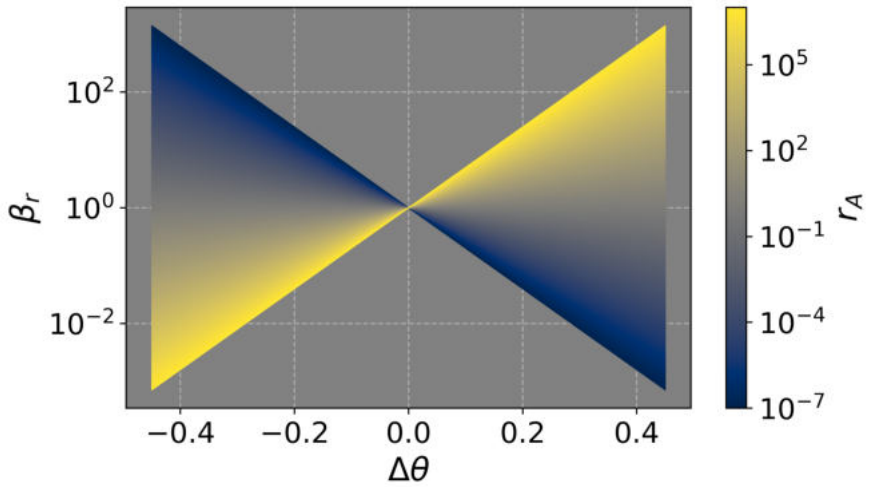

Figure 4.13: The distortion ratio (β_r) as a function of the change in θ, colored by the ratio of drainage area between two points.

Having highlighted the most basic feature of Figure 4.13, we can expand upon the nature of distortion, which is a function of (i) how different the local θ is from the global best fit and (ii) the differences in drainage area amongst the compared channel reaches.

To illustrate the behavior, consider two slope patches, *sensu* (Royden and Taylor Perron, 2013), with a contrast in k_{sn} of r_k and a contrast in drainage area

r_A. Several scenarios can be considered which can relate potential dangerous distortion in real landscapes.

First, assume that these two slope patches are contiguous, within the same river and without any significant tributary joining between them (i.e., they will have similar drainage areas). Their r_A will typically be very low, *e.g.* between 0.9 and 1.1, depending on the source dataset and local context. As illustrated in Figure 4.13, distortion for a low ratio of drainage areas is insignificant, with a distortion of the ratio in the order of 1.05 in the worst cases. It suggests using non-optimal θ will not impact the importance of local knickpoints, relative to their immediate surroundings.

This might give one confidence that we do not need to worry about distortion when identifying knickpoints based on k_{sn} data. However, many studies base interpretation of factors driving the presence of knickpoints by their spatial distribution (Crosby and Whipple, 2006, e.g.). Because river channels feature many fluctuations in gradient, simply looking for changes in k_{sn} may result in large numbers of potential knickpoints (e.g. Gailleton et al., 2019), so we must compare the relative magnitude of knickpoints in different channels, which will inevitably have different drainage areas. In this case distortion due to non-optimal θ becomes problematic. If we consider two knickpoints having the same Δk_{sn} contrast if the most likely θ is used (i.e., $\Delta\theta = 0$), but one of these is in a small tributary (*e.g.* $1e^5 m^2$) and another one in the more prominent channel (*e.g.* $1e^9 m^2$, r_A in the order of $1e4$), the distortion β_r can rapidly rise up to 20 times higher/lower depending on the $\delta\theta$. This confirms earlier observations from topographic analysis suggesting the location of contrasts in k_{sn} does not move with different values of θ but their relative importance would be modified (Gailleton et al., 2019).

Next, consider two slope patches of differing drainage area located within the same watershed. This can represent a wide range of possible scenarios in real landscapes, for example contiguous slope patches up and downstream of a tributary junction, slope patches on different rivers, or slope patches on the same river that lie some distance from each other. The resulting distortion from

varying the θ value can either generate new contrasts, erase existing ones or even invert the steepness signals (Figure 4.13), as observed in the Loess Plateau in section 4.6.1. For example, a point with lower k_{sn} in the main river relative to a tributary will see the contrast between the two shrink with potential inversion of the two values if the θ value is increased (i.e., $\Delta\theta > 0$). On the other hand, the ratio of k_{sn} will grow exponentially larger with $\Delta\theta < 0$. The exact nature of the distortion is case specific when it comes to changes in drainage area and needs to be considered carefully. Figure 4.13 can be used, along with constraints on θ, to assess the risk of distortion for particular cases. Figure 4.13 also shows that the key parameter in determining the degree of distortion is the drainage area.

4.6.2 Influence of concavity values on the distortion of the χ coordinate

Analytical formulation of χ distortion

Expressing the analytical distortion of χ linked to varying concavity is less straightforward than for k_{sn}, which is solely defined by constant S and A values. The χ coordinate at a given point x of the river profile, is dependent on the downstream river network and tributaries as it integrates $(\frac{A_0}{A(x)})^\theta$ for the outlet to x. This has two direct consequences.

First, the χ value depends on the location of base level, x_0. This issue is out of the scope of the present study and has been thoroughly discussed in multiple studies (e.g Forte and Whipple, 2018; Seagren and Schoenbohm, 2019), we direct the interested reader to figure 2 in Forte and Whipple (2018) for an illustration of the significant impact of base level choice on χ contrasts.

Secondly, solving for distortion requires constraining the downstream shape of the river network. However, river flow distance x as a function of drainage area varies from river to another. For analytical solution, we use an approximation by expressing the distance from the outlet, x, as a function of drainage area, A:

$$A(x) = (X_0 - x)^\rho \tag{4.22}$$

where X_0 is the maximum distance of the river to the outlet (*i.e.* the distance from the source to the chosen base level), and ρ a positive exponent approximating the rate at which drainage area decreases toward head water. This is a variation of Hack's law (Hack, 1957), as Hack's law described A as a function of flow distance downstream. Although very simplified, equation 4.22 can simulate realistic drainage area distribution along river profiles. We can then use the standard definition of the χ coordinate (e.g. Perron and Royden, 2013):

$$\chi(x) = \int_{x_b}^{x} \left[\frac{A_0}{(X_0 - x)^{-\rho}} \right]^{\theta} dx \tag{4.23}$$

Integrated, this becomes

$$\chi(x) = \frac{A_0^{\theta}(X_0 - x)^{(1-\rho\theta)}}{\rho\theta - 1} - \frac{A_0^{\theta}(X_0 - x_b)^{(1-\rho\theta)}}{\rho\theta - 1} \tag{4.24}$$

By definition, the outlet, x_b, has a coordinate of 0 (x is defined as the distance from the outlet), so inserting this we arrive at:

$$\chi = -\frac{A_0^{\theta}}{\rho\theta - 1} \left[(X_0 - x)^{(1-\rho\theta)} - X_0^{(1-\rho\theta)} \right] \tag{4.25}$$

Willett et al. (2014) suggested that differences in the χ coordinate across drainage divides indicated disequilibrium in tectonic forcing and that drainage divides would migrate away from the side of the divide with a lower χ value. Conversely, if the χ value is the same on either side of the divide for two points with the same elevation, then the divide should be stable.

We can explore the impact of changing θ on the χ coordinate on either side of the divide if we further simplify equation 4.27 by setting $A_0 = 1$ m^2 (this is the value chosen in most studies). In addition, the χ coordinate used to evaluate differences across divides is typically extracted at a critical drainage area (A_c) (e.g Forte and Whipple, 2018; Willett et al., 2014). We can calculate the distance from the outlet of this critical drainage area from equation 4.22:

$$x_c = X_0 - {A_c}^{1/\rho} \tag{4.26}$$

Inserting equation 4.26 into equation 4.27 and setting $A_0 = 1$ m^2, we arrive at:

$$\chi_d = -\frac{1}{\rho\theta - 1}\left({A_c}^{1/\rho-\theta} - X_0^{(1-\rho\theta)}\right) \tag{4.27}$$

Now consider two points on either side of a divide with the same elevation and the same χ coordinate. The basins on either side of the divide could have different topology, so could have different values of ρ and different values of X_0. If we call these values in the second catchment ρ_1 and X_1, we can fix the two χ coordinates to the same value:

$$\frac{1}{\rho\theta - 1}\left({A_c}^{1/\rho-\theta} - X_0^{(1-\rho\theta)}\right) = \frac{1}{\rho_1\theta - 1}\left({A_c}^{1/\rho_1-\theta} - X_1^{(1-\rho_1\theta)}\right) \tag{4.28}$$

If we assign the value of X_1, we can solve equation 4.28 for ρ_1.

Using these values of ρ, $_0$, ρ_1, and X_1 from basins that have the same value of χ at a critical drainage area of A_c, and which we have defined as being at equilibrium so therefore having the same elevation at these points, we can then alter the value of θ by some offset, $\Delta\theta$. When θ is modified, the χ coordinate will change in each basin. But the two new χ values will not be the same, generating an difference in χ at the divide that is an artefact of choosing an incorrect value of θ.

We find that the offset in χ at the divide caused by selecting an incorrect value of θ is most sensitive to the correct value of θ, the value of $\Delta\theta$, and the ratio between the lengths of the basins that share a divide, X_1/X_0. We plot results as the percent offset in χ at the divide, which under some parameter values can exceed 40% (Figure 4.14.

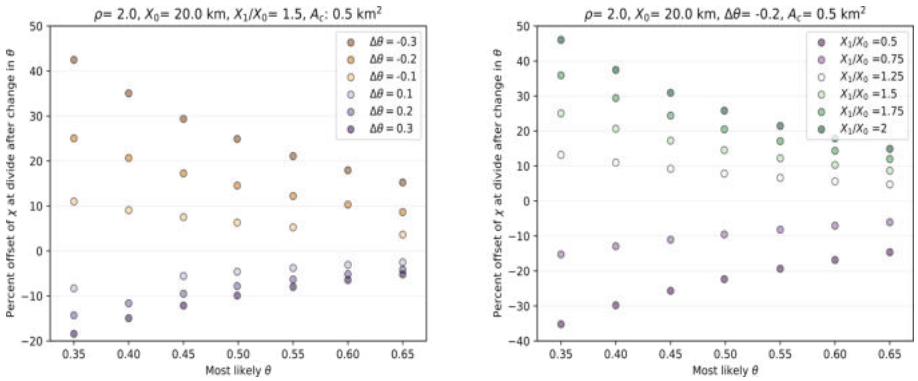

Figure 4.14: Percent difference in the χ coordinate for two basins whose χ values are the same for one value of θ, but are different lengths (X_0 and X_1), resulting in distortion of the χ coordinate when θ is changed by $\Delta\theta$. In the left panel, we show the sensitivity to $\Delta\theta$ whereas we show the sensitivity to the difference in length between the two catchments.

Spurious offsets in χ at the divide are greater when the correct value of θ is smaller. Unsurprisingly, offsets are greater for greater values of $\Delta\theta$. The value of χ is greater in the longer catchment if θ has been overestimated (e.g., $\Delta\theta < 0$). In the nomenclature of (Willett et al., 2014), if θ has been overestimated, the shorter basin will spuriously appear to be the aggressor. We have shown in Section 4.5.3 that most likely values of θ can vary substantially from the central value of 0.45. If the most likely value is high, such as in the Allegheny Plateau or in the Ukraine (Table 4.5.3), the distortion for choosing a concavity index of 0.45 will result in relatively small distortions of around 10%, but the errors will be much larger in locations with low concavity values if a θ value of 0.45 is used. We should remind the reviewer that our analytical examples use the rudimentary approximation of the relationship between length and area described by equation 4.22, so we now move on to examples in real catchments.

Illustration of χ distortion in real landscapes

We select 3 sites in different geographical and geological contexts to explore the ratio of χ values across selected divides for a range of θ values. Figure 4.15 presents the results for the three test sites. The first site (Figure 4.15a and d) is the island of Corsica (France), which is subject to differential climatic, tectonic and lithologic forcings (e.g Fellin et al., 2005; Forzoni et al., 2015). The island

does feature a common base level of the Mediterranean Sea. The second site (Figure 4.15b and e) is located in the Loess Plateau (People's Republic of China); the site described in Section 4.5.1 lies within this area. We fix the base level at the Wei River, close to the relief front and at similar elevation. Finally we explore the Carpathian Mountain Range (Figure 4.15c and f) and the main divide across the Eastern and South Eastern Carpathians, with calculation of χ using the Black Sea as base level. For the sake of readability, we chose to display the maps with the widely used $\theta = 0.45$ and the θ tested are 0.05,0.25,0.45,0.65,0.85.

Corsica's cross-divide χ–ratios show a nearly systematic pattern: to the North, the western basins on the island have higher χ values near the divide, whereas this pattern is reversed in the South. This pattern, as well as the crossing point separating the two areas is not affected by the variations in θ. However, the magnitude of the ratios varies as we traverse values of θ: the highest values of θ result in relatively uniform values of χ across the divide. As the values of θ are reduced, contrasts in χ across the divide grow in magnitude.

The analytical solutions (Figure 4.14) suggest that reducing the value of θ will result in longer catchments having greater values of χ at the divide. In southern catchments on Corsica, the longer basins are in the West, and we can see from Figure 4.15d that these western catchments have higher values of χ at the divide as θ values decrease. In the North, the higher values of χ are in the eastern catchments for decreasing values of θ, consistent with our analytical results.

The Loess Plateau's cross-divide χ–ratio at $\theta = 0.45$ suggests a relatively stable contrast across the area, consistent with previous findings of (Willett et al., 2014). The two basins on either side of the divide have a most likely θ value of 0.4, very close to $\theta = 0.45$. The absence of large changes in the offset of χ across the divide for different values of θ in comparison to the other two study sites is also consistent with the analytical solutions: the basins on either side of the divide feature similar distances between base level and the divide. In this landscape it seems that selecting a value of θ inconsistent with the most likely value of θ would not have a large impact on the χ offset at the divide. However if χ is used to derive k_{sn}, the same distortion as the previous section are expected

to occur.

The third test site in the Carpathians is the largest of the three and the most heterogeneous: the χ calculation encompasses the entire whole mountain range and major sedimentary basins with very low relief as described in Section 4.5.4. The rivers on the southern and eastern side of the divide are linked more closely, in terms of flow distance, to the Black Sea whereas the rivers on the Western side of the divide travel around the Southern Carpathians through the Pannonian basin, flowing along the Danube and Olt rivers. As shown in the section investigating the spatial variations in θ in the region, the most likely values of θ are very heterogeneous. The patterns at the start and at the end of the divide profile are inverted when switching from low to high θ.

Again, we can use the analytical solutions to inform these results. At the southern section of the divide, the western basin is flows along the Olt river, which we can see in Figure 4.15c dissecting the southern Carpathians, leading to a relatively modest difference in flow length across the divide. In the center of the divide, the basins on the western side of the divide flow a much greater distance, and so for decreasing values of θ the difference of χ across the divide grows much greater, to values on the west more than 3.5 times those on the east.

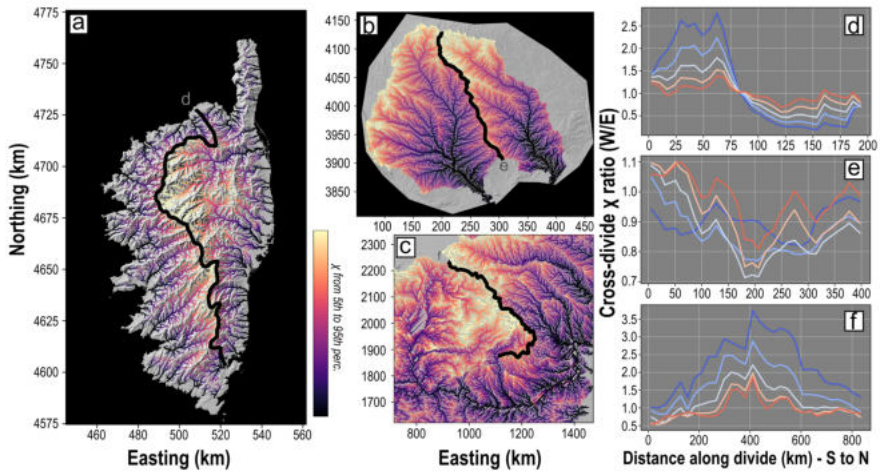

Figure 4.15: Illustration of χ distortion effect on real landscapes. a) b) and c) show the χ map at $\theta = 0.45$ for respectively Corsica (France, WGS84-UTM35N), Loess Plateau (People's Republic of China) and the Carpathians-Pannonian-Black Sea are (Czech Republic, Slovakia, Hungary, Romania, Bulgaria, Ukraine, Moldova, Poland, Serbia). χ color scheme is based on the 5^{th} to the 95^{th} percentile for each of the respective maps. the investigated divides are displayed in bold black lines. d), e) and f) shows the cross divide for the three respective field sites. The ratio is calculated for a window of 20 km across divide for Corsica and 40 km for the others. The colors on d,e,f represent the concavity index from 0.1 (blue) to 0.8 (red).

4.7 Conclusions

In this contribution, we expanded methods to determine most likely value of the concavity index, θ, using disorder metrics (e.g. Goren et al., 2014; Hergarten et al., 2016; Mudd et al., 2018; Shelef et al., 2018) that quantify both the uncertainties in θ and the degree to which changes from the most likely value of θ affect the overall disorder of the channel network. Because determination of normalized channel steepness index k_{sn} requires the assignment of a reference value of θ, these metrics can give the user insight into the degree to which each basin is likely distorted by a θ value that differs from its most likely value in a particular basin.

We go on to explore variation in most likely θ values across numerous catchments using the disorder metric. This mirrors earlier studies which aimed to constrain θ using S–A methods (Tucker and Whipple, 2002). Our results indicate that θ values have a central tendency of 0.425 similar to that suggested

previously from S–A analysis (e.g., Whipple et al., 2013, and references therein). The first and third quartiles across 5033 basins are 0.225 and 0.575. Given this range, we suggest authors should never assume a reference value of θ without testing for the most likely values.

As fixing a reference θ will result in calculating k_{sn} using a θ value that is not the most likely value for each basin, we assessed, both analytically and numerically, the extent to which selection of θ distorts k_{sn}. When comparing values from different points in the channel network, the contrast in drainage area and $|\Delta\theta|$ controls the magnitude of the distortion, which can reach several order of magnitudes. We demonstrate that changing θ can change the spatial distribution of k_{sn}, leading to the risk of misinterpretation of uplift or erosion signals. We also find that existing contrasts between areas of high and low k_{sn} can be inverted or erased. On the other hand, local adjacent contrasts are are not affected if no tributary junction separate them, meaning that detection of knickpoints is unlikely to be affected by changing θ.

We have not explored strategies to circumvent spatially varying θ in k_{sn} studies, but can speculate on possible approaches based on our analyses of the spatial variance of θ across a wide range of landscapes. One approach would be to non-dimentionalize k_{sn} using, for example, a statistical representation of its distribution. Another approach, if one is studying a large enough landscape, is to compare populations of basins that share the same most likely value of θ. Finally, one could simply reject analysis of basins with outlying most likely θ values.

We also investigated how χ values evaluated across divides are affected by changes in θ. Differences in the χ coordinate have been used as a proxy for drainage divide migration (e.g. Willett et al., 2014), so if the difference in χ across the divide is affected by changes to θ there is a risk of misinterpreting the presence or absence of divide migration. We first explored simple analytical solution of χ distortion across a divide and found that basins with lower values of θ were more sensitive to χ distortion. One key control is the length to base level of basins on either side of the divide. We find that for lower values of θ, longer basins will have increasing χ values, so reductions in θ will can result in longer basins being

spuriously interpreted as "victims" catchments using the nomenclature of (Willett et al., 2014). Applications on real landscapes suggested that at spatially constant θ, the basins interpreted as aggressors were rarely inverted across drainage divides, but the magnitude of the χ offset varied by, in some cases, a factor of 3 with large changes in θ. It implies that can be extremely challenging to ensure relevant χ comparisons across divides in locations with spatially varying θ.

Chapter 5

Tectonics from topography in lithologically ambiguous landscape

The work presented in this chapter is to be submitted in JGR-Earth Surface in collaboration with Sinclair H.D., Mudd S.M., Graf E.L.S. and Maţenco L.C . This research was conducted in collaboration with the named co-authors, who helped to edit the manuscript. I wrote the topographic analysis algorithms, performed the analyses, created the figures, and wrote the manuscript. The co-authors edited the final manuscripts and figures.

Abstract

Fluvial morphology is affected by a wide range of forcing factors, which can be external, such as faulting and changes in climate, or internal, such as variations in rock hardness or degree of fracturing. When both types of forcing occur coevally, or in the same location, it presents a challenge to isolate for one of them. Failure to account for both factors lead to misinterpretation, such as where steepening of a channel network due to lithologic contrast could be misinterpreted as a function of increased tectonic displacements. These misinterpretations are enhanced over large areas, where landscape properties needed to calculate channel steepness (*e.g.* channel concavity) can vary significantly in space. In this study we investigate the relative channel steepness over the Eastern Carpathians where it has been proposed that ongoing, syn-orogenic rock uplift in the Southeastern Carpathians part gives way N- and NW-wards to ca. 8 Myrs of post-orogenic quiescence. We develop a technique to quantify relative channel steepness based on a wide range of concavities, and show that the main signal shows an increase in channel steepness from east to west across the range. Rock hardness measurements suggest this difference is driven by lithology. When we isolate channel steepness by lithology to test for ongoing rock uplift along the range, we find steeper channels in the south of the study area along tectonic units of the frontal ranges. This supports interpretations from longer timescale geological data that active rock uplift is fastest in the southern Southeastern Carpathians, and indicates that this is dominantly a characteristic of the frontal portions of the thrust wedge.

5.1 Introduction

Surface topography in upland landscapes and their surroundings is shaped by the competition between climatic and tectonic processes (e.g., Avouac and Burov, 1996b; Beaumont et al., 1992; Whipple, 2009; Willett, 1999). Tectonically induced surface motions can both build topography (e.g. mountain ranges by stacking tectonic units at convergent boundaries between plates) and create accommodation space in foreland basins that are filled with erosional products

(e.g., Sinclair, 2012). Surface processes, mainly driven by climatic forcing, will naturally tend toward equilibrating the mass surplus and deficits *via* erosion, transport and deposition of sediment (e.g., Allen, 2017; Matenco et al., 2013; Sinclair et al., 1991; Tucker and Beek, 2013). In theory, this competing system tends to make landscapes evolve towards a steady-state where surface motions are balanced by erosion and deposition (e.g., Hack, 1960; Penck, 1953; Willett and Brandon, 2002a). When perturbed, these landscapes will move away from steady state forms, and geomorphologists have been developing methods to unravel the occurrence, magnitude and timing of tectonic activity using the shape of the landscape (e.g., Arrowsmith et al., 1998; Hurst et al., 2013; Kirby and Whipple, 2012; Lapparent and Lapparent, 1896; Mudd, 2017; Tapponnier and Molnar, 1977; Zielke et al., 2010).

Studies aiming to link topography with tectonics have focused on the main erosive engine of non-glaciated landscapes: the river system (e.g., Ahnert, 1970; Goren, 2016; Hack, 1960; Kirby and Whipple, 2012; Schoenbohm et al., 2004; Seagren and Schoenbohm, 2019; Willett et al., 2014). Amongst quantitative tools developed to describe fluvial morphology, channel steepness or its normalised equivalent integrating discharge has been perhaps most widely used. With the reasonable assumption that surface motions directly alter the gradient of channel networks, the contrasts in steepness have been interpreted as direct (steepening at fault contact) or indirect (transient migration of steepening) signs of tectonic activity (e.g., Kirby and Whipple, 2012). However, a variety of different forcings can affect channel steepness resulting in similar morphological expressions; lithology being a key factor. Where softer rocks give way downstream to harder rocks, a steadily eroding channel will steepen (e.g., Bernard et al., 2019; Forte et al., 2016; Perne et al., 2017; Yanites et al., 2017). Critically, fault displacements commonly juxtapose different rock types resulting in uncertainty about whether different channel steepnesses on either side of a fault are a function of different uplift rates, rock strength, or both. This common feature of geologically heterogeneous landscapes generates mixed signals in the river network, resulting in ambiguity in interpreting the main forcing controlling the steepening (e.g. Strong

et al., 2019).

Here, we attempt to isolate the different forcings affecting channel steepness where both tectonic activity and lithology play a role. We initially focus on the Romanian Carpathians, where extracting the spatial distribution of active tectonic motions from river profiles is confounded by lithologic contrasts. We use a combination of (i) topographic analysis to extract channel steepness from Digital Elevation Models (DEMs) and (ii) field observations and measurements to constrain rock strengths for the main lithologies. We then trace lithological units laterally from regions where active tectonics are thought to play a role, northward to where the range has been inactive for several millions of years. Through this exercise, we isolate the signal of active rock uplift on the river profiles from the role of lithology, and hence test tectonic models for the region.

5.2 Theoretical background

5.2.1 Fluvial geomorphometry

Scaling between channel steepness and discharge, or its proxy drainage area, has been qualitatively suggested and observed for over a century: "In general we may say that, if all else is equal, declivity bears an inverse relation to quantity of water" (p. 114 of Gilbert (1877)). In the mid-1950s,Hack (1957) and Morisawa (1962) quantified that observation, describing a systematic relationship between drainage area and channel gradient. These studies led to the formulation by Morisawa (1962) and later Flint (1974) of a power law describing the commonly observed decrease of channel gradient with increasing drainage area:

$$S = k_s A^{-\theta} \tag{5.1}$$

where S is the river gradient ($S = \frac{dz}{dx}$ where z is the elevation and x the distance along the channel); k_s the steepness index and represents the overall gradient of a river system, a single river or one of its reaches; A the drainage area; and θ the concavity index dictating the rate at which channel gradient declines downstream.

In order to compare different rivers over one or several networks, θ is commonly fixed to a reference value, frequently denoted θ_{ref}, in order to extract comparable steepness index values (*i.e.* normalised to the same value of the concavity index). k_s is then referred as k_{sn}, the normalised channel steepness.

Calculating k_s (or k_{sn}) and determining θ (or θ_{ref}) has been traditionally done by applying linear regressions of $log(S) - log(A)$ plots, where the gradient is $-\theta$ and the intercept k_s (e.g. Flint, 1974; Kirby and Whipple, 2012; Wobus et al., 2006a). However, slope-area plots suffer from significant limitations, mainly linked to the inherently noisy nature of channel gradient derived from DEMs (e.g. Perron and Royden, 2013). It requires the use of averaging methods, ensuing inexorable data-loss, to exploit the data (e.g. binning by drainage area and averaging the slope). An alternative method has been developed to mitigate the effects of topographic noise and binning of drainage area(Perron and Royden, 2013; Royden et al., 2000). It consists in integrating Eq.5.1 over the distance of the channel :

$$z(x) = z(x_b) + \left(\frac{k_s}{A_0^\theta}\right) \int_{x_b}^{x} \left(\frac{A_0}{A(x)}\right)^\theta dx \tag{5.2}$$

where x_b is the local base-level chosen for the analysis (e.g. a basin outlet or fixed elevation (Forte and Whipple, 2018)) and A_0, a reference drainage area, which is introduced to non-dimensionalize drainage area. From this equation, Royden et al. (2000) defined a longitudinal coordinate χ as:

$$\chi = \int_{x_b}^{x} \left(\frac{A_0}{A(x)}\right)^\theta dx \tag{5.3}$$

Any point of the channel can be defined using χ such as:

$$z(x) = z(x_b) + \left(\frac{k_s}{A_0^\theta}\right) \chi \tag{5.4}$$

The χ approach normalises the river profile to a θ_{ref} and provides an alternative method to explore S-A relationships. If A_0 is set to a value of unity in Equation 5.3, then the gradient of χ–elevation is equal to k_s (e.g. Perron and Royden, 2013). χ has been widely used in various geomorphological studies linking

channel morphology to surface processes, to investigate the evolution of drainage divides (e.g Forte and Whipple, 2018; Giachetta and Willett, 2018a; Seagren and Schoenbohm, 2019; Willett et al., 2014) or derive topographic metrics to describe river networks (e.g. Gailleton et al., 2019; Hergarten et al., 2016; Wang et al., 2017).

5.2.2 Channel steepness, tectonics and lithology

k_s has been widely used as a proxy for geomorphological processes: compilations of detrital cosmogenic nuclide concentrations (e.g. ^{10}Be), used to quantify average erosion rates for a given river catchment area (e.g. Biermann and Steig, 1996; Lal, 1991), have demonstrated a direct positive correlation between erosion rate and k_s (e.g Codilean et al., 2018; DiBiase et al., 2010; Harel et al., 2016; Kirby and Whipple, 2012; Mandal et al., 2015; Scherler et al., 2014). This is a direct quantification of early hypotheses that steeper channels should tend to erode more rapidly (e.g. Gilbert, 1877; Lapparent and Lapparent, 1896). Changes in erosion rates can result from tectonic or climatic forcings, enabling the use of k_s to study tectonic or climatic evolution over large areas.

In tectonically active landscapes, changes in k_s have been interpreted as a direct proxy for differential tectonic activity. Wobus et al. (2006b) linked a sharp increase in channel steepness of the Marsyandi River as it crossed the region of the Main Central Thrust of the central Himalaya with a rock uplift signal linked to the structure using other proxies of erosion rates to support this hypothesis. This relationship between rock uplift and k_s has been thoroughly explored in a range of settings (e.g. Lavé and Avouac, 2001; Seagren and Schoenbohm, 2019; Wobus et al., 2006a). Previous studies using both topographic data (e.g. Kirby and Whipple, 2012) and numerical models (e.g. Eizenhöfer et al., 2019) have highlighted potential explanations for large breaks in channel steepness. In both these studies, concentrated relative uplift could be caused by deep structures (e.g., midcrustal ramps) under the mountain belt. k_s has also been interpreted as an indirect expression of base-level change resulting from tectonics (e.g. Hurst et al., 2019; Ouimet et al., 2009; Royden and Taylor Perron, 2013; Steer et al.,

2019; Wobus et al., 2006a) or climate (Crosby and Whipple, 2006; Neely et al., 2017) driven, where steepened high k_s patches migrate upstream. Recent studies (e.g. Giachetta and Willett, 2018a; Seagren and Schoenbohm, 2019) have also highlighted the effect of stream piracy on k_s, where captured areas disrupt the upstream drainage area and sediment supply balance, affecting the downstream channel steepness.

As tectonics, climate and stream piracy can affect channel steepness by inducing external forcings to the river channels, intrinsic forcings (*e.g.* fractures, weathering, lithology) will also affect k_s. Amongst these intrinsic forcings, the effect of differential lithology on fluvial morphology has been a recent focus in geomorphological studies (e.g. Bernard et al., 2019; Bezerra and Peifer Bezerra, 2018; Campforts et al., 2019; Forte et al., 2016; Kirby et al., 2003; Seagren and Schoenbohm, 2019; Strong et al., 2019; Thaler and Covington, 2016; Yanites et al., 2017). Rivers flowing over harder rocks tend to have steeper channels and affect the overall landscape morphology (e.g Forte et al., 2016; Tucker and Slingerland, 1996; Yanites et al., 2017). This effect is linked to the sole fact that harder lithologies are more difficult to erode, forcing the channel to steepen to maintain a constant erosion rate. Studies of entire mountain ranges (e.g. Bernard et al., 2019; Duvall, 2004; Gabet, 2019) have demonstrated the important effect of lithology on channel steepness in syn to post-orogenic settings, with a positive correlation between k_{sn} and rock strength appearing to be the controlling forcing on landscape morphology in non-glaciated areas. Careful acknowledgement of lithological heterogeneities still permits the interpretation of climatic and tectonic signals from river morphology (e.g Campforts et al., 2019; Kirby et al., 2003), but can also confuse the signal (e.g. Strong et al., 2019) and potentially lead to misinterpretation. In this study, we focus on cases where contrasts in the erodibility of rock are co-located with contrasts in rock uplift. In that case, the origin of channel steepening remains difficult to interpret.

5.3 The orogenic and geomorphological evolution of the Eastern and Southeastern Carpathians

The Carpathians are an arcuate mountain range located in the eastern continuation of the Alpine orogenic belt (Fig. 5.1). Previous studies have shown that the overall Carpathian structure formed in response to the Triassic to Tertiary opening and closure of two oceanic realms by subduction and continental collision (details in Csontos and Vörös, 2004; Mațenco and Matenco, 2017; Sandulescu, 1988; Schmid et al., 2019). In a plate tectonics scenario, the studied area of the Eastern and Southeastern Carpathians is made up by two basement-bearing continental mega-units in an upper plate position, the European (*sensu largo*) continental foreland in a lower plate position, and a thin-skinned thrust and fold belt deformed at or near their subduction contact (Figs. 5.1 and 5.2). The European foreland is furthermore overlain by a foredeep that locally reaches 13 km in the area of the Focsani Basin (Fig. 5.2, Tarapoanca et al., 2003).

5.3.1 Tectonic evolution

The Middle Jurassic opening of the Alpine Tethys was followed by the Cretaceous - Miocene closure of its Pienides-Magura and Ceahlău-Severin branches (Fig. 5.1, Plasienka, 2018; Sandulescu, 1988; Schmid et al., 2008). The closure scraped off sediments deposited over the subducting ocean and its eastern passive continental margin by forming a thin-skinned system of thrust sheets, grouped in nappes emplaced in a foreland-breaking sequence from the Cretaceous (Ceahlău), late Oligocene – early Miocene (Convolute Flysch, Audia/Macla), middle Miocene (Tarcau, Marginal Folds), to late middle Miocene – early late Miocene (Subcarpathian) times (Figs. 5.1 and 5.2). The thin-skinned deformation took place until around 9-8 Ma when the main crustal subduction zone was locked by the continental collision (Schmid et al. 2008 and references therein, Mațenco and Matenco 2017). Low temperature thermochronology studies, primarily apatite fission tracks and apatite U-Th/He, have shown that the thin-skinned accretion was associated with gradual exhumation. Exhumation of up to 6 km took place

at average rates of below 1 mm/yr and peaked between 13 and 8 Ma during the Miocene collision (Gröger et al., 2008; Merten et al., 2010; Necea, 2010; Sanders et al., 1999). The exhumation was spatially distributed throughout the thin-skinned nappes with higher values in their centre (around the Tarcau and Marginal Folds nappes in Fig. 5.2). Similar exhumation rates were also interpreted in the northern part of the Eastern Carpathians during two periods of exhumation, one more rapid between 12 and 5 Ma and another after 5 Ma. In this area, the exhumation history is interpreted to be driven by the erosion of a thickened wedge after the cessation of shortening at 12-11 Ma, associated either with slab break-off or with the end of subduction (Andreucci et al., 2015).

While tectonic activity remained minor elsewhere, a further deformation episode took place after 8 Ma in the area of the Southeastern Carpathians. The formation of high-angle thick-skinned reverse faults truncating both the basement and the overlying thin-skinned thrust belt at depth, and created a crustal root located beneath the external parts of the thrust belt (Fig. 5.2) was proven by seismic, gravity and magnetic studies (e.g. Bocin et al., 2005, 2009; Hauser et al., 2007). This deformation was associated with gradually accelerating exhumation at values between 1.5 - 5 mm/yr in the external part of the orogenic wedge, located above the thick-skinned reverse faults (Merten et al., 2010; Necea, 2010). This presently active deformation was also coeval with subsidence in the foreland at values of 1-3 mm/yr, which created the overall synclinal geometry of the Focsani Basin (Fig. 5.2, Leever et al., 2006; Matenco et al., 2007; Tarapoanca et al., 2003). It was also coeval with smaller amounts of subsidence in the order of hundreds of meters, creating the shallow Braşov and Tg. Secuiesc intramontane basins, which covered most of the internal part of the orogenic wedge and its Dacia basement (Fig. 5.1). These differential vertical motions are thought to be related to an asthenospheric circuit driven by the sinking Vrancea slab, still (barely) attached to the overlying lithosphere in the final stages of slab detachment (Ismail-Zadeh et al., 2012; Martin and Wenzel, 2006; Matenco et al., 2016). The post-8 Ma tectonic structures of the Southeastern Carpathians, deformation along thick skinned reverse faults and the larger underlying mantle circuit, are presently active, as demonstrated

by the large intermediate mantle (70 - 220 km) seismicity of the Vrancea slab, the moderate seismicity of the overlying crust (Bocin et al., 2009; Ismail-Zadeh et al., 2012; Oncescu and Bonjer, 1997; Radulian et al., 2000), and GPS movements reaching up to 7 mm/yr (Hoeven et al., 2005; Schmitt et al., 2007), together with interpretations from studies of the mantle structure, anisotropy and attenuation (Bokelmann and Rodler, 2014; Ivan, 2007; Martin and Wenzel, 2006; Popa et al., 2008; Popa et al., 2005; Russo et al., 2005).

5.3.2 Lithology and geomorphology

The Eastern and Southeastern Carpathians show a large diversity of mostly clastic, but also carbonatic lithologies across the orogenic strike, which maintains a remarkable continuity in the same tectonic units over hundreds of kilometers along its strike. The Cretaceous - Paleogene sedimentation is generally dominated by a deep-water mixture between pelagic and dominantly turbiditic ("flysch") sedimentation, with shallower shelf to alluvial coarse sediments deposited in forearc basins over the accretionary wedge during peak tectonic moments (such as the Albian Ceahlău conglomerates), well described in numerous regional or local studies (e.g. Belayouni et al., 2009; Melinte-Dobrinescu et al., 2008; Miclaus et al., 2009; Olariu et al., 2014; Roban et al., 2017; Sandulescu et al., 1981a,b). A gradual transition towards a regressive basin fill ("molasse") and coarser deposition took place during the Miocene continental collision in the more external Marginal Folds and Subcarpathian nappes, while the foredeep contains a middle Miocene - Pleistocene transition from shallow water marine and lacustrine sedimentation dominated by an orbitally-forced cyclicity to a deltaic and alluvial continental sedimentation (e.g. Jipa and Olariu, 2013; Sandulescu et al., 1981a; Stoica et al., 2013; Vasiliev et al., 2004).

Geomorphological studies available in the Eastern and Southeastern Carpathians (Radoane et al. (2017) and references therein) are in general agreement with the tectonic scenario described above. These studies have inferred that the Eastern Carpathians have a general topography that mirrors the decay of an older (Miocene) orogenic buildup, with longitudinal river profiles trending towards an

equilibrium and sediments generated dominantly by river channel erosion. In contrast, the Southeastern Carpathians have a young and actively changing topography, shown by a significant disequilibrium in longitudinal river profiles, sediments generated dominantly by recycling landslides, rapid uplift observed in geomorphic makers such as terraces, migration of knickpoints, water divides, and possible piracy events derived from chi profiles (see also Balteanu et al., 2010; Borgh, 2013b; Cristea, 2015; Cristea, 2014; Leever, 2007; Necea et al., 2013; Necea et al., 2005; Radoane et al., 2003). These studies also suggested that recent tectonics may have shifted the presently observed main water divide separating rivers draining to the European foreland from the ones draining to the Transylvanian hinterland and the middle of the thin-skinned wedge in the central part of Southeastern Carpathians (compare maps in Fig. 5.1). Furthermore, the tectonic-induced differential vertical movements may have triggered a general drainage re-organization with rivers being deflected towards the center of the Focsani Basin (Fielitz and Seghedi 2005 and references therein). While all these indications point towards a differentiation in the Eastern and Southeastern Carpathians between the erosion of an older tectonic relief and a topography controlled by active tectonics, respectively, the mechanisms responsible for the significant variability observed locally are less understood. For instance, structural and geomorphological studies have suggested that the Pleistocene to recent uplift of the Southeastern Carpathians has migrated eastwards through time towards the Focsani Basin (Fig. 5.2, Molin et al., 2012; Necea et al., 2013; Necea et al., 2005), qualitatively interpreted as an effect of the Vrancea slab steepening and retreat in the same direction (e.g. Matenco et al., 2007). On this first order pattern, the locally observed influence of lithological strength contrasts on the surface morphology and heterogeneities in normalized channel steepness (Cristea, 2015; Radoane et al., 2017) still has to be quantified.

In summary, all previous studies have suggested that the fluvial morphology is controlled by regional and local tectonics modulated by lithological variations. We build on these studies by applying our fluvial geomorphometry and channel steepness analysis at the scale of the entire Eastern and Southeastern Carpathians

for rivers draining into the European hinterland. Furthermore, we avoid using a single reference concavity that impacts the channel steepness calculations. We delimit the area into three regions controlled by different base levels (Fig. 5.1): (i) the Focsani Basin area, which aggregates rivers draining into the Southeastern Carpathians foreland basin, (ii) the Siret base level, aggregating rivers into the foreland basin along the entire chain, and (iii) the Prut base lexvel and the associated drainage system, which is used as a reference area located far into the European foreland that is not directly linked with Carpathians mountain building processes. Our analysis specifically excludes the southern-most termination of the Southeastern Carpathians (the Ialomita catchment) with a Danube river base level (Fig. 5.1), which is affected by significant strike-slip to transpressive deformation and recent salt diapirism (Matenco and Bertotti, 2000). In the same area, our analysis also excludes the comparatively smaller internal part of the orogenic wedge that drains into the Transylvanian hinterland.

5.4 Methods

5.4.1 Digital Elevation Model, preprocessing and river network

We use the publicly available ALOS World 3D 30 (AW3D30) meter resolution topographic dataset for the study (Tadono et al., 2016). It has been shown to better capture accurate channel elevations than 30m SRTM data and in some cases 12 m TanDEM-X topographic data (Boulton and Stokes, 2018; Schwanghart and Scherler, 2017).

The raw DEM has some internal depressions, which spuriously stop flow routing in the DEM and therefore break the drainage area accumulation. Different solutions to filling such depressions exist, but we chose to use a carving algorithm (Lindsay, 2016). Filling algorithms tend to affect an area upstream of numerical dams or depressions, and we wish to minimize the number of pixels affected by pre-processing.

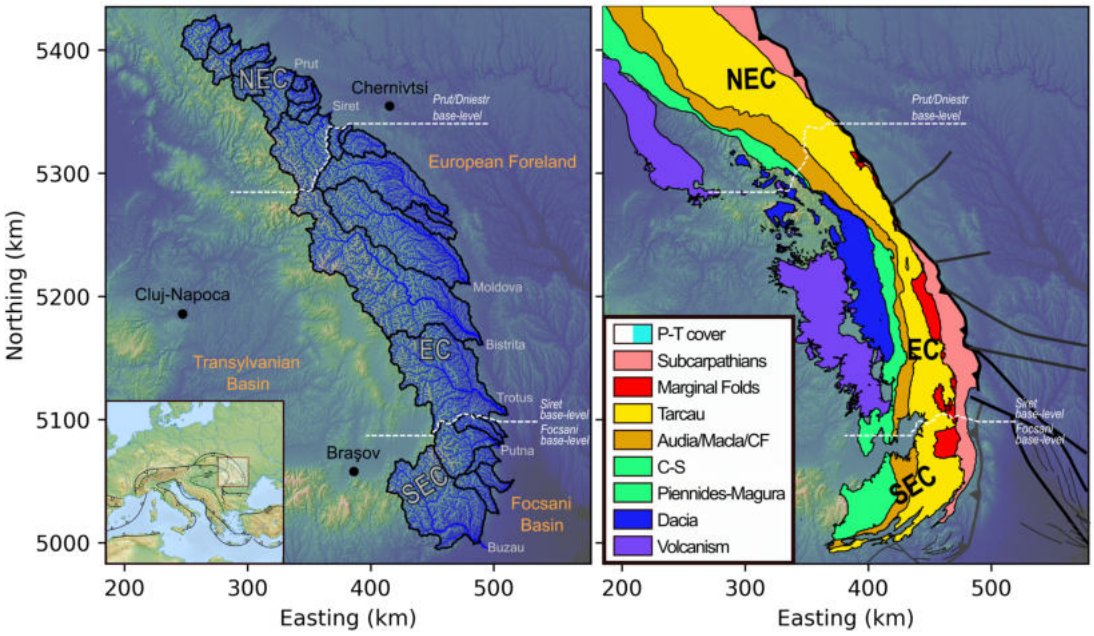

Figure 5.1: Location of the extracted channel network and the tectonic units in the Eastern and Southeastern Carpathians (Adapted from Andreucci et al. (2015) and Mațenco and Matenco (2017)). Note the different references used for Prut/Dniestr, Siret and Focsnani base-levels. EC = Eastern Carpathians, SEC = South-Eastern Carpathians, NEC = North-Eastern Carpathians, P-T = Post-Tectonic cover (*sensu* post Late Miocene Collision), CF = Convolute Flyshes and C-S = Ceahlău-Severin. Note the P-T cover is not displayed on that figure for clarity purposes. The main frontal thrust is displayed in black where reaching the surface and grey where buried below the sediments of the Focsani basin. Inset showing location of map in the context of the European tectonic system is adapted from Matenco et al., 2016.

A preliminary step is however required as AW3D30 contains a small number of pit artifacts. These can be tens of meters deep and based on inspection of satellite imagery appear to be correlated with reflective surfaces (the AW3D30 dataset is generated from multispectral imagery). Although their area is small enough to not significantly affect the river extraction, they affect the carving algorithm by forcing unrealistic trenches to drain them. We therefore use a localised filling algorithm on these pits prior to the carving to minimise DEM corrections while ensuring realistic flow routing. Details about the process are available in the supplementary materials.

Drainage area and flow direction is extracted using a D8 algorithm (O'Callaghan and Mark, 1984) and we extract the channel network using a drainage area threshold of 450000 m^2 for all the drainage basins draining to topographic mountain

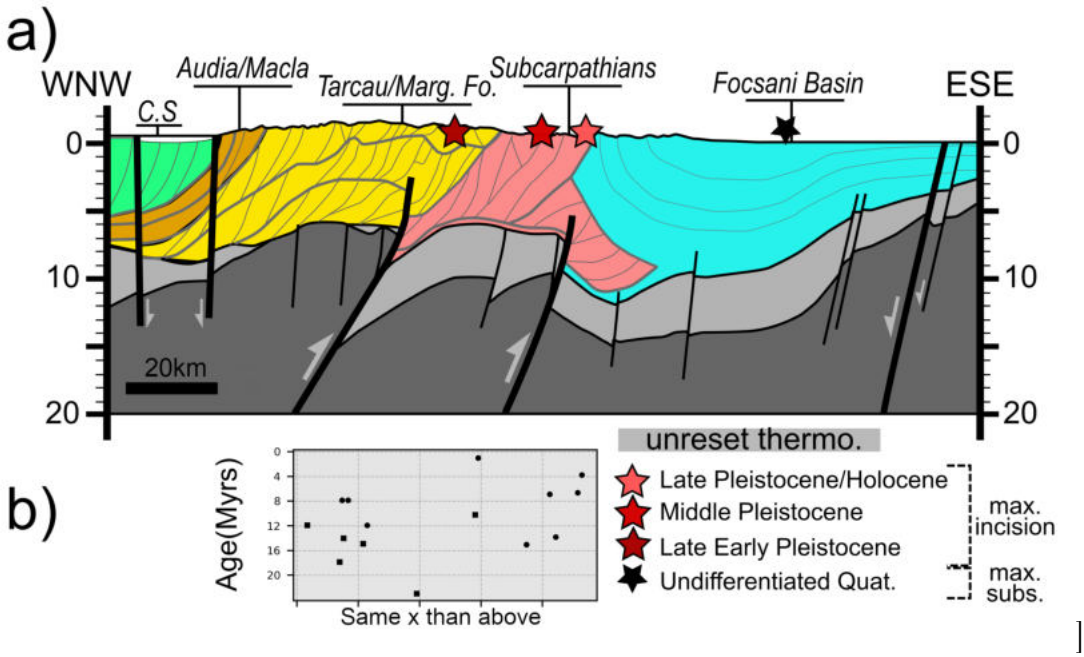

Figure 5.2: a) Cumulative rates of vertical motion in Pleistocene to Holocene time, from Necea et al. (2013), confirmed by present-day GPS vertical motions from Hoeven et al. (2005). b) Sketch of simplified cross-section across the South-East Carpathians, modified from Matenco et al. (2013). Only the fault motions playing a role during Quaternary time are displayed. Note the potentially reactivated thick-skinned fault. c) Apatite Helium thermochronometres ages from Necea (2010). Note that a) b) and c) share the same x axis as distance along the cross-section.

front in the study area (Romanian South-Eastern and Eastern Carpathians).

5.4.2 k_{sn} extraction

As demonstrated in Section 5.2.1, k_{sn} can be represented as gradient of χ-elevation profiles. To calculate these, we must first make some decisions about how to calculate the χ coordinate: the choice of base level (x_b), reference drainage area (A_0) and the reference concavity of the overall river network (θ_{ref}). We set $A_0 = 1$ so that the gradient in χ–elevation space is equal to k_{sn}. As demonstrated by Forte and Whipple (2018), the choice of base level affects the value of χ, but not its gradient. We therefore arbitrarily fix the base levels at the mountain front draining the eastern foreland basins.

k_{sn} and River concavity

We take particular care when selecting the concavity index, as only k_{sn} values extracted with a same reference concavity (θ_{ref}) can be relevantly compared. Following Niemann et al. (2001) and Wobus et al. (2006c), Mudd et al. (2018) developed theory to show that if the correct concavity index is selected, tributaries and the main stem channel should be co-linear, even in transient landscapes. We use a set of algorithms described in Mudd et al. (2018) and Hergarten et al. (2016) aiming to maximise the co-linearity of χ-elevation space for each watershed, which is then selected as the most likely value of θ_{ref} for that watershed. Uncertainty around that best-fit is also calculated by calculating best fit for subsets of connected rivers within each watersheds (Mudd et al., 2018).

Segmentation of χ-Elevation profiles

Once θ_{ref} has been determined, k_{sn} can be calculated using the gradient of elevation as a function of χ. Direct, pixel-by-pixel, determination of k_{sn} is sensitive to inherent DEM noise and would require the use of some form of post-processing (e.g., a moving average window) to exploit the results. Such a method would smooth over discontinuities such as knickpoints. Instead use the algorithm described in Mudd et al. (2014), which uses a statistical method to select the most likely combination of linear segments in χ–elevation: these linear segments are predicted by the theoretical work of (Royden and Taylor Perron, 2013).

The Mudd et al. (2014) algorithm first selects a user-defined number of adjacent river nodes, referred as n_{tg}. The algorithm calculates all the combinations of segments composed of a minimum amount of nodes and calculates best-fit metrics for each combination of segments. A good fit to the data is balanced against too high a number of segments (e.g., over fitting) using the Aikake Information Criterion (Akaike, 1974). Each segment describes a section of river profile as:

$$z_{seg} = M_\chi * \chi + b_\chi \tag{5.5}$$

where $M_\chi = k_{sn}$ if χ has been calculated with $A_0 = 1$ and b_χ represent the

intercept of each segment. To make sure that small-scale noise does not affect the results, this algorithm repeats this segmentation a user-defined amount of time following a Monte Carlo scheme where n_{sk} nodes are skipped in average at each iteration. k_{sn} values for each node is the mean value of all the segment slopes having involved it.

Calculating k_{sn} with the Mudd et al. (2014) algorithm relies on a certain number of subjective user-defined parameters. Some can be determined via other means, like the choice of A_0 and θ_{ref} addressed in section 5.4.2, but others need to be carefully justified as their choice will affect the segmentation process. The size of the segments is a particularly important factor to consider: it will determine the scale represented by k_{sn} variations extracted with that algorithm. The size is determined by the number of nodes targeted by each algorithm iteration (n_{tg}) and the number of nodes skipped at each Monte Carlo iteration (n_{sk}). Higher values for these parameters will tend to generate larger segments and therefore averaging longer river reaches whereas smaller values will generate smaller segments representing small-scale features. Detailed effect of varying these parameters have been explored in Gailleton et al. (2019).

Relative steepness index

As demonstrated in the previous sections, calculating k_{sn} depends on a number of parameters which affect (i) the absolute value of k_{sn} and (ii) the scale it represents via the relative size of segments in the profiles. Two populations of k_{sn}, for example from different watersheds, are directly comparable only if the metric has been calculated with the same parameters (e.g. Hurst et al., 2019; Kirby and Whipple, 2012).

Different values of θ, for example, will generate different orders of magnitude of k_{sn}. Large areas such as entire mountain ranges, will naturally have spatial variation in concavity and concavity indices (e.g. Chen et al., 2019; Seagren and Schoenbohm, 2019). In this study, we propose to circumvent this limitation by (i) calculating k_{sn} for a wide range of parameters in order to represent as many processes as possible and (ii) comparing cross-parameter results with a relative

steepness index.

To calculate a relative channel steepness index, we use a statistical metric called the modified z-score (Crosby et al., 1994), which we denote with M_i. M_i represents the statistical distribution of a population and allows us to quantify how it varies in space. The modified z-score is a nonparametric version of the z-score and suits our dataset better as k_{sn} values are not expected to be normally distributed, particularly in a transient environment.

In this study, a population is defined by all the comparable values of k_{sn} calculated with the same parameters, namely n_{tg}, n_{sk} and θ_{ref}, and is calculated as follows:

$$M_{i,j} = \frac{0.6745 * (k_{sn,i,j} - \tilde{k}_{sn,j})}{MAD_j} \tag{5.6}$$

where $M_{i,j}$ is the modified z-score for pixel i and parameter value combination j, note that the constant is part of the original formulation of the tool (Crosby et al., 1994). Each pixel has a channel steepness index for a given parameter combination $k_{sn,i,j}$. In addition, for each parameter combination we calculate the median channel steepness index, $\tilde{k}_{sn,j}$ and the median absolute deviation (MAD) for that parameter combination MAD_j:

$$MAD_j = median(|k_{sn,i,j} - \tilde{k}_{sn,j}|) \tag{5.7}$$

$M_{i,j}$ quantifies the absolute values of each population in regards to its median. $M_{ik_{sn}} = 0$ equals to the median and higher and lower values denote respectively higher and lower samples compare to the overall population. This method, which is traditionally widely used to detect outliers in large datasets (e.g. Giustacchini et al., 2017). Because all values of $M_{i,j}$ are normalized to the median values and median absolute deviations of each parameter value combination, we can use these to compare relative channel steepness amongst k_{sn} data with different parameter values. We therefore refer to the $M_{i,j}$ data as the "relative channel steepness" in all our figures, with values greater than 0 representing parts of the channel network that have steepness greater than the median, and values less than zero

representing parts of the channel network that are gentler than the median k_{sn} values.

5.4.3 Rock strength

We apply a semi-qualitative approach to estimate rock strength. First, the extent of the tecto-lithologic units is estimated using the compilation of 1:50,000, 1:200,000 and 1:500,000 geological maps (published by the Geological Institute of Romania), Matenco et al. (2010) and Matenco and Matenco (2017). The Ukrainian section of the map has been completed and extrapolated using the extent of tectonic units in Andreucci et al. (2015), with some spatial approximations and unit grouping match nomenclature in the different datasets. We also acknowledge that lithostratigraphic variation can occur within the each tectonic unit, and we take account of potential internal major changes using (e.g. Matenco and Bertotti, 2000) which compile local stratigraphic information (e.g. Joja et al., 1968; Sandulescu, 1984). The chosen grouping allows to (i) follow the continuous northward evolution of channel steepness along similar units, and (ii) encompass large-scale signals.

We then measure the uniaxial compressive strength of the rock through the study area. Schmidt hammer measurements are carried out in the field on rock outcrops, where we focused on fresh rock surfaces. The Schmidt hammer, type N in this study, records a "rebound value" between 10 and 100 where higher values denote high elastic strength of the rock. We also record the outcrops where the rock was too soft to be tested, *i.e.* where the Schmidt hammer did not encountered enough resistance from the rock to return a measurement. The rebound value can be converted to compressive strength using a chart provided and calibrated with the equipment used on field.

Each measurement point consists of 30 to 50 Schmidt hammer impacts on a same spot and the median value is gathered. Several points are tested per outcrop in order to (i) ensure the consistency of the method and (ii) check local variability in potential heterogeneity in the fracture network or weathering intensity.

5.5 Results

5.5.1 Rock strength

We collected a total of 347 rock strength measurements across the tectonic units in the SEC. The results are quantified using two different metrics: (i) the rebound values (medians and quartiles for each tectonic units excluding the non-responsive data points) and (ii) the proportion of non-responsive measurements for each tectonic units (Figure 5.3).

Rock strength measurements show a wide range of rock strength values. The range in values reflect the stratified nature of the lithologic units where softer rocks are interbedded with harder rocks. However, the data does suggest a trend: two different groups of lithologic units behave differently. The first group include the CS, Audia, Macla, Tarcau and Marginal Folds units which show higher rebound values and fewer measurements resulting in a non-response from the Schmidt hammer as a proportion of the total measurements. The second group includes the two frontal units, the Subcarpathians and the Focsani Basin, with lower rebound values and higher proportions of non-responsive measurements.

These results are consistent with qualitative field observations. The first group shows more resistant lithofacies and crops out more frequently in the landscape than the second, which show less, thinner and sparser resistant layers.

5.5.2 Concavity index

Ranges of most likely θ_{ref} values for all the basins outlined in Figure 5.1 are shown in Figure 5.4 by (i) northing position in the horizontal axis, as rough proxy for tectonic activity in the Romanian Carpathians (see section 5.3) and (ii) the median and quartiles of the most likely values on the vertical axis.

The results show several trends. We find across all studied basins that the concavity indices have a median of 0.35 ± 0.10 (red square in Figure 5.4) for our study area. In the Southeastern Carpathians (basins with northing values ranging from 5000 to 5100 km, see fig. 5.1), the range of values is narrower than in the

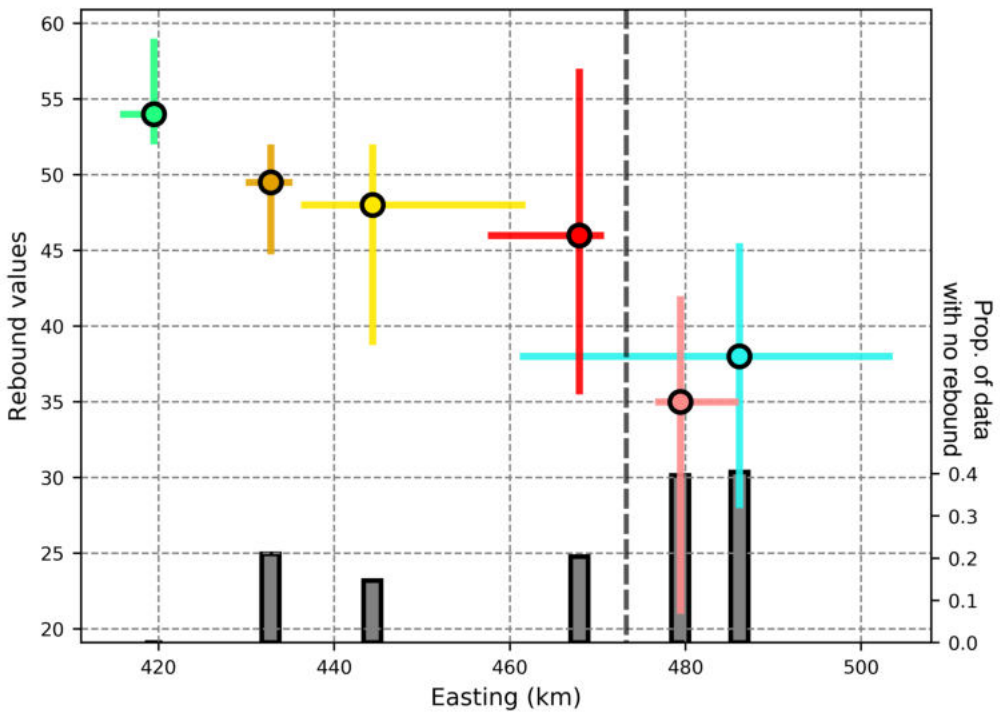

Figure 5.3: Schmidt hammer rebound values summarising the measurements across the Romanian Carpathians. The color of data points correspond to the tectonic units on the location map (Fig.5.1). The data points represents the median rebounds values, and the error bar the first and third quartiles. The proportion of non-responsive point is also displayed, as an indirect proxy for the proportion of weak rocks within each units.

Eastern Carpathians (basins with northing values greater than 5100 km). The smaller basins within the South-Eastern Carpathians, mainly draining the frontal units (Focsani Basin), tend to show higher concavity indexes than larger basins. Concavity indices in the Eastern Carpathians are more heterogeneous than in other parts of the study area. On the basis of these data, we chose the range 0.2 - 0.6 for investigating the relative distribution of k_{sn} through our landscape, as it includes all the most likely values in individual basins (excluding two outliers) and most of the interquartile values (fig.5.4).

5.5.3 Relative channel steepness

We calculated k_{sn} for 486 different sets of parameters (θ^{ref} from 0.2 to 0.6 with a spacing of 0.05, n_{tg} from 20 to 100 with a spacing of 10 and n_{sk} from 0 to 4

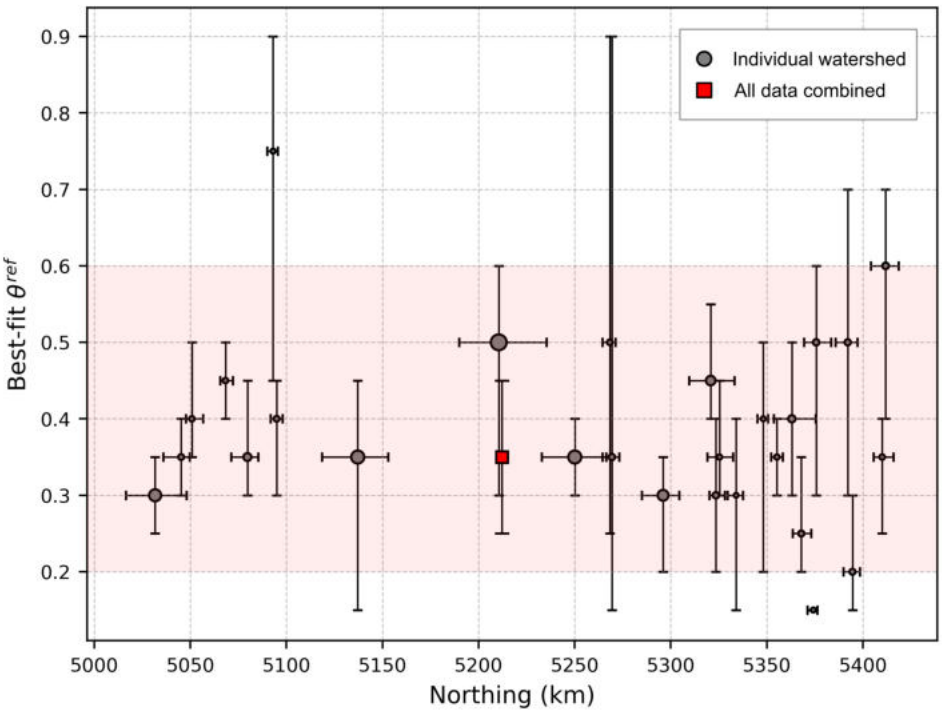

Figure 5.4: Concavity ranges calculated in the study area. Each point represent a single basin, where the x axis is the median and quartiles northing (in km UTM zone 35), and the y axis is the median and quartile of all the best-fits for all the different combination of river tested for each basins. The red square represents a compilation of all the data along the study area.

with a spacing of 1 and for $n_{sk} = 10$). For each individual set, we calculated the relative steepness index from our combined dataset, resulting in 560,636,671 data points.

Regional distribution of channel steepness

Figure 5.5 shows the relative steepness index as a function of the northing coordinate. This provides an overview of channel steepness in regards to the different areas of differential tectonics suggested in section 5.3. The data is noisy, however, and does not show an obvious N-S trend. There is a sharp increase in the relative steepness index between northing values of 5000 km and 5030 km, which may be linked to the bending of the mountain range and incorporating a few and unrepresentative data points in the extreme South of Buzau watershed (Fig.5.1). Three

regions host steep channels compared to the rest of the landscape: (i) The Focsani Basin area (northing 5000 to 5080 kilometers, HS1 on Fig.6.2 and Fig. 5.5), (ii) in the heart of the EC (northing 5125 to 5240 kilometers, HS2 on Fig.6.2 and Fig. 5.5) and (iii) a less prominent steep area in the Northeastern Carpathians from 5340 kilometers. These three areas are connected by two regions of lower relative steepness.

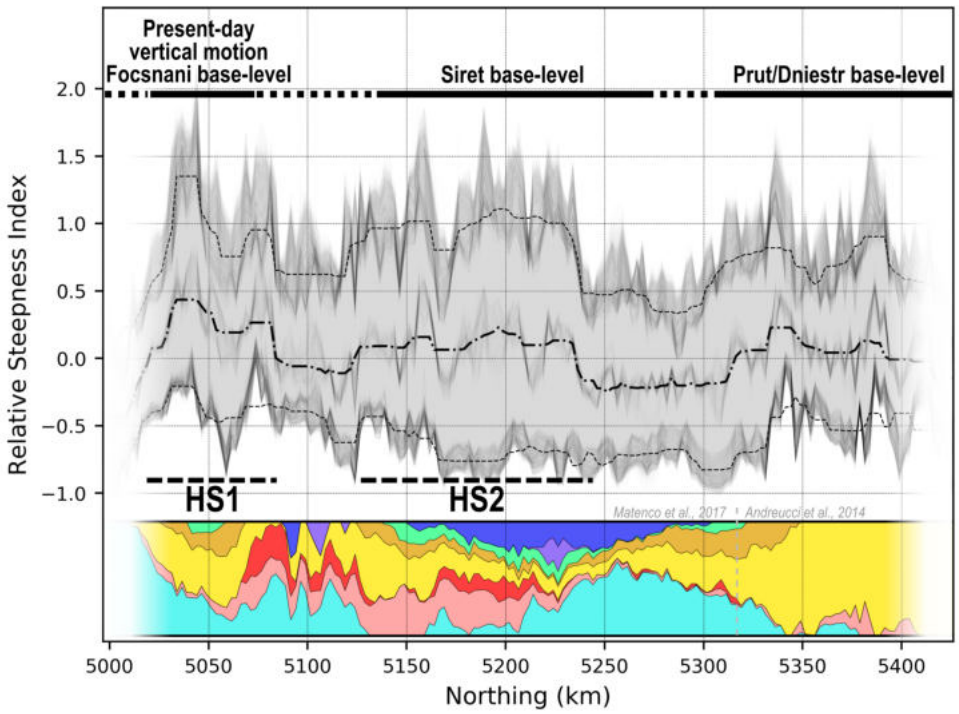

Figure 5.5: Relative steepness index binned by northing coordinates. The binning size is 2500m in UTM zone 35 and is used as rough proxy for tectonic activity to differentiate the Southeastern Carpathians from the rest of the Eastern Carpathians (see section 5.3). Transparent thin grey lines represent each different population of Relative Channel Steepness calculated for different combinations of parameters (see section 5.4.2) and the thicker black lines are a running median window across 9 points. Bottom lines, middle and top lines are respectively the third quartiles, medians and first quartiles of all values within each bin. The bottom figure represents the proportion of lithology across the landscape for each Northing point, it uses the same colors than figure 5.1 to identify the different tectonic units.

The absence of a monotonic N-S trend is also expressed in a map view (Fig.6.2) where the median of all the relative steepness indices suggest a compartmentalised dataset. A clear N-S mid-range linear feature sharply separates an eastern region

of lower steepness and a western region of higher steepness. This main break in steepness is labelled MBiS on Fig.6.2. The sharpness of the contact is less clear south of 5160 km. Other less clearly expressed trends can be observed with this map view. (i) Within the Western region of high steepness, high patches are pointing out, particularly at kilometers 5030 (HS1), 5130. (ii) Within that same region, localised patches of low values express the presence of high-elevation low-gradient valleys in the Buzau, Trotus, Bistrita and Prut watershed (labelled HELG on Fig.6.2). (iii) A region of lower steepness occurs within the Moldova watershed, with a sharp decrease of the values occurring at the drainage boundary between the Bistrita and Moldova watersheds.

Channel steepness as a function of lithology and tectonic units

Figure 5.7 shows relative channel steepness plotted as a function of the northing coordinate for each litho-tectonic unit. Large-scale trends stand out: the Western Focsani Basin and its northern foredeep continuation, Subcarpathians and Marginal folds nappes show a gradual northward decay of their values, with a flattening or unsignificant increase North to km 5200 (*i.e* North of the Bistrita watershed). The Tarcau nappe shows high values until the same km 5200 while sharply decreasing northwards. The Audia/Macla/Convolute Flysh and Ceahlău-Severin nappes behave differently with (i) low, heterogeneous values in the Southeastern Carpathians, (ii) a peak around the same kilometer 5200 in the Bistrita watershed (Fig.5.1) (iii) followed by a sharp decrease until kilometer 5300 (*i.e.* the Northern part of the Siret baselevel) and (iv) high values in the Northernmost area, linked to Prut and Dniestr base level, North to kilometre 5300. Finally, the basement rocks of Dacia units locally imposes patches of high relative steepness in the Eastern Carpathians where these rocks are largely exposed.

Figure 5.7 also highlights multiple notable behaviors differing from a northward monotonic decay as one moves away from the active vertical motions of the Southeastern Carpathians. (i) Although the Subcarpathian nappe has its highest values in the Focsani area, it also displays a local peak north of kilometer 5200, denoting greater proportion of steeper channels within the Subcarpathians

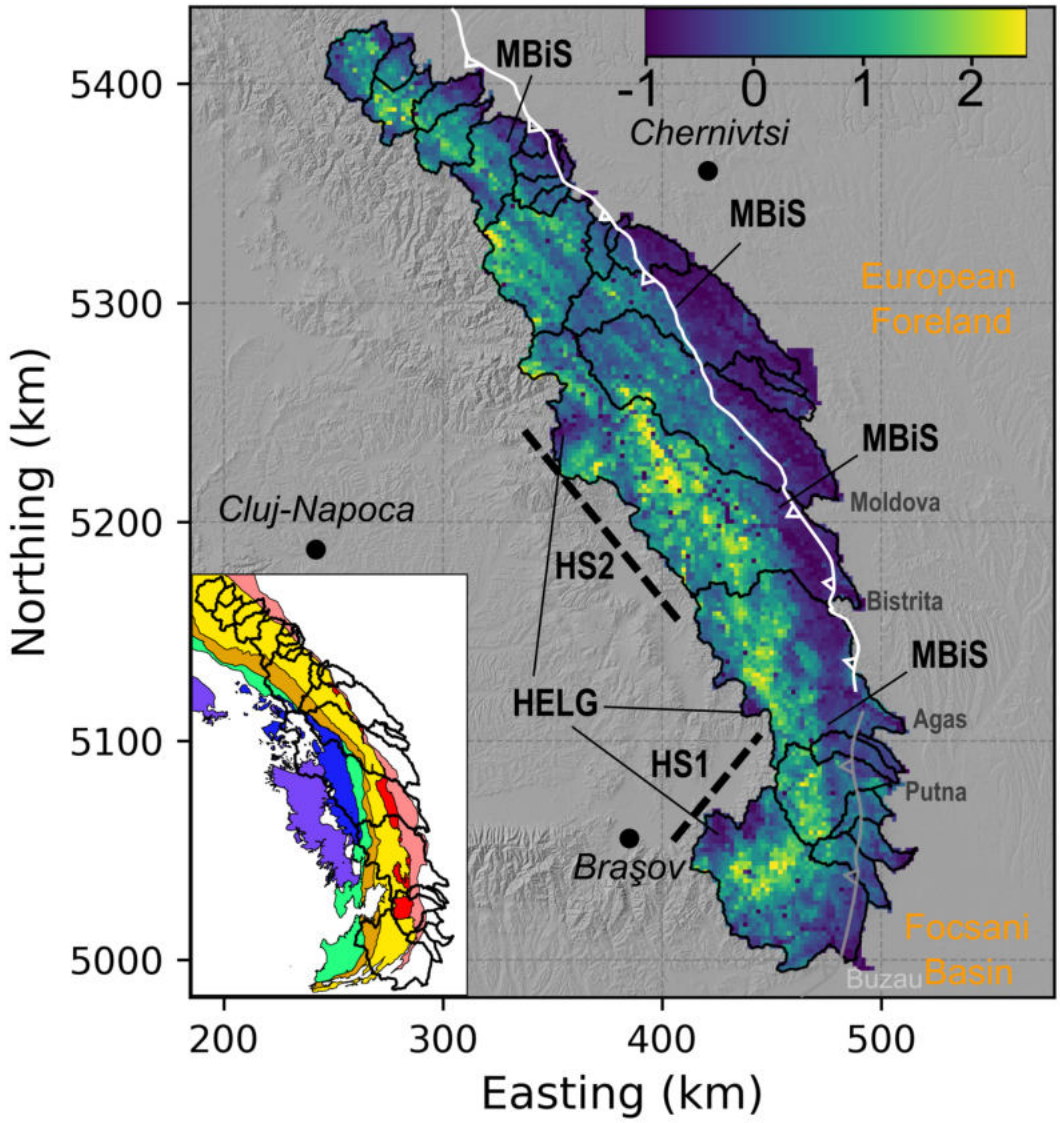

Figure 5.6: Relative steepness index binned in 2D using median binning of the median of relative steepness indices calculated for every set of parameters. The first and third quartile maps are available in the Supplemental Materials.

nappe in the area. Note that the exposed surface of this unit decreases Northward (Fig.5.5), increasing potential effect of noise on the data. (ii) Tracau nappe shows a sharp northward decay rather than a progressive one, as well as high variability. (iii) Audia/Macla and Ceahlău-Severin units do not show northward decay in channel steepness but variable local trends. They also outcrop less within the river network (Fig.5.5).

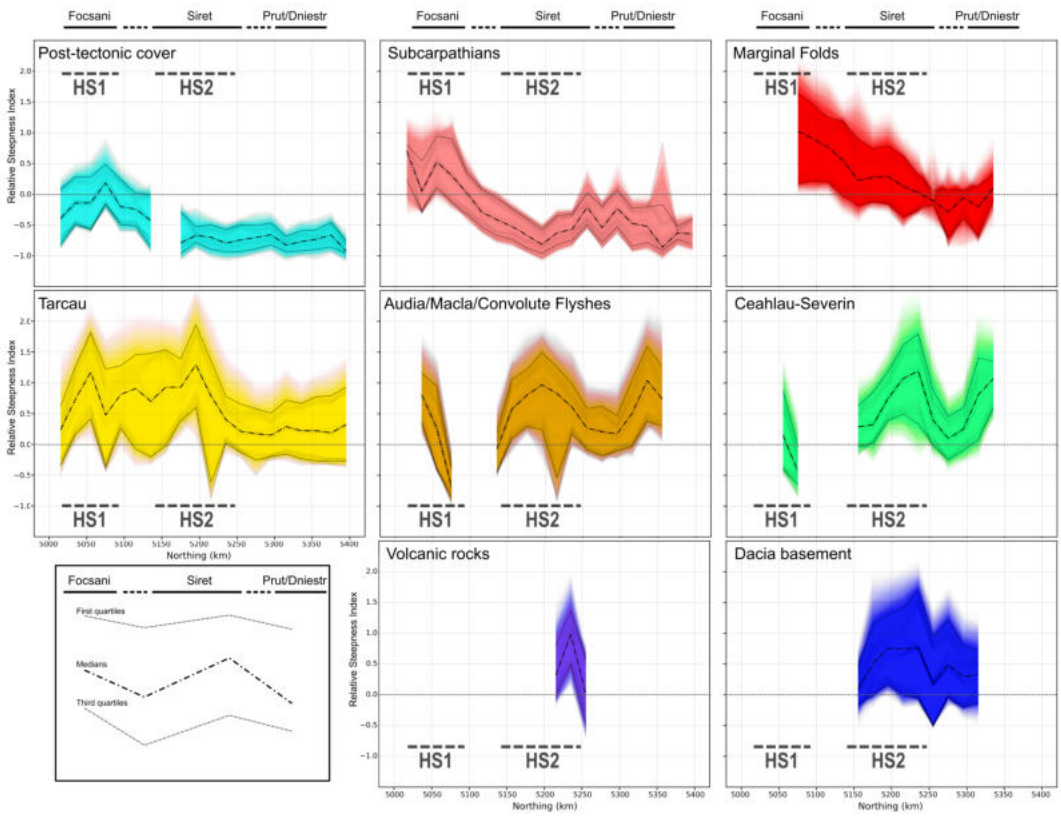

Figure 5.7: Relative steepness index binned by litho-tectonic units and by northing, using the same approach than fig.5.5. For each litho-tectonic units, relative channel steepness index calculated for all the different sets of parameters are diplayed in fine shaded lines binned by northing (25000 m in UTM zone 35). The thicker lines are moving median windows over the first quartiles, medians and third quartiles (3 points). The colors correspond to the tectonic units on fig.5.1.

5.6 Discussion

5.6.1 Spurious tectonic signals

A prominent break in channel steepness can be seen in Figure 6.2 to the east of the main drainage divide that extends along the entire N-S axis of the study area. Section 5.2.2 highlighted tectonics as a common forcing able to generate similar features. In the Carpathians, recent tectonic activity is concentrated in the Southeastern bend of the mountain range (see 5.3). However, the break in channel steepness observed in Figure 6.2 extends far beyond the region where deformation is inferred from other independent proxies. Our rock strength data (Figure 5.3) combined with apparent tectonic inactivity north of the South-Eastern Carpathi-

ans point to lithology as the main driver of the break in channel steepness. This is concentrated where the evaporite-rich and highly fractured rocks of the Subcarpathians and sandstone-rich Tarcau and Marginal fold units lie in contact (e.g. Bernard et al., 2019; Yanites et al., 2017).

This line of reasoning also suggests lithology as a control on more local channel steepness contrasts, for example: (i) The patch of high relative channel steepness at the top of the Bistrita watershed, described in Section 5.5.3. Its boundaries correspond to the magmato-metamorphic rocks of the Dacia basement units and the volcanic rocks linked to Neogene volcanism. (ii) The sharp and significant drop of relative steepness index (Fig.6.2 and 5.7) that occurs within the Tarcau nappe around northing kilometres 5200 to 5250 (see Fig.5.7). Local lithostratigraphic data compilation (Matenco and Bertotti, 2000) highlights that this also corresponds to a lithological change from coarse-grained resistant sandstones in the Bistrita valley to finer-grained, often shaly turbidites in the Moldova valley (see Fig.6.2). It is also nearly perfectly co-located with the drainage divide between the Bistrita and Moldova watersheds (Fig.6.2); this represents another possible expression of lithologic forcing by 'pinning' drainage divides on resistant rocks (e.g. Bernard et al., 2019; Seagren and Schoenbohm, 2019). (iii) The low steepness values are observed at the highest, westernmost part of the Bistrita watershed, corresponding to a switch from the resistant rocks of the Dacia basement to softer sedimentary rocks belonging to the Transylvanian Basin (Maţenco and Matenco, 2017).

Figure 5.8 and 5.9 illustrates how regional and local lithologic forcings can generate relative steepness contrasts which can potentially lead to spurious tectonic interpretations.

5.6.2 Global integration of relative channel steepness index in the Tectonics model

Knowing that lithology can influence the patterns of relative channel steepness, we must then consider strategies for extracting tectonic signals from lithologically

complex terrain. We do this by calculating the relative channel steepness by litho-tectonic units, as described in Section 5.5.3. This analysis reveals both large scale and more localised patterns, discussed in this section 5.6.3.

Within litho-tectonic units at the eastern edge of the range, *i.e.* the whole area east to the main break of steepness (MBiS on Fig.6.2), we find higher values of relative channel steepness index in the South Eastern Carpathians (HS1 area of units Subcarpathians and Post-Tectonic on Figure 5.7). This suggests that there is a tectonic signal of increasing rock uplift rates from north to south in the frontal units that is superimposed over the lithological signal. This pattern is consistent with previous studies suggesting recent to present tectonically-driven vertical motions in the South-East Carpathians (e.g. Mațenco and Matenco, 2017). This pattern is particularly clear for the Marginal Folds, the Subcarpathians and the Focsani/Post-Tectonics units, with all showing a monotonic northward decrease in channel steepness. When looking at channel steepness patterns over the entire mountain range, the changes in steepness from different lithologies are greater than the N–S trends within the frontal litho-tectonic units, highlighting how tectonic patterns may be masked by lithologic contrasts in rock erodibility.

Closer analysis of terrace systems within the SEC by Necea et al. (2013) suggest an eastward migration of the rock uplift and subsidence pattern through Holocene time. Thermochronometers (e.g. Matenco et al., 2013; Necea, 2010; Sanders et al., 1999) suggest enhanced Quaternary exhumation of the Tarcau and Marginal Folds units but mostly show unreset ages in the covering sediments that were deposited after cessation of the main mountain building phase. These inferred Quaternary motions are spatially correlated with deep, thick-skinned faults imaged by geophysical studies (e.g. Bocin et al., 2013; Bocin et al., 2005, 2009), suggesting their reactivation. The combination of different proxies for differential vertical rock motions indicate eastward migration of rock uplift from Quaternary to present (Mațenco and Matenco, 2017).

Although the sharpness of the main break in channel steepness is partly a response to a lithologic forcing, the channel steepness data supports the theory that uplift in the South-East Carpathians may be caused by the reactivation

of deep faults and that it is now migrating eastward toward the Focsani Basin (fig.5.2). This eastward migration is also confirmed by the channel steepnesses in the mountain front of the Focsani area, where soft rocks form up to 1 km of relief.

The Tarcau unit does not show the same gradual decrease of channel steepness from the South-East Carpathians to the Eastern Carpathians, although the thermochronometres would suggest similar behaviour than the Marginal Folds Unit (Mațenco and Matenco, 2017). This unit is characterised by the hardest lithology of the South-Eastern Carpathians, with many thick layers of sandstone. When reaching the Eastern Carpathians, a sharp lithologic change operate (Figure 5.9), where softer, finer and more distal sedimentary rocks replace the sandtones. We suggest (i) the presence of the hard bed add some noise to the signal with high steepness patches while (ii) the rather sharp lithologically driven decrease in channel steepness hides any gradual signal. At global scale, the lithologic signal fully overwrite the tectonics one in this tectonic units. However, it does not invalidate the tectonic interpretations.

5.6.3 Non lithologic low-gradient area within the South-East Carpathians

Although rock hardness measurements in the South-East Carpathians do not suggest significant lithologic contrasts between the Ceahlău-Severin, Audia/Macla and Tarcau units (Fig.5.3), the upper parts of the Buzau basin show low values of channel steepness, mostly in the Audia, Macla, Convolute Flyshes and Cretaceous units, but also at lesser extent in the Tarcau unit. We explain this different behaviour using local data from these units. (i) Thermochronometers have indicated an older episode and a lower magnitude of exhumation of these units in the South-East Carpathians (in the Buzau watershed; Merten et al. (2010)), which has been related to long-wavelength exhumation related to slab-retreat (e.g. Mațenco and Matenco, 2017; Picotti and Pazzaglia, 2008). (ii) Fielitz and Seghedi (2005) suggest a drainage reorganisation to explain these high elevation

low-gradient valleys. Our dataset is consistent with these previous observations, showing steep "aggressive" (*sensu* Willett et al. (2014)) rivers in the Buzau watershed juxtaposed with an upstream low gradient, diffusive landscape. These values appear anomalous relative to the regional pattern of tectonic activity, *i.e.* high tectonic activity in the South-east Carpathians and post-collisional decay in the Eastern Carpathians, and bias the global distribution of relative channel steepness (Fig.5.5 and 6.2) by reducing the regional values.

The reduction in channel steepness due to drainage capture can be linked as differential rock uplift is a common driver for drainage divide reorganisation (e.g. Giachetta and Willett, 2018a; Seagren and Schoenbohm, 2019; Willett et al., 2014). Fig.5.9 summarises the local signals observed within the Buzau watershed, illustrating the diversity of local expression of channel steepness.

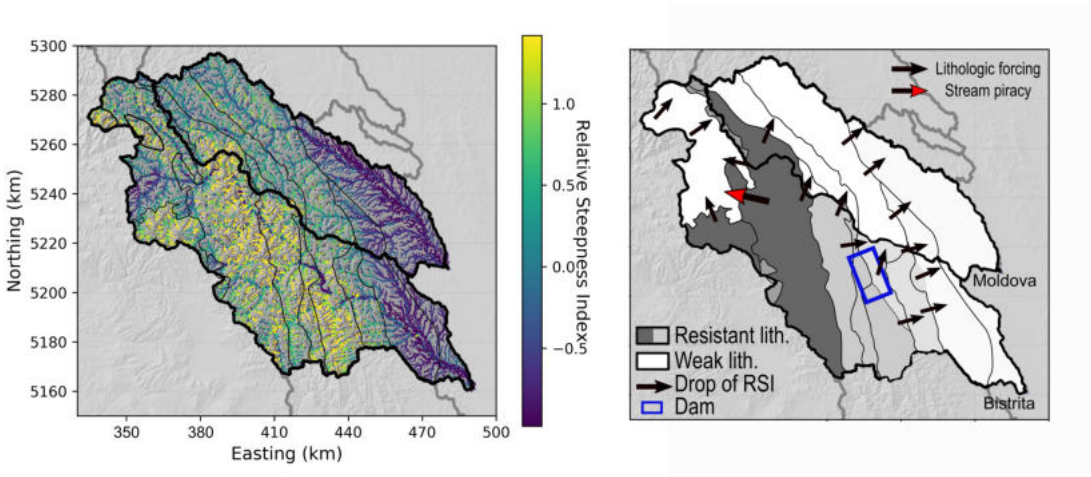

Figure 5.8: Illustration of the diversity of forcings generating potentially spurious tectonic signal by inducing steepness contrasts within the Eastern Carpathians.

5.7 Conclusions

Based on thermochronometry, modern GPS data, and geomorphic evidence (i.e., terraces), past research has suggested a gradient in tectonically induced rock uplift along the Ukrainian and Romanian Carpathians. However, detecting these signals from topographic data is challenging because the mountain range is, like most mountain ranges, lithologically heterogeneous. In addition exploring chan-

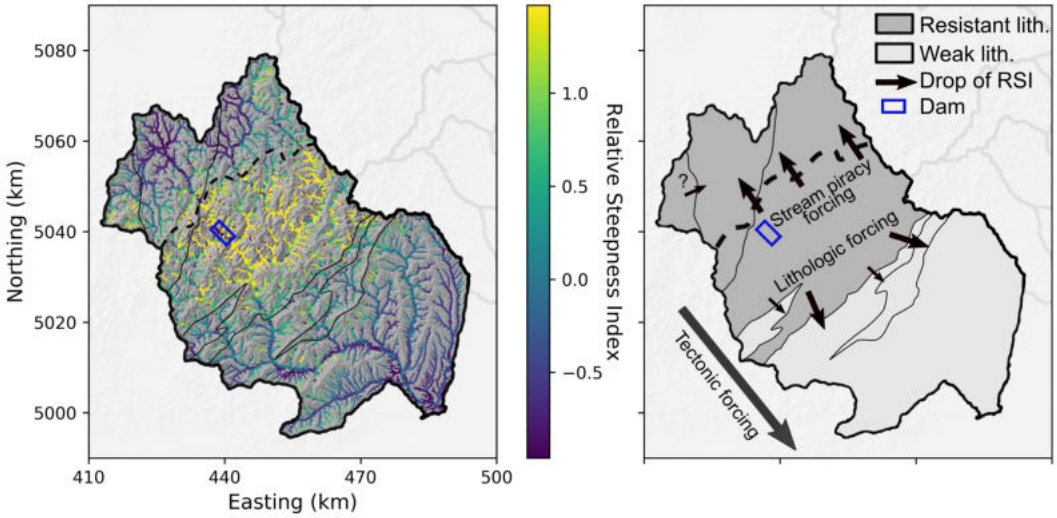

Figure 5.9: Illustration of the diversity of local expression of tectonics, lithologic and stream piracy forcings in the South-Eastern Carpathians within the Buzau watershed.

nel steepness across a wide geographical range will almost inevitably encompass basins with differing concavities, which can cloud interpretation of channel steepness. We find that the concavity index, which affects normalized steepness values (k_{sn}) varies between approximately 0.2 and 0.6 in the Ukrainian and Romanian Carpathians. Choosing a single reference concavity might result in misleading k_{sn} values so we developed a method for calculating relative steepness that can be applied across basins that have different concavities using a modified z–score method that takes into account the non-normal distribution of channel steepness values across all catchments.

The first order values of relative steepness across the range show a large contrast between the gentle eastern front of the range and steep areas near the drainage divide. The north to south increase in rock uplift rates from the east to the south-east Carpathians are not obviously reflected in the relative steepness data at this scale. However, when we group steepness by litho-tectonic units, we find that different units have different relative steepness between these regions.

We collected rock hardness data across the litho-tectonic units and find that the hardness can be broadly grouped into hard and soft units. This grouping is reflected in the relative channel steepness data.

By separating the relative steepness by litho-tectonic units, a N–S spatial pattern appears. In the units at the mountain front, this pattern is most clear: relative steepness is highest in the part of the mountain range where thermochronometers have recorded the highest, long-term exhumation rates. In addition, steepness data confirms the migration of the surface uplift pattern towards the east, where thermochronometers show unreset ages and cannot be used to estimate exhumation. Without accounting for lithology, this tectonic signal would have been entirely masked by differences in rock hardness. Spatial trends in the harder rocks toward the peaks of the range show more localised patterns. For example, high-elevation low-gradient valleys record localised stream piracy and lithologic variations within hard units explain other, less prominent contrasts in relative steepness.

Evaluation of variable rock uplift from channel steepness measurements on the scale of an entire mountain range is challenged by the variability in rock strength and the concavity of the channel profile. This is particularly true when faulted units juxtapose rocks of contrasting hardness, as is common in thrust belts. However, through characterisation of channel concavities, independent measures of rock strength and comparison of channel steepnesses within each litho-tectonic unit it is possible to isolate for the role of tectonics versus lithology .

Chapter 6

Discussion and Conclusion

My overall aim in this thesis has been to improve methods of extracting topographic metrics from digital data, and then applying these metrics to interpretation of these metrics in a lithologically and tectonically complex landscape: the Romanian Carpathians. This chapter looks first at insights gained from the new methods I developed, and then discusses future directions of research based on these insights. I then discuss the complexities of applying these methods to a real landscape and what this means for future studies combining topographic analysis and landscape interpretation.

6.1 Extraction and interpretation of χ, θ and k_{sn}

Chapter 3 focuses on determining the magnitude and location of slope breaks along channel profiles. Chapter 4 focuses on constraining the concavity indices across different field sites. The aim of these methods is to allow geomorphologists to extract Flint's metrics at regional scales to, for example, unravel tectonics from fluvial geomorphology over a mountain range.

I undertook this research because of the limitations of existing methods in terms of applicability at large scales (see the development on slope–area plots in Chapter 4). A number of the limitations of existing methods are linked to the need for a number of subjective inputs to ensure correct processing of the data.

From a computational point of view, the numerical methods I present in this

thesis achieve relative objectivity: they will suggest the location of knickpoint and optimal θ values that depend much less on user defined parameters than previous methods, although I have not been able to entirely eliminate parameter sensitivity. However, the methods are algorithmic so different users entering the same parameters will achieve the same results if they use the same underlying topographic data. This property is also true for the algorithm extracting k_{sn} that I use in this thesis (Mudd et al., 2014).

The algorithms do rely on choices that cannot be automated or made objective because they depend on the ultimate goal of the user. These choices, such as picking the θ value best fitted for a region or the relative size of the segments used to calculate k_{sn}, will have implications in the results of data processing and users will need to carefully justify their choice. Parameter choices and algorithm limitations are explored in Chapters 3 and 4.

Discussing these choices can quickly lead to circumnavigations through an almost unending series of caveats and pitfalls. For example, k_s requires accurate constraint of θ; if it isn't well constrain k_{sn} will be subject to distortions (Chapter 4). But k_{sn} values not calculated with same θ_{ref} are not comparable, and hence any regional study of k_{sn} requires selection of a regional θ_{ref}. If the optimal value of θ varies in space, and Chapter 4 suggests this is far from uncommon, one bounces between facing distorted k_{sn} signals and reducing comparability between basins. Solutions to such problems are evasive and case-specific. Chapter 3 and 4 explore the impacts of these choices and the subsequent distortion of topographic metrics. However they do not explore the solutions in any depth. Here I take the opportunity to discuss the scale at which these metrics are extracted and used, and how this can influence the choice of parameters.

6.1.1 The choice of θ_{ref} to interpret k_{sn}

Quantification of the most likely value of θ depends on the scale of the channel networks used to constrain it. With the χ-based disorder method Hergarten et al. (e.g. 2016) and Mudd et al. (2018), the scaling factor is directly controlled by the choice of the outlet location (and subsequent size of the upstream basin). It

also depends on drainage density of the extracted river network. The resulting fits of θ and its uncertainty can have different interpretations depending on how many rivers it represents and their spatial spreading. Hence, constraining θ from a relatively small basin may determine the optimal local value, whereas θ over large basins may represent the value which minimises regional distortion while not necessarily being optimal for some local sections of the river network.

There is no good or bad practice, as ultimately one needs to fix θ to extract χ and k_{sn}. Calculating θ for many small-scale basins may misrepresent the major rivers setting their base level; calculating θ for large-scale basins might hide local anomalous regions where the values display spurious signals that result from χ and k_{sn} distortions (Chapter 4). Balancing a fit of θ for small or large rivers is for example relatively straightforward for homogeneous areas displaying similar optimal concavity, but it large distortions of topographic metrics are possible when facing heterogeneity at small or large scales.

Chapter 5 provides an example working with spatially varying θ. Because k_{sn} is investigated within the same tectonic units, with similar lithology, I proceeded under the assumption that extracting channel steepness for the range of observed θ across the field site was appropriate, in order to ensure consistency of k_{sn} values. Cross-θ comparison can be achieved using a statistical non-dimensionalisation of k_{sn}. This approach is also applied in Bernard et al. (2019), where the watershed are similarly composed of consistent tectonic units, in the Pyrenees mountain range. Hurst et al. (2019) uses the median best-fit of their study area to compare k_{sn}, this can be justified as the θ are relatively homogeneous.

I suggest, however, that some situations require particular care, with potentially unsolvable cases. If two juxtaposed basins, or group of basins, show large differences in optimal θ, comparing χ and k_{sn} values can generate large distortions, regardless of the chosen value of θ. Systematic comparison of k_{sn} for ranges of θ values can be a solution if the geological and climatic context is comparable, but any inconsistency in the signal (i.e., spatial patterns of k_{sn}) across the different values of θ would lead to ambiguity. Moreover, as all values would be distorted, using k_{sn} as a proxy for erosion rate would be dangerous in this context,

as the spatial signal would not be clear.

One possibility to mitigate this behaviour would be to develop a method to "non-dimensionalise" k_{sn} with regards to θ. This could be done by manipulating the equations used to quantify k_{sn} distortion in Chapter 4 section 4.6.1. As the equations presented in Chapter 4 allows one to quantify the distortion between two points for a given Δ_θ, one could "undistort" both k_{sn} values compared to a fixed, theoretical point with a given drainage area. This approach, although theoretically possible, would be limited to comparison of two points at a time. To quantify distortion over the entire landscape, you would need to analyse ever pair of pixels in the channel network. The number of calculations follows the binomial equation, and for example a river network with 100000 pixels would require nearly 5 billion combinations.

6.1.2 The choice of θ_{ref} to interpret χ

χ is sensitive to both the choice of θ and it also requires the justification of a base-level location or elevation (Forte and Whipple, 2018). In addition, where k_{sn} values only depend on the local slope patch and θ, χ value at any point integrates all the downstream χ from the base-level, which can amplify distortions.

Analysing χ contrasts across a range of θ values may not be representative as different parts of the downstream river network might be distorted to different extents. χ is also function of the flow distance, which cannot be expressed in an equation, and one cannot suggest a potential "undistortion" as one could for k_{sn}. One solution would be to finely constrain θ and ensure similar amount of distortion across the study area. Any asymmetry would imply ambiguity in the observed signals. Alternative metrics can be considered as more suitable in the case of studying drainage divide stability in landscapes with spatially varying θ (Forte and Whipple, 2018; Young and Hilley, 2018).

At very large scales, from continentals to the entire planet, results from this thesis suggest that none of the aforementioned methods can be applied. The magnitude of slope breaks and k_{sn} values are certain to be distorted in any very large landscape no matter which value of θ is chosen.

Results from such studies are, however, not necessarily without merit. Hilley et al. (2019) for example suggest a maximum threshold for k_{sn} across the world. Changing θ values is unlikely to change that observation. However it will modify the absolute value of this threshold. Possible circumvention of this caveat would be to separate the world into subsets of basins with similar θ and recompute the threshold within each subset.

Clustering basins by values is not applicable to large scale studies investigating χ contrasts, as restricting the study to watersheds with similar θ will still not aid the additional problem of setting a universal base-level choice, which depends on local gravity, relative sea level rise, lithology and other factors. Continental and world-scale datasets of χ values (e.g. Giachetta and Willett, 2018c) will be affected by distortions linked to spatially varying θ, questioning the actual meaning of the values and whether they represent geomorphic processes or mathematical artefacts.

6.1.3 Variability of observed θ

Although Chapter 4 demonstrates a number of limitations in using slope–area plots , it remains the only way to express θ and k_s "natively" without any assumptions. Another question of scale of θ variations therefore deserves to be raised: how to discriminate between a change in θ and a change in k_s along a single river. As demonstrated in this thesis and other works (e.g. Bernard et al., 2019; Mudd et al., 2018; Tucker and Whipple, 2002), θ varies spatially. If it varies spatially amongst different watersheds, it can also vary within a single river. Most studies consider basins as whole entities having a constant θ, which is not in accordance with my own observations (Chapter 4. However measuring the scales of internal variations is not possible with the integral method as θ is already integrated within its calculation. Slope–Area methods are difficult to apply on real landscapes: minor differences in the processing method impacts the observed value of θ. Finally, the relation between observed concavity and theoretical laws depends on the formulation of the latter and different morphologies can be explained with different laws (e.g. Tucker and Whipple, 2002; Wickert and

Schildgen, 2019).

6.2 Implications for landscape evolution models

Results from this thesis demonstrate that spatial variability in θ is an important factor in many ways. It can occur from a watershed to another as well as from a mountain range to another. At a river-scale, internal changes in θ are expected, particularly if the river is far from a steady state form (Whipple et al., 2013). However, landscape evolution models are most commonly using a single value for θ (e.g. Braun and Willett, 2013; Goren et al., 2014), which can be expressed as a function of the erosion and deposition laws used in the model. In some rare cases θ is discriminated for transport-limited and for detachment-limited regions (i.e., two values are used) (Tucker et al., 2001), but the difference between the two is solely linked to the availability of sediments, not to topography or other factors, and the values are fixed through time. The reason is that it is difficult to determine the extent to which these parameters change, how to objectively attribute different parameter values or determine their spatial distribution.

Landscape evolution models frequently simplify the characteristics of a landscape in order to isolate the effect of one or a few specific forcings. The question this thesis raises is not about the need of simplifying a landscape in order to model it, but at which point is it still reasonable to assume spatially constant θ when simulating a landscape through millions of year. If one believes that θ varies in space, then θ can vary through time as well under the effect of external forcings (Whipple et al., 2013). For example testing the migration of transient signal following a base-level fall on river long profile with constant θ might lead to misinterpretations. Whipple et al. (2013) and references therein highlighted that transient reaches, or simply reaches in equilibrium with different forcings, could be described with different values of k_s and/or θ. This comes back to the principle of "slope patches" by Royden and Taylor Perron (2013), but the patches could have different θ in addition to different k_s. Note that in this case, the term "slope" is slightly misleading, as this is the slope in a transformed long profile,

and not the channel gradient S.

In the simplest detachment-limited landscape evolution model $\theta = m/n$, the ratio between the slope and area exponents. They represent a balance between the effect of slope and drainage area, and models use fixed values for m and n. External factors affecting either the slope or the drainage area asymmetrically can disturb that balance and it is not clear how the stream power will re-equilibrate to the new state.

One of the most striking example has been indirectly raised by Seagren and Schoenbohm (2019) at a conceptual level. They argue that stream piracy, and especially the effect of beheading a river channel, linearly increases channel steepness for the aggressor river, and linearly decreases channel steepness of the victim river. However I argue here that this is not clear how this translates in application as (i) it depends on the actual value of the beheaded slope and (ii) it also induces a big change in θ. This is illustrated in Figure 6.1, where the effect of river beheading is simulated on an hypothetical river in steady-state. The drainage area follows equation 1.7 and slope is generated with equation 1.16 for arbitrary chosen $k_{sn} = 20$ and $\theta = 0.45$. The beheading is imposed by simply removing part of the channel headwaters and subtracting the drainage area removed. The immediate effect is a diminution of both θ, which now varies spatially, and k_s if calculated with varying θ. Note that also k_{sn}, if calculated with original θ, would also diminish.

The topic of river response to stream piracy has been explored by Whipple et al. (2017a), and they also detail the χ and k_{sn} signatures, however they also assume spatially constant θ. Implementing varying θ in Landscape Evolution Models would therefore need to be dynamic, and not static. The most sensible possibility would be to express it as a function of the current topography at a time t. Because external forcings can affect θ, then θ is not only function of the fluvial erosion law utilised at $t-1$, but also on other forcings and event happening, *e.g.* tectonics motions, varying geology through exhumation or stream piracy.

Future work on concavity could investigate methods to implement varying θ in landscape evolution models and its impacts. One particular challenge will

be that a river reach can be described with numerous combinations of k_s and θ, however I speculate that only few should be physically possible. One could suggest that as the slope is not affected, the change would be induced to the m exponent of equation 1.24.

I highlighted this effect with a striking example of θ change, or at least observed θ, but more subtle changes can be imagined in other scenarios. A base-level fall can add some topography to the river profile, for example topography that was previously below sea or lake level, and the newly exposed topography could have a different θ. Base level drop will "fire" a slope patch upstream that would gradually modify the overall θ. The timing of exhumation is likely to be a controlling factor on whether θ is modified by the new conditions or the new topography or integrated within the context of the previously existing river network.

So far I have discussed the implications of changes in drainage area, but this last is used as a proxy for discharge. If the data allows it, any modification of discharge through time and space can theoretically affect θ. For example changes to precipitation, infiltration, evaporation or groundwater flow via eroding 3D structures can eventually affect θ. Linked to the latter suggestion, Mudd et al. (2018) demonstrated that differential lithology could be linked with different θ, in some landscapes. If this is the case, changes in the map-view lithology field (*id est* erodibility field) can result in changes to the θ value. The challenge with the aforementioned cases, is that it will be difficult in some cases to differentiate between small-scale changes in k_s and θ.

6.3 Channel steepness from very high-resolution topography

This thesis builds on existing knowledge about channel steepness (Chapter 1) to understand the different factors controlling it. It emphasises the cases of heterogeneous landscape, where different forcings are likely to generate composite, ambiguous morphologies. Chapter 5 investigates a case study where surface vertical motions vary spatially at small scale (order of kilometres), alongside striking

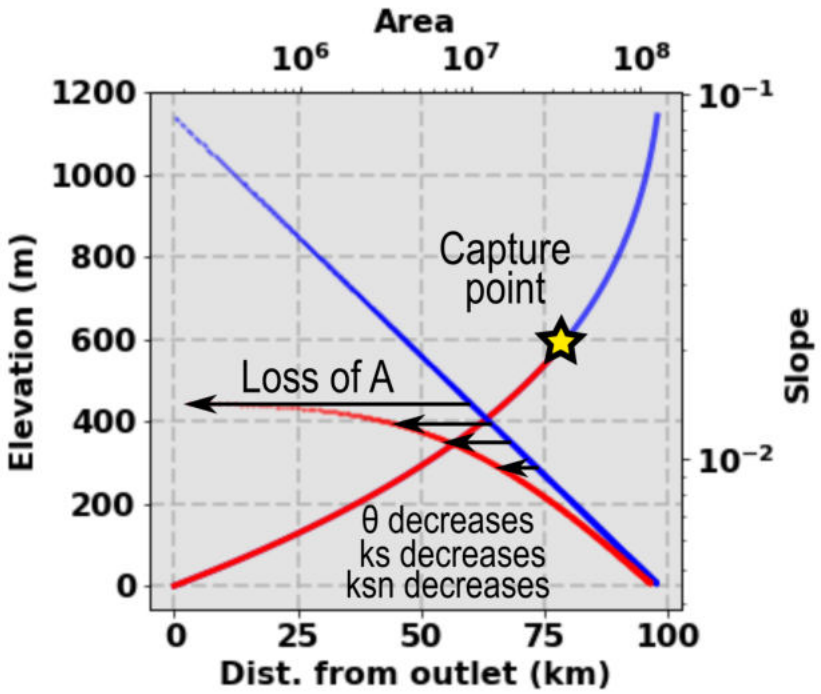

Figure 6.1: Effect of river beheading on the river long profile and the slope–area relationship. In blue, the river state before the capture and in red the river after the capture. Note the non-linear effect of the loss of drainage area on all the metrics.

changes in rock strength. However as detailed in Chapter 1, other forcings can also affect channel steepness, such as climate or channel width. In this subsection I first discuss some limitations linked to the methodology of integrating these forcings into channel steepness, then I highlight a future work direction in order to do so.

River width can affect channel steepness, as explained in Chapter 1. A river with a certain steepness will not have the same meaning if it is 5 metres wide or 20. Channel width will impact erosion potential. I refer the reader to Whipple et al. (2013, and references therein) for a review on this subject. It raises a methodological limitation when it comes to integrating channel width within topographic analysis: most of the analysis described in this thesis relies on river modelled as successions of single pixels following the steepest descent route. Using digital elevation models such as SRTM (30 metres), it does not make a difference as the rivers are contained within a single pixel most of the time, and may eventually become a problem only if studying very wide rivers. River width can then be either modelled as function of drainage area (Hack, 1957), or measured from an independent dataset, but there is no direct way to integrate channel width data with k_{sn} from the same source.

With the rise of airborne LiDAR data, however, the availability of digital elevation models of very high resolution is getting more common ($<$5 metres). In this case, it becomes ambiguous whether a river can still be represented with a single-pixel flow line. Calculating drainage area or discharge can use multiple flow direction methods (e.g. Bovy, 2019; Davy et al., 2017), however if the river extraction does not take account of multiple flow, the metrics are then biased. Constraining k_{sn} would benefit from the development of such a method, which could be applied to the fields of topographic analysis as well as landscape evolution modelling, where multiple flow direction is suspected to be an important factor in determining topographic outcomes (Armitage, 2019).

Different ways of dealing with this problem can be imagined. First, one can consider the rivers as entities defined by several independent pixels. The metrics are then calculated as independent interactions between pixels, or the sum of all

interactions involving one pixel. In the following demonstration, I assume that a generic law distributes flow amongst all its down-slope neighbouring pixels, splitting drainage area (or discharge) fluxes. Let's consider a point i and his receivers j_n with n being the ID of the receivers, i.e. $j_1, j_2, ..., j_N$ with N the total number of receiver. In this reference frame, Flint's Law can be redefined in different manners.

It can be defined as the sum of all interactions:

$$k_{sni} = \sum_{n=1}^{N} \frac{\Delta z_{ijn}}{\Delta x_{ijn}} k_{Aijn} A_i^{\theta_{ref}} \tag{6.1}$$

where k_{sni} is the channel steepness at node i, $\frac{\Delta z_{ijn}}{\Delta x_{ijn}}$ the slope between the node i and a given receiver j_n, A_i the drainage area (or discharge) at the node i and k_{Aijn} the proportion of flow between the node i and the receiver j_n satisfying $\sum_{n=1}^{N} k_{Aijn} = 1$. In this scenario, each pixel has one k_{sn} values, and the effect of width is "passively" accounted for in k_{sn} by splitting its effect in multiple pixels.

Another way would be to have one k_{sn} value for each interaction between pixels:

$$k_{snijn} = k_{Aijn} \frac{\Delta z_{ijn}}{\Delta x_{ijn}} A_i^{\theta_{ref}} \tag{6.2}$$

where k_{snijn} is a value valid for a location in between node i and a receiver j_n. In this referential, there is one k_{sn} value for each connection between a node and its receivers. Both of these approaches can be expected to be noisy in real landscapes, but would be better at capturing the distributed nature of flow that is the reality on 1 metre resolution that is common for LiDAR data.

For the case of topographic analysis on real landscapes, a second approach can be suggested. Still assuming the same generic law distributing flows through pixels, rivers can considered discrete entities, separated form the grid. Such a method would "re-grid" a river network superposed on the top of the digital elevation model. This can be done by using a variation of the stack order (Braun and Willett, 2013) suitable for multiple flow (e.g. Bovy, 2019). Once drainage area (or discharge) flux is calculated, a first step would consist in determining

which node is within a river. The simplest solution is to apply a drainage are threshold, but more sophisticated solutions linked to local agglomerated maxima of drainage area can be envisaged. A second step would consist in determining the dominant flow direction of the area. This can be done by iterating through windows around each river pixel and finding the average flow azimuth. Finally, it would be possible to extract river points from the grid.

Starting at base-level nodes, one can iterate through the stack and apply an asymmetric window with a long axis perpendicular to the dominant flow azimuth around the node. The window can gather all the surrounding river nodes into a single new river point having the median elevation, median coordinates, the cumulative drainage area and a river width calculated directly from the channel pixels. Every node would be grouped within new river points. In the case of a landscape evolution model, the simplified node graph can have its own fluvial law and then the topographic variation could be applied to the underlying nodes on the grid. In the case of topographic analysis, Flint's metrics can be calculated from the extracted network. These methods would have the advantage of "actively" encompassing width while reducing the effect of local noise. However implementation would be complex and grouping nodes always raise the risk of erasing potentially meaningful details. It would also allow the integration of potentially more sophisticated hydrology, which would improve the modelling of geomorphic processes (e.g. Davy et al., 2017).

6.4 Channel steepness, tectonics and erosion in the Eastern Carpathians

Chapter 5 demonstrates that in heterogeneous landscapes, different forcings can coexist and affect channel steepness in a combined manner. The combination of forcings means that topographic signals cannot easily be isolated. These signals can, however, be deciphered with careful, systematic extraction of channel steepness in correlation with other factors. Hence in the Eastern Carpathians, I have aimed to isolate the expression of active tectonics, depsite its overprinting

by lithological factors. Although lithology is responsible for the most prominent changes in k_{sn}, tectonics can still be unravelled as secondary signal, and correlates well with other proxies for tectonics in the region (Maţenco and Matenco, 2017), even offering spatial interpolation of it. However, the study focuses mainly on the relative steepening of different areas and how to interpret it into meaningful tectonics.

Chapter 1 demonstrates that one of the most useful features of k_{sn} is that it correlates positively with erosion rates in a wide range of landscapes. It is not straightforward in the Carpathians to explore that relationship: tectonic and lithologic gradients have short wavelengths, locally affected by stream piracy. Another complicating factor is that the base-level on either side of the mountain range is asymmetric (Maţenco and Matenco, 2017, and references therein). For example, the Transylvanian basin, alongside the elevated Brasov Basin and Neogene volcanism, create a high eastern base level for the area whereas the actively subsiding Focsani basin maintains a low base level, near sea level, one on the western flank. Finally the same flank north of the the Focsani basin is of intermediate height, as it is passively rebounding in a post-orogenic state.

A potential future use of channel steepness in the Carpathians will be to integrate new proxies for recent erosion in the Eastern Carpathians to complete the dataset. This can be done using already published luminescence-dated terrace data (Necea et al., 2013) and expand the terrace extraction to all mountain front rivers using topographic analysis (F.J., 2017). During my field work in support of this thesis, I collected samples for ^{10}Be cosmogenic dating analysis at the mountain front of the main rivers on both side of the drainage divide, in the Focsani Basin and in the European foreland. I also collected nested sample at the base of suspected stream captures, and in smaller basins mostly draining single lithologic units. Future results of these analysis will allow (i) the quantification of erosion rates with reasonably high density of samples and (ii) eventual tools to constrain parameters from erosion law and use landscape evolution models to investigate the area.

6.5 Concluding remarks

This thesis reaches a number of main conclusions:

1. *Developing methods and algorithms to objectively extract Flint's metrics is an essential prerequisite to challenge their use across diverse landscapes.* In this thesis I develop and apply objective methods to investigate (i) the location and magnitude of knickpoints, (ii) constrain θ and estimate their spatial variability, (iii) estimate the distortion of χ and k_{sn} if θ is not optimal and (iv) extract k_{sn} with different parameters and non-dimentionalise its value to enable comparison of channel steepness across basins with different values of θ. The limitations of these algorithms are explored with sensitivity analyses, demonstrating that the parameters used to calculate k_{sn}, its breaks in slope and constraining θ need to be carefully justified and their impact on results need to be acknowledged. The tools used in this thesis are all open-source, free from paywalls, documented and packaged within a version-controlled repository to ensure reproducibility and accessibility.
2. *Knickpoints and waterfall, no matter the mechanism of their genesis, can be located and their magnitude quantified based on k_{sn} methods.* The algorithm is based on breaking χ–elevation plots into segments to identify the most probable location of the break in slopes. It uses the variation of k_{sn} and elevation at segment boundaries to provide an objective value of the knickpoints magnitude while ensuring a high level of objectivity and reproducibility for the method. It also demonstrates that the scale of the break in slope is important to relate knickpoint morphology to geomorphic processes.
3. *θ varies spatially at all scales. Using unconstrained values can distort χ and k_{sn} and generate spurious signals.* The method developed in this thesis allows users to constrain θ at mountain range scale as well as the scale of individual basins, and I suggest a method to estimate the goodness of fit of a specific value for watersheds in the study area, as ultimately, a value of θ has to be chosen. The results show that θ varies significantly worldwide

between 0.05 and 0.8 and is far from being systematically the median value of 0.45. Investigations on the effect of calculating k_{sn} and χ with non-optimal θ_{ref} unravelled critical distortions to their spatial patterns across and within the watersheds. The magnitude of the distortion depends on the geographical context and the scales of variation in the θ values.

4. *Lithologic and tectonic forcings can be deciphered from channel steepness in the Eastern Carpathians, despite the prevalence of the lithologic effect.* Channel steepness patterns, carefully extracted acknowledging heterogeneity in θ values in the Carpathians, demonstrate that despite significant vertical motions in the Eastern Carpathians, the most prominent contrasts in channel steepness were linked to lithology. However, tectonics is still expressed and can be unravelled from the lithologic signal thanks to systematic correlation of channel steepness with lithologic units. Channel steepness therefore demonstrates its use to spatially expand long-term exhumation and erosion history determined by earlier geomorphological studies. Future advances in the region will need to incorporate recent erosion rate data in order to determine which part of the steepened landscape has a commensurate increase in erosion rates.

5. This thesis highlights the potential of more work about understanding the forcings hidden behind Flint's metrics. It mostly opens on methodological developments about (i) incorporating variability of θ in landscape evolution models and in global geomorphometry, (ii) Developing method to extract these metrics with more realistic hydrology and (iii) adapting the methods to very-high resolution digital elevation models where rivers cannot be represented with single succession of pixel as a line. Finally, works on composite forcings affecting channel steepness need to be preformed in other heterogeneous landscape where multiple forcings are ambiguously present.

Bibliography

Abbühl, L. M., K. P. Norton, J. D. Jansen, F. Schlunegger, A. Aldahan, and G. Possnert (2011). "Erosion rates and mechanisms of knickzone retreat inferred from 10Be measured across strong climate gradients on the northern and central Andes Western Escarpment". In: *Earth Surface Processes and Landforms* 36.11, pp. 1464–1473. DOI: 10.1002/esp.2164.

Abrams, M., B. Bailey, H. Tsu, and M. Hato (2010). "The ASTER Global DEM". In: *Photogrammetric Engineering and Remote Sensing* 76.4, pp. 344–348.

Adams, J. M., N. M. Gasparini, D. E. Hobley, G. E. Tucker, E. W. Hutton, S. S. Nudurupati, et al. (2017). "The Landlab v1.0 OverlandFlow component: A Python tool for computing shallow-water flow across watersheds". In: *Geoscientific Model Development* 10.4, pp. 1645–1663. DOI: 10.5194/gmd-10-1645-2017.

Ahnert, F. (1970). "Functional relationships between denudation, relief, and uplift in large, mid-latitude drainage basins". In: *American Journal of Science* 268.3, pp. 243–263. DOI: 10.2475/ajs.268.3.243.

Akaike, H. (1974). "A New Look at the Statistical Model Identification". In: *IEEE Transactions on Automatic Control* 19.6, pp. 716–723. DOI: 10.1109/TAC.1974.1100705. arXiv: arXiv:1011.1669v3.

Alkmim, F. F. and S. Marshak (1998). "Transamazonian Orogeny in the Southern São Francisco Craton Region, Minas Gerais, Brazil: evidence for Paleoproterozoic collision and collapse in the Quadrilátero Ferrifero". In: *Precambrian Research* 90.1, pp. 29–58. DOI: 10.1016/S0301-9268(98)00032-1.

Allen, P. A. (2017). *Sediment routing systems : the fate of sediment from source to sink*, p. 407.

Alturani, I. M., A. Mahmoud, and I. Alturani (2013). *Review on Sorting Algorithms A Comparative Study*. Tech. rep. 3, pp. 120–126.

Andreucci, B., A. Castelluccio, S. Corrado, L. Jankowski, S. Mazzoli, R. Szaniawski, et al. (2015). "Interplay between the thermal evolution of an orogenic wedge and its retro-wedge basin: An example from the Ukrainian Carpathians". In: *Bulletin of the Geological Society of America* 127.3-4, pp. 410–427. DOI: 10.1130/B31067.1.

Armitage, J. J. (2019). "Short communication: Flow as distributed lines within the landscape". In: *Earth Surface Dynamics* 7.1, pp. 67–75. DOI: 10.5194/esurf-7-67-2019.

Arrowsmith, J. R., D. D. Rhodes, and D. D. Pollard (1998). "Morphologic dating of scarps formed by repeated slip events along the San Andreas Fault, Carrizo Plain, California". In: *Journal of Geophysical Research: Solid Earth* 103.B5, pp. 10141–10160. DOI: 10.1029/98jb00505.

Attal, M., P. A. Cowie, A. C. Whittaker, D. Hobley, G. E. Tucker, and G. P. Roberts (2011). "Testing fluvial erosion models using the transient response of bedrock rivers

to tectonic forcing in the Apennines, Italy". In: *Journal of Geophysical Research: Earth Surface* 116.2, F02005. DOI: 10.1029/2010JF001875.

Attal, M. and J. Lavé (2006). "Changes of bedload characteristics along the Marsyandi River (central Nepal): Implications for understanding hillslope sediment supply, sediment load evolution along fluvial networks, and denudation in active orogenic belts". In: *Special Paper of the Geological Society of America* 398, pp. 143–171. DOI: 10.1130/2006.2398(09).

Attal, M., G. E. Tucker, A. C. Whittaker, P. A. Cowie, and G. P. Roberts (2008). "Modelling fluvial incision and transient landscape evolution: Influence of dynamic Channel adjustment". In: *Journal of Geophysical Research: Earth Surface* 113.3, F03013. DOI: 10.1029/2007JF000893.

Aurelio, M. A., J. B. Galapon, V. T. Hizon, and D. B. Sadsad (2009). "Stress behavior from fault data sets within a transtensional zone, South Central Cordillera, Luzon, Philippines: Implications for mineral occurrences". In: *Island Arc* 18.1, pp. 144–154. DOI: 10.1111/j.1440-1738.2009.00661.x.

Avouac, J. P. and E. B. Burov (1996a). "Erosion as a driving mechanism of intracontinental mountain growth". In: *Journal of Geophysical Research: Solid Earth* 101.B8, pp. 17747–17769. DOI: 10.1029/96jb01344.

Avouac, J. P. and E. B. Burov (1996b). "Erosion as a driving mechanism of intracontinental mountain growth". In: *Journal of Geophysical Research: Solid Earth* 101.B8, pp. 17747–17769. DOI: 10.1029/96jb01344.

Baldwin, J. A., K. X. Whipple, and G. E. Tucker (2003). "Implications of the shear stress river incision model for the timescale of postorogenic decay of topography". In: *Journal of Geophysical Research: Solid Earth* 108.B3. DOI: 10.1029/2001JB000550.

Balteanu, D., V. Chendes, M. Sima, and P. Enciu (2010). "A country-wide spatial assessment of landslide susceptibility in Romania". In: *Geomorphology* 124.3-4, pp. 102–112. DOI: 10.1016/j.geomorph.2010.03.005.

Bamber, J. L., J. P. Muller, and A. Mandanayake (1997). "A Global 5 arc minute Digital Elevation Model derived from the geodetic phase of ERS-1". In: *European Space Agency, (Special Publication) ESA SP* 414 PART 3, pp. 1779–1787.

Barbosa, G. (1980). "Superfícies de erosão no Quadrilátero Ferrífero, Minas Gerais". In: *Brazilian Journal of Geology* 10.1, pp. 89–101.

Barnes, R., C. Lehman, and D. Mulla (2014). "Priority-flood: An optimal depression-filling and watershed-labeling algorithm for digital elevation models". In: *Computers and Geosciences* 62, pp. 117–127. DOI: 10.1016/j.cageo.2013.04.024. arXiv: 1511.04463.

Barnes, R. (2016a). "Parallel Priority-Flood depression filling for trillion cell digital elevation models on desktops or clusters". In: *Computers and Geosciences* 96, pp. 56–68. DOI: 10.1016/j.cageo.2016.07.001. arXiv: 1606.06204.

Barnes, R. (2016b). *RichDEM: Terrain Analysis Software*.

Barnes, R., K. L. Callaghan, and A. D. Wickert (2019). "Computing water flow through complex landscapes, Part 2: Finding hierarchies in depressions and morphological segmentations". In: *Computing water flow through complex landscapes, Part 2: Finding hierarchies in depressions and morphological segmentations*, pp. 1–19. DOI: 10.5194/esurf-2019-34.

Barrell, J. (1920). "The Piedmont terraces of the Northern Appalachians". In: *American Journal of Science* Series 4 V.293, pp. 327–362. DOI: 10.2475/ajs.s4-49.293.327.

Bascom, F. (1921). "Cycles of Erosion in the Piedmont Province of Pennsylvania". In: *The Journal of Geology* 29.6, pp. 540–559. DOI: 10.1086/622809.

Baynes, E. R. C., M. Attal, S. Niedermann, L. A. Kirstein, A. J. Dugmore, and M. Naylor (2015). "Erosion during extreme flood events dominates Holocene canyon evolution in northeast Iceland". In: *Proceedings of the National Academy of Sciences* 112.8, pp. 2355–2360. DOI: 10.1073/pnas.1415443112.

Baynes, E. R., D. Lague, M. Attal, A. Gangloff, L. A. Kirstein, and A. J. Dugmore (2018). "River self-organisation inhibits discharge control on waterfall migration". In: *Scientific Reports* 8.1, p. 2444. DOI: 10.1038/s41598-018-20767-6.

Beaumont, C. (1981). "Foreland basins". In: *Geophysical Journal International* 65.2, pp. 291–329. DOI: 10.1111/j.1365-246X.1981.tb02715.x.

Beaumont, C., P. Fullsack, and J. Hamilton (1992). "Erosional control of active compressional orogens". In: *Thrust Tectonics*. Dordrecht: Springer Netherlands, pp. 1–18. DOI: 10.1007/978-94-011-3066-0_1.

Behnel, S., R. Bradshaw, C. Citro, L. Dalcin, D. S. Seljebotn, and K. Smith (2011). "Cython: The Best of Both Worlds". In: *Computing in Science Engineering* 13.2, pp. 31–39. DOI: 10.1109/MCSE.2010.118.

Belayouni, H., A. Di Staso, F. Guerrera, M. Martín Martín, C. Miclăuş, F. Serrano, et al. (2009). "Stratigraphic and geochemical study of the organic-rich black shales in the Tarcău Nappe of the Moldavidian Domain (Carpathian Chain, Romania)". In: *International Journal of Earth Sciences* 98.1, pp. 157–176. DOI: 10.1007/s00531-007-0226-7.

Bennett, G. L., S. R. Miller, J. J. Roering, and D. A. Schmidt (2016). "Landslides, threshold slopes, and the survival of relict terrain in the wake of the Mendocino Triple Junction". In: *Geology* 44.5, pp. 363–366. DOI: 10.1130/G37530.1.

Bernard, T., H. D. Sinclair, B. Gailleton, S. M. Mudd, and M. Ford (2019). "Lithological control on the post-orogenic topography and erosion history of the Pyrenees". In: *Earth and Planetary Science Letters* 518, pp. 53–66. DOI: 10.1016/j.epsl.2019.04.034.

Bezerra, D. P. and D. Peifer Bezerra (2018). "The pattern and style of landscape evolution in post-orogenic settings". In: p. 271.

Biermann, P. and E. Steig (1996). "Estimating rates of denudation using cosmogenic isotope abundances in sediment". In: *Earth Surface Processes and Landforms* 21.2, pp. 125–139. DOI: 10.1002/(sici)1096-9837(199602)21:2<125::aid-esp511>3.0.co;2-8.

Bishop, P. (2007). "Long-term landscape evolution: Linking tectonics and surface processes". In: *Earth Surface Processes and Landforms* 32.3, pp. 329–365. DOI: 10.1002/esp.1493.

Bishop, P. and G. Goldrick (2010). "Lithology and the evolution of bedrock rivers in post-orogenic settings: constraints from the high-elevation passive continental margin of SE Australia". In: *Geological Society, London, Special Publications* 346.1, pp. 267–287. DOI: 10.1144/SP346.14.

Bocin, A., R. Stephenson, L. Matenco, and V. Mocanu (2013). "Gravity and magnetic modelling in the Vrancea Zone, south-eastern Carpathians: Redefinition of the edge of the East European Craton beneath the south-eastern Carpathians". In: *Journal of Geodynamics* 71, pp. 52–64. DOI: 10.1016/j.jog.2013.08.003.

Bocin, A., R. Stephenson, A. Tryggvason, I. Panea, V. Mocanu, F. Hauser, et al. (2005). "2.5D seismic velocity modelling in the south-eastern Romanian Carpathians Orogen and its foreland". In: *Tectonophysics* 410.1-4, pp. 273–291. DOI: 10.1016/j.tecto.2005.05.045.

Bocin, A., R. Stephenson, V. Mocanu, and L. Matenco (2009). "Architecture of the south-eastern Carpathians nappes and Focsani Basin (Romania) from 2D ray tracing of densely-spaced refraction data". In: *Tectonophysics* 476.3-4, pp. 512–527. DOI: 10.1016/j.tecto.2009.07.027.

Bokelmann, G. and F. A. Rodler (2014). "Nature of the Vrancea seismic zone (Eastern Carpathians) - New constraints from dispersion of first-arriving P-waves". In: *Earth and Planetary Science Letters* 390, pp. 59–68. DOI: 10.1016/j.epsl.2013.12.034.

Bookhagen, B. and D. W. Burbank (2010). "Toward a complete Himalayan hydrological budget: Spatiotemporal distribution of snowmelt and rainfall and their impact on river discharge". In: *Journal of Geophysical Research: Earth Surface* 115.F3.

Borgh, M. M. ter (2013a). "Connections between sedimentary basins during continental collision". PhD thesis, p. 204.

Borgh, M. M. ter (2013b). "Connections between sedimentary basins during continental collision : how tectonic, surface and sedimentary processen shaped the Paratethys". PhD. Utrecht University.

Boulton, S. J. and M. Stokes (2018). "Which DEM is best for analyzing fluvial landscape development in mountainous terrains?" In: *Geomorphology* 310, pp. 168–187. DOI: 10.1016/j.geomorph.2018.03.002.

Bovy, B. and G. McBain (2019). "benbovy/xarray-simlab: 0.3.0". In: DOI: 10.5281/ZENODO.3465820.

Bovy, B. (2019). "fastscape-lem/fastscape: v0.1.0alpha". In: DOI: 10.5281/ZENODO.3479426.

Braun, J. (2010). "The many surface expressions of mantle dynamics". In: *Nature Geoscience* 3.12, pp. 825–833. DOI: 10.1038/ngeo1020.

Braun, J. and S. D. Willett (2013). "A very efficient O(n), implicit and parallel method to solve the stream power equation governing fluvial incision and landscape evolution". In: *Geomorphology* 180-181, pp. 170–179. DOI: 10.1016/j.geomorph.2012.10.008.

Braun, J., T. Simon-Labric, K. E. Murray, and P. W. Reiners (2014). "Topographic relief driven by variations in surface rock density". In: *Nature Geosci* 7.7, pp. 534–540. DOI: 10.1038/NGEO2171.

Brown, E. T., R. F. Stallard, M. C. Larsen, G. M. Raisbeck, and F. Yiou (1995). "Denudation rates determined from the accumulation of in situ-produced 10Be in the luquillo experimental forest, Puerto Rico". In: *Earth and Planetary Science Letters* 129.1-4, pp. 193–202. DOI: 10.1016/0012-821X(94)00249-X.

Buffon, G. (1767). *Histoire naturelle générale et particulière.(Théorie de la terre; histoire naturelle de l'homme; animaux quadrupèdes) Par Buffon et Daubenton.*

Burbank, D. W., J. Leland, E. Fielding, R. S. Anderson, N. Brozovic, M. R. Reid, et al. (1996). "Bedrock incision, rock uplift and threshold hillslopes in the northwestern Himalayas". In: *Nature* 379.6565, pp. 505–510. DOI: 10.1038/379505a0.

Campforts, B., W. Schwanghart, and G. Govers (2017). "Accurate simulation of transient landscape evolution by eliminating numerical diffusion: The TTLEM 1.0 model". In: *Earth Surface Dynamics* 5.1, pp. 47–66. DOI: 10.5194/esurf-5-47-2017.

Campforts, B., V. Vanacker, F. Herman, M. Vanmaercke, W. Schwanghart, G. Tenorio, et al. (2019). "Lithology and orographic precipitation control river incision in the tropical Andes". In: *Earth Surface Dynamics Discussions*, pp. 1–43. DOI: 10.5194/esurf-2019-48.

Castelltort, S., L. Goren, S. D. Willett, J.-D. Champagnac, F. Herman, and J. Braun (2012). "River drainage patterns in the New Zealand Alps primarily controlled by

plate tectonic strain". In: *Nature Geoscience* 5.10, pp. 744–748. DOI: 10.1038/ngeo1582.

Chemale, F., C. A. Rosière, and I. Endo (1994). "The tectonic evolution of the Quadrilátero Ferrífero, Minas Gerais, Brazil". In: *Precambrian Research* 65.1, pp. 25–54. DOI: 10.1016/0301-9268(94)90098-1.

Chen, S.-A., K. Michaelides, S. W. D. Grieve, and M. B. Singer (2019). "Aridity is expressed in river topography globally". In: *Nature* 573.7775, pp. 573–577. DOI: 10.1038/s41586-019-1558-8.

Chen, Y. C., Q. Sung, and K. Y. Cheng (2003). "Along-strike variations of morphotectonic features in the Western Foothills of Taiwan: Tectonic implications based on stream-gradient and hypsometric analysis". In: *Geomorphology* 56.1-2, pp. 109–137. DOI: 10.1016/S0169-555X(03)00059-X.

Clark, M. K., L. M. Schoenbohm, L. H. Royden, K. X. Whipple, B. C. Burchfiel, X. Zhang, et al. (2004). "Surface uplift, tectonics, and erosion of eastern Tibet from large-scale drainage patterns". In: *Tectonics* 23.1.

Clubb, F. J., S. M. Mudd, D. T. Milodowski, M. D. Hurst, and L. J. Slater (2014). "Objective extraction of channel heads from high-resolution topographic data". In: *Water Resources Research* 50.5, pp. 4283–4304. DOI: 10.1002/2013WR015167. arXiv: 2014WR016527 [10.1002].

Clubb, F. J., B. Bookhagen, and A. Rheinwalt (2019). "Clustering River Profiles to Classify Geomorphic Domains". In: *Journal of Geophysical Research: Earth Surface* 124.6, pp. 1417–1439. DOI: 10.1029/2019JF005025.

Clubb, F. J., S. M. Mudd, M. D. Hurst, and S. W. Grieve (2020). "Differences in channel and hillslope geometry record a migrating uplift wave at the Mendocino triple junction, California, USA". In: *Geology* 48.2, pp. 184–188. DOI: 10.1130/G46939.1.

Codilean, A. T., H. Munack, T. J. Cohen, W. M. Saktura, A. Gray, and S. M. Mudd (2018). "OCTOPUS: An open cosmogenic isotope and luminescence database". In: *Earth System Science Data* 10.4, pp. 2123–2139. DOI: 10.5194/essd-10-2123-2018.

Condat, L. (2013). "A Direct Algorithm for 1D Total Variation Denoising". In: *IEEE SIGNAL PROC. LETTERS* 20.11, pp. 1054–1057. DOI: 10.1109/LSP.2013.2278339.

contributors, G. (2020). Open Source Geospatial Foundation.

Cook, K. L., J. M. Turowski, and N. Hovius (2013). "A demonstration of the importance of bedload transport for fluvial bedrock erosion and knickpoint propagation". In: *Earth Surface Processes and Landforms* 38.7, pp. 683–695. DOI: 10.1002/esp.3313.

Cordonnier, G., B. Bovy, and J. Braun (2018). "A Versatile, Linear Complexity Algorithm for Flow Routing in Topographies with Depressions". In: *Earth Surface Dynamics Discussions* 7.2, pp. 1–18. DOI: 10.5194/esurf-2018-81.

Cristea, A. I. (2015). "Spatial analysis of channel steepness in a tectonically active region: Putna river catchment (South-Eastern Carpathians)". In: *Geographia Technica* 10.1, pp. 19–27.

Cristea, A. I. (2014). "Assessment of recent tectonic evolution and geomorphic response in SE Carpathians (Romania) using hypsometric analysis". In: *GEOREVIEW: Scientific Annals of Stefan cel Mare University of Suceava. Geography Series* 24.1, pp. 76–88. DOI: 10.4316/GEOREVIEW.2014.24.1.265.

Croissant, T. and J. Braun (2014). "Constraining the stream power law: A novel approach combining a landscape evolution model and an inversion method". In: *Earth Surface Dynamics* 2.1, pp. 155–166. DOI: 10.5194/esurf-2-155-2014.

Crosby, B. T. and K. X. Whipple (2006). "Knickpoint initiation and distribution within fluvial networks: 236 waterfalls in the Waipaoa River, North Island, New Zealand". In: *Geomorphology* 82.1-2, pp. 16–38. DOI: 10.1016/j.geomorph.2005.08.023.

Crosby, T., B. Iglewicz, and D. C. Hoaglin (1994). "How to Detect and Handle Outliers". In: *Technometrics* 36.3, p. 315. DOI: 10.2307/1269377.

Csontos, L. and A. Vörös (2004). *Mesozoic plate tectonic reconstruction of the Carpathian region*. DOI: 10.1016/j.palaeo.2004.02.033.

Cyr, A. J., D. E. Granger, V. Olivetti, and P. Molin (2010). "Quantifying rock uplift rates using channel steepness and cosmogenic nuclide–determined erosion rates: Examples from northern and southern Italy". In: *Lithosphere* 2.3, pp. 188–198. DOI: 10.1130/L96.1.

Dahlen, F. A. (1990). "Critical taper model of fold-and-thrust belts and accretionary wedges". In: *Annual Review of Earth Planetary Sciences* 18, pp. 55–99. DOI: 10.1146/annurev.ea.18.050190.000415.

Davis, W. M. (1889). "The Geographical Cycle". In: *The Geographical Journal* 14.5, pp. 481–504. DOI: 10.1086/521238.

Davy, P. and D. Lague (2009). "Fluvial erosion/transport equation of landscape evolution models revisited". In: *Journal of Geophysical Research: Solid Earth* 114.3. DOI: 10.1029/2008JF001146.

Davy, P., T. Croissant, and D. Lague (2017). "A precipiton method to calculate river hydrodynamics, with applications to flood prediction, landscape evolution models, and braiding instabilities". In: *Journal of Geophysical Research: Earth Surface* 122.8, pp. 1491–1512. DOI: 10.1002/2016JF004156.

DiBiase, R. A., K. X. Whipple, A. M. Heimsath, and W. B. Ouimet (2010). "Landscape form and millennial erosion rates in the San Gabriel Mountains, CA". In: *Earth and Planetary Science Letters* 289.1-2, pp. 134–144. DOI: 10.1016/j.epsl.2009.10.036.

DiBiase, R. A. and K. X. Whipple (2011). "The influence of erosion thresholds and runoff variability on the relationships among topography, climate, and erosion rate". In: *Journal of Geophysical Research: Earth Surface* 116.4. DOI: 10.1029/2011JF002095.

Dickinson, W. R. (1974). "Plate tectonics and sedimentation". In:

Dietrich, W. E., D. G. Bellugi, L. S. Sklar, J. D. Stock, A. M. Heimsath, and J. J. Roering (2003). "Geomorphic transport laws for predicting landscape form and dynamics". In: *Geophysical Monograph Series*. Vol. 135, pp. 103–132. DOI: 10.1029/135GM09.

Dingle, H. E., D. H. Sinclair, M. Attal, A. Rodés, and V. Singh (2018). "Temporal variability in detrital 10Be concentrations in a large Himalayan catchment". In: *Earth Surface Dynamics* 6.3, pp. 611–635. DOI: 10.5194/esurf-6-611-2018.

"Dominance of tectonics over climate in himalayan denudation" (2014). In: *Geology* 42.3, pp. 243–246. DOI: 10.1130/G35342.1.

Dorr, J. V. N. (1969). "Physiographic, stratigraphic, and structural development of the Quadrilatero Ferrifero, Minas Gerais, Brazil". In: *Geological Survey Professional Paper* 641-A, p. 110.

Duley, F. L. and M. F. Miller (1923). *Erosion and surface runoff under different soil conditions*.

Duvall, A. (2004). "Tectonic and lithologic controls on bedrock channel profiles and processes in coastal California". In: *Journal of Geophysical Research* 109.F3. DOI: 10.1029/2003jf000086.

Eizenhöfer, P. R., N. McQuarrie, E. Shelef, and T. A. Ehlers (2019). "Landscape Response to Lateral Advection in Convergent Orogens Over Geologic Time Scales". In: *Journal of Geophysical Research: Earth Surface* 124.8, pp. 2056–2078. DOI: 10.1029/2019jf005100.

F.J., C. (2017). *Controls on fluvial networks in upland landscapes : from hillslopes to floodplains*.

Faccenna, C. and T. W. Becker (2010). "Shaping mobile belts by small-scale convection". In: *Nature* 465.7298, pp. 602–605. DOI: 10.1038/nature09064.

Farr, T. G., P. A. Rosen, E. Caro, R. Crippen, R. Duren, S. Hensley, et al. (2007). "The shuttle radar topography mission". In: *Reviews of Geophysics* 45.2. DOI: 10.1029/2005RG000183.

Fellin, M. G., M. Zattin, V. Picotti, P. W. Reiners, and S. Nicolescu (2005). "Relief evolution in northern Corsica (western Mediterranean): Constraints on uplift and erosion on long-term and short-term timescales". In: *Journal of Geophysical Research: Earth Surface* 110.1, F01016. DOI: 10.1029/2004JF000167.

Fielitz, W. and I. Seghedi (2005). "Late Miocene–Quaternary volcanism, tectonics and drainage system evolution in the East Carpathians, Romania". In: *Tectonophysics* 410.1, pp. 111–136. DOI: 10.1016/j.tecto.2004.10.018.

Flint, J. J. (1974). "Stream gradient as a function of order, magnitude, and discharge". In: *Water Resources Research* 10.5, pp. 969–973. DOI: 10.1029/WR010i005p00969.

Font, M., D. Amorese, and J. L. Lagarde (2010). "DEM and GIS analysis of the stream gradient index to evaluate effects of tectonics: The Normandy intraplate area (NW France)". In: *Geomorphology* 119.3-4, pp. 172–180. DOI: 10.1016/j.geomorph.2010.03.017.

Forbes, R. H. (1902). "The river irrigating waters of Arizona - Their character and effects". In: *University of Arizona Agricultural Experiment Station Bulletin* 44, pp. 147–214.

Forte, A. M., B. J. Yanites, and K. X. Whipple (2016). "Complexities of landscape evolution during incision through layered stratigraphy with contrasts in rock strength". In: *Earth Surface Processes and Landforms* 41.12, pp. 1736–1757. DOI: 10.1002/esp.3947.

Forte, A. M. and K. X. Whipple (2018). "Criteria and tools for determining drainage divide stability". In: *Earth and Planetary Science Letters* 493, pp. 102–117. DOI: 10.1016/j.epsl.2018.04.026.

Forte, A. M. and K. X. Whipple (2019). "Short communication: The Topographic Analysis Kit (TAK) for TopoToolbox". In: *Earth Surface Dynamics* 7.1, pp. 87–95. DOI: 10.5194/esurf-7-87-2019.

Forzoni, A., J. E. A. Storms, T. Reimann, J. Moreau, and G. Jouet (2015). "Non-linear response of the Golo River system, Corsica, France, to Late Quaternary climatic and sea level variations". In: *Quaternary Science Reviews* 121, pp. 11–27. DOI: 10.1016/j.quascirev.2015.04.021.

Fox, M., L. Goren, D. A. May, and S. D. Willett (2014). "Inversion of fluvial channels for paleorock uplift rates in Taiwan". In: *Journal of Geophysical Research: Earth Surface* 119.9, pp. 1853–1875. DOI: 10.1002/2014jf003196.

Gabet, E. J. (2019). "Lithological and structural controls on river profiles and networks in the northern Sierra Nevada (California, USA)". In: *GSA Bulletin*. DOI: 10.1130/b35128.1.

Gailleton, B., S. M. Mudd, F. J. Clubb, D. Peifer, and M. D. Hurst (2019). "A segmentation approach for the reproducible extraction and quantification of knickpoints from river long profiles". In: *Earth Surface Dynamics* 7.1, pp. 211–230. DOI: 10.5194/esurf-7-211-2019.

Gallen, S. F., K. W. Wegmann, and D. W. R. Bohnenstiehl (2013). "Miocene rejuvenation of topographic relief in the southern Appalachians". In: *GSA Today* 23.2, pp. 4–10. DOI: 10.1130/GSATG163A.1.

Gallen, S. F. and K. W. Wegmann (2017). "River profile response to normal fault growth and linkage: An example from the Hellenic forearc of south-central Crete, Greece". In: *Earth Surface Dynamics* 5.1, pp. 161–186. DOI: 10.5194/esurf-5-161-2017.

Gasparini, N. M., G. E. Tucker, and R. L. Bras (2004). "Network-scale dynamics of grain-size sorting: implications for downstream fining, stream-profile concavity, and drainage basin morphology". In: *Earth Surface Processes and Landforms* 29.4, pp. 401–421. DOI: 10.1002/esp.1031.

Gasparini, N. M. and M. T. Brandon (2011). "A generalized power law approximation for fluvial incision of bedrock channels". In: *Journal of Geophysical Research: Earth Surface* 116.2, pp. 1–16. DOI: 10.1029/2009JF001655.

Gasparini, N. M. and K. X. Whipple (2014). "Diagnosing climatic and tectonic controls on topography: Eastern flank of the northern Bolivian Andes". In: *Lithosphere* 6.4, pp. 230–250. DOI: 10.1130/L322.1.

Gasparini, N. M., K. X. Whipple, and R. L. Bras (2007). "Predictions of steady state and transient landscape morphology using sediment-flux-dependent river incision models". In: *Journal of Geophysical Research: Earth Surface* 112.3. DOI: 10.1029/2006JF000567.

Gesch, D., M. Oimoen, J. Danielson, and D. Meyer (2016). "Validation of the Aster Global Digital Elevation Model Version 3 Over the Conterminous United States". In: *ISPRS - International Archives of the Photogrammetry, Remote Sensing and Spatial Information Sciences* XLI-B4, pp. 143–148. DOI: 10.5194/isprs-archives-xli-b4-143-2016.

Gesch, D. B., K. L. Verdin, and S. K. Greenlee (1999). "New land surface digital elevation model covers the earth". In: *Eos* 80.6, pp. 69–70. DOI: 10.1029/99EO00050.

Giachetta, E. and S. D. Willett (2018a). "Effects of river capture and sediment flux on the evolution of plateaus: Insights from numerical modeling and river profile analysis in the upper blue nile catchment". In: *Journal of Geophysical Research: Earth Surface* 123.6, pp. 1187–1217. DOI: 10.1029/2017JF004252.

Giachetta, E. and S. D. Willett (2018b). "A global dataset of river network geometry". In: *Scientific data* 5, p. 180127.

Giachetta, E. and S. D. Willett (2018c). "Data Descriptor: A global dataset of river network geometry". In: *Scientific Data* 5.1, pp. 1–10. DOI: 10.1038/sdata.2018.127.

Gilbert, G. K. (1877). *Geology of the Henry Mountains*. USGS Unnumbered Series. Washington, D.C.: Government Printing Office, p. 196.

Gilbert, G. (1880). "Report on the Geology of the Henry Mountains". In:

Gillies, S. et al. (2007). *Shapely: manipulation and analysis of geometric objects*.

Gillies, S. et al. (2019). *Rasterio: geospatial raster I/O for Python programmers*.

Giustacchini, A., S. Thongjuea, N. Barkas, P. S. Woll, B. J. Povinelli, C. A. Booth, et al. (2017). "Single-cell transcriptomics uncovers distinct molecular signatures of stem cells in chronic myeloid leukemia". In: *Nature Medicine* 23.6, pp. 692–702. DOI: 10.1038/nm.4336.

Gleadow, A. J., I. R. Duddy, and J. F. Lovering (1983). "Fission Track Analysis: a New Tool for the Evaluation of Thermal Histories and Hydrocarbon Potential." In: *APEA journal* 23.pt 1, pp. 93–102. DOI: 10.1071/aj82009.

Glenn, L. (1911). *Denudation and erosion in the southern Appalachian region*. Tech. rep. 9, pp. 474–478. DOI: 10.1080/14702541108554043.

Goldrick, G. and P. Bishop (1995). "Differentiating the roles of lithology and uplift in the steepening of bedrock river long profiles: an example from southeastern Australia". In: *Journal of Geology* 103.2, pp. 227–231. DOI: 10.1086/629738.

Goldrick, G. and P. Bishop (2007). "Regional analysis of bedrock stream long profiles: Evaluation of Hack's SL form, and formulation and assessment of an alternative (the DS form)". In: *Earth Surface Processes and Landforms* 32.5, pp. 649–671. DOI: 10.1002/esp.1413.

Gonga-Saholiariliva, N., Y. Gunnell, D. Harbor, and C. Mering (2011). "An automated method for producing synoptic regional maps of river gradient variation: Procedure, accuracy tests, and comparison with other knickpoint mapping methods". In: *Geomorphology* 134.3-4, pp. 394–407. DOI: 10.1016/j.geomorph.2011.07.013.

Goren, L., M. Fox, and S. D. Willett (2014). "Tectonics from fluvial topography using formal linear inversion: Theory and applications to the Inyo Mountains, California". In: *Journal of Geophysical Research F: Earth Surface* 119.8, pp. 1651–1681. DOI: 10.1002/2014JF003079.

Goren, L. (2016). "A theoretical model for fluvial channel response time during time-dependent climatic and tectonic forcing and its inverse applications". In: *Geophysical Research Letters* 43.20, pp. 10, 753–10, 763. DOI: 10.1002/2016GL070451.

Graf, E., M. Attal, S. Mudd, and B. Yanites (2017). *The role of lithology in controlling the rate of landscape response to perturbations*. Tech. rep., pp. 2017–6890.

Grieve, S. W. D., T. C. Hales, R. N. Parker, S. M. Mudd, and F. J. Clubb (2018). "Controls on Zero-Order Basin Morphology". In: *Journal of Geophysical Research: Earth Surface* 123.12, pp. 3269–3291. DOI: 10.1029/2017JF004453.

Grieve, S. W., S. M. Mudd, D. T. Milodowski, F. J. Clubb, and D. J. Furbish (2016). "How does grid-resolution modulate the topographic expression of geomorphic processes?" In: *Earth Surface Dynamics* 4.3, pp. 627–653. DOI: 10.5194/esurf-4-627-2016.

Gröger, H. R., B. Fügenschuh, M. Tischler, S. M. Schmid, and J. P. Foeken (2008). "Tertiary cooling and exhumation history in the Maramures area (internal eastern Carpathians, northern Romania): Thermochronology and structural data". In: *Geological Society Special Publication* 298.1, pp. 169–195. DOI: 10.1144/SP298.9.

Guerit, L., X.-P. Yuan, S. Carretier, S. Bonnet, S. Rohais, J. Braun, et al. (2019). "Fluvial landscape evolution controlled by the sediment deposition coefficient: Estimation from experimental and natural landscapes". In: *Geology* 47.9, pp. 853–856. DOI: 10.1130/g46356.1.

Gupta, S. (1997). "Himalayan drainage patterns and the origin of fluvial megafans in the Ganges foreland basin". In: *Geology* 25.1, pp. 11–14. DOI: 10.1130/0091-7613(1997)025<0011:HDPATO>2.3.CO;2.

Hack, J. T. (1960). "Interpretation of erosional topography in humid temperate regions". In: *American Journal of Science* 258-A.A, pp. 80–97.

Hack, J. (1957). *Studies of longitudinal stream profiles in Virginia and Maryland*, p. 97.

Hack, J. T. (1973). "Stream-profile analysis and stream-gradient index". In: *Journal of Research of the us Geological Survey* 1.4, pp. 421–429.

Harder, E. C. and R. T. Chamberlin (1915). "The Geology of Central Minas Gerais, Brazil: Part II". In: *The Journal of Geology* 23.5, pp. 385–424. DOI: 10.1086/622256.

Harel, M. A., S. M. Mudd, and M. Attal (2016). "Global analysis of the stream power law parameters based on worldwide 10Be denudation rates". In: *Geomorphology* 268, pp. 184–196. DOI: 10.1016/j.geomorph.2016.05.035.

Harkins, N., E. Kirby, A. Heimsath, R. Robinson, and U. Reiser (2007). "Transient fluvial incision in the headwaters of the Yellow River, northeastern Tibet, China". In: *Journal of Geophysical Research: Earth Surface* 112.3. DOI: 10.1029/2006JF000570.

Hauser, F., V. Raileanu, W. Fielitz, C. Dinu, M. Landes, A. Bala, et al. (2007). "Seismic crustal structure between the Transylvanian Basin and the Black Sea, Romania". In: *Tectonophysics* 430.1-4, pp. 1–25. DOI: 10.1016/j.tecto.2006.10.005.

Haviv, I., Y. Enzel, K. X. Whipple, E. Zilberman, A. Matmon, J. Stone, et al. (2010). "Evolution of vertical knickpoints (waterfalls) with resistant caprock: Insights from numerical modeling". In: *Journal of Geophysical Research: Earth Surface* 115.3, F03028. DOI: 10.1029/2008JF001187.

Hayakawa, Y. S. and T. Oguchi (2006). "DEM-based identification of fluvial knickzones and its application to Japanese mountain rivers". In: *Geomorphology* 78.1-2, pp. 90–106. DOI: 10.1016/j.geomorph.2006.01.018.

Hein, A. S., T. J. Dunai, N. R. Hulton, and S. Xu (2011). "Exposure dating outwash gravels to determine the age of the greatest Patagonian glaciations". In: *Geology* 39.2, pp. 103–106. DOI: 10.1130/G31215.1.

Heipke, C., H. Mayer, C. Wiedemann, and O. Jamet (1997). *Evaluation of Automatic Road Extraction*. Tech. rep., pp. 151–156. DOI: 10.1.1.30.7686.

Hergarten, S., J. Robl, and K. Stuwe (2016). "Tectonic geomorphology at small catchment sizes-extensions of the stream-power approachand the x method". In: *Earth Surface Dynamics* 4.1, pp. 1–9. DOI: 10.5194/esurf-4-1-2016.

Hilley, G. E., S. Porder, F. Aron, C. W. Baden, S. A. Johnstone, F. Liu, et al. (2019). "Earth's topographic relief potentially limited by an upper bound on channel steepness". In: *Nature Geoscience* 12.10, pp. 828–832. DOI: 10.1038/s41561-019-0442-3.

Hobley, D. E., J. M. Adams, S. Siddhartha Nudurupati, E. W. Hutton, N. M. Gasparini, E. Istanbulluoglu, et al. (2017). "Creative computing with Landlab: An open-source toolkit for building, coupling, and exploring two-dimensional numerical models of Earth-surface dynamics". In: *Earth Surface Dynamics* 5.1, pp. 21–46. DOI: 10.5194/esurf-5-21-2017.

Hoeven, A. A. van der, V. Mocanu, W. Spakman, M. Nutto, A. Nuckelt, L. Matenco, et al. (2005). "Observation of present-day tectonic motions in the Southeastern Carpathians: Results of the ISES/CRC-461 GPS measurements". In: *Earth and Planetary Science Letters* 239.3-4, pp. 177–184. DOI: 10.1016/j.epsl.2005.09.018.

Horton, R. E. (1945). "Erosional Development of Streams and their Drainage Basins: Hydrophysical Approach to Quantitative Morphology". In: *GSA Bulletin* 56.3, pp. 275–370. DOI: 10.1130/0016-7606(1945)56[275:edosat]2.0.co;2.

Houk, I. (1918). "Calculation of Flow in Open Channels: State of Ohio, the Miami Conservancy District". In:

Howard, a. D. (1965). "Geomorphological systems; equilibrium and dynamics". In: *American Journal of Science* 263, pp. 302–312. DOI: 10.2475/ajs.263.4.302.

Howard, A. D. and G. Kerby (1983). "Channel changes in badlands". In: *Geological Society of America Bulletin* 94.6, p. 739. DOI: 10.1130/0016-7606(1983)94<739:CCIB>2.0.CO;2.

Howard, A. D., W. E. Dietrich, and M. A. Seidl (1994). "Modeling fluvial erosion on regional to continental scales". In: *Journal of Geophysical Research: Solid Earth* 99.B7, pp. 13971–13986. DOI: 10.1029/94JB00744.

Hunter, J. D. (2007). "Matplotlib: A 2D graphics environment". In: *Computing in Science and Engineering* 9.3, pp. 99–104. DOI: 10.1109/MCSE.2007.55.

Hurst, M. D., S. M. Mudd, M. Attal, and G. Hilley (2013). "Hillslopes record the growth and decay of landscapes". In: *Science* 341.6148, pp. 868–871. DOI: 10.1126/science.1241791.

Hurst, M. D., S. W. Grieve, F. J. Clubb, and S. M. Mudd (2019). "Detection of channel-hillslope coupling along a tectonic gradient". In: *Earth and Planetary Science Letters* 522, pp. 30–39. DOI: 10.1016/j.epsl.2019.06.018.

Hurtrez, J.-E., F. Lucazeau, J. Lavé, and J.-P. Avouac (1999). "Investigation of the relationships between basin morphology, tectonic uplift, and denudation from the study of an active fold belt in the Siwalik Hills, central Nepal". In: *Journal of Geophysical Research: Solid Earth* 104.B6, pp. 12779–12796. DOI: 10.1029/1998jb900098.

Hurvich, C. M. and C. L. Tsai (1989). *Regression and time series model selection in small samples*. Tech. rep. 2, pp. 297–307. DOI: 10.1093/biomet/76.2.297.

Ismail-Zadeh, A., L. Matenco, M. Radulian, S. Cloetingh, and G. Panza (2012). *Geodynamics and intermediate-depth seismicity in Vrancea (the south-eastern Carpathians): Current state-of-the art*. DOI: 10.1016/j.tecto.2012.01.016.

Ivan, M. (2007). "Attenuation of P and pP waves in Vrancea area - Romania". In: *Journal of Seismology* 11.1, pp. 73–85. DOI: 10.1007/s10950-006-9038-7.

James, P. E. (1933). "The surface configuration of southeastern Brazil". In: *Annals of the Association of American Geographers* 23.3, pp. 165–193.

Jipa, D. C. and C. Olariu (2013). "Sediment routing in a semi-enclosed epicontinental sea: Dacian Basin, Paratethys domain, Late Neogene, Romania". In: *Global and Planetary Change* 103.1, pp. 193–206. DOI: 10.1016/j.gloplacha.2012.06.009.

Joja, T., V. Mutihac, and M. Muresan (1968). *Crystalline-Mesozoic and Flysch Complexes of the East Carpathians (Northern Sector)*. Geological Institute, pp. 5–63.

Jones, E., T. Oliphant, P. Peterson, et al. (2015). *SciPy: Open Source Scientific Tools for Python, 2001 (http://www.scipy.org/)*.

Jones, O. T. (1924). *The upper Towy drainage-system*. Tech. rep. 1-4, pp. 568–609. DOI: 10.1144/GSL.JGS.1924.080.01-04.27.

King, L. C. (1956). "A geomorfologia do Brasil oriental". In: *Revista Brasileira de Geografia* 2, pp. 147–265.

Kirby, E. and K. Whipple (2001a). "Quantifying differential rock-uplift rates via stream profile analysis". In: *Geology* 29.5, pp. 415–418. DOI: 10.1130/0091-7613(2001)029<0415:QDRURV>2.0.CO;2.

Kirby, E. and K. Whipple (2001b). "Quantifying differential rock-uplift rates via stream profile analysis". In: p. 4.

Kirby, E., K. X. Whipple, W. Tang, and Z. Chen (2003). "Distribution of active rock uplift along the eastern margin of the Tibetan Plateau: Inferences from bedrock channel longitudinal profiles". In: *Journal of Geophysical Research: Solid Earth* 108.B4, p. 2217. DOI: 10.1029/2001jb000861.

Kirby, E. and K. X. Whipple (2012). *Expression of active tectonics in erosional landscapes*. DOI: 10.1016/j.jsg.2012.07.009.

Knopf, E. B. (1924). "Correlation of residual erosion surfaces in the eastern appalachian highlands". In: *Bulletin of the Geological Society of America* 35.3, pp. 633–668. DOI: 10.1130/GSAB-35-633.

Krieger, G., A. Moreira, H. Fiedler, I. Hajnsek, M. Werner, M. Younis, et al. (2007). "TanDEM-X: A satellite formation for high-resolution SAR interferometry". In: *IEEE Transactions on Geoscience and Remote Sensing*. Vol. 45. 11, pp. 3317–3340. DOI: 10.1109/TGRS.2007.900693.

Lague, D. and P. Davy (2003). "Constraints on the long-term colluvial erosion law by analyzing slope-area relationships at various tectonic uplift rates in the Siwaliks Hills (Nepal)". In: *Journal of Geophysical Research: Solid Earth* 108.B2. DOI: 10.1029/2002jb001893.

Lague, D. (2014). "The stream power river incision model: Evidence, theory and beyond". In: *Earth Surface Processes and Landforms* 39.1, pp. 38–61. DOI: 10.1002/esp.3462.

Lal, D. (1991). "Cosmic ray labeling of erosion surfaces: in situ nuclide production rates and erosion models". In: *Earth and Planetary Science Letters* 104.2-4, pp. 424–439. DOI: 10.1016/0012-821X(91)90220-C.

Lam, S. K., A. Pitrou, and S. Seibert (2015). "Numba". In: *Proceedings of the Second Workshop on the LLVM Compiler Infrastructure in HPC - LLVM '15*. New York, New York, USA: Association for Computing Machinery (ACM), pp. 1–6. DOI: 10.1145/2833157.2833162.

Lambeck, K. and J. Chappell (2001). "Sea level change through the last glacial cycle." In: *Science (New York, N.Y.)* 292.5517, pp. 679–86. DOI: 10.1126/science.1059549.

Lapparent, A. de and A. A. C. de Lapparent (1896). *Lecons de géographie physique*. Masson et. Paris: Masson et c', éditeurs, p. 390.

Lavé, J. and J. P. Avouac (2001). "Fluvial incision and tectonic uplift across the Himalayas of central Nepal". In: *Journal of Geophysical Research: Solid Earth* 106.B11, pp. 26561–26591. DOI: 10.1029/2001jb000359.

Leever, K. A., L. Matenco, D. Garcia-Castellanos, and S. A. P. L. Cloetingh (2011). "The evolution of the Danube gateway between Central and Eastern Paratethys (SE Europe): Insight from numerical modelling of the causes and effects of connectivity between basins and its expression in the sedimentary record". In: *Tectonophysics* 502.1-2, pp. 175–195. DOI: 10.1016/j.tecto.2010.01.003.

Leever, K. (2007). "Foreland of the Romanian Carpathians, controls on late orogenic sedimentary basin evolution and Paratethys paleogeography". PhD. VU University Amsterdam.

Leever, K. A., L. Matenco, G. Bertotti, S. Cloetingh, and G. G. Drijkoningen (2006). "Late orogenic vertical movements in the Carpathian Bend Zone - Seismic constraints on the transition zone from orogen to foredeep". In: *Basin Research* 18.4, pp. 521–545. DOI: 10.1111/j.1365-2117.2006.00306.x.

Leever, K. A., L. Matenco, T. Rabagia, S. Cloetingh, W. Krijgsman, and M. Stoica (2010). "Messinian sea level fall in the Dacic Basin (Eastern Paratethys): Palaeogeographical implications from seismic sequence stratigraphy". In: *Terra Nova* 22.1, pp. 12–17. DOI: 10.1111/j.1365-3121.2009.00910.x.

Lehner, B., K. Verdin, and A. Jarvis (2008). "New global hydrography derived from spaceborne elevation data". In: *Eos* 89.10, pp. 93–94. DOI: 10.1029/2008EO100001.

Lensen, G. J. (1964). "The General Case of Progressive Fault Displacement of Flights of Degradational Terraces". In: *New Zealand Journal of Geology and Geophysics* 7.4, pp. 864–870. DOI: 10.1080/00288306.1964.10428134.

Leopold, I. B. and J. P. Miller (1962). "Ephemeral sttreams - hydraulic factors and their relation to the drainage net." In: *USGS Professional Paper* 282a, pp. 1–35. DOI: 10.3133/PP282A.

Leopold, L. B. and T. J. Maddock (1953). *The Hydraulic Geometry of Stream Channels and Some Physiographic Implications*. Tech. rep., p. 57.

Libby, W. F., E. C. Anderson, and J. R. Arnold (1949). "Age determination by radiocarbon content: World-wide assay of natural radiocarbon". In: *Science* 109.2827, pp. 227–228. DOI: 10.1126/science.109.2827.227.

Lindsay, J. B. (2016). "Efficient hybrid breaching-filling sink removal methods for flow path enforcement in digital elevation models". In: *Hydrological Processes* 30.6, pp. 846–857. DOI: 10.1002/hyp.10648.

Lindvall, S. C. and C. M. Rubin (2008). *Slip Rate Studies along the Sierra Madre–Cucamonga Fault System Using Geomorphic and Cosmogenic Surface Exposure Age Constraints: Collaborative Research with Central Washington University and William Lettis Associates, Inc.* Tech. rep. US Geological Survey final report 03HQGR0084, p. 13.

Mackin, J. H. (1948). "Concept of the graded river". In: *GSA Bulletin* 59.5, pp. 463–512. DOI: 10.1130/0016-7606(1948)59[463:cotgr]2.0.co;2.

Mandal, S. K., M. Lupker, J.-P. Burg, P. G. Valla, N. Haghipour, and M. Christl (2015). "Spatial variability of 10Be-derived erosion rates across the southern Peninsular Indian escarpment: A key to landscape evolution across passive margins". In: *Earth and Planetary Science Letters* 425, pp. 154–167. DOI: 10.1016/j.epsl.2015.05.050.

Maritan, A., A. Rinaldo, R. Rigon, A. Giacometti, and I. Rodríguez-Iturbe (1996). "Scaling laws for river networks". In: *Physical Review E - Statistical Physics, Plasmas, Fluids, and Related Interdisciplinary Topics* 53.2, pp. 1510–1515. DOI: 10.1103/PhysRevE.53.1510.

Martin, M. and F. Wenzel (2006). "High-resolution teleseismic body wave tomography beneath SE-Romania - II. Imaging of a slab detachment scenario". In: *Geophysical Journal International* 164.3, pp. 579–595. DOI: 10.1111/j.1365-246X.2006.02884.x.

Matenco, L. and G. Bertotti (2000). "Tertiary tectonic evolution of the external East Carpathians (Romania)". In: *Tectonophysics* 316.3-4, pp. 255–286. DOI: 10.1016/S0040-1951(99)00261-9.

Matenco, L. C., P. A. M. Andriessen, P. A. M. Andriessen, C. Avram, G. Bada, F. Beekman, et al. (2013). "Quantifying the mass transfer from mountain ranges to deposition in sedimentary basins: Source to sink studies in the danube basin-black sea system". In: *Global and Planetary Change* 103.1, pp. 1–18. DOI: 10.1016/j.gloplacha.2013.01.003.

Matenco, L., G. Bertotti, K. Leever, S. Cloetingh, S. M. Schmid, M. Tărăpoancă, et al. (2007). "Large-scale deformation in a locked collisional boundary: Interplay between subsidence and uplift, intraplate stress, and inherited lithospheric structure in the late stage of the SE Carpathians evolution". In: *Tectonics* 26.4, n/a–n/a. DOI: 10.1029/2006TC001951.

Matenco, L., C. Krézsek, S. Merten, S. Schmid, S. Cloetingh, and P. Andriessen (2010). "Characteristics of collisional orogens with low topographic build-up: An example

from the Carpathians". In: *Terra Nova* 22.3, pp. 155–165. DOI: 10.1111/j.1365-3121.2010.00931.x.

Matenco, L., I. Munteanu, M. ter Borgh, A. Stanica, M. Tilita, G. Lericolais, et al. (2016). "The interplay between tectonics, sediment dynamics and gateways evolution in the Danube system from the Pannonian Basin to the western Black Sea". In: *Science of the Total Environment* 543, pp. 807–827. DOI: 10.1016/j.scitotenv.2015.10.081.

Maţenco, L. and L. C. Matenco (2017). "Tectonics and exhumation of Romanian carpathians: Inferences from kinematic and thermochronological studies". In: *Springer Geography*. Ed. by M. Radoane and A. Vespremeanu-Stroe. Cham: Springer International Publishing, pp. 15–56. DOI: 10.1007/978-3-319-32589-7_2.

Mather, A. E. (2000). "Adjustment of a drainage network to capture induced base-level change: an example from the Sorbas Basin, SE Spain". In: *Geomorphology* 34.3, pp. 271–289. DOI: 10.1016/S0169-555X(00)00013-1.

McKinney, W. (2010). "Data Structures for Statistical Computing in Python". In: *Proceedings of the 9th Python in Science Conference*. Ed. by S. van der Walt and J. Millman, pp. 51–56.

Melinte-Dobrinescu, M. C., D. C. Jipa, T. Brustur, and S. Szobotka (2008). "Eastern Carpathian Cretaceous Oceanic Red Beds: Lithofacies, Biostratigraphy, and Paleoenvironment". In: *SEPM Special Publication*, pp. 111–119. DOI: 10.2110/sepmsp.091.111.

Merten, S., L. Matenco, P. T. Foeken, F. M. Stuart, and P. A. M. Andriessen (2010). "From nappe stacking to out-of-sequence postcollisional deformations: Cretaceous to Quaternary exhumation history of the SE Carpathians assessed by low-temperature thermochronology". In: *Tectonics* 29.3, n/a–n/a. DOI: 10.1029/2009TC002550.

Miclaus, C., F. Loiacono, D. Puglisi, and D. Baciu (2009). "Eocene-Oligocene sedimentation in the external areas of the Moldavide Basin (Marginal Folds Nappe, Eastern Carpathians, Romania): Sedimentological, paleontological and petrographic approaches". In: *Geologica Carpathica* 60.5, pp. 397–417. DOI: 10.2478/v10096-009-0029-9.

Molin, P., G. Fubelli, M. Nocentini, S. Sperini, P. Ignat, F. Grecu, et al. (2012). "Interaction of mantle dynamics, crustal tectonics, and surface processes in the topography of the Romanian Carpathians: A geomorphological approach". In: *Global and Planetary Change* 90, pp. 58–72. DOI: 10.1016/j.gloplacha.2011.05.005.

Moodie, A. J., F. J. Pazzaglia, and C. Berti (2017). "Exogenic forcing and autogenic processes on continental divide location and mobility". In: *Basin Research*. DOI: 10.1111/bre.12256.

Morisawa, M. E. (1962). "Quantitative Geomorphology of Some Watersheds in the Appalachian Plateau". In: *GSA Bulletin* 73.9, pp. 1025–1046. DOI: 10.1130/0016-7606(1962)73[1025:QGOSWI]2.0.CO;2.

Mouchené, M., P. van der Beek, F. Mouthereau, and J. Carcaillet (2017). "Controls on Quaternary incision of the Northern Pyrenean foreland: Chronological and geomorphological constraints from the Lannemezan megafan, SW France". In: *Geomorphology* 281, pp. 78–93. DOI: 10.1016/j.geomorph.2016.12.027.

Mudd, S. M., F. J. Clubb, B. Gailleton, D. A. Valters, M. D. Hurst, and S. W. D. Grieve (2019a). "LSDMappingTools". In: DOI: 10.5281/ZENODO.2560166.

Mudd, S. M., F. J. Clubb, S. W. D. Grieve, D. T. Milodowski, M. D. Hurst, B. Gailleton, et al. (2019b). *LSDTopoTools2*. DOI: 10.5281/ZENODO.3245041.

Mudd, S. M., F. J. Clubb, B. Gailleton, and M. D. Hurst (2018). "How concave are river channels ?" In: *Earth Surface Dynamics Discussions* 25.February, pp. 1–34. DOI: 10.5194/esurf-2018-7.

Mudd, S. M., M. Attal, D. T. Milodowski, S. W. Grieve, and D. A. Valters (2014). "A statistical framework to quantify spatial variation in channel gradients using the integral method of channel profile analysis". In: *Journal of Geophysical Research: Earth Surface* 119.2, pp. 138–152. DOI: 10.1002/2013JF002981.

Mudd, S. M. (2017). "Detection of transience in eroding landscapes". In: *Earth Surface Processes and Landforms* 42.1, pp. 24–41. DOI: 10.1002/esp.3923.

Muhs, D. R., K. R. Simmons, R. R. Schumann, L. T. Groves, S. B. DeVogel, S. A. Minor, et al. (2014). "Coastal tectonics on the eastern margin of the Pacific Rim: Late Quaternary sea-level history and uplift rates, Channel Islands National Park, California, USA". In: *Quaternary Science Reviews* 105, pp. 209–238. DOI: 10.1016/j.quascirev.2014.09.017.

NASA-JPL (2013). "NASA Shuttle Radar Topography Mission Global 1 arc second number". In: *Nasa Lp Daac*. DOI: 10.5067/MEaSUREs/SRTM/SRTMGL1N.003.

Naylor, M. and H. D. Sinclair (2008). "Pro- vs. retro-foreland basins". In: *Basin Research* 20.3, pp. 285–303. DOI: 10.1111/j.1365-2117.2008.00366.x.

Necea, D. (2010). "High-resolution morpho-tectonic profiling across an orogen: tectonic-controled geomorphology and multiple dating approach in the SE Carpathians". In: *Tectonic-controlled geomorphology and multiple dating approach in the SE Carpathians*.

Necea, D., W. Fielitz, A. Kadereit, P. A. M. Andriessen, and C. Dinu (2013). "Middle Pleistocene to Holocene fluvial terrace development and uplift-driven valley incision in the SE Carpathians, Romania". In: *Tectonophysics* 602.October 2016, pp. 332–354. DOI: 10.1016/j.tecto.2013.02.039.

Necea, D., W. Fielitz, and L. Matenco (2005). "Late Pliocene-Quaternary tectonics in the frontal part of the SE Carpathians: Insights from tectonic geomorphology". In: *Tectonophysics* 410.1-4, pp. 137–156. DOI: 10.1016/j.tecto.2005.05.047.

Neely, A. B., B. Bookhagen, and D. W. Burbank (2017). *An automated knickzone selection algorithm (KZ-Picker) to analyze transient landscapes: Calibration and validation*. DOI: 10.1002/2017JF004250.

Niemann, J. D., N. M. Gasparini, G. E. Tucker, and R. L. Bras (2001). "A quantitative evaluation of playfair's law and its use in testing long-term stream erosion models". In: *Earth Surface Processes and Landforms* 26.12, pp. 1317–1332. DOI: 10.1002/esp.272.

Niemi, N. A., M. Oskin, D. W. Burbank, A. M. Heimsath, and E. J. Gabet (2005). "Effects of bedrock landslides on cosmogenically determined erosion rates". In: *Earth and Planetary Science Letters* 237.3-4, pp. 480–498. DOI: 10.1016/j.epsl.2005.07.009.

O'Callaghan, J. F. and D. M. Mark (1984). "The extraction of drainage networks from digital elevation data." In: *Computer Vision, Graphics, Image Processing* 28.3, pp. 323–344. DOI: 10.1016/S0734-189X(84)80011-0.

Ohmori, H. (1991). "Change in the mathematical function type describing the longitudinal profile of a river through an evolutionary process". In: *Journal of Geology* 99.1, pp. 97–110. DOI: 10.1086/629476.

Olariu, C., D. C. Jipa, R. J. Steel, and M. C. Melinte-Dobrinescu (2014). "Genetic significance of an Albian conglomerate clastic wedge, Eastern Carpathians (Romania)". In: *Sedimentary Geology* 299, pp. 42–59. DOI: 10.1016/j.sedgeo.2013.10.004.

Oncescu, M. C. and K. P. Bonjer (1997). "A note on the depth recurrence and strain release of large Vrancea earthquakes". In: *Tectonophysics* 272.2-4, pp. 291–302. DOI: 10.1016/S0040-1951(96)00263-6.

Orlandini, S., P. Tarolli, G. Moretti, and G. Dalla Fontana (2011). "On the prediction of channel heads in a complex alpine terrain using gridded elevation data". In: *Water Resources Research* 47.2. DOI: 10.1029/2010WR009648.

Ouimet, W. B., K. X. Whipple, and D. E. Granger (2009). "Beyond threshold hillslopes: Channel adjustment to base-level fall in tectonically active mountain ranges". In: *Geology* 37.7, pp. 579–582. DOI: 10.1130/G30013A.1.

Passalacqua, P., T. Do Trung, E. Foufoula-Georgiou, G. Sapiro, and W. E. Dietrich (2010). "A geometric framework for channel network extraction from lidar: Nonlinear diffusion and geodesic paths". In: *Journal of Geophysical Research: Earth Surface* 115.F1, F01002. DOI: 10.1029/2009JF001254.

Pelletier, J. D. (2013). "A robust, two-parameter method for the extraction of drainage networks from high-resolution digital elevation models (DEMs): Evaluation using synthetic and real-world DEMs". In: *Water Resources Research* 49.1, pp. 75–89. DOI: 10.1029/2012WR012452.

Penck, W. (1953). *Morphological analysis of landforms: Translation of 1924 German book by H. Czech and K.C. Boxwell.*

Perne, M., M. D. Covington, E. A. Thaler, and J. M. Myre (2017). "Steady state, erosional continuity, and the topography of landscapes developed in layered rocks". In: *Earth Surface Dynamics* 5.1, pp. 85–100. DOI: 10.5194/esurf-5-85-2017.

Perron, J. T. (2017). "Climate and the Pace of Erosional Landscape Evolution". In: *Annual Review of Earth and Planetary Sciences* 45.1, pp. 561–591. DOI: 10.1146/annurev-earth-060614-105405.

Perron, J. T. and L. Royden (2013). "An integral approach to bedrock river profile analysis". In: *Earth Surface Processes and Landforms* 38.6, pp. 570–576. DOI: 10.1002/esp.3302.

Picotti, V. and F. J. Pazzaglia (2008). "A new active tectonic model for the construction of the Northern Apennines mountain front near Bologna (Italy)". In: *Journal of Geophysical Research: Solid Earth* 113.8. DOI: 10.1029/2007JB005307.

Pinter, N., S. B. Lueddecke, E. A. Keller, and K. R. Simmons (1998). "Late Quaternary slip on the Santa Cruz Island fault, California". In: *Bulletin of the Geological Society of America* 110.6, pp. 711–722. DOI: 10.1130/0016-7606(1998)110<0711:LQSOTS>2.3.CO;2.

Pinter, N., M. Hardiman, A. C. Scott, and R. S. Anderson (2018). "Discussion of "Fluvial system response to late Pleistocene-Holocene sea-level change on Santa Rosa Island, Channel Islands National Park, California" (Schumann et al., 2016. Geomorphology, 268: 322–340)". In: *Geomorphology* 301, pp. 141–143. DOI: 10.1016/j.geomorph.2017.03.028.

Plasienka, D. (2018). "Continuity and Episodicity in the Early Alpine Tectonic Evolution of the Western Carpathians: How Large-Scale Processes Are Expressed by the Orogenic Architecture and Rock Record Data". In: *Tectonics* 37, pp. 2029–2079.

Playfair, J. (1802). *Illustrations of the Huttonian theory of the earth.* Edinburgh: Neill and Co. Printers.

Popa, M., M. Radulian, C. Panaiotu, and F. Borleanu (2008). "Lithosphere-asthenosphere interaction at the Southeastern Carpathian Arc bend: Implications for anisotropy". In: *Tectonophysics* 462.1-4, pp. 83–88. DOI: 10.1016/j.tecto.2008.03.017.

Popa, M., M. Radulian, B. Grecu, E. Popescu, and A. O. Placinta (2005). "Attenuation in Southeastern Carpathians area: Result of upper mantle inhomogeneity". In: *Tectonophysics* 410.1-4, pp. 235–249. DOI: 10.1016/j.tecto.2004.12.037.

Powell, J. W. (1875). *Exploration of the Colorado River of the West and its tributaries: Explored in 1869, 1870, 1871, and 1872, under the direction of the Secretary of the Smithsonian Institution*. USGS Unnumbered Series. Washington, D.C.: Government Printing Office, p. 368.

Pritchard, D., G. G. Roberts, N. J. White, and C. N. Richardson (2009). "Uplift histories from river profiles". In: *Geophysical Research Letters* 36.24, p. L24301. DOI: 10.1029/2009GL040928.

Queiroz, G. L., E. Salamuni, and E. R. Nascimento (2015). "Knickpoint finder: A software tool that improves neotectonic analysis". In: *Computers and Geosciences* 76, pp. 80–87. DOI: 10.1016/j.cageo.2014.11.004.

Radoane, M., N. Radoane, and D. Dumitriu (2003). "Geomophological evolution of longitudinal river profiles in the Carpathians". In: *Geomorphology* 50.4, pp. 293–306. DOI: 10.1016/S0169-555X(02)00194-0.

Radoane, M., I. Cristea, D. Dumitriu, and I. Perșoiu (2017). "Geomorphological evolution and longitudinal profiles". In: *Springer Geography*. Springer, pp. 427–442. DOI: 10.1007/978-3-319-32589-7_18.

Radulian, M., F. Vaccari, N. Mândrescu, G. F. Panza, and C. L. Moldoveanu (2000). "Seismic hazard of Romania: Deterministic approach". In: *Pure and Applied Geophysics*. Vol. 157. 1-2. Springer, pp. 221–247. DOI: 10.1007/pl00001096.

Rigon, R., I. Rodriguez-Iturbe, A. Maritan, A. Giacometti, D. G. Tarboton, and A. Rinaldo (1996). "On Hack's law". In: *Water Resources Research* 32.11, pp. 3367–3374. DOI: 10.1029/96WR02397.

Ringenbach, J. C., N. Pinet, J. Delteil, and J. F. Stephan (1992). "Analyse des structures engendrees en regime decrochant par le seisme de Nueva Ecija du 16 juillet 1990, Luzon, Philippines". In: *Bulletin - Societe Geologique de France* 163.2, pp. 109–123.

Roban, R. D., C. Krézsek, and M. C. Melinte-Dobrinescu (2017). "Cretaceous sedimentation in the outer Eastern Carpathians: Implications for the facies model reconstruction of the Moldavide Basin". In: *Sedimentary Geology* 354, pp. 24–42. DOI: 10.1016/j.sedgeo.2017.04.001.

Royden, L. H., C. M. K., K. X. Whipple, H. Royden Leigh, K. Clark Marin, X. Whipple Kelin, et al. (2000). "Evolution of river elevation profiles by bedrock incision; analytical solutions for transient river profiles related to changing uplift and precipitation rates". In: *Eos, Transactions, American Geophysical Union*. Vol. 81. 48. Fall Meeting Supplement, pp. 1–2.

Royden, L. and J. Taylor Perron (2013). "Solutions of the stream power equation and application to the evolution of river longitudinal profiles". In: *Journal of Geophysical Research: Earth Surface* 118.2, pp. 497–518. DOI: 10.1002/jgrf.20031.

Russo, R. M., V. Mocanu, M. Radulian, M. Popa, and K. P. Bonjer (2005). "Seismic attenuation in the Carpathian bend zone and surroundings". In: *Earth and Planetary Science Letters* 237.3-4, pp. 695–709. DOI: 10.1016/j.epsl.2005.06.046.

Safran, E. B., P. R. Bierman, R. Aalto, T. Dunne, K. X. Whipple, and M. Caffee (2005). "Erosion rates driven by channel network incision in the Bolivian Andes". In: *Earth Surface Processes and Landforms* 30.8, pp. 1007–1024. DOI: 10.1002/esp.1259.

Salgado, R., A. Augusto, R. Braucher, A. Chicarino, F. Coun, A. Fortes, et al. (2008). "Relief evolution of the Quadrilátero Ferrífero (Minas Gerais, Brazil) by means of

10Be cosmogenic nuclei". In: *Zeitschrift für Geomorphologie* 52.September, pp. 317–323.

Sanders, C. A. E., P. A. M. Andriessen, and S. A. P. L. Cloetingh (1999). "Life cycle of the East Carpathian orogen: Erosion history of a doubly vergent critical wedge assessed by fission track thermochronology". In: *Journal of Geophysical Research: Solid Earth* 104.B12, pp. 29095–29112. DOI: 10.1029/1998jb900046.

Sandulescu, M., M. Stefanescu, A. Butac, I. Patrut, and P. Zaharescu (1981a). *Genetical and structural relations between flysch and molasse (The East Carpathians)*. Tech. rep. Carp.-Balc. Assoc., XII Congr.

Sandulescu, M., H. G. Krautner, I. Balintoni, D. Russo-Sandulescu, and M. Micu (1981b). *The structure of the East Carpathians (Moldavia-Maramures area)*. Tech. rep. Carp.-Balc. Assoc., XII Congr.

Sandulescu, M. (1984). *Geotectonica României*. Tehnica.

Sandulescu, M. (1988). "Cenozoic Tectonic History of the Carpathians". In: *The Pannonian Basin: A Study in Basin Evolution* 45, pp. 17–25.

Scheingross, J. S. and M. P. Lamb (2016). "Sediment transport through self-adjusting, bedrock-walled waterfall plunge pools". In: *Journal of Geophysical Research F: Earth Surface* 121.5, pp. 939–963. DOI: 10.1002/2015JF003620.

Scheingross, J. S., D. Y. Lo, and M. P. Lamb (2017). "Self-formed waterfall plunge pools in homogeneous rock". In: *Geophysical Research Letters* 44.1, pp. 200–208. DOI: 10.1002/2016GL071730.

Scherler, D., B. Bookhagen, and M. R. Strecker (2014). "Tectonic control on 10Be-derived erosion rates in the Garhwal Himalaya, India". In: *Journal of Geophysical Research: Earth Surface* 119.2, pp. 83–105. DOI: 10.1002/2013JF002955.

Schmid, S. M., B. Fügenschuh, A. Kounov, L. C. Matenco, P. Nievergelt, R. Oberhänsli, et al. (2019). "Tectonic units of the Alpine collision zone between Eastern Alps and western Turkey". In: *Gondwana Research*. DOI: 10.1016/j.gr.2019.07.005.

Schmid, S. M., D. Bernoulli, B. Fügenschuh, L. Matenco, S. Schefer, R. Schuster, et al. (2008). "The Alpine-Carpathian-Dinaridic orogenic system: correlation and evolution of tectonic units". In: *Swiss Journal of Geosciences* 101.1, pp. 139–183. DOI: 10.1007/s00015-008-1247-3.

Schmitt, G., A. Nuckelt, A. Knöpfler, and C. Marcu (2007). "Three dimensional plate kinematics in Romania". In: *International Symposium on Strong Vrancea Earthquakes and Risk Mitigation*. Bucharest, Romania.

Schoenbohm, L. M., K. X. Whipple, B. C. Burchfiel, and L. Chen (2004). "Geomorphic constraints on surface uplift, exhumation, and plateau growth in the Red River region, Yunnan Province, China". In: *Bulletin of the Geological Society of America* 116.7-8, pp. 895–909. DOI: 10.1130/B25364.1.

Schumann, R. R., J. S. Pigati, and J. P. McGeehin (2016). "Fluvial system response to late Pleistocene-Holocene sea-level change on Santa Rosa Island, Channel Islands National Park, California". In: *Geomorphology* 268, pp. 322–340. DOI: 10.1016/J.GEOMORPH.2016.05.033.

Schwanghart, W. and D. Scherler (2014). "Short Communication: TopoToolbox 2 - MATLAB-based software for topographic analysis and modeling in Earth surface sciences". In: *Earth Surface Dynamics* 2.1, pp. 1–7. DOI: 10.5194/esurf-2-1-2014.

Schwanghart, W. and N. J. Kuhn (2010). "TopoToolbox: A set of Matlab functions for topographic analysis". In: *Environmental Modelling and Software* 25.6, pp. 770–781. DOI: 10.1016/j.envsoft.2009.12.002.

Schwanghart, W. and D. Scherler (2017). "Bumps in river profiles: Uncertainty assessment and smoothing using quantile regression techniques". In: *Earth Surface Dynamics* 5.4, pp. 821–839. DOI: 10.5194/esurf-5-821-2017.

Seagren, E. G. and L. M. Schoenbohm (2019). "Base Level and Lithologic Control of Drainage Reorganization in the Sierra de las Planchadas, NW Argentina". In: *Journal of Geophysical Research: Earth Surface* 124.6, pp. 1516–1539. DOI: 10.1029/2018JF004885.

Seeber, L. and V. Gornitz (1983). "River profiles along the Himalayan arc as indicators of active tectonics". In: *Tectonophysics* 92.4, pp. 335–367.

Shaler, N. S. (1899). "Spacing of rivers with reference to hypothesis of baseleveling". In: *Bulletin of the Geological Society of America* 10.1, pp. 263–276. DOI: 10.1130/GSAB-10-263.

Shean, D. (2017). "High Mountain Asia 8-meter DEM Mosaics Derived from Optical Imagery, Version 1". In: *2002-2016. Boulder, Colorado USA. NASA National Snow and Ice Data Center Distributed Active Archive Center.* DOI: https://doi.org/10.5067/KXOVQ9L172S2.

Shelef, E., I. Haviv, and L. Goren (2018). "A potential link between waterfall recession rate and bedrock channel concavity". In: *Journal of Geophysical Research: Earth Surface* 0.0. DOI: 10.1002/2016JF004138.

Shulits, S. (1936). "Fluvial morphology in terms of slope, abrasion, and bed-load". In: *Eos, Transactions American Geophysical Union* 17.2, pp. 440–444. DOI: 10.1029/TR017i002p00440.

Shulits, S. (1941). "Rational equation of river-bed profile". In: *Eos, Transactions American Geophysical Union* 22.3, pp. 622–631. DOI: 10.1029/TR022i003p00622.

Sinclair, H. D., B. J. Coakley, P. A. Allen, and A. B. Watts (1991). "Simulation of Foreland Basin Stratigraphy using a diffusion model of mountain belt uplift and erosion: An example from the central Alps, Switzerland". In: *Tectonics* 10.3, pp. 599–620. DOI: 10.1029/90TC02507.

Sinclair, H. (2012). "Thrust Wedge/Foreland Basin Systems". In: *Tectonics of Sedimentary Basins: Recent Advances*, pp. 522–537. DOI: 10.1002/9781444347166.ch26.

Sklar, L. and W. Dietrich (1998). "River longitudinal profiles and bedrock incision models: Stream power and the influence of sediment supply". In: *Rivers over rock: fluvial processes in bedrock channels* December, pp. 237–260. DOI: 10.1029/GM107p0237.

Snow, A. D., J. Whitaker, M. Cochran, J. V. den Bossche, C. Mayo, J. de Kloe, et al. (2020). "pyproj4/pyproj: 2.6.0 Release". In: DOI: 10.5281/ZENODO.3714221.

Snyder, N. P., K. X. Whipple, G. E. Tucker, and D. J. Merritts (2000). "Landscape response to tectonic forcing: Digital elevation model analysis of stream profiles in the Mendocino triple junction region, Northern California". In: *Bulletin of the Geological Society of America* 112.8, pp. 1250–1263. DOI: 10.1130/0016-7606(2000)112<1250:LRTTFD>2.0.CO;2.

Soille, P. and C. Gratin (1994). "An efficient algorithm for drainage network extraction on dems". In: *Journal of Visual Communication and Image Representation* 5.2, pp. 181–189. DOI: 10.1006/jvci.1994.1017.

Steer, P., T. Croissant, E. Baynes, and D. Lague (2019). "Statistical modelling of coseismic knickpoint formation and river response to fault slip". In: *Earth Surface Dynamics* 7.3, pp. 681–706. DOI: 10.5194/esurf-7-681-2019.

Sternberg, H. (1875). "Untersuchungen uber Langen-und Querprofil geschiebefuhrender Flusse". In: *Zeitshrift fur Bauwesen* 25, pp. 483–506.

Stock, J. and W. E. Dietrich (2003). "Valley incision by debris flows: Evidence of a topographic signature". In: *Water Resources Research* 39.4. DOI: 10.1029/2001WR001057.

Stock, J. D. and D. R. Montgomery (1999). "Geologic constraints on bedrock river incision using the stream power law". In: *Journal of Geophysical Research: Solid Earth* 104.B3, pp. 4983–4993. DOI: 10.1029/98JB02139.

Stoica, M., I. Lazăr, W. Krijgsman, I. Vasiliev, D. Jipa, and A. Floroiu (2013). "Paleoenvironmental evolution of the East Carpathian foredeep during the late Miocene-early Pliocene (Dacian Basin; Romania)". In: *Global and Planetary Change* 103.1, pp. 135–148. DOI: 10.1016/j.gloplacha.2012.04.004.

Strahler, A. N. (1957). "Quantitative analysis of watershed geomorphology". In: *Eos, Transactions American Geophysical Union* 38.6, pp. 913–920. DOI: 10.1029/TR038i006p00913.

Strauch, R., E. Istanbulluoglu, S. Siddhartha Nudurupati, C. Bandaragoda, N. M. Gasparini, and G. E. Tucker (2018). "A hydroclimatological approach to predicting regional landslide probability using Landlab". In: *Earth Surface Dynamics* 6.1, pp. 49–75. DOI: 10.5194/esurf-6-49-2018.

Strong, C. M., M. Attal, S. M. Mudd, and H. D. Sinclair (2019). "Lithological control on the geomorphic evolution of the Shillong Plateau in Northeast India". In: *Geomorphology* 330, pp. 133–150. DOI: 10.1016/j.geomorph.2019.01.016.

Tadono, T., H. Nagai, H. Ishida, F. Oda, S. Naito, K. Minakawa, et al. (2016). "Generation of the 30 M-MESH global digital surface model by alos prism". In: *International Archives of the Photogrammetry, Remote Sensing and Spatial Information Sciences - ISPRS Archives* 41, pp. 157–162. DOI: 10.5194/isprsarchives-XLI-B4-157-2016.

Takaku, J., T. Tadono, K. Tsutsui, and M. Ichikawa (2018). "Quality improvements of 'AW3D' global DSM derived from ALOS PRISM". In: *International Geoscience and Remote Sensing Symposium (IGARSS)*. Vol. 2018-July. Institute of Electrical and Electronics Engineers Inc., pp. 1612–1615. DOI: 10.1109/IGARSS.2018.8518360.

Tapponnier, P. and P. Molnar (1977). "Active faulting and tectonics in China". In: *Journal of Geophysical Research* 82.20, pp. 2905–2930. DOI: 10.1029/jb082i020p02905.

Tarapoanca, M., G. Bertotti, L. Maţenco, C. Dinu, and S. A. P. L. Cloetingh (2003). "Architecture of the Focşani Depression: A 13 km deep basin in the Carpathians bend zone (Romania)". In: *Tectonics* 22.6, n/a–n/a. DOI: 10.1029/2002tc001486.

Tarboton, D. G. (1997). *A new method for the determination of flow directions and upslope areas in grid digital elevation models*. Tech. rep. 2, pp. 309–319. DOI: 10.1029/96WR03137.

Tarboton, D. G., R. L. Bras, and I. Rodriguez-Iturbe (1992). "A physical basis for drainage density". In: *Geomorphology* 5.1-2, pp. 59–76. DOI: 10.1016/0169-555X(92)90058-V.

Tarolli, P. and S. Mudd (2020). *Remote Sensing of Geomorphology*. Ed. by P. Tarolli and S. Mudd. 1st. Vol. 23. Elsevier, p. 400.

Thaler, E. A. and M. D. Covington (2016). "The influence of sandstone caprock material on bedrock channel steepness within a tectonically passive setting: Buffalo National River Basin, Arkansas, USA". In: *Journal of Geophysical Research: Earth Surface* 121.9, pp. 1635–1650. DOI: 10.1002/2015JF003771.

Troiani, F. and M. Della Seta (2008). "The use of the Stream Length-Gradient index in morphotectonic analysis of small catchments: A case study from Central Italy". In: *Geomorphology* 102.1, pp. 159–168. DOI: 10.1016/j.geomorph.2007.06.020.

Truong, C., L. Oudre, and N. Vayatis (2018). "A review of change point detection methods". In: arXiv: 1801.00826.

Tucker, G. E. and K. X. Whipple (2002). "Topographic outcomes predicted by stream erosion models: Sensitivity analysis and intermodel comparison". In: *Journal of Geophysical Research: Solid Earth* 107.B9, ETG 1–1–ETG 1–16. DOI: 10.1029/2001JB000162.

Tucker, G. E. and P. van der Beek (2013). "A model for post-orogenic development of a mountain range and its foreland". In: *Basin Research* 25.3, pp. 241–259. DOI: 10.1111/j.1365-2117.2012.00559.x.

Tucker, G., S. Lancaster, N. Gasparini, and R. Bras (2001). "The Channel-Hillslope Integrated Landscape Development Model (CHILD)". In: *Landscape Erosion and Evolution Modeling*. Boston, MA: Springer US, pp. 349–388. DOI: 10.1007/978-1-4615-0575-4_12.

Tucker, G. E. and R. Slingerland (1996). "Predicting sediment flux from fold and thrust belts". In: *Basin Research* 8.3, pp. 329–349. DOI: 10.1046/j.1365-2117.1996.00238.x.

Tucker, G. E. (2004). "Drainage basin sensitivity to tectonic and climatic forcing: Implications of a stochastic model for the role of entrainment and erosion thresholds". In: *Earth Surface Processes and Landforms* 29.2, pp. 185–205. DOI: 10.1002/esp.1020.

Turowski, J. M. (2020). "Mass balance, grade, and adjustment timescales in bedrock channels". In: *Earth Surface Dynamics* 8.1, pp. 103–122. DOI: 10.5194/esurf-8-103-2020.

Van Der Walt, S., S. C. Colbert, and G. Varoquaux (2011). "The NumPy array: A structure for efficient numerical computation". In: *Computing in Science and Engineering* 13.2, pp. 22–30. DOI: 10.1109/MCSE.2011.37. arXiv: 1102.1523.

Varajão, G. V. (1991). "a Questão Da Correlacão Das Superfícies De Erosão Do Quadrilátero Ferrífero , Minas Gerais". In: *Revista Brasileira de Geociências* 21.2, pp. 138–145.

Vasiliev, I., W. Krijgsman, C. G. Langereis, C. E. Panaiotu, L. M. Senco, and G. Bertotti (2004). "Towards an astrochronological framework for the eastern Paratethys Mio-Pliocene sedimentary sequences of the Focsani basin (Romania)". In: *Earth and Planetary Science Letters* 227, pp. 231–247. DOI: 10.1016/j.epsl.2004.09.012.

Walker, R. and S. Skiena (1992). "Implementing Discrete Mathematics: Combinatorics and Graph Theory with Mathematica". In: *The Mathematical Gazette* 76.476, p. 286. DOI: 10.2307/3619148.

Wang, L. and H. Liu (2006). "An efficient method for identifying and filling surface depressions in digital elevation models for hydrologic analysis and modelling". In: *International Journal of Geographical Information Science* 20.2, pp. 193–213. DOI: 10.1080/13658810500433453.

Wang, Y., H. Zhang, D. Zheng, J. Yu, J. Pang, and Y. Ma (2017). "Coupling slope-area analysis, integral approach and statistic tests to steady-state bedrock river profile analysis". In: *Earth Surface Dynamics* 5.1, pp. 145–160. DOI: 10.5194/esurf-5-145-2017.

Wegener, A. L. P. and J. G. A. Skerl (1925). "The Origin of Continents and Oceans". In: *The Geographical Journal* 66.1, p. 70. DOI: 10.2307/1783259.

Whipple, K. X., R. A. DiBiase, and B. T. Crosby (2013). "Bedrock Rivers". In: *Treatise on Geomorphology*. Vol. 9. Fluvial Geomorphology, pp. 550–573. DOI: 10.1016/B978-0-12-374739-6.00254-2.

Whipple, K. X., A. M. Forte, R. A. DiBiase, N. M. Gasparini, and W. B. Ouimet (2017a). "Timescales of landscape response to divide migration and drainage capture: Implications for the role of divide mobility in landscape evolution". In: *Journal of Geophysical Research: Earth Surface* 122.1, pp. 248–273. DOI: 10.1002/2016JF003973.

Whipple, K. X., E. Kirby, and S. H. Brocklehurst (1999). "Geomorphic limits to climate-induced increases in topographic relief". In: *Nature* 401.6748, pp. 39–43. DOI: 10.1038/43375.

Whipple, K. X., R. A. DiBiase, W. B. Ouimet, and A. M. Forte (2017b). "Preservation or piracy: Diagnosing low-relief, high-elevation surface formation mechanisms". In: *Geology* 45.1, pp. 91–94. DOI: 10.1130/G38490.1.

Whipple, K. X. and G. E. Tucker (1999). "Dynamics of the stream-power river incision model: Implications for height limits of mountain ranges, landscape response timescales, and research needs". In: *Journal of Geophysical Research: Solid Earth* 104.B8, pp. 17661–17674. DOI: 10.1029/1999JB900120.

Whipple, K. X. (2002). "Implications of sediment-flux-dependent river incision models for landscape evolution". In: *Journal of Geophysical Research* 107.B2, p. 2039. DOI: 10.1029/2000JB000044.

Whipple, K. X. (2004). "Bedrock Rivers and the Geomorphology of Active Orogens". In: *Annual Review of Earth and Planetary Sciences* 32.1, pp. 151–185. DOI: 10.1146/annurev.earth.32.101802.120356.

Whipple, K. X. (2009). "Erratum: The influence of climate on the tectonic evolution of mountain belts (Nature Geoscience 2, 97104 (2009))". In: *Nature Geoscience* 2.10, p. 730. DOI: 10.1038/ngeo638.

Whittaker, a. C. (2012). "How do landscapes record tectonics and climate?" In: *Lithosphere* 4.2, pp. 160–164. DOI: 10.1130/RF.L003.1.

Wickert, A. D. and T. F. Schildgen (2019). "Long-profile evolution of transport-limited gravel-bed rivers". In: *Earth Surface Dynamics* 7.1, pp. 17–43. DOI: 10.5194/esurf-7-17-2019.

Wiener, N. (1949). *Extrapolation, interpolation, and smoothing of stationary time series: with engineering applications*. Technology Press of the Massachusetts Institute of Technology.

Willemin, J. H. (2000). "Hack's law: Sinuosity, convexity, elongation". In: *Water Resources Research* 36.11, pp. 3365–3374. DOI: 10.1029/2000WR900229.

Willett, S. D. (1999). "Orogeny and orography: The effects of erosion on the structure of mountain belts". In: *Journal of Geophysical Research: Solid Earth* 104.B12, pp. 28957–28981. DOI: 10.1029/1999jb900248.

Willett, S. D. and M. T. Brandon (2002a). "On steady states in mountain belts". In: *Geology* 30.2, pp. 175–178. DOI: 10.1130/0091-7613(2002)030<0175:OSSIMB>2.0.CO;2.

Willett, S. D., S. W. McCoy, J. Taylor Perron, L. Goren, and C. Y. Chen (2014). "Dynamic reorganization of River Basins". In: *Science* 343.6175, p. 1248765. DOI: 10.1126/science.1248765.

Willett, S. D. and M. T. Brandon (2002b). "On steady state in mountain belts". In: *Geology* 30.2, pp. 175–178. DOI: 10.1130/0091-7613(2002)030<0175.

Winterberg, S. and S. D. Willett (2019). "Greater Alpine river network evolution, interpretations based on novel drainage analysis". In: *Swiss Journal of Geosciences* 112.1, pp. 3–22. DOI: 10.1007/s00015-018-0332-5.

Wobus, C., K. X. Whipple, E. Kirby, N. Snyder, J. Johnson, K. Spyropolou, et al. (2006a). "Tectonics from topography: procedurses, promise, and pitfalls". In: *Geological Society of America Special Paper* 398.04, pp. 55–74. DOI: 10.1130/2006.2398(04)..

Wobus, C. W., K. X. Whipple, and K. V. Hodges (2006b). "Neotectonics of the central Nepalese Himalaya: Constraints from geomorphology, detrital 40Ar/39Ar thermochronology, and thermal modeling". In: *Tectonics* 25.4. DOI: 10.1029/2005TC001935.

Wobus, C. W., B. T. Crosby, and K. X. Whipple (2006c). "Hanging valleys in fluvial systems: Controls on occurrence and implications for landscape evolution". In: *Journal of Geophysical Research: Earth Surface* 111.2. DOI: 10.1029/2005JF000406.

Wolman, G. (1955). *The Natural Channel of Brandy wine Creek Pennsylvania*. Tech. rep., 56p.

Yanites, B. J., G. E. Tucker, and R. S. Anderson (2009). "Numerical and analytical models of cosmogenic radionuclide dynamics in landslide-dominated drainage basins". In: *Journal of Geophysical Research: Earth Surface* 114.1, F01007. DOI: 10.1029/2008JF001088.

Yanites, B. J., J. K. Becker, H. Madritsch, M. Schnellmann, and T. A. Ehlers (2017). "Lithologic Effects on Landscape Response to Base Level Changes: A Modeling Study in the Context of the Eastern Jura Mountains, Switzerland". In: *Journal of Geophysical Research: Earth Surface* 122.11, pp. 2196–2222. DOI: 10.1002/2016JF004101.

Yin, A. (2006). "Cenozoic tectonic evolution of the Himalayan orogen as constrained by along-strike variation of structural geometry, exhumation history, and foreland sedimentation". In: *Earth-Science Reviews* 76.1, pp. 1–131.

Young, H. H. and G. E. Hilley (2018). "Millennial-scale denudation rates of the Santa Lucia Mountains, California: Implications for landscape evolution in steep, high-relief, coastal mountain ranges". In: *Bulletin of the Geological Society of America* 130.11-12, pp. 1809–1824. DOI: 10.1130/B31907.1.

Yuan, X. P., J. Braun, L. Guerit, D. Rouby, and G. Cordonnier (2019). "A New Efficient Method to Solve the Stream Power Law Model Taking Into Account Sediment Deposition". In: *Journal of Geophysical Research: Earth Surface*. DOI: 10.1029/2018JF004867.

Zahra, T., U. Paudel, Y. S. Hayakawa, and T. Oguchi (2017). "Knickzone Extraction Tool (KET) - A new ArcGIS toolset for automatic extraction of knickzones from a DEM based on multi-scale stream gradients". In: *Open Geosciences* 9.1, pp. 73–88. DOI: 10.1515/geo-2017-0006.

Zhang, Y., M. A. Hassan, L. King, X. Fu, E. Istanbulluoglu, and G. Wang (2020). "Morphometrics of China's Loess Plateau: The spatial legacy of tectonics, climate, and loess deposition history". In: *Geomorphology* 354, p. 107043. DOI: 10.1016/j.geomorph.2020.107043.

Zhou, G., Z. Sun, and S. Fu (2016). "An efficient variant of the Priority-Flood algorithm for filling depressions in raster digital elevation models". In: *Computers and Geosciences* 90, pp. 87–96. DOI: 10.1016/j.cageo.2016.02.021.

Zielke, O., J. Ramón Arrowsmith, L. G. Ludwig, and S. O. Akciz (2010). "Slip in the 1857 and earlier large earthquakes along the Carrizo Plain, San Andreas Fault". In: *Science* 327.5969, pp. 1119–1122. DOI: 10.1126/science.1182781.

Appendix of Chapter 3: A segmentation approach for the reproducible extraction and quantification of knickpoints from river long profiles

Overview

This document contains supplementary materials for Chapter 3, with additional details about the analysis on landscapes and the sensitivity analysis for testing the effect of user-defined parameters on the method.

Example parameter files

We have provided example parameter files for running the analyses performed in the manuscript, which can be found in directory "`Example_parameter_files`". It contains a detailed readme file with instructions on how to adapt it for another analysis.

DEM metadata and parameter files

We have provided the specific parameter files used for each analysis in order to make it fully reproducible. The files containing the supplemental materials is published with the manuscript available at https://doi.org/10.5194/esurf-7-211-2019. The structure of the directory is as follows:

```
|--Analysis_files
   |--Santa_Cruz_Island
   |--QF
```

The directory "`Analysis_files`" contains the parameter files used to run the analysis on the two test sites, where each site is contained its own subdirectory. Each file can be used to run the analysis and reproduce the results shown in the main manuscript. In addition to the parameter files for running the full knickpoint analysis, we also have included georeferencing information for the sites in the form of ENVI "hdr" files which contain the coordinate system and extent

of each DEM analysed. Users can download lidar 1 m data for the Smugglers catchment within the dataset *2010 Channel Islands Lidar Collection* available on http://opentopo.sdsc.edu/datasetMetadata?otCollectionID=OT.082012.26911.1. After downloading the data, the user must project it into UTM coordinates and clip to the correct extent with the information in the "hdr" files. We have done this using GDAL. You can find instructions `https://lsdtopotools.github.io/LSDTT_documentat`
We also provide the metadata for the Quadrilatero Feriferro site (Brazil), however we are not allowed to share the TanDEM-x 10m DEM following the terms of its licence. The SRTM 30m version of it can also be accessed on https://www.opentopography.org.

The source code required to run these parameter files are in the GitHub repository `https://github.com/LSDtopotools/LSDTopoTools_ChiMudd2014`. You will find instruction to install and use the software at `https://lsdtopotools.github.io/LSDT`
or you can see the documentation for "Channel steepness analysis with LSDTopoTools" at the main LSDTopoTools documentation website `https://lsdtopotools.github.io/`
Documentation specific to the knickpoint analysis can be found in the knickpoint section of the documentation at `https://lsdtopotools.github.io/LSDTT_documentation/LS`

Sensitivity to parameters in natural landscapes

In order to test the sensitivity of the knickpoint detection method to user-defined parameters, we ran a set of sensitivity analyses. The results are presented below, and the scripts used to generate the raw data and the figures are provided in the following directories:

```
|--Sensitivity_analyses
   |--Concavity_index_lambda
   |--Concavity_index
   |--Target_node_n_skip
   |--MC_iterations
   |--Combining_window
   |--Step_window_coeff
   |--A0
```

We provide the scripts that were used to run the sensitivity analyses on the parameters needed for different part of the algorithm toolchain: *Concavity_index_lambda*, *Target_node_n_skip*, *MC_iterations*, *Step_window*, *Combining_window*, *Grid_Resolution* and *A0*. These files can be found in the directory "`Sensitivity_analyses`" and are written in *Python* to provide basic control of the *C++* code. Each file follows the same structure: they automatically write and execute the parameter files for ranges of parameters (combined or not). It then uses the Python *subprocess* module to call the analysis (compiled *C++* LSDTopoTools) and plotting (LSDMappingTools) codes and automatically organises the results in subfolders using Python's *os* module. Running the sensitivity analyses can take a significant amount of computation time. We therefore used Python's *multiprocessing* module to take advantage of the now common multi-core CPUs and run several analysis at the same time. The scripts used to then generate violin plots and the z-score are available in the supplementary materials. They can be used to (i) reproduce our results or (ii) generate new range of tests or new combination of parameters in case of specific studies.

Sensitivity to the regulation parameter

The λ parameter (*lamda_TVD*) controls the denoising intensity in the Total Variation Denoising algorithm from Condat (2013). We tested a range of λ values from 0.1 to 100000 for k_{sn} calculated using a range of concavity indexes from 0.1 to 0.9, as θ controls the order of magnitude of k_{sn}. We then determined the best λ for each value of θ by plotting the k_{sn} extracted with the Mudd et al. (2014) algorithm and the denoised signal against χ, as shown in Figure S1.

Results from this analysis show that a default λ value can be suggested for each value of θ (Table S1). Although we have implemented these default values into the algorithm, this parameter can still be adapted by the user if required.

Sensitivity to the concavity index

We also ran a sensitivity analysis on the concavity index θ. This parameter describes the overall concavity of the river long profile and should be carefully

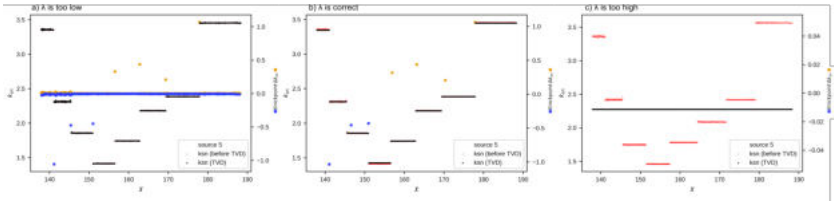

Figure S1. λ parameter selection for the denoising of k_{sn} data. a) A λ value which is too low: variations are not de-noised and many low magnitude knickpoints (blue squares for negatives and red squares for positive) are detected. The combining process cannot clean these low magnitude knickpoints as they alternate between positive and negative magnitudes. b) A more appropriate value of λ: most of the small variations in k_{sn} are flattened without altering the main signal and the few remaining are combined by the algorithm. c) A λ which is too high: all the variations are flattened by the denoising algorithm. This data has been extracted from the Smugglers catchment described in the main manuscript.

θ	0.1	0.15	0.2	0.25	0.3	0.35	0.4	0.45	0.5	0.55	0.6	0.65	0.7	0.75	0.8	0.85	0.9
λ	0.1	0.3	0.5	2	3	5	10	20	40	100	200	300	500	1000	2000	5000	10000

Table S1. List of default regulation parameter (λ) values for each concavity (θ).

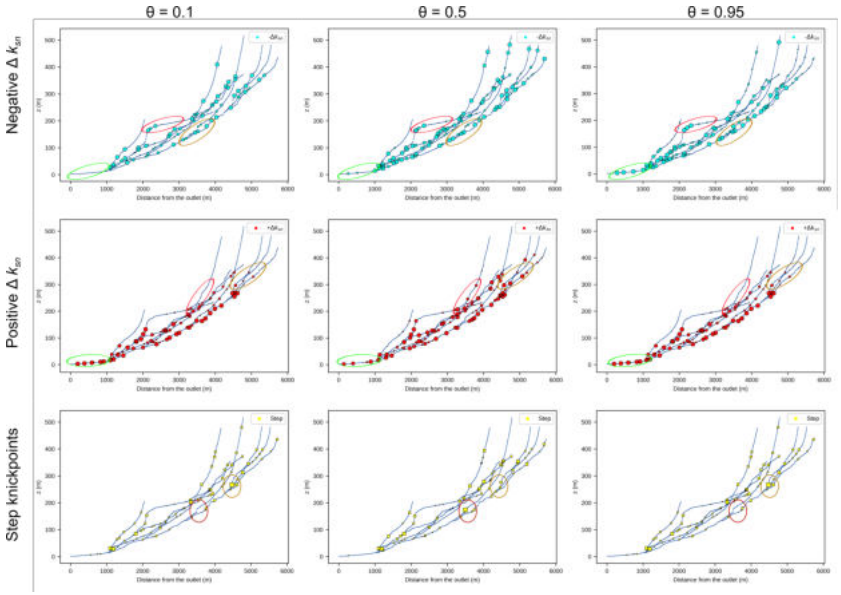

Figure S2. Effect of θ used to calculate χ prior to the calculation of k_{sn}. These profiles, calculated for various θ, show that the relative magnitude of the knickpoints is affected. For each knickpoint morphology (i.e., a decrease of k_{sn}, an increase of k_{sn} and stepped knickpoints), we circle example zones where the relative magnitude of knickpoints is significantly impacted by the change in θ. The largest knickpoints are the ones with an absolute $\Delta k_{sn} > 3^{rd}$ quartile of the population and the smallest knickpoints the ones with an absolute $\Delta k_{sn} < 1^{st}$ quartile of the population for each θ. This data has been extracted from the Smugglers catchment described in the main manuscript.

chosen (e.g., Mudd et al., 2018). However, we ran a sensitivity analysis to assess the extent of its effect on the knickpoint extraction as discussed in the main manuscript. We ran the algorithm for a range of θ from 0.1 to 0.95 in 0.5 increments. We find that the relative magnitude of knickpoints is affected by the concavity value, but the location of knickpoints does not significantly change (see Figure S2).

Sensitivity to channel steepness extraction

As discussed in the main manuscript, `target_nodes` and `n_skip` control the size of the segments in the k_{sn} extraction using the Mudd et al. (2014) algorithm. We ran a combined sensitivity analysis on these parameters to assess the effect of segment size in knickpoint extraction. Our results show that the segment size can impact the results of the knickpoint detection, and therefore we suggest that these parameters need to be carefully chosen by the user. Although reference values can be set (e.g. 80 target nodes and a skip value of 2), these parameters depends on data quality: smaller segments will fit the profiles with more fidelity but will therefore be noise sensitive, whereas larger segments can average noise at the risk of ignoring small variations. Therefore, these parameters cannot be set as defaults and depend on the data source (e.g. SRTM 90 m vs airborne lidar). Figure S3 shows results for a wide range of segment size jointly controlled by the 2 parameters. It shows that smaller segments fit the river profile with higher fidelity. It also impacts the knickpoint extraction: smaller segments tend to catch steep reaches (e.g. waterfalls) by fitting a segment to it (and therefore 2 slope break knickpoints) when larger segments tend to express such reaches with a step (and therefore as a stepped knickpoint). It also slightly changes the knickpoint location on the river long profiles, as different river nodes are used depending on the segment size.

Another parameter linked to k_{sn} extraction is the number of iterations used in the segment-fitting algorithm (*e.g.* how many times a sub-set of nodes is picked following a Monte-Carlo sampling scheme). We ran a sensitivity analysis with a range from 1 to 1000. The results shows that more iterations tend to

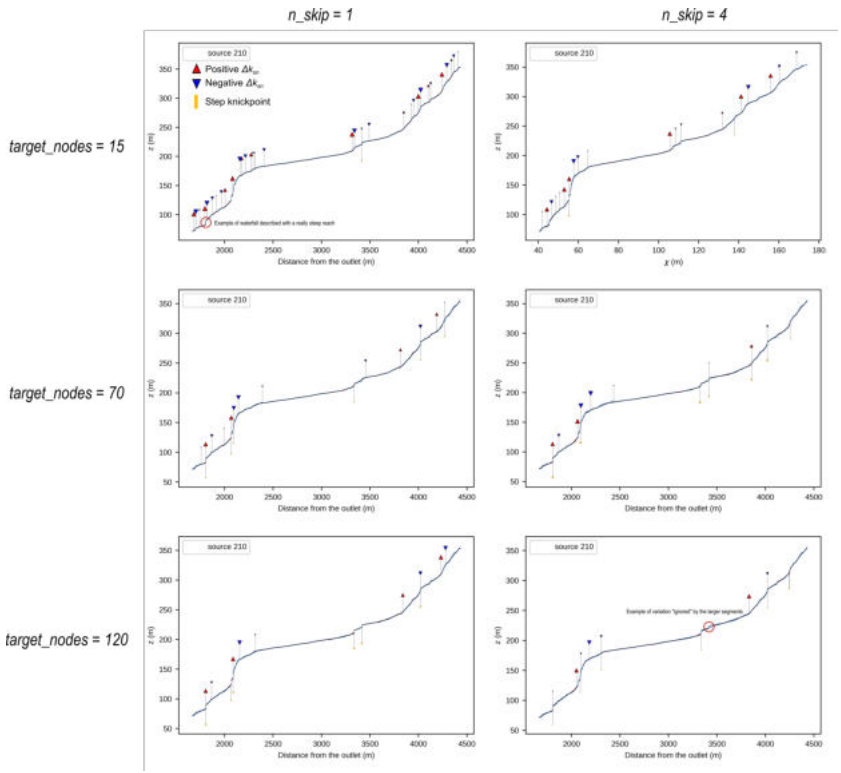

Figure S3. Effect of ***target_nodes*** and ***n_skip*** on knickpoint extraction. Smaller values (top-left) generate smaller segments than high values (bottom-right). River profiles are diplayed in blue, with the segments extracted with the Mudd et al. (2014) algorithm on top in black. Knickpoints are represented with marker offset to the river profile in order to highlight the segment boundaries. This data has been extracted from the Smugglers catchment described in the main manuscript.

produce cleaner signals and we therefore recommend a minimum value of 50 for this parameter. However, increasing this parameter to above 50 will not significantly affect the algorithm output.

Sensitivity to the combining window

Despite using a denoising algorithm to clean our k_{sn} data, some stepped knickpoints can still be expressed as a succession of slope break knickpoints. We therefore use a combining window to solve this problem (full explanation in the main manuscript). We ran a sensitivity analysis on the size of this window, with a range of 0 to 100 nodes. Results showed in the main manuscript and in Figure S4 suggest that this parameter does not have a significant influence on the results, except when set with extreme values ($<$10 or $>$50). A combining window of 0 can result in underestimating knickpoint magnitudes in steepened reaches and

therefore bias the statistical sorting of knickpoints. High values, on the other hand, can result in the merging of unrelated knickpoints.

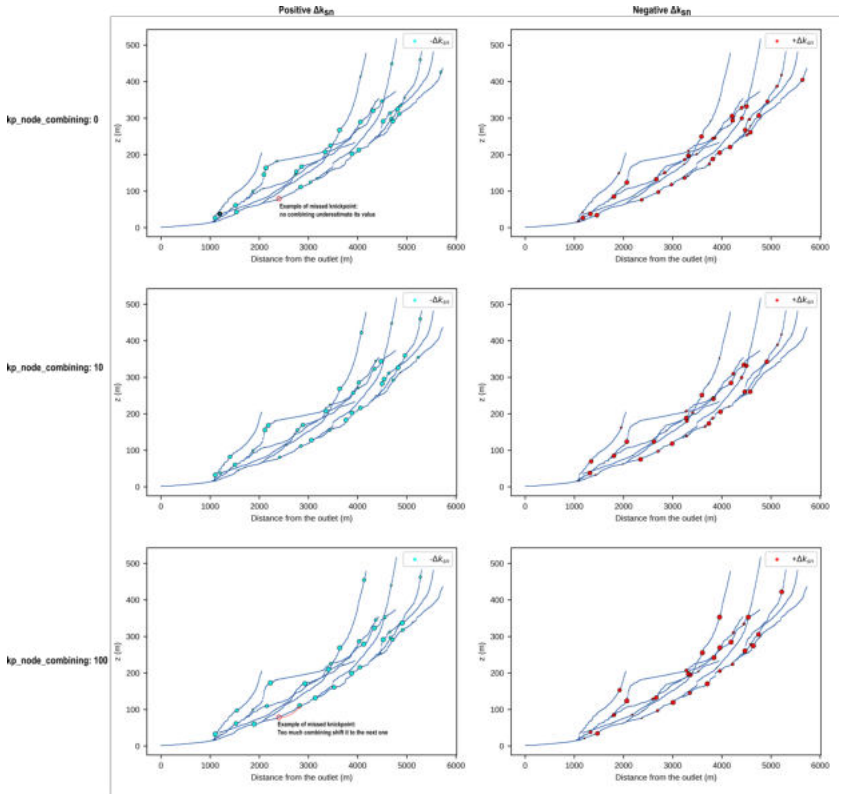

Figure S4. Effect of *kp_combining_node* on knickpoint extraction. Values are calculated and sorted with the same threshold as in the main manuscript. It shows that the results are not significantly affected as long as the size of the combining window is within a reasonable range. This data has been extracted from the Smugglers catchment described in the main manuscript.

Sensitivity to step knickpoint detection

Stepped knickpoint detection is controlled by two parameters: *window_stepped_kp_detection*, which we call r_W in the manuscript, and *std_dev_coeff_stepped_kp*, which we call T_σ in the main manuscript. We ran a combined sensitivity analysis to determine their values as discussed on the main manuscript and shown in Figure S5. r_W tends to not significantly alter the results as long as it is set with a minimum size of 80 nodes (we recommend 100 to 150 based on our tests). T_σ needs to be selected more carefully: a low value generates a high number of artifacts (e.g. each node of a steep reach would be picked) and a high value inhibits knickpoint detection. However results show that effective values are within a relatively

narrow range (from 6 to 8).

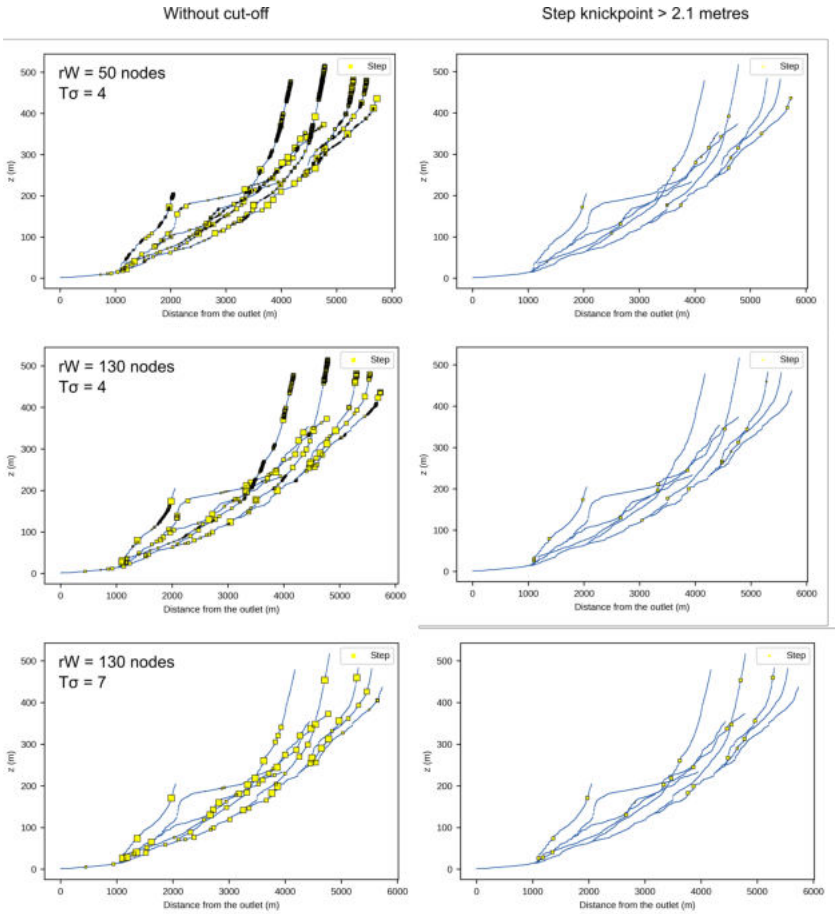

Figure S5. Sensitivity of knickpoint detection to r_W and T_σ. On the left the basin-wide river profiles show the raw data and on the right the data after applying the same threshold as in the main manuscript. This data has been extracted from the Smugglers catchment described in the main manuscript.

Sensitivity to reference area

As discussed in the main manuscript, deriving k_{sn} from χ-elevation profiles can be affected by the difference in the realtive magnitude of χ and elevation. As θ increases, the values of χ decrease, but elevation is not affected. For high values of θ (e.g., 0.85) it is not unusal for the change in χ to be several orders of magnitude less than the change in elevation over a single segment. We compare the slope break knickpoints by their drop or increase of k_{sn}, and therefore these extreme values can bias data sorting by overestimating the importance of such knickpoints. We therefore tested the sensitivity of A_0 from the χ equation. Increasing the

value of A_0 correspondingly increases the absolute value of the χ coordinates, and therefore removes this bias. However, if A_0 is not equal to 1, the magnitude of the knickpoint can no longer be described in terms of k_{sn}. In these cases it is equivalent to $M_\chi = \frac{E}{K * A_0^m}^{1/n}$ as described in Mudd et al. (2014). Therefore, we suggest that A_0 should only be modified from 1 if the extracted θ values are very high.

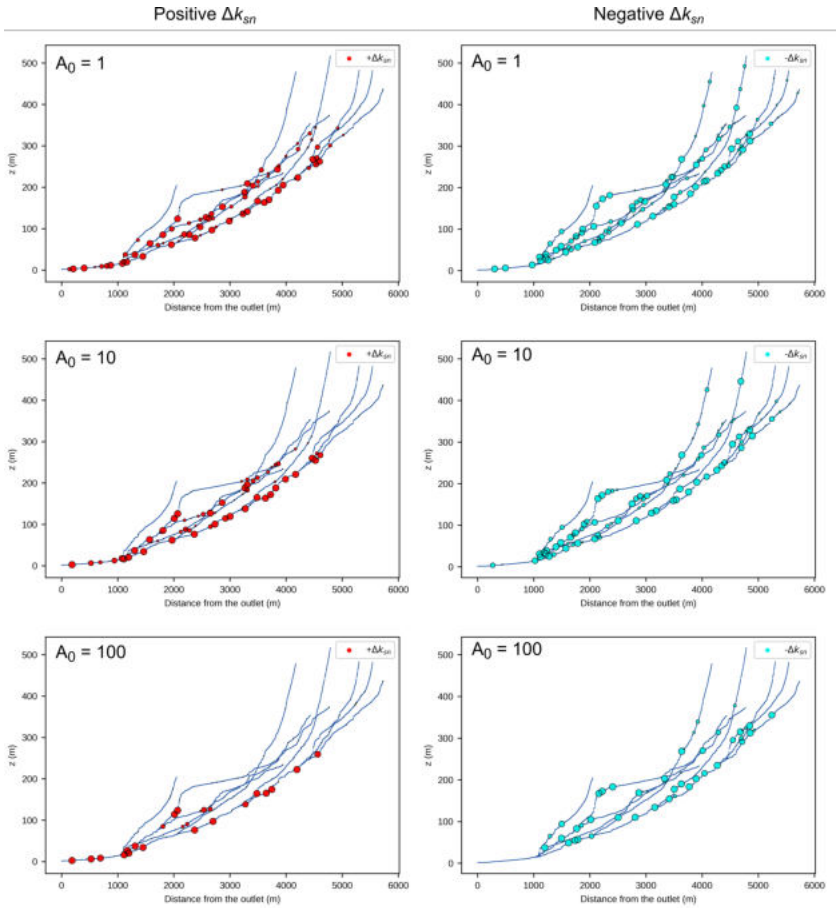

Figure S6. Sensitivity of knickpoint detection to the A_0 parameter. Extraction has been performed with a high $\theta = 0.85$ in order to highlight the effect of A_0 on the k_{sn} values. Note that the high-magnitude knickpoints on the steepened reach tend to decrease in magnitude and even disappear when increasing A_0. This data has been extracted from the Smugglers catchment described in the main manuscript, but with a significantly different θ for the specific aim of this sensitivity analysis.

Sensitivity to grid resolution

As suggested in the main manuscript, grid resolution affects knickpoint extraction. The segmentation process used to calculate k_{sn} depends on the number of

nodes describing each river. Lower grid resolution leads to a lower number of nodes describing each river and therefore a lower number of segments. Knickpoints are located at segment boundaries, so fewer segments will result in fewer extracted knickpoints. This behaviour is illustrated in Figure S7, where we extracted the knickpoint with $n_{tg} = 10$ and $n_{sk} = 1$ for a grid resolution downgraded using "GDAL" from the original Smugglers 1m lidar DEM from 5 meters, 10 meters (e.g. TanDEM-x) and 30 meters (e.g. SRTM, Aster).

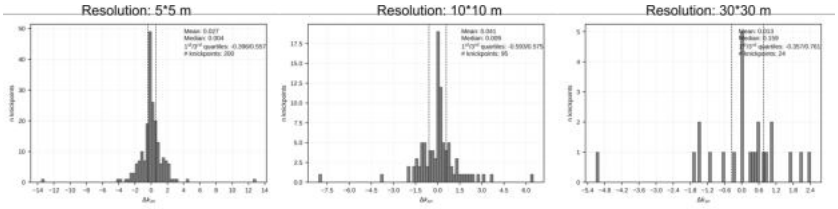

Figure S7. Sensitivity of knickpoint identification to grid resolution in the Smugglers catchment. Knickpoints have been extracted for a range of downgraded DEM grids. The statistical distribution and the number of slope-break knickpoints shows that coarser grid resolution results in the extraction of significantly fewer knickpoints than extraction from finer grid resolutions.

Additional methodological details

The main manuscript tests the algorithm on two sites: The Smugglers catchment on Santa Cruz Island (California, USA), chosen because of its well constrained topography, freely available high resolution topographic data (lidar) and independently picked knickpoints; and the Caraca catchment (Quadrilatero Ferrifero, Mina Gerais, Brazil), chosen because of field knowledge from the area. We present and discuss the results in the main manuscript, but we provide here more details of the different outputs produced with the algorithms.

The Smugglers catchment (California, USA)

Channel head extraction:

We took advantage of the high-precision 1-metre airborne lidar DEM to extract channel heads using the Pelletier (2013) method. The extracted sources and the resulting channel network are presented in Figure S8.

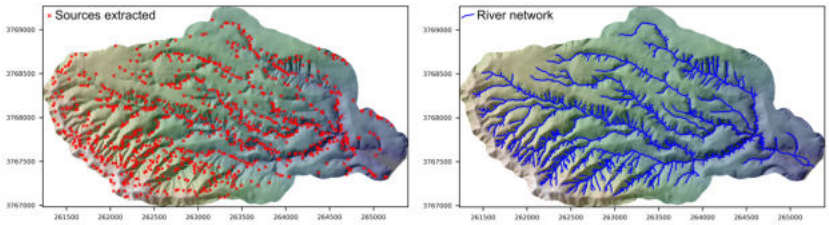

Figure S8. Extraction of the channel heads or sources (left) and the subsequent channel network (right) in the Smugglers catchment. All the sources have an ID which allowed us to select same channels as in the calibration dataset.

Concavity

After extracting the river network, we determine a best-fit concavity using the method implemented in Mudd et al. (2018). The best-fit range of concavities is shown in Figure S9. For this paper we used a value of 0.25, consistent with Neely et al., 2017, which was within the range of best-fit suggested by the results of this algorithm.

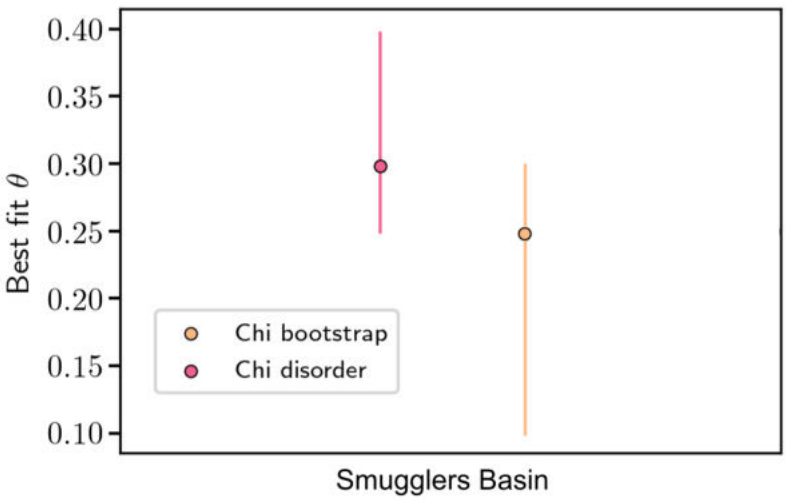

Figure S9. Best-fit concavity using the boostrap and disorder methods described in Mudd et al. (2018) applied to the Smugglers catchment. Both of these include 0.25 in their best-fit range, which was the value used in Neely et al (2017).

Knickpoint extraction

The knickpoint extraction was performed using the following parameters (all the non-specified parameters have been set to default values, we refer to `https://lsdtopotools.github` presented in Table S2:

The extraction first produces a dense network of knickpoints, shown in Figure

Parameter	Value	Parameter	Value
channel heads fname	smugglers_Psources	min_slope_for_fill	0.0001
m_over_n	0.25	ksn_knickpoint_analysis	true
force_skip_knickpoint_analysis	1	force_n_iteration_knickpoint_analysis	500
target_nodes	30	n_nodes_to_visit	30
TVD_lambda	1.7	kp_node_combining	10
window_stepped_kp_detection	120	std_dev_coeff_stepped_kp	7

Table S2. List of non-default parameters used for knickpoint extraction.

S10. Knickpoints are sized by magnitude as described in the main manuscript.

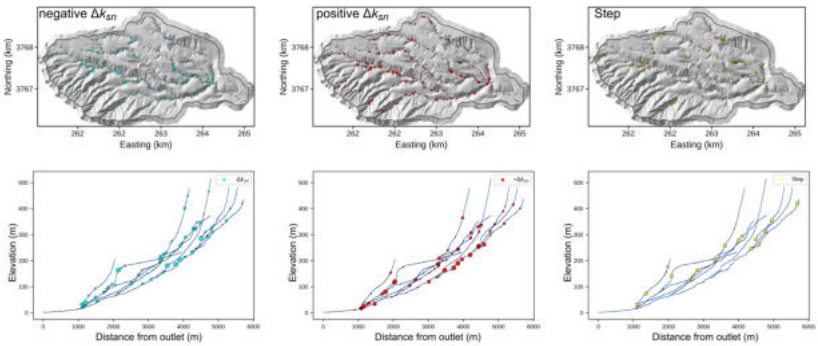

Figure S10. Raw knickpoint extraction in the Smugglers catchment displayed by type of knickpoint: left column shows the knickpoints expressing a drop of k_{sn}, middle column the knickpoints expressing an increase of k_{sn}, and the right column the vertical step knickpoints.

We sorted this dataset using the statistical distribution of these knickpoints, in order to select relevant cut-off values. These cut-offs have been selected in the specific aim to (i) match with the calibration dataset for comparison purposes, (ii) remove insignificant knickpoints (those with very low magnitude). The knickpoint distributions and cut-off values are shown in Figure S11.

The main results after the sorting procedure are shown in the main manuscript, but here we present an extended version (Figure S12) where knickpoints are separated by morphology.

Caraca, Quadrilatero Ferrifero (Brazil)

Our second test site in the Caraca Basin (QF, Brazil), we provide below more details about the analysis.

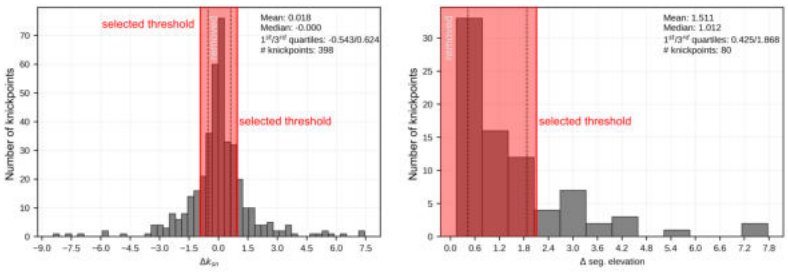

Figure S11. Distribution of knickpoint magnitude by knickpoint type from the extraction in Figure S10: on the left the Δk_{sn} and on the right the increase of z_{seg}. The chosen cut-off values are illustrated by the vertical bar. The red areas represent the removed knickpoints.

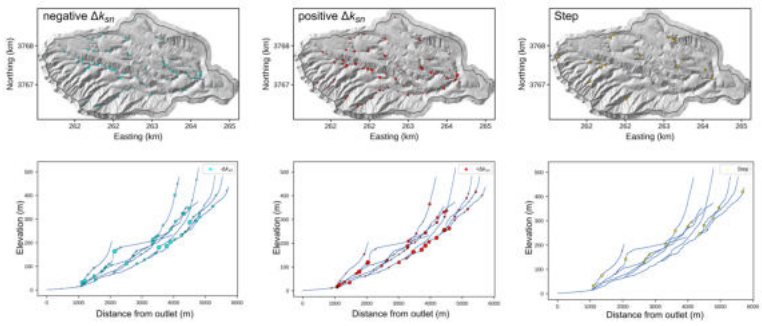

Figure S12. Knickpoint extraction separated by knickpoint morphology after knickpoint cutoff determined in Figure S11: left column shows the knickpoints expressing a drop of k_{sn}, middle column the knickpoints expressing an increase of k_{sn} and the right column the knickpoints expressing step knickpoints.

Geological context

One of the features of the Caraca region is its heterogeneous lithology that exerts a control on the drainage network. We provide here the lithological map of the Caraca basin to illustrate this complexity, on the following Figure S13.

Knickpoint extraction

Using the same procedure as the previous analysis on the Smugglers catchment, we first produced a statistical distribution of extracted knickpoints. Figure S14 shows a histograms of the detected slope-break and stepped knickpoints.

We also provide a detailed basin-wide profile view per knickpoint type (Fig. S15) and in map view (Fig. S16).

This first extraction has been used to select cut-off values to thin the dataset and extract significant knickpoints, as discussed in the main manuscript. We

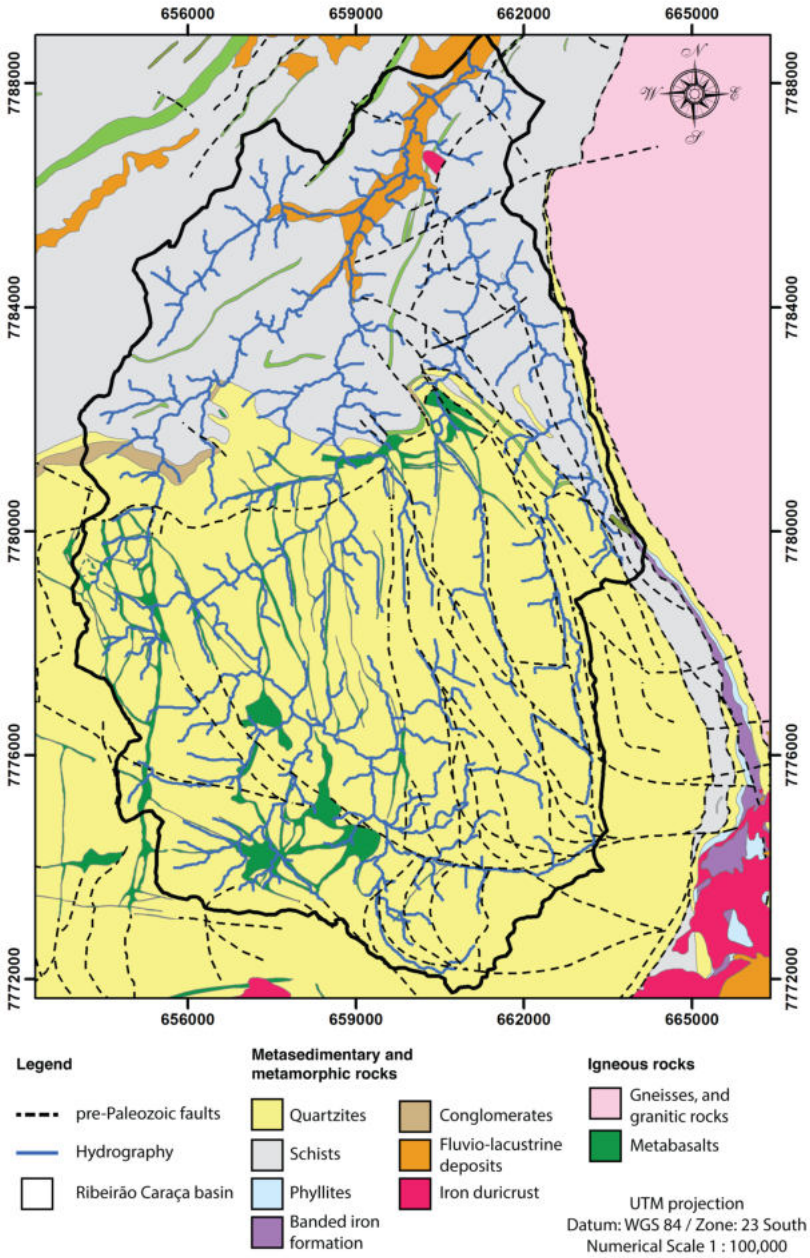

Figure S13. Lithology of the Caraca Basin (QF, Brazil).

also provide an additional figure comparing the detected knickpoints to known field-mapped locations.

Denoising river profiles

In the discussion, we mentioned trying to reduce the θ dependency of the denoising λ parameter by applying our TVD routine to the elevation. This cannot be directly applied to elevation as the TVD routine is designed to flatten a signal

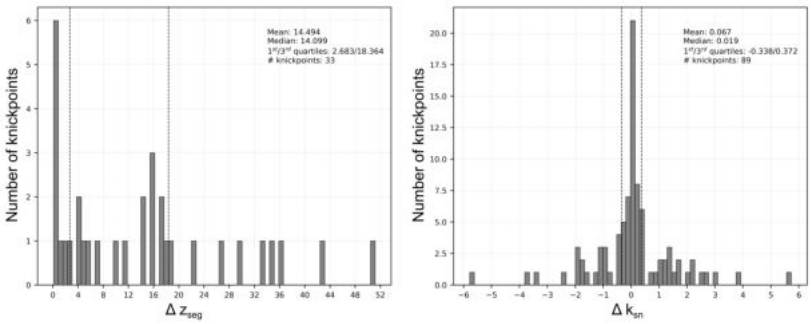

Figure S14. Histograms of the different knickpoint types in the Caraca Basin.

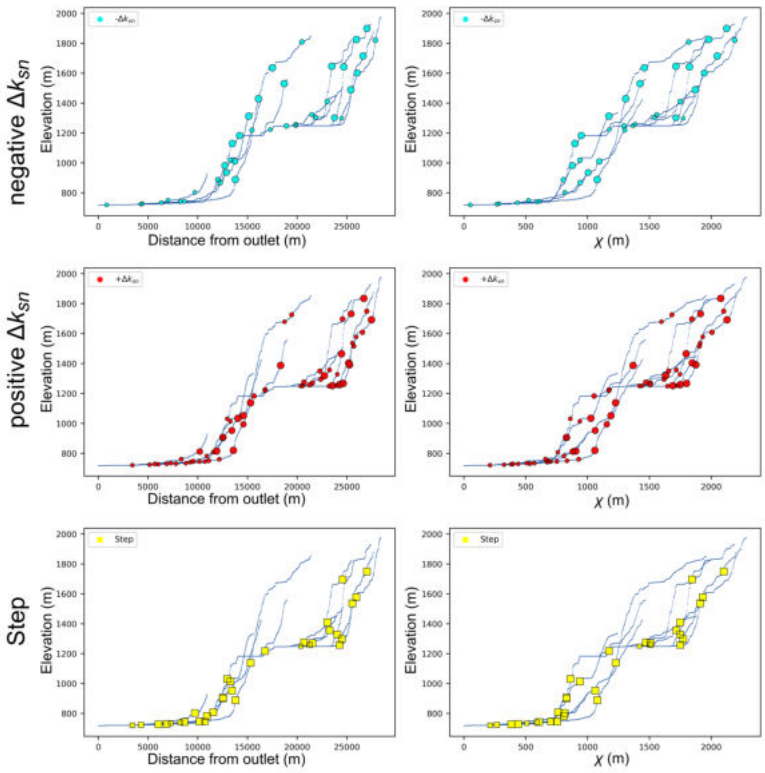

Figure S15. Long and χ profile (left and right columns, respectively) for the Caraca catchment for each type of knickpoint.

and elevation increases monotonically along river profiles. We therefore apply it on Δ of elevation in order to flatten patches of δz and then retrend the profile from base to top. Figure S18 shows the effect of denoising on the original profile.

The following Figures (S19 and S20) show knickpoint extraction in a map view and profile view, respectivly, after denoising the profile with $\lambda = 5$, and then applying the same thinning strategy described in the manuscript. Note that

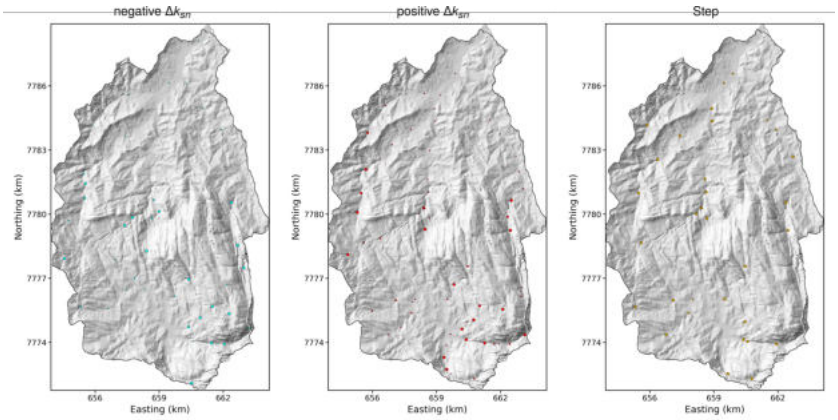

Figure S16. Map view of each type of knickpoint, extracted for the Caraca basin before thinning.

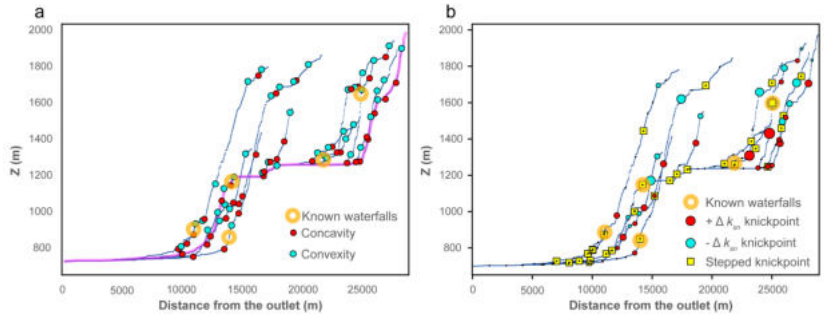

Figure S17. Additional comparison between knickpoints picked by the algorithm described in the main manuscript and those identified by field mapping in the Caraca basin. a) Thinned selection of knickpoints focused on increase and drop of k_{sn} compared to field mapping. b) Raw knickpoint detection before thinning.

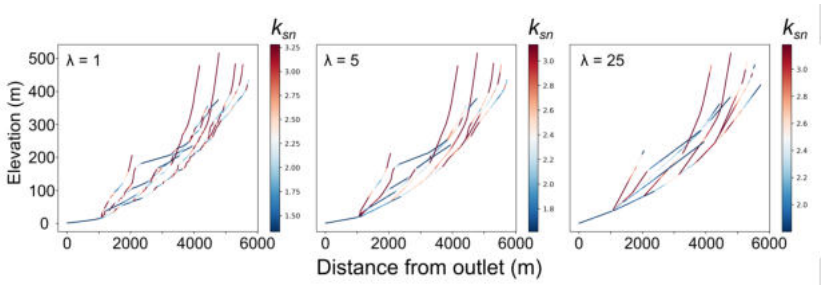

Figure S18. Denoised river profile for different values of (λ) in the Smugglers catchment. The original data is altered by this process and we do not recommend its implementation.

denoising has the effect of removing all the step knickpoints.

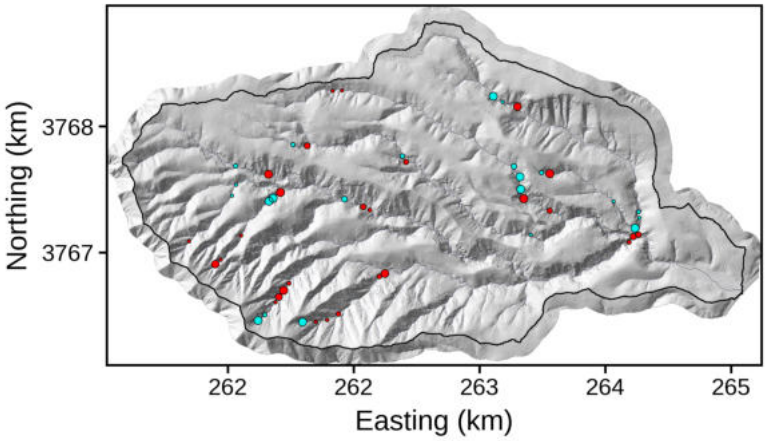

Figure S19. Map view of knickpoint extracted with denoised profile in the Smugglers catchment. Denoising intensity λ has been set to 5.

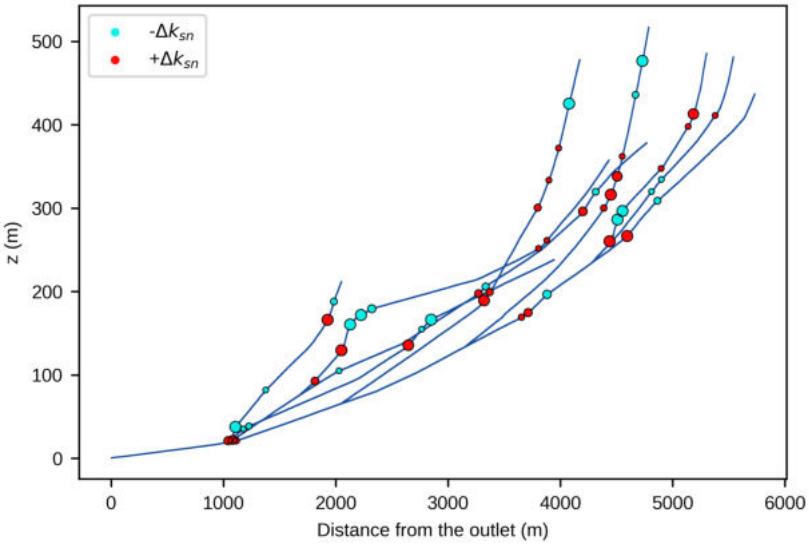

Figure S20. Profile view of knickpoints extracted with the denoised profile in the Smugglers catchment. Denoising intensity λ has been set to 5.

Extra test site

In the main manuscript, we applied our method to specific test sites for the reasons detailed in Section 3. These test sites happen to have high resolution DEMs (1-m lidar and 12.5-m TanDEM-x) available. Here we test the method on a lower resolution dataset.

Saline Valley (CA, USA)

This test site has been explored in Kirby and Whipple's (2012) review on

tectonic geomorphology and provides an example of knickpoints expressed by reductions in channel steepness. These knickpoints have been interpreted to result from fault activity (see Figure 12 in the review paper). We therefore extracted these "negative k_{sn}" knickpoints from SRTM data (downloaded from opentopography.org) and compared the results with the knickpoints manually extracted in the original study. Figure S21 depicts the results.

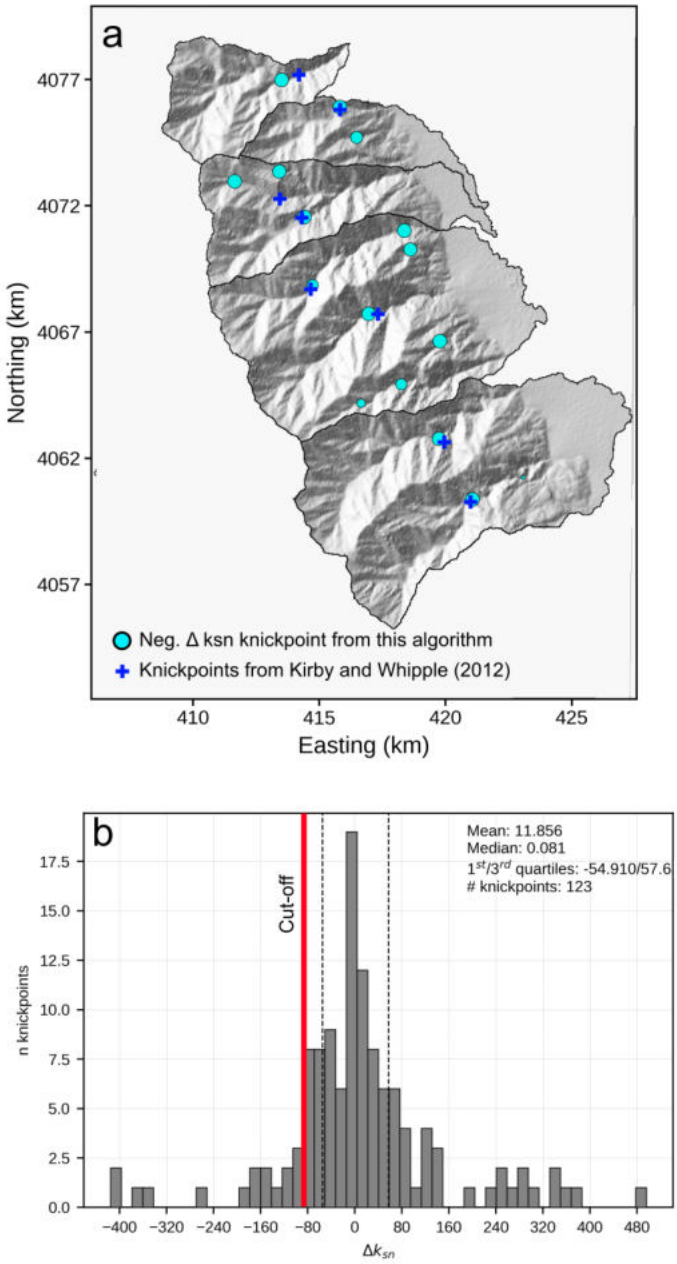

Figure S21. a) Map view of knickpoints in the Saline Valley site, both from Kirby and Whipple (2012) and extracted using our algorith with $\theta = 0.45$ (suggested in Kirby and Whipple (2012)); $n_{tg} = 80$; $n_{sk} = 2$; $n_{MC} = 200$; $\lambda = -1$ (automatic); and $r_{comb} = 15$. b) Statistical distribution of raw knickpoint magnitude and chosen threshold of -80 to extract significant drops of channel steepness.